A RADIO MEASUREMENT OF THE STAR FORMATION HISTORY OF THE UNIVERSE

Allison Matthews
Gorham, Maine

B.S. Physics, B.S. Mathematics, Lafayette College, 2015

M.S. Astronomy, University of Virginia, 2017

A Dissertation Presented to the Graduate
Faculty of the University of Virginia
in Candidacy for the Degree of
Doctor of Philosophy

Department of Astronomy

University of Virginia
August 2021

Committee Members:

James J. Condon
Eric J. Murphy
Mark Whittle
Mark Lacy
Jeffrey Holt

Abstract

Most of the stars in the universe were formed by disk galaxies like our own Milky Way during an era poetically called "cosmic noon." This era, occurring $t \approx 3$ billion years after the Big Bang, marked the peak of not only star formation, but also black hole growth and dust attenuation. The dust that permeates all galaxies absorbs and scatters the ultraviolet and optical light primarily generated by massive stars, whose lives are so short that they provide an effectively instantaneous measurement of the star formation rate. Understanding the formation and evolution of galaxies at cosmic noon is essential to understanding how the universe appears and acts today—but the uncertainties imposed by dust are worst during this influential period. Radio emission is entirely unaffected by dust and is generated by supernova remnants of the same massive stars emitting primarily in the UV and optical. Radio observations of star-forming galaxies are therefore a powerful tracer of star formation rate, but it has not been until the past decade that radio observations have been sensitive enough to detect Milky Way-like galaxies at cosmic noon. In this dissertation, I calculate and combine the source counts from the deepest radio continuum image to date with the local luminosity function of radio sources to model the star formation history of the universe.

I determined the local luminosity functions for both star-forming galaxies (SFGs) and active galactic nuclei (AGNs) using $N \sim 10,000$ radio sources from the NRAO VLA Sky Survey (NVSS) cross-identified with galaxies in the 2MASS Extended (2MASX) catalog (Chapter 2). The AGNs and SFGs were separated using only radio and infrared data rather than optical emission-line diagnostics, which are not good quantitative measures of AGN-powered radio emission. Our sample of radio sources with $\log[L_{1.4\,\mathrm{GHz}}(\mathrm{W\,Hz^{-1}})] > 19.3$ account for $> 99\%$ of the total 1.4 GHz energy density in the nearby universe. The local radio-derived star formation rate density (SFRD) value of $0.0128\,M_\odot\,\mathrm{yr^{-1}\,Mpc^{-3}}$ is consistent with previous models for the SFRD derived using ultraviolet and infrared data.

In Chapter 3, I present radio source counts across eight decades of flux density

spanning $0.25\,\mu\mathrm{Jy} < S < 25\,\mathrm{Jy}$ determined from the deepest $\nu = 1.4\,\mathrm{GHz}$ radio continuum image taken by the MeerKAT radio interferometer in South Africa and the archival NVSS component catalog. With an rms noise $\sigma = 0.56\,\mu\mathrm{Jy\,beam}^{-1}$ and a resolution of $\theta_{1/2} = 7\overset{\prime\prime}{.}6$, the MeerKAT DEEP2 image is confusion-limited, so below $S = 10\,\mu\mathrm{Jy}$ I calculated the source counts statistically from the confusion brightness distribution $P(D)$. Above $S = 10\,\mu\mathrm{Jy}$ the source counts were measured directly from the DEEP2 image and the NVSS component catalog.

The evolving energy-density function $u_{\mathrm{dex}}(L_\nu|z)$ is the comoving energy density of radiation produced by sources at redshift z having spectral luminosity ($\mathrm{W\,m^{-2}\,Hz^{-1}}$) L_ν at frequency ν. Simple equations relate the brightness-weighted differential source counts $S^2 n(S)$ with $u_{\mathrm{dex}}(L_\nu|z)$ integrated over all redshifts (Appendix C). Using a combination of luminosity and density evolution, I developed evolutionary models (Chapter 4) for SFGs and AGNs that accurately predict the observed source counts given the local luminosity functions. Through the FIR/radio correlation, the product of luminosity and density evolution of radio sources is directly related to the total SFRD evolution $\psi(z)$, describing how many stars (by mass) were formed per year per comoving cubic megaparsec. The radio-derived model for SFRD evolution is similar to previous models based on UV/IR data, but predicts stronger star-formation evolution. Chapter 5 reviews the main conclusions of this dissertation and discusses future work.

Acknowledgements

In the third grade my Father chaperoned a class hike up a nearby mountain, from the top of which you could spy an antenna tower. Pointing it out to my teacher, I exasperatedly said something like "that's what my Dad designs, it is sooo booooring." Twenty years later, antennas have become integral to myself as a radio astronomer—I literally could not have done this work without them. So, I'd like to start these acknowledgments with an apology.

To my Father: I am sorry that I grew up thinking the world of antennas was boring. I hope that our nerdy phone conversations about waveguide and RF fields have shown that I have changed my opinion since then, I love antennas. Growing up, you never got tired of answering my many questions, taught me math beyond my years, and gave me the freedom to be curious about everything. As both my parents know far too well, I want to know *everything*.

To my Mother: Hearing you talk about going into computer science in the 80s—even though it wasn't always easy—was the best example a daughter could ask for. Growing up, I never questioned whether I could do anything; I knew I could. Thank you for always being there for a chat on the phone, especially when I was working too much. I needed you to tell me when "enough is enough."

To my brothers: Thank you for keeping me grounded in reality, for making me laugh, and for being my biggest cheerleaders.

To my advisor Jim: Thank you for agreeing to advise a quiet yet curious stranger who walked into your office years ago. I could never quantify how much you've taught me or how much I have appreciated every long conversation in your office, sincerely thank you. I look forward to working on more projects in the future.

To my first advisor, David: I cannot think of a better first research advisor. By introducing me to pulsars you converted me into an astronomer. Thank you for all the support and opportunities you gave me, it is a huge reason I'm here now.

To Kelsey: You turned out to be so much more than a research advisor. Your encouragement and belief in me has meant the world. I hope to be as fierce as you someday.

Graduate school is never easy, but sometimes there are additional factors that make it unbearably scary and seemingly impossible. The love and support I felt from my fellow graduate students was beyond what I ever could have imagined. Thank you, always, from the bottom of my heart.

To my cohort: you are all amazing humans. Thank you for the long heart-to-heart walks, shenanigans in the office, and delicious meals we shared. And to those not in my cohort, thank you for the lovely trips to vineyards, for getting a puppy so I could puppy-sit, and for all the (mostly online, these days) conversations that have kept me going. To everyone in DSBK (especially Assessments), thank you for pushing me outside of my comfort zone and reminding me to have fun. Volunteering with you all has been one of the most rewarding experiences.

To Sandy: You have a lifetime of getting sappy cards from me, so I'll keep this one short. Thank you for being you, but especially for being the Dog to my Cat.

To Joe: Thank you for being there through it all. You made even the hardest parts of this process fun and I'm lucky to have had your enduring support. I can't tell you enough how much I appreciate you, and will continue to do so.

To Patches: You aren't here anymore, and if you were you wouldn't be able to read this, but you were the sweetest gutter cat there ever was. Thank you for waiting outside my door every day until I got home, for giving me the stink eye when I needed to sleep, and for reminding me there is always good in this world.

Table of contents

List of Figures

List of Tables

Chapter 1

Introduction

1.1 The Star Formation History of the Universe

The electromagnetic energy and "heavy" elements (anything with an atomic number greater than that of Helium) in today's universe were forged by the cumulative star formation activity that came before. When astronomers began measuring how quickly stars formed at a given time (the star formation rate; SFR) $\sim$7 billion years ago (a redshift of $z \sim 1$), they found that galaxies had SFRs dramatically greater than those today at $z = 0$ (e.g. Songaila et al. 1994; Ellis et al. 1996; Lilly et al. 1996). Astronomers continued this work and began measuring the SFRs of increasingly distant galaxies, finding that at the beginning of the universe's history, the star formation rate density (SFRD; the SFR per unit comoving volume) rose rapidly until it peaked at an age of $\sim$ 3 billion years and has been exponentially declining ever since.

1.1.1 Cosmic Dawn

Within the first few hundred million years after the big bang (the exact time is still debated), the universe expanded and cooled down enough to allow dense hydrogen and helium gas to succumb to gravity and collapse into the first population of stars. These stars coalesced into the first galaxies, and somewhere along with them grew the

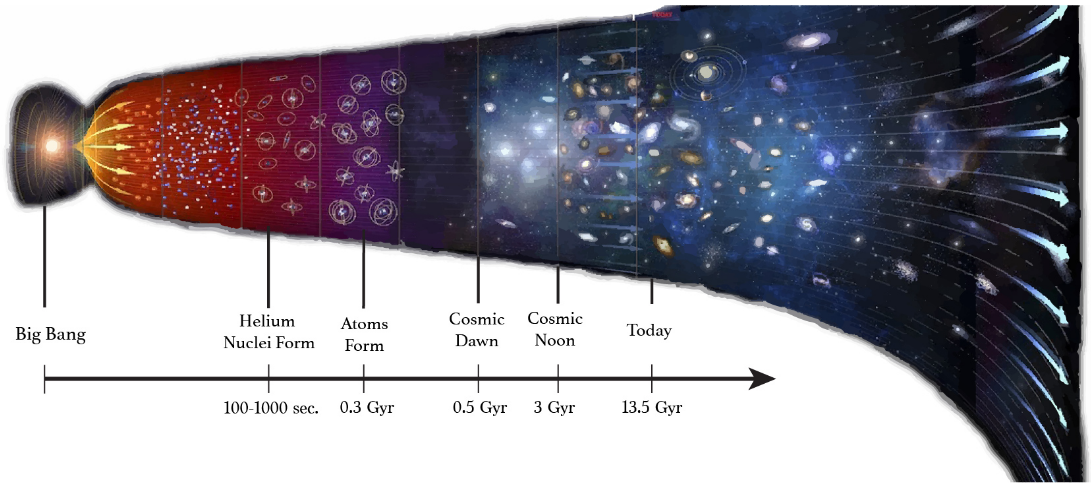

Figure 1.1. Graphic representation of the evolutionary eras of the universe adapted from National Geographic. "Cosmic Dawn" and "Cosmic Noon" are labeled on the non-linear timeline.

first black holes. The exact processes of how the first stars, galaxies, and black holes formed may be unknown, but a quick glance at the nearby universe assures us that it did indeed happen. As the first stars fused hydrogen in their cores, their radiation ionized the dark, neutral atoms that filled the universe at that time. This period is poetically referred to as "cosmic dawn" (labeled in reference to the evolution of the universe in Figure 1.1). Detecting signatures from this "epoch of reionization" could inform us on the physical conditions and formation mechanisms behind the first stars, galaxies, and black holes. Unsurprisingly, it is among the hottest pursuits in modern astronomy, but this thesis focuses on the peak epoch of star formation and evolution—cosmic noon.

1.1.2 Cosmic Noon

The production rate of stars, galaxies, and black holes rose rapidly after cosmic dawn until reaching a peak when the universe was $t \approx 3$ billion years old (Madau & Dickinson 2014). Keeping with the theme, this period is known as "cosmic noon." Approximately half of the stars in our universe (by mass) were formed in the $\sim 3\,\mathrm{Gyr}$ years surrounding cosmic noon when the universe was $t = 2-5$ Gyr years old. During this period, the universe was only $1/4 - 1/2$ of its current size and galaxies and stars were undergoing more-frequent mergers and had more interstellar gas. Interactions in merging systems create dense environments that drive the collapse of gas into protostars, leading to an extreme burst of star formation. Even in individual star-forming disk galaxies at cosmic noon, the rate of star formation was $\sim 10\times$ that of disk galaxies today (see Figure 1.2).

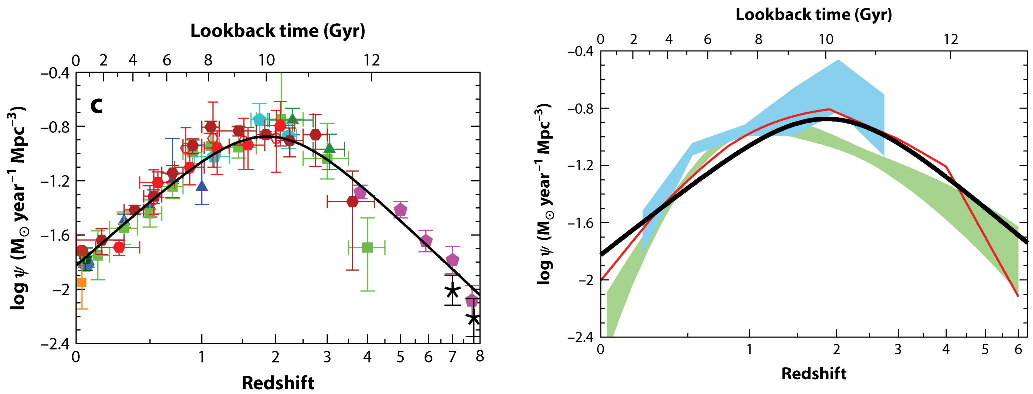

Figure 1.2. Left: From Madau & Dickinson (2014), the rate of star formation (in solar masses per year) per comoving cubic megaparsec (Mpc^3) as a function of redshift. The data points are independent measurements of the SFRD from UV or IR observations and the black curve shows the best model of the SFRD evolution based on these data. The peak of star formation, cosmic noon, occurs at $z \approx 2$. Right: From Madau & Dickinson (2014), the black curve shows the same evolutionary model for the SFRD as shown in the left panel. The blue and green shaded regions and red curve show measurements of the black hole growth (in mass) as a function of redshift. This similarity between these curves is evidence that the stellar masses and black hole masses of galaxies coevolve.

There are several reasons why the star formation rate began to decline after cosmic noon. For one, much of the massive gas reservoirs powering the boom had been converted into stars, thus limiting the supply for the production of future stellar generations. Further, gas needs to be both dense *and* cold in order for gravity to dominate over the internal pressure of a molecular cloud and cause it to collapse into stars. There are a number of processes that impart energy in the form of heat into gas clouds and prevent star formation from continuing: supernovae, stellar winds, and active galactic nuclei (to name a few).

An "active galactic nucleus" (AGN) occurs when the central supermassive black hole (widely believed to exist in nearly every galaxy; Kormendy & Ho 2013) is accreting surrounding gas. Observations of black hole masses and calculations of their accretion rates have revealed that the evolution of black hole growth follows a strikingly similar function as that of star formation (see right panel of Figure 1.2). This is one piece of evidence that the feedback of energy from supermassive black holes in the center of galaxies regulates the amount of star formation—in other words, galaxies and black holes co-evolve (e.g. Kormendy & Ho 2013).

1.2 Star Formation Rate Measures

Every measure of an extragalactic star formation rate fundamentally measures the rate at which *massive* stars are forming. Stars greater than $8M_\odot$ have lifetimes $\tau \leq 30\,\mathrm{Myr}$, significantly less than the lifetime of a galaxy—making them a relatively instantaneous probe of how many stars are forming at a given time. In order to understand the *total* mass of stars forming, astronomers extrapolate to lower masses using an initial mass function (IMF), which specifies the relative rate of star formation as a function of mass down to $\sim 0.1\,M_\odot$. The various IMFs (e.g. Chabrier 2003; Salpeter 1955) indicate different numbers of lower mass ($M < 8\,M_\odot$) stars forming for a given star formation rate of massive stars. Thus the choice of an IMF heavily influences the total SFR of a galaxy and introduces a major systematic uncertainty in the measurements of extragalactic star formation. Astronomers specify the IMFs they are using, so comparisons between different measures of SFRs done at various wavelengths remain valid.

Stars with masses $M > 8\,M_\odot$ emit primarily in the ultraviolet portion of the electromagnetic spectrum, making observations at these wavelengths desirable for determining the SFR of a galaxy. Ultraviolet observations of nearby galaxies are inaccessible from the ground, but at redshifts $z \geq 1.4$ the rest-frame ultraviolet emission is redshifted into the ground-observable optical bands. While the UV emission of a galaxy directly probes the formation rate of massive stars, it has a major downside; it is easily obscured by dust. At the peak of star formation, at redshift $z \sim 2$, measurements of the dust attenuation imply that $> 80\%$ of star formation is obscured (Reddy et al. 2012; Howell et al. 2010).

Dust particles obscuring the UV radiation re-emit it at mid-infrared (MIR; $8 - 25\,\mu$m) and far-infrared (FIR; $42.5 - 122.5\,\mu$m) wavelengths, making the luminosity of a galaxy at these wavelengths a practical method of measuring its SFR. The total infrared spectrum of a galaxy ($8 - 1000\,\mu$m) is complex, and the reradiation of UV photons from massive stars is not the sole source of emission. The metallicity and geometry of dust particles affects how much of the UV luminosity they absorb, and at wavelengths longer than $\lambda \sim 100\,\mu$m the infrared luminosity is powered primarily by dust heated by evolved stars (Hirashita et al. 2003; Bendo et al. 2010). The warm dust in the surrounding areas of massive stars emits at MIR wavelengths and is therefore tightly correlated with star formation, but polycyclic aromatic hydrocarbons (PAHs) complicate the emission spectrum near $\lambda = 8\,\mu$m and active galactic nuclei (AGNs) dilute these PAH features while also contributing significantly to the $24\,\mu$m continuum emission.

1.3 Sources of Radio Emission

Radio sources in galaxies (the leftmost line in Figure 1.3) contribute only a small fraction of the electromagnetic background. Most of the electromagnetic energy in the universe is in radiation left over from the big bang—the cosmic microwave background (CMB). Nevertheless, the radio sky provides a unique window to some of the most energetic and extreme objects (e.g. black holes and pulsars). "Normal" objects such as star-forming, disk galaxies also emit at radio frequencies, but they are much weaker sources than the most luminous AGNs. Early observations of the radio sky were dominated by luminous AGN-powered radio galaxies and quasars, but recent upgrades to the receivers and computers of radio telescopes have paved the way for

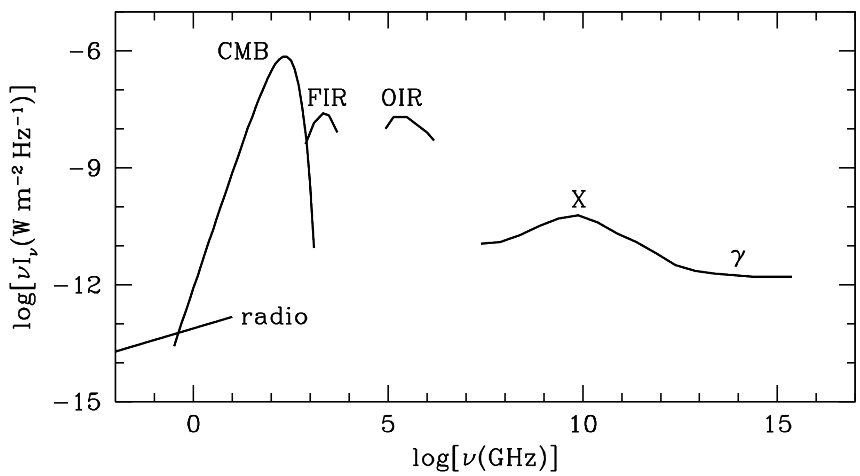

Figure 1.3. The spectral energy distribution of the sky as a function of logarithmic frequency. The emission of radio sources comprises a small fraction of the overall electromagnetic energy budget of the universe.

observations of normal galaxies—often providing an independent and complementary perspective from other wavelengths. Sources of radio emission include

- powerful radio galaxies and quasars powered by supermassive black holes;
- spectral-line emission from cold interstellar gas;
- pulsars and magnetars;
- the cosmic microwave background;
- neutral hydrogen in and among galaxies;
- star formation.

1.4 Radio Emission from Star-Forming Galaxies

Stars more massive than $8M_{\odot}$ end their short lives in a dramatic explosion, and the remaining supernova remnants are threaded with magnetic field lines. The relativistic, free electrons that permeate the surrounding area spiral around the magnetic field lines and, due to this acceleration, emit radio light in the form of synchrotron emission. This emission can be described by a power-law in the form $S \propto \nu^{\alpha}$, where α is the spectral index ($\alpha \sim -0.8$ for pure synchrotron radiation). In this way, radio

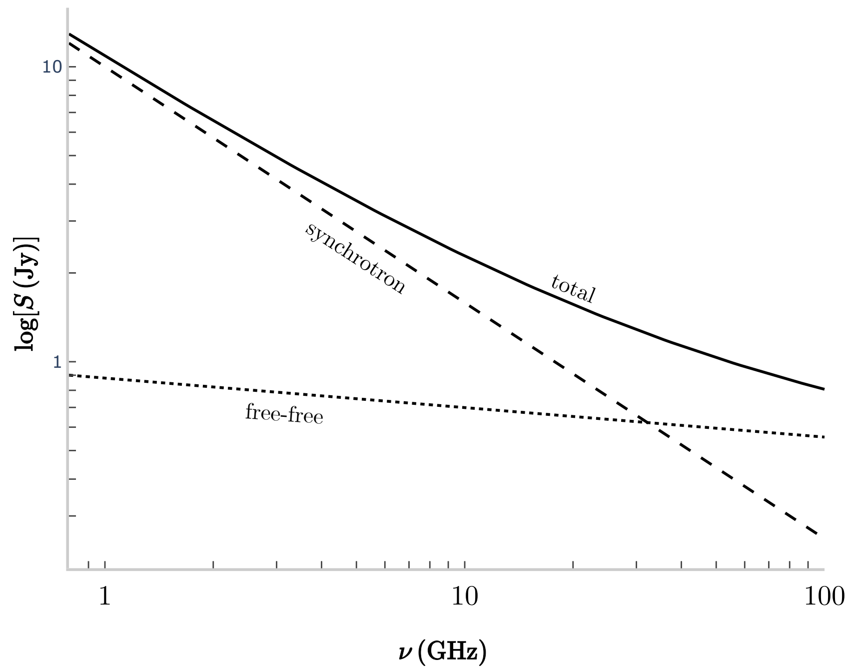

Figure 1.4. A typical radio spectrum of a star-forming galaxy from 1 to 100 GHz. Synchrotron radiation with a spectral index of $\alpha = -0.8$ is shown as the dashed line. Free-free emission with a spectral index of $\alpha = -0.1$ is shown as the dotted line. Only above $\nu \sim 30\,\mathrm{GHz}$ that the weaker free-free emission starts to dominate the spectrum.

observations of normal galaxies are sensitive to the star formation rate of massive stars.

There is another radiative process contributing to the radio spectrum of a star-forming galaxy that is directly correlated to the number of ionizing photons from massive stars: free-free emission. Also called bremsstrahlung (from the German *bremsen* to brake and *strahlung* radiation), it occurs when a free electron is accelerated by the electric field of an ion (usually a proton), but remains a free particle both before and after the interaction. Massive, short-lived stars emit radiation that ionizes surrounding gas, creating a plethora of free electrons and protons that frequently interact and emit free-free radiation at radio frequencies.

Free-free emission is a minor component of the total radiation at $\nu \sim 1\,\mathrm{GHz}$ (see Figure 1.4). Only at frequencies $\nu > 10\,\mathrm{GHz}$ does it start to dominate over synchrotron radiation. A well-understood relation between radio, dust-unaffected free-free emission and massive stars makes it a valuable tracer of star formation in galaxies. There are, unfortunately, a few obstacles preventing it from being the obvious choice of radio astronomers for tracing star formation.

First, it is an unavoidable reality that the free-free emission of a SFG is weak at low GHz frequencies, but more importantly it is much weaker than the synchrotron emission at 1.4 GHz. This leads to longer integration times in order to detect it in distance sources. Second, observing at these higher frequencies is more difficult and necessitates dryer weather conditions—at frequencies above 20 GHz absorption by atmospheric water vapor absorbs radio radiation and emits noise. Third, both the primary beam (field of view) becomes smaller and the resolution increases at these frequencies. This makes it observationally expensive to survey a large area of sky, and the lower surface brightness sensitivity introduces the possibility of resolving out (or partially resolving) faint objects whose angular sizes are larger than the restoring beam.

The next generation of radio telescopes (e.g. the next-generation VLA; ngVLA) will alleviate many of these concerns. Increasing the number of dishes and redesigning the dishes to have unblocked apertures will enhance the sensitivity of radio observations at these frequencies. It will then be much more tractable and enticing to use free-free emission to trace extragalactic star formation both nearby and at cosmic noon. Until then, synchrotron radiation at lower frequencies $\nu \sim 1\,\mathrm{GHz}$ remains the dependable workhorse for radio observations of star-forming galaxies. It, of course, comes with its own selection of problems; it lacks a physical derivation connecting itself to the star formation rate and is also generated by active galactic nuclei (AGNs). Fortunately, there is strong empirical evidence connecting synchrotron radiation with star formation—the FIR/radio correlation found for nearby galaxies.

1.4.1 The FIR/radio Correlation

The relation between synchrotron luminosity and SFR is not well understood theoretically. The physics governing the steps from the supernova explosion to the acceleration of relativistic electrons in the supernova remnant, to the cooling of the cosmic rays as they propagate through the galaxy is poorly understood. The reliability of radio synchrotron emission as a SFR tracer is therefore dependent on confirmation from multi-wavelength observations.

The release of the *IRAS Point Source Catalog* in 1985 provided an optimal comparison sample for 1.4 GHz radio observations of normal galaxies. The far-infrared (FIR) flux, combined from 60 and 100 μm measurements, should be an excellent indicator of star formation activity since dust heating in disk galaxies and starbursts is dominated by young massive stars (Sauvage & Thuan 1992; Bell et al. 2003; Bendo et al. 2012). From a sample of 38 *IRAS* sources with corresponding $\nu = 1.4\,\mathrm{GHz}$ observations the FIR flux in $\mathrm{W\,m^{-2}}$

$$\mathrm{FIR} = 1.26 \times 10^{-14}[2.58 f_\nu(60\,\mu\mathrm{m}) + f_\nu(100\,\mu\mathrm{m})], \tag{1.1}$$

where $f_\nu(60\,\mu\mathrm{m})$ and $f_\nu(100\,\mu\mathrm{m})$ are flux densities in Jy, was compared with the $S_\nu(1.4\,\mathrm{GHz})$ flux density in Jy. Helou et al. (1985) found a tight correlation between FIR and radio flux densities in normal galaxies across "a wide range of objects and conditions: from quiescent disks like M31, to the steady state activity in late-type spirals, to galaxies dominated by a nuclear starburst."

Helou et al. (1985) defined the parameter q as the logarithm of the FIR/radio flux-density ratio:

$$q = \log\left[\frac{\mathrm{FIR}/(3.75 \times 10^{12}\,\mathrm{Hz})}{S_\nu(1.4\,\mathrm{GHz})}\right], \tag{1.2}$$

where 3.75×10^{12} Hz is the bandwidth spanned by the 60 μm and 100 μm flux densities and $S_\nu(1.4\,\mathrm{GHz})$ is in $\mathrm{W\,m^{-2}\,Hz^{-1}}$, has been measured for thousands of additional galaxies since the initial studies in the late 1980s. The correlation has held for galaxies with magnetic field strengths, star formation rates, and stellar masses spanning multiple orders of magnitude, earning itself a reputation as a "conspiracy." The physical processes responsible for the FIR and radio emission are quite different, so it is remarkable that they are so tightly correlated.

The FIR-radio correlation (Figure 1.5) was initially derived from galaxies in our

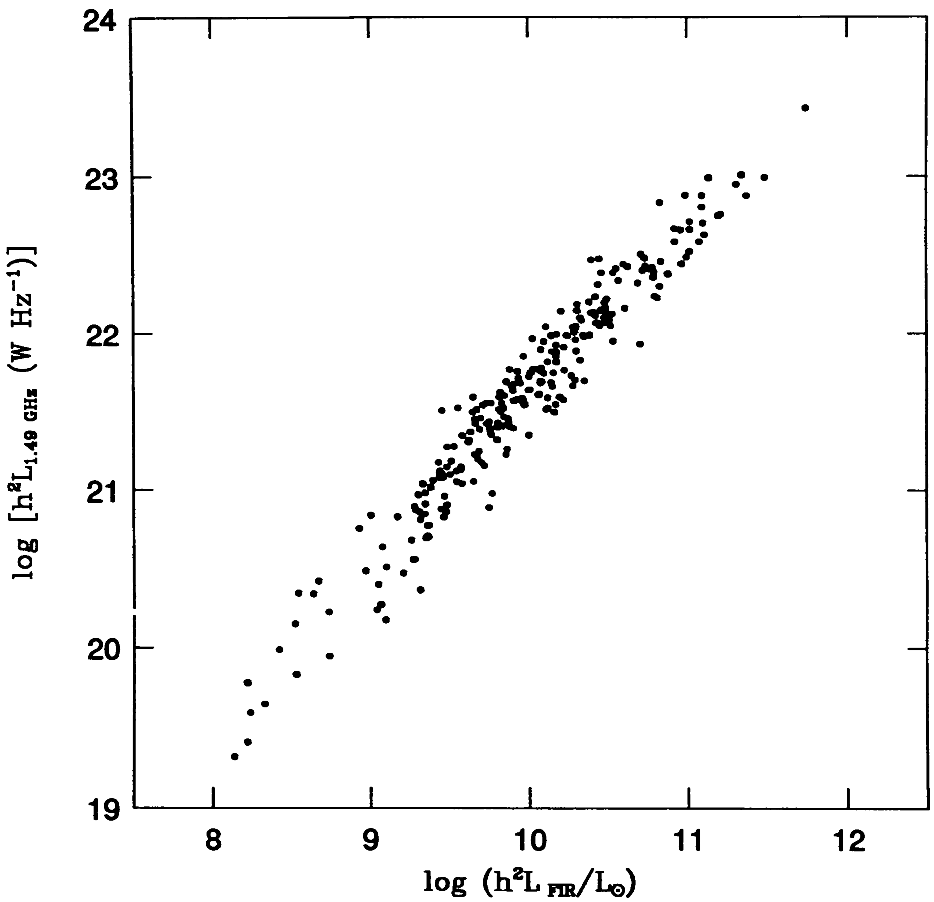

Figure 1.5. The FIR/radio correlation as presented in Condon (1992) for galaxies in the *IRAS* Revised Bright Galaxy Sample.

local universe, so its validity as a tracer of the star formation rate of distant galaxies hinges upon either a lack of evolution with redshift or a detailed understanding of its evolution. There is a theoretical reason to be concerned that the radio luminosity due to synchrotron radiation may evolve with redshift (Condon 1992). The total energy density of a galaxy is the combination of its magnetic energy density $U_{\rm m}$ and its radiation energy density $U_{\rm r}$ such that $U_{\rm t} = U_{\rm m} + U_{\rm r}$. The ratio of the magnetic energy density $U_{\rm m}$ to total energy density $U_{\rm t}$ dictates the fraction of relativistic electrons (and positrons) that cool due to synchrotron radiation and the fraction $U_{\rm r}/U_{\rm t}$ is lost to inverse Compton scattering. In order for the FIR/radio correlation to hold in distant galaxies, this ratio $U_{\rm m}/U_{\rm t}$ needs to remain nearly constant with redshift.

Locally, the radiation energy density component U_{r} comes primarily from stars. As redshift increases, the radiation energy density from the Cosmic Microwave Background (CMB) increases as $U_{\mathrm{CMB}} \propto (1+z)^4$ and will eventually dominate over the magnetic energy density of star-forming galaxies. Under this scenario, the radio luminosity would begin to decrease with redshift for the same FIR luminosity and q would increase.

In studies that report slight evolution of the FIR/radio correlation q with redshift, the opposite trend was observed. These have found that the radio luminosity seems to be increasing with redshift for the same FIR luminosity. Recently, using $\nu = 3\,\mathrm{GHz}$ VLA data from the Cosmological Evolution Survey (COSMOS), Delhaize et al. (2017a) found that the ratio of FIR to radio luminosities q has evolved as $q \propto (1+z)^k$ with $k = -0.21 \pm 0.1$. A further study of the same data by Molnár et al. (2018) split the sample of star-forming galaxies into those dominated by disks to those dominated by spheroids. They found that there is no evolution with redshift for the disk-dominated galaxies, but the q ratio of spheroid-dominated galaxies evolves with an exponent k similar to that of Delhaize et al. (2017a). It is important to note that there have also been numerous studies which have found no evolution of q with redshift (Sargent et al. 2010; Bourne et al. 2011; Barger et al. 2012; Del Moro et al. 2013; Pannella et al. 2015). These results are all based on the assumption that the FIR/radio ratio is linear and do not clearly distinguish between evolution with z and nonlinearity. It largely remains unclear whether q indeed evolves with z or if the measured evolution is simply a symptom of systematic uncertainty. Sargent et al. (2010) noted that using flux-limited samples selected solely from radio or infrared surveys can introduce a bias that artificially produces an evolution in the FIR/radio correlation.

1.5 Star-forming galaxies in the nearby universe

Regardless of the wavelength astronomers use to measure the cosmic evolution of the star formation rate density (SFRD) they first need to understand the current level of star formation activity. While dust properties within and among local galaxies can differ greatly depending on environment (Dale & Helou 2002; Smith et al. 2007), the FIR/radio correlation is remarkably tight across orders of magnitude changes in the physical characteristics of galaxies.

In the case that the waveband of observation is dominated by young stars (e.g. radio, FIR), the primary method for measuring how much star formation is occurring in our local universe is through the local luminosity function of star-forming galaxies. The local luminosity function $\rho(L)$ describes the mean space density of galaxies as a function of luminosity. The range of spectral luminosities spanned by galaxies is so large that it is convenient to define a logarithmic spectral luminosity function,

$$\rho_{\rm dex}(L_\nu) \equiv \rho(L_\nu)\frac{dL}{d\log(L)} = \ln(10)\,L\,\rho(L), \tag{1.3}$$

specifying the space density of sources per decade of spectral luminosity. While the luminosity function is the basic measurement, we are more interested in the energy output per unit volume as a function of luminosity—that is what contains information on the star formation rate. The energy density function generated by sources with luminosities between L and $L + dL$ is

$$u(L) = L\rho(L). \tag{1.4}$$

It is similarly convenient to define a logarithmic spectral power density (or energy density) function

$$u_{\rm dex}(L) \equiv \ln(10)Lu(L) = L\rho_{\rm dex}(L), \tag{1.5}$$

which specifies the energy density per decade of spectral luminosity. The total energy produced by star formation per unit volume is the integral of the local radio energy density function over luminosity:

$$U_{\rm SF} = \int_0^\infty u_{\rm SF}(L)\,dL. \tag{1.6}$$

For an energy density function measured at radio frequencies, the total energy put out by star-forming galaxies is related to the local SFRD through the FIR/radio correlation. The local radio-derived SFRD value is an essential ingredient for determining the evolution of radio galaxies (and the SFRD) across cosmic time. In the next section I will describe the second essential ingredient for determining the star formation history of the universe at early times: radio source counts.

1.6 Radio Source Counts

Some radio galaxies and quasars are so luminous that they are strong radio sources even at cosmological distances. In 1955, the steep slope of the integral source counts from the 2C radio survey implied dramatic cosmic evolution for this population of "radio stars" in luminosity or space density (Ryle & Scheuer 1955; Shakeshaft et al. 1955), contradicting the prevailing "Steady-State" cosmology (Hoyle 1948; Bondi & Gold 1948). This result was rejected years later after it was found that the majority of the 2C sources were instead "confusion bumps" caused by the blending of multiple faint sources within the beam (Mills & Slee 1957). When the Cambridge group of astronomers compiled the subsequent 3C and 4C surveys—well aware of the problem of confusion—they had a new tool at their disposal: the $P(D)$ analysis, which can statistically extract the true source count from a confusion-limited survey Scheuer (1957).

The 1960's brought a consensus in the source counts brighter than $S > 0.1$ Jy: a steeper than Euclidean slope above 1 Jy followed by a decrease to sub-Euclidean slopes below 1 Jy (Hewish 1961; Gower 1966). In the 1980's, the discovery of a flattening of the source count slope around $S \sim 1$ mJy (see Figure 1.6) implied the emergence of a new population of faint radio sources corresponding to star-forming galaxies (SFGs) (Condon & Mitchell 1984; Windhorst et al. 1985; Hopkins et al. 1998).

There were large discrepancies among previous attempts to measure the source counts of faint radio sources below $S \sim 1$ mJy (see Figure 1.6). Many of the measurements were made using high angular resolution observations that enable observers to distinguish among galaxies in crowded fields (e.g. Owen & Morrison 2008; Murphy

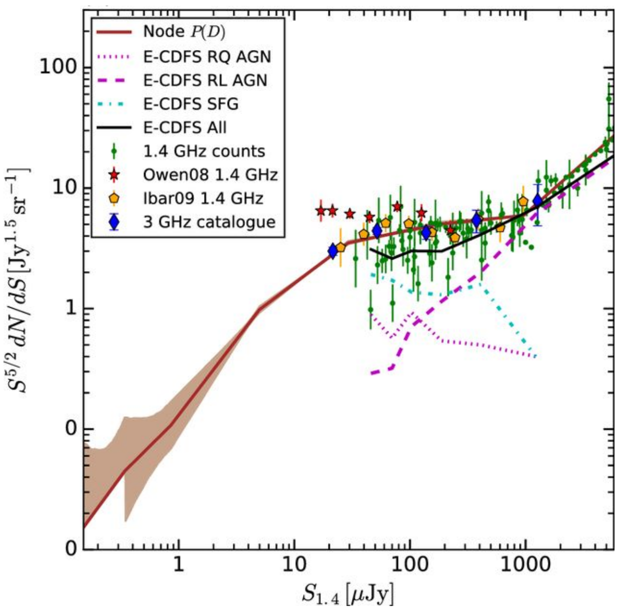

Figure 1.6. Figure from Vernstrom et al. (2016). Euclidean-normalized differential source counts at 1.4 GHz. Counts measured at 3 GHz were converted to 1.4 GHz assuming a spectral index $\alpha = -0.7$.

et al. 2017; Smolčić et al. 2017). While having high angular resolution ensures astronomers do not fall into the same predicament of the 2C survey, it carries its own caveats. As the image resolution θ approaches the intrinsic angular size of the source ϕ the sources become resolved. Image sensitivity limits are brightnesses in units of flux density per beam solid angle. Since the flux density of a resolved source is spread over several beam solid angles, the peak brightness is lowered and the source may fall below the detection limit. Even if the integrated flux density S of a source is above the flux-limit of an observation, if the peak flux density S_{p} is below the detection limit it will be missing from the observations.

The presence of resolved (or partially resolved) sources necessitates corrections on population statistics such as source counts and angular size distributions. The large and uncertain corrections for missing sources are responsible for large discrepancies in the source counts of galaxies around $S \sim 100\,\mu\mathrm{Jy}$ (Figure 1.6). These persistent discrepancies among source counts are much larger than Poisson counting errors and cannot be reconciled by taking galaxy clustering into account (Heywood et al. 2013).

Observations of the same field taken at multiple angular resolutions and similar sensitivity levels yield better corrections, but take significant amounts of telescope time (e.g. Cotton et al. 2018). Counts from a statistical analysis of the confusion distribution $P(D)$ avoid the source-resolution problem because they are made using images with $\theta > \phi$. However, sources much bigger than the beam (e.g. sources with $\phi \gg \theta$) also alter the $P(D)$ distribution. Fortunately, Cotton et al. (2018) showed that nearly all sources in the μJy population have small angular sizes $\phi < 1''$, so $P(D)$ counts made from images with $\theta \sim 7''\!.6$ as in the MeerKAT DEEP2 image need no resolution corrections.

1.6.1 The μJy Radio Population

Star-forming galaxies are not the only sources of radio synchrotron emission. At flux densities $S \geq 400\,\mu$Jy, most of the observed radio sources are high redshift ($z > 1$) AGNs. In order to accurately measure the source counts of star-forming galaxies, SFGs must be disentangled from the population of sources powered by AGNs. The possibility of contamination by AGNs in a sample of star-forming galaxies is a leading source of uncertainty in radio continuum measurements of extragalactic star formation. Fortunately, at fainter flux densities the primary driver of radio emission is no longer AGNs. Below $S \sim 100\,\mu$Jy, star-forming galaxies comprise $> 60\%$ of the radio sources (Van der Vlugt et al. 2020; Vernstrom et al. 2016). Recent studies suggest that below $S \sim 30\,\mu$Jy at 3 GHz ($S \sim 50\,\mu$Jy at 1.4 GHz assuming a spectral index $\alpha \approx -0.7$), the fraction of radio sources primarily powered by star formation approaches unity (Algera et al. 2020).

1.6.2 Measuring Source Counts Through Confusion

The number of radio sources per unit solid angle detectable in an image and reliability of their measured properties is limited by (1): the rms noise of the image σ_{n}, and (2) the angular resolution of the observation. A combination of these factors—especially poor angular resolution—leads to "confusion", sky-brightness fluctuations caused by numerous faint sources in the telescope beam. Ignoring the effects of confusion can lead to errors in the number counts due to the blending of radio sources, spurious sources by the unfortunate superposition of sidelobes, and false enhancement of the apparent intensities of genuine radio sources. Figure 1.7 shows a 3D view of sources in a detailed simulation of a radio observation with the MeerKAT telescope, where the height reflects the flux density of the source(s). The 2D contour view atop the 3D model shows what the radio image would look like, with the black dots showing the positions of simulated sources with flux densities greater than $S \sim 0.1\,\mu$Jy. It is clear from both the fluctuations in the 3D view and the clustering of black points within a "source" in the contour map that it is impossible to accurately measure the flux densities and positions of individual sources.

The brightness of a pixel in a radio image is determined by the underlying distribution of radio sources, the rms image noise fluctuations $\sigma_{\rm n}$, the size of the resolving beam $\theta_{1/2}$, and the primary beam attenuation pattern. For a two-element interferometer, Scheuer (1957) derived a relationship between the differential source counts $n(S)\,dS$—the mean number of radio sources per steradian in the flux density interval dS—and the probability $P(D)$ that the measured deflection D lies in the interval dD. The term "deflection" D was used historically for the deflection of the needle on a chart recorder when recording a signal. The modern equivalent of the deflection D is pixel brightness or peak flux density $S_{\rm p}$ with units (Jy beam^{-1}). The theory has been expanded beyond the two-element interferometer to apply to modern arrays (e.g. Condon 1974) and has been used to constrain radio source counts of point sources so faint that they are blended in the beam and can no longer be counted individually.

The observed $P(D)$ distribution is a convolution of the noiseless $P(D)$ distribution (how the sources would appear in a noiseless image) and the rms image noise distribution. Since these two components are independent, the two rms widths add quadratically to yield the rms width of the observed $P(D)$ confusion distribution. If the noise distribution is Gaussian and uniform throughout the image (as it is in aperture synthesis images), it can be deconvolved to yield the noiseless $P(D)$ distribution that is directly related to the differential source counts.

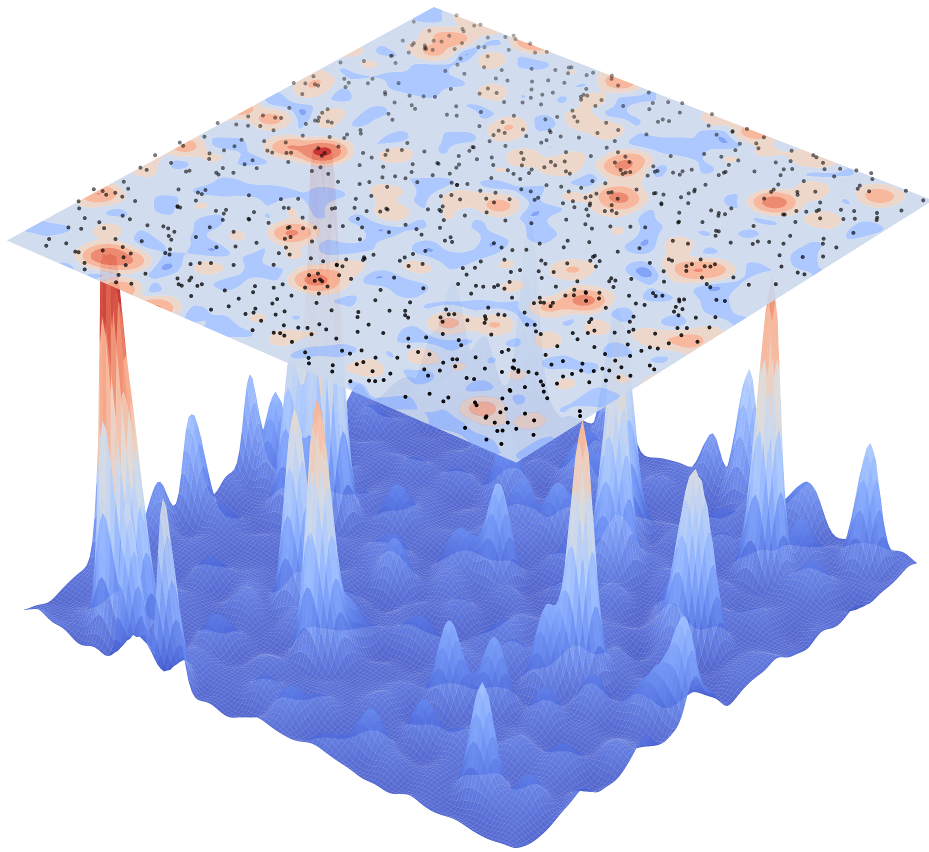

Figure 1.7. A 3D model of the confusion-limited DEEP2 image, where the height of the peaks reflects the strength of the signal. The color scale “heat” map plotted above displays the 2D view typical of a radio image. The black points represent positions of all sources stronger than $0.1\,\mu$Jy, demonstrating the flux enhancement of sources and obstruction of faint sources.

Analytical expressions for the noiseless $P(D)$ distribution can only be derived for differential source counts following a power-law (e.g. $n(S) \propto S^{-\gamma}$), where the value γ determines the shape of the distribution. Figure 1.8 shows $P(D)$ distributions for two values of γ. The value of $\gamma = 1.5$ is representative of source counts below $S \sim 10\,\mu$Jy, where the nature of confusion changes completely. When $\gamma = 1.5$, at any flux density the ratio of the numbers of stronger to fainter sources is much higher than when γ is larger. Sub-μJy sources are more likely to be obscured by stronger sources than to

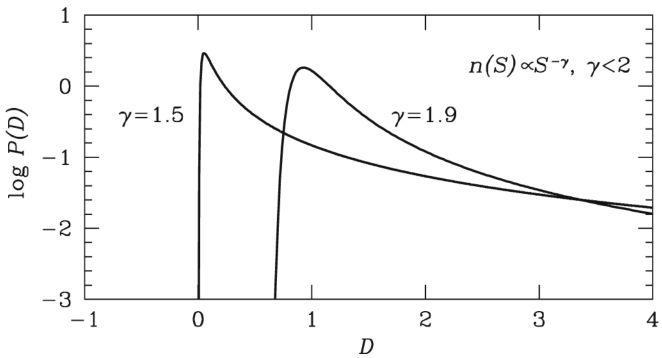

Figure 1.8. Noiseless $P(D)$ distributions derived analytically from power law differential source counts. The value of γ determines the shape of the distribution. These two values $\gamma = 1.5, 1.9$ are appropriate approximates for the source counts below $S \sim 10\,\mu$Jy and in the range $10\,\mu\text{Jy} < S < 0.1\,$Jy.

be boosted in flux density by a background of even fainter sources.

Real source counts across many orders of magnitude in flux density do not follow a simple power law. Since it is impossible to derive an analytic formula for their noiseless $P(D)$ distribution, computer simulations of the radio population are necessary to constrain the counts. In Chapter 3, I describe how creating a detailed and careful simulation of a deep radio field uncovered source counts down to sub-μJy flux densities.

1.7 Modeling the evolution of radio sources

Evolutionary functions applied to the local ($z \sim 0$) luminosity function $\rho_{\rm dex}(L_\nu|0)$ predict the luminosity function at any redshift z. The same is true for the luminosity-weighted spectral luminosity function, the energy density function $u_{\rm dex}$:

$$u_{\rm dex}(L_\nu|z) = g(z)u_{\rm dex}\left[\frac{L_\nu}{f(z)}|0\right], \tag{1.7}$$

where $f(z)$ describes the luminosity evolution and $g(z)$ describes the density evolution. Figure 1.9 plots the energy density function at a redshift of $z \sim 0$ from Condon et al. (2019) and again at a redshift of $z \sim 2$ assuming either pure luminosity evolution or pure density evolution. Pure positive luminosity evolution shifts the energy density

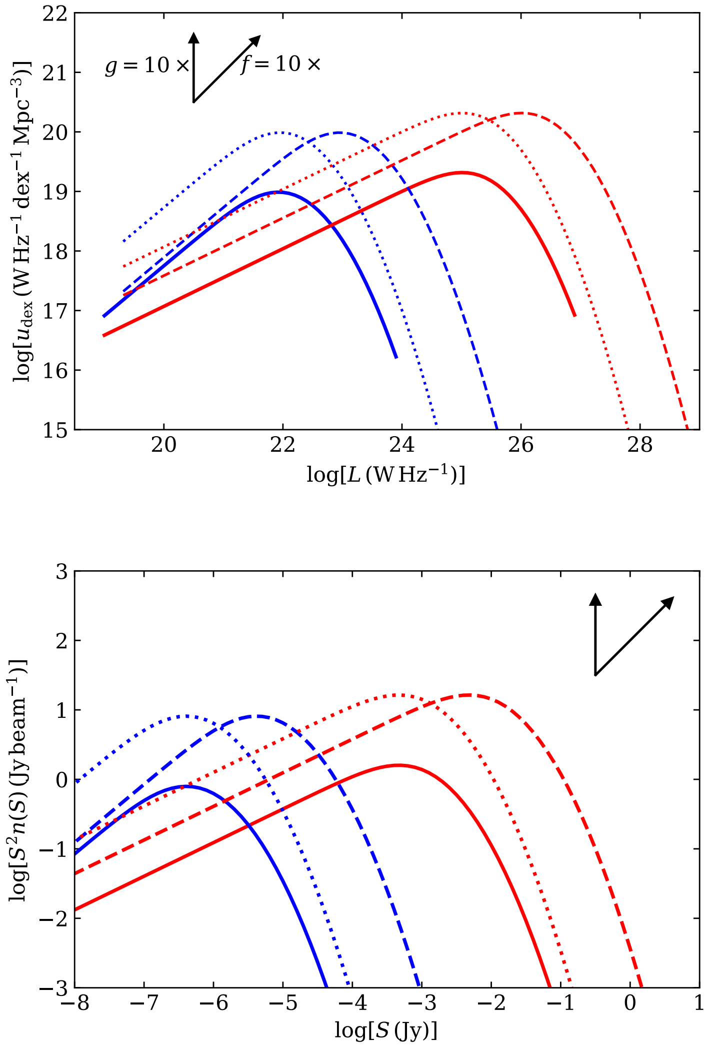

Figure 1.9. Top: local energy-density functions for SFGs and AGNs from Condon et al. (2019) are plotted as the blue and red solid lines, respectively. If local radio sources experienced $10\times$ luminosity or density evolution at redshift $z \approx 2$ the energy-density functions would appear as the dashed and dotted lines, respectively. Bottom: the brightness-weighted radio source counts at redshift $z \approx 2$ assuming no evolution (solid), pure luminosity evolution (dashed), and pure density evolution (dotted) for SFGs (blue) and AGNs (red), respectively.

function equally upward and rightward, while pure positive density evolution shifts $u_{\rm dex}$ directly upward.

The energy density function, which describes the spectral luminosity output per unit volume, is directly related to the total brightness-weighted source counts (see Appendix C)

$$S^2 n(S) = \frac{D_{\mathrm{H}_0}}{4\pi \ln(10)} \int_0^\infty u_{\mathrm{dex}}(L_\nu | z) \left[\frac{(1+z)^{\alpha-1}}{E(z)}\right] dz, \tag{1.8}$$

where D_{H_0} is the Hubble distance, α is the spectral index at frequency ν, and $E(z)$ describes the evolution of the Hubble parameter $H(z)$

$$E(z) = \frac{H(z)}{H_0} = \sqrt{\Omega_r(1+z)^4 + \Omega_m(1+z)^3 + \Omega_\Lambda}\ , \tag{1.9}$$

where Ω_r, Ω_m, and Ω_Λ are the present radiation energy density, matter density, and dark energy density. The observed source counts from Matthews et al. (2021) are plotted for the SFGs and AGNs in Figure 1.9. The form of the brightness-weighted source counts is similar to that of the local energy density function. This is no coincidence—both the brightness-weighted source counts and the energy density function have dimensions of brightness. Applying luminosity and density evolutionary functions shifts the source counts in the same directions as for the energy density function.

The SFRD at redshift z can be expressed in terms of the luminosity and density evolutionary functions

$$\frac{\psi(z)}{\psi_0} = f(z)g(z), \tag{1.10}$$

where $\psi_0 = \psi(z = 0)$ is the SFRD now. Radio source counts constrain ψ by determining the evolutionary functions $f(z)$ and $g(z)$ that evolve the local luminosity function to correctly predict the observed source counts. This method does not require redshifts of individual galaxies, but rather determines the evolution independent of redshift measurements by modeling the entire SFG and AGN population across cosmic time.

Figure 1.10. The MeerKAT array in the Karoo desert in the Northern Cape of South Africa.

1.8 MeerKAT

The MeerKAT telescope (Figure 1.10) was established as a precursor to the Square Kilometer Array (SKA) and resides in the dry Karoo desert in the Northern Cape of South Africa. The location is far from bustling civilization so as to minimize the effects of radio interference. It is composed of 64 antennas, each of which is 13.5 m in diameter but is just as sensitive as a 25 m VLA dish. The 64 dishes are arranged in a centrally concentrated group of 48 antennas (good for surface brightness sensitivity) with the remaining dishes at longer baselines (good for resolution) with a maximum baseline of 8 km. It currently operates at frequencies from ~ 500 MHz to ~ 1.7 GHz, but will expand this range into higher frequencies as construction of the larger SKA continues.

Chapter 2

Local Radio Luminosity Function

2.1 Preface

The star formation rate density (SFRD) of the local universe can be measured from the local luminosity function (the mean space density of galaxies as a function of spectral luminosity) of star-forming galaxies and the FIR/radio correlation. This chapter presents the 1.4 GHz local luminosity functions based on a large sample ($N \sim 10^4$) of radio sources stronger than 2.45 mJy at 1.4 GHz in the NRAO VLA Sky Survey (NVSS) identified with bright galaxies ($k_{20\mathrm{fe}} < 11.75$) in the 2 Micron All-Sky Survey eXtended (2MASX). The 2MASX sample at $\lambda = 2.16\,\mu$m—a wavelength at which dust extinction is fairly weak and luminosity is roughly proportional to total stellar mass—is spectroscopically complete and covers a sky area of $\Omega = 7.016\,$sr. The remainder of this chapter has been published in the Astrophysical Journal (Condon et al. 2019).

2.2 Abstract

We identified 15,658 NRAO VLA Sky Survey (NVSS) radio sources among the 55,288 2 Micron All-Sky Survey eXtended (2MASX) galaxies brighter than $k_{20\mathrm{fe}} = 12.25$ at $\lambda = 2.16\,\mu$m and covering the $\Omega = 7.016$ sr of sky defined by J2000 $\delta > -40°$

and $|b| > 20°$. The complete sample of 15,043 galaxies with 1.4 GHz flux densities $S \geq 2.45\,\mathrm{mJy}$ contains a 99.9% spectroscopically complete subsample of 9517 galaxies with $k_{20\mathrm{fe}} \leq 11.75$. We used only radio and infrared data to quantitatively distinguish radio sources powered primarily by recent star formation from those powered by active galactic nuclei. The radio sources with $\log[L(\mathrm{W\,Hz^{-1}})] > 19.3$ that we used to derive the local spectral luminosity and power-density functions account for $> 99\%$ of the total 1.4 GHz spectral power densities $U_{\mathrm{SF}} = (1.54 \pm 0.20) \times 10^{19}\,\mathrm{W\,Hz^{-1}\,Mpc^{-3}}$ and $U_{\mathrm{AGN}} = (4.23 \pm 0.78) \times 10^{19}\,\mathrm{W\,Hz^{-1}\,Mpc^{-3}}$ in the universe today, and the spectroscopic subsample is large enough that the quoted errors and dominated by cosmic variance. The recent comoving star formation rate density indicated by U_{SF} is $\psi \approx 0.015\,M_{\odot}\,\mathrm{yr^{-1}\,Mpc^{-3}}$.

2.3 Introduction

The 1.4 GHz continuum emission from galaxies is powered by a combination of recent star formation in star-forming galaxies (SFGs) and supermassive black holes (SMBHs) in active galactic nuclei (AGNs). The tight and nearly linear far-infrared (FIR)/radio correlation observed among low-redshift galaxies makes 1.4 GHz spectral luminosity a good dust-unbiased tracer proportional to the recent star-formation rate (SFR) (Condon 1992), while sources that are radio-loud relative to the FIR/radio correlation reveal the presence of radio-dominant AGNs, even those deeply embedded in dust.

This paper presents separate local radio luminosity functions for both source types. When used in conjunction with sensitive radio surveys made by the JVLA, MeerKAT, the SKA, or the ngVLA, local luminosity functions anchor models for the cosmological co-evolution of star formation and SMBH growth. Our large ($N = 9,517$) spectroscopically complete sample of the brightest ($k_{20\mathrm{fe}} \leq 11.75$ and $S_{1.4\ \mathrm{GHz}} \geq 2.45$ mJy) galaxies covers most of the extragalactic sky ($\Omega = 7.016$ sr) in order to (1) reach the low radio spectral luminosities $\log[L_{1.4\ \mathrm{GHz}}(\mathrm{W\ Hz})^{-1}] \geq 19.3$ needed constrain the full range of sources accounting for nearly all ($> 99\%$) recent star formation and SMBH growth and (2) minimize cosmic variance.

Bright galaxies are also more likely to have the multiwavelength data needed to distinguish between radio sources powered by star formation and by AGNs. The total radio emission from any galaxy is actually the sum of both types, so quantitatively accurate criteria are needed to determine which is dominant. We used only quantitative FIR, MIR (mid-infrared), and radio data to determine which type is energetically dominant. We did not use BPT diagrams (Baldwin et al. 1981) or other optical emission-line diagnostics because they are not good *quantitative* measures of AGN-powered radio emission. It turns out, however, that the Mauch & Sadler (2007) AGN/SFG classifications based on optical spectra agree surprisingly well with ours.

The cosmological evolution of radio sources is so strong that nearby sources comprise only a small fraction of all sources in flux-limited samples. Radio continuum emission alone cannot separate the nearby needles from the haystack of distant sources, so statistically complete and reliable samples of nearby radio sources are usually selected by position-coincidence cross-identifications with optical or infrared samples of bright galaxies. For example, of all NRAO VLA Sky Survey (NVSS) (Condon et al. 1998) sources stronger than $S \approx 2.5$ mJy at $\nu = 1.4$ GHz, $< 1\%$ can be identified with galaxies brighter than $m_{\rm p} = 14.5$ (Condon et al. 2002). About 85% of those sources are in relatively low-luminosity star-forming galaxies (SFGs) whose median face-on surface brightness is just $\langle T_{\rm b} \rangle \sim 1$ K at $\nu = 1.4$ GHz (Hummel 1981), so reasonably complete samples of nearby radio sources can be constructed only from radio surveys having lower surface-brightness detection limits. The NVSS is suitable because its sensitivity limit is $T_{\rm b} = 5\sigma_{\rm T} \approx 0.7$ K.

This paper presents and analyzes a large catalog of NVSS sources identified with 2 Micron All-Sky Survey eXtended (2MASX) galaxies (Jarrett et al. 2000) brighter than $k_{\rm 20fe} = 12.25$ at $\lambda = 2.16\,\mu$m, where $k_{\rm 20fe}$ is the magnitude measured inside the 20 mag arcsec^{-2} isophote. The 2MASX galaxy sample is described in Section 2.4, and the NVSS radio identification procedure is explained in Section 2.5. The resulting 2MASX/NVSS catalog (Section 2.6) contains a statistically complete sample of 15,043 galaxies brighter than $k_{\rm 20fe} = 12.25$ and 1.4 GHz flux densities $S \geq 2.45$ mJy. Most of the analysis in this paper is based on the spectroscopically complete subsample of 9,517 galaxies with $k_{20\mathrm{fe}} \leq 11.75$ and $S \geq 2.45$ mJy. All but 19 had published spectroscopic redshifts, and we measured new spectroscopic redshifts for 12 of the 19 (Appendix 2.7.1). Only FIR, MIR (mid-infrared), and radio data were used to distinguish 2MASX/NVSS radio sources primarily powered by recent star formation from those dominated by AGNs (Section 2.6.1). The counts of 2MASX/NVSS sources powered by star formation and AGNs as functions of 1.4 GHz flux density are plotted and discussed in Section 2.6.2. Separate 1.4 GHz local luminosity functions for SFGs and AGNs are reported in Section 2.8, and Section 2.9 presents the corresponding spectral power density functions. Cosmic variance exceeds the Poisson variance for the large 2MASX/NVSS spectroscopic sample (Section 2.10). The total 1.4 GHz spectral energy density produced by SFGs today, $U_{\mathrm{SF}} = (1.54 \pm 0.20) \times 10^{19}$ W Hz^{-1} Mpc^{-3}, indicates that the recent SFRD is $\psi \approx 0.015\ M_{\odot}$ yr^{-1} Mpc^{-3}.

All calculations of absolute quantities (comoving distance, spectral luminosity,. . .) from the observables (redshift, flux density,. . .) are based on the relativistically correct equations for a ΛCDM universe from Condon & Matthews (2018) with $\Omega_{\mathrm{m}} = 0.3$, $\Omega_{\Lambda} = 0.7$, and $H_0 = 70$ km s^{-1} Mpc^{-1} ($h = 0.70$).

2.4 The 2MASX Galaxy Sample

Large samples of bright galaxies necessarily cover a significant fraction of the sky. The Two Micron All Sky Survey (2MASS) (Skrutskie et al. 2006) Extended Source Catalog (2MASX) (Jarrett et al. 2000) is ideal because:

(1) It is complete and reliable over the whole extragalactic sky for galaxies brighter than $k_{\mathrm{s}} \approx k_{20\mathrm{fe}} + 0.2 \approx 13.5$ ($S_{2.16\,\mu\mathrm{m}} \approx 2.9$ mJy) at the longest infrared wavelength ($\lambda \approx 2.16\,\mu$m) yielding good atmospheric transparency. Dust extinction in our Galaxy and dust absorption in nearby galaxies are both small at this wavelength, and confusion by stars is negligible at galactic latitudes $|b| \geq 20°$.

(2) The $\lambda = 2.16\ \mu$m luminosity of a normal galaxy is nearly proportional to its total stellar mass (Bell et al. 2003) because dust absorption is low and late-type stars dominate the near-infrared (NIR) luminosity. Thus the 2MASX sample most directly

samples the stellar masses in galaxies; it is less biased than optical or FIR samples by recently formed massive stars. The NVSS/2MASX flux-density ratio is a good measure of the recent star formation rate per unit stellar mass, or the specific star-formation rate (SSFR), which is a constraint on the star-formation history of the universe.

(3) The 2MASX photometric errors for galaxies brighter than $k_s \sim 12.5$ are $\lesssim 4\%$.

(4) Nearly all 2MASX galaxies have such small absolute position errors ($< 1''$ rms) that complete and reliable radio identifications of 2MASX galaxies can be made by position coincidence alone.

(5) Spectroscopic redshifts are now available for nearly all galaxies brighter than $k_{20\mathrm{fe}} = 11.75$ (Huchra et al. 2012).

Our 2MASX galaxy sample includes all galaxies with: (1) 2MASX catalog fiducial magnitudes $k_{20\mathrm{fe}} \leq 12.25$ mag measured within the 20 mag arcsec^{-2} ($\approx 3\sigma$) fiducial elliptical aperture. According to the 2MASS Explanatory Supplement (), the measured fiducial flux density typically contains about 85% of the extrapolated total flux density.

(2) 2MASX fiducial semi-major axes $r_{20\mathrm{fe}} \geq 5''$, above which the 2MASX catalog is nominally complete, and

(3) J2000 $\delta > -40°$, the NVSS southern declination limit, and absolute galactic latitude $|b| > 20°$, the limit of the *InfraRed Astronomical Satellite (IRAS)* Faint Source Catalog (FSC) (Moshir et al. 1992). This $\Omega \approx 7.016$ sr (Appendix C) sky area is shown in Figure 2.1.

The 2MASX all-sky data release catalog (https://www.ipac.caltech.edu/2mass/releases/allsky/) contains $N_{\mathrm{IR}} = 55,288$ infrared galaxies satisfying all three requirements. Their mean sky density is $\rho_{\mathrm{IR}} \approx 2.40$ deg^{-2}.

2.5 NVSS Identifications of 2MASX Galaxies

To find all plausible NVSS identification candidates for the 2MASX galaxies, we used the NVSS catalog browser (http://www.cv.nrao.edu/nvss/NVSSlist.shtml)

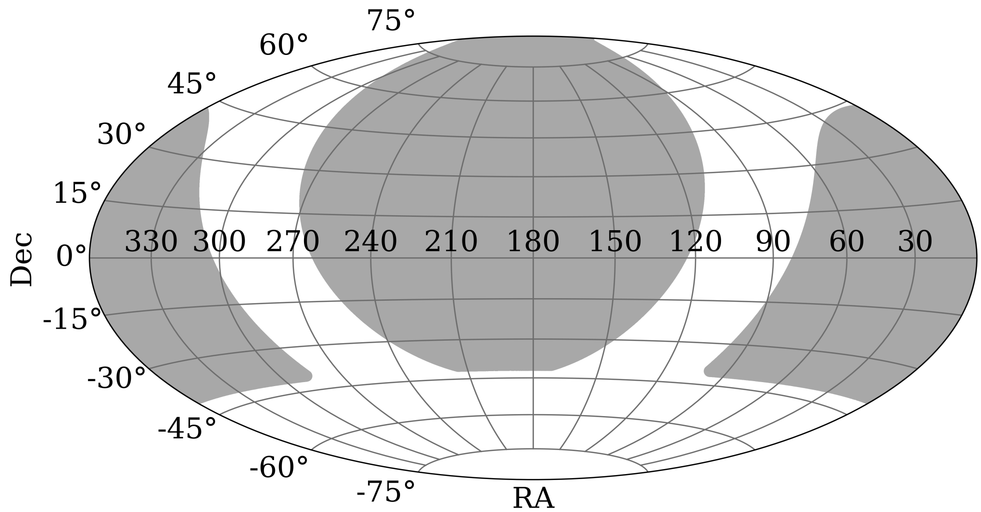

Figure 2.1. The shaded 2MASX/NVSS area in this equal-area Hammer projection covers the $\Omega \approx 7.016$ sr (56% of the sky) with J2000 $\delta > -40°$ and absolute galactic latitude $|b| > 20°$.

to select the 18,360 2MASX sample galaxies having (1) at least one NVSS radio component within a search radius $r_{\rm s} = 60''$ or (2) at least 2 NVSS components within $r_{\rm s} = 120''$. These search radii are compromises large enough to ensure high completeness but small enough to avoid including too many unrelated background sources. Note that the NVSS catalog lists elliptical Gaussian radio *components* fitted to peaks on NVSS images, so the extended radio *source* produced by one galaxy may be represented by more than one radio component. If the radio emission from a galaxy is confused, asymmetric, or significantly larger than the $\theta = 45''$ FWHM Gaussian NVSS beam, the radio positions may be significantly offset from the host galaxy position. This is the case for $\sim 5\%$ of 2MASX/NVSS galaxies, so initial search radii much larger than the combined 2MASX and NVSS position errors are needed to capture all radio identifications and include all of their radio emission.

Our large search areas contain an unacceptable number of unrelated background sources because the mean sky density of NVSS components is $\rho \approx 53$ deg^{-2}. The rms statistical sampling error in a catalog of $N \sim 10^4$ identifications is $N^{1/2} \sim 10^2$, so exploiting the statistical power of such a large catalog requires identification reliability

$\gtrsim 99\%$. Most background radio sources are so distant (mean $\langle z \rangle \sim 1$) that they are quite randomly distributed on the sky. Thus the Poisson probability P that one or more unrelated NVSS components will lie within $r_\mathrm{s} = 60''$ of any 2MASX galaxy is

$$P(\geq 1) = 1 - P(0) = 1 - \exp(-\pi \rho r_\mathrm{s}^2) \approx 0.045 \;, \tag{2.1}$$

where the mean number of unrelated components in a search circle is $\mu = \pi \rho r_\mathrm{s}^2$ and the probability of finding none is $P(0) = \exp(-\mu)$. In addition, some 2MASX galaxies are members of physical groups and clusters, so the radio emission from close companion galaxies must be excluded. Thus *at least* $N_\mathrm{IR} P(\geq 1) = 55,288 \times 0.045 \gtrsim 2500$ of the 18360 candidate fields with $r_\mathrm{s} = 60''$ are likely to contain unrelated NVSS components, leaving $\lesssim 16,000$ genuine 2MASX/NVSS identifications. The probability of finding two or more background sources within $r_\mathrm{s} = 120''$ is

$$\begin{aligned} P(\geq 2) =& 1 - P(0) - P(1) \\ =& 1 - (1 - \pi \rho r_\mathrm{s}^2) \exp(-\pi \rho r_\mathrm{s}^2) \approx 0.015 \;. \end{aligned} \tag{2.2}$$

Genuine 2MASX/NVSS identifications with neither a single component within $60''$ nor two or more components within $120''$ are rare but may have been missed.

Recognizing and weeding out the background sources required extensive and time-consuming human intervention, as described below.

Most of the radio sources produced by bright 2MASX galaxies are fairly compact or at least symmetric. Nearly all 2MASX galaxies have rms position errors $\sigma_\alpha \approx \sigma_\delta \ll 1''$, and NVSS position errors for unresolved components decline with catalog flux density from $\sigma_\alpha \approx \sigma_\delta \approx 5''$ at $S = 2.45$ mJy to $\lesssim 1''$ for $S > 15$ mJy. Such candidates can be reliably accepted or rejected on the basis position coincidence alone. We define σ as the quadratic sum of the 2MASX and NVSS rms position errors in each coordinate,

$$m \equiv r_\mathrm{s} / \sigma \tag{2.3}$$

as the identification search radius in units of σ, and

$$k \equiv 1 + 2\pi\rho\sigma^2 \ . \tag{2.4}$$

For $\rho = 53 \text{ deg}^{-2} \approx 4.09 \times 10^{-6} \text{ arcsec}^{-2}$ and the worst case $\sigma \approx 5''$, $k \approx 1.000642$. In terms of m and k the completeness of the identifications is (Condon et al. 1975)

$$C = \frac{1 - \exp(-m^2 k/2)}{k} \ . \tag{2.5}$$

Even when $\sigma = 5''$, $m = 3$ ($r_\mathrm{s} = 15''$) ensures $C \approx 0.99$. The fraction of 2MASS galaxies actually having NVSS counterparts is $f \approx 15,658/55,288 \approx 0.3$. The identification reliability (Condon et al. 1975)

$$R = C\left[\frac{1}{f} + \left(1 - \frac{1}{f}\right)\exp[m^2(1-k)/2] - \exp\left(-\frac{m^2 k}{2}\right)\right]^{-1} \tag{2.6}$$

is also $\gtrsim 99\%$ because the probability that an unrelated NVSS source lies within $3\sigma \approx 15''$ of any position is < 0.003.

Figures 2.2 and 2.3 present examples illustrating both typical and difficult 2MASX/NVSS cross-identifications. The upper left panel of Figure 2.2 shows the Digitized Sky Survey (DSS) gray-scale optical image, the NVSS 1.4 GHz brightness contours, and the *IRAS* 2σ position error ellipse for the typical spiral galaxy IC 1526. Its 1.4 GHz flux density $S = 5.4 \pm 0.5$ mJy and its 2MASX/NVSS position offset $r = 3\overset{''}{.}8$ ($m = 1.3$) are close to the sample medians. The radio sources in nearly all spiral galaxies are fairly symmetric and roughly coextensive with their optical host galaxies of stars.

Nonetheless, some radio sources in spiral galaxies could not be found by position coincidence alone. In the upper right panel of Figure 2.2, the confused 2MASX position of NGC 5668 is marked by the cross on a bright spot $\sim 22''$ north of the galaxy nucleus. A few large face-on and edge-on spiral galaxies have significantly offset or even multiple 2MASX positions that can be recognized most easily by visual inspection of finding charts like this one.

The NVSS contours and accurate 2MASX position for the very extended low-brightness galaxy M74 are shown in the middle row, left panel of Figure 2.2. The closest NVSS catalog component is $93''$ from the 2MASX position, so M74 is not in the list of candidates within the $r_{\rm s} = 60''$ search radius. To find similar cases, we searched for identifications among all galaxies in the 1.49 GHz atlas of spiral galaxies with $B_{\rm T} \leq 12$ (Condon 1987). M74 emphasizes the importance of high surface-brightness sensitivity for identifying reasonably complete radio samples of nearby galaxies. Its total 1.4 GHz flux density is $S \approx 180$ mJy, but its surface brightness is barely above the NVSS $5\sigma \approx 5 \times 0.45$ mJy beam$^{-1} \approx 2.3$ mJy beam^{-1} detection limit.

The price of high brightness sensitivity is low angular resolution. The $\theta = 45''$ NVSS beam only marginally resolves the pair of galaxies UGC 00644 and UGC 00644 NOTES01 (Figure 2.2 middle row, right panel), and the NVSS catalog lists only a single extended Gaussian component whose radio centroid position is midway between the galaxies. Finding charts make it easy for humans to recognize such blends and decompose the radio sources into unresolved components on the galaxy positions.

The majority of AGN-powered radio galaxies are also sufficiently compact and/or symmetric to permit simple position-coincidence identifications. The lower left panel of Figure 2.2 shows the radio emission from an anonymous $S = 15.0$ mJy (about the median flux density of AGNs in the sample) galaxy. However, a significant minority of low-luminosity radio galaxies are distinctly asymmetric. In the lower right panel in Figure 2.2 are the 2MASX position cross and NVSS contours of a head-tail radio galaxy whose centroid is significantly offset to the north. The head-tail morphology of this source is confirmed by the high-resolution VLA image of Owen et al. (1993). Slightly bent radio jets are common, but truly one-sided radio jets are rare in low-luminosity radio sources. The radio galaxy IC 1695 in the cluster Abell 0193 appears in the upper left panel of Figure 2.3. About half of its flux density arises from a compact component in the galaxy, and half originates in a slightly curved one-sided jet extending $\sim 1'$ to the northeast (Owen & Ledlow 1997).

Radio galaxies powered by AGNs may emit most or even all of their power in jets and lobes lying well outside the host galaxies of stars. Thus it is necessary to search for radio components quite far from each 2MASX position, *whether or not* there is a radio component close to the 2MASX position. The right panel in the top row of Figure 2.3 is centered on an anonymous elliptical galaxy at redshift $z \approx 0.0885$, so this $6' \times 6'$ finding chart is ≈ 640 kpc on a side and the triple radio source is even larger. Mauch & Sadler (2007) identified only the $S = 17.5$ mJy central NVSS component with the 2MASX galaxy, even though other NVSS components lie within their $r_{\rm s} = 3'$ candidate search radius and yield a total flux density $S \approx 680$ mJy. Sources like this are difficult to recognize from component lists alone; there is no substitute for visual inspection of finding charts that extend at least $\pm 3'$ in both directions. The much larger $\pm 8'$ finding chart in the left panel, middle row of Figure 2.3 is centered on the $S \approx 430$ mJy triple radio galaxy 2MASX J15280499+0544278. Only the $S = 45.1$ mJy central component was identified by Best & Heckman (2012), and the lobes are only partially visible and not easily recognized on our usual $6' \times 6'$ finding chart, so we might have missed other sources with even more widely separated lobes. Although large triple sources like these are rare among bright galaxies, they are usually so luminous that capturing their total flux densities is important for deriving accurate radio luminosity functions.

Some "empty double" radio sources have no NVSS components within $60''$ of their 2MASX host galaxies. To find them, we searched for pairs or multiple components offset by up to $120''$. The nearest NVSS components in the X-shaped radio source 4C +32.25 = B2 0828+32 (right panel, middle row of Figure 2.3) are the bright FR II lobes symmetrically offset from 2MASX J08312752+3219270 by $104''$ and $119''$. The larger but fainter north-south extension has a steep radio spectrum and may be the relic of an earlier outburst in a precessing system (Parma et al. 1985). Most coreless double sources can be recognized because their lobes have roughly equal flux densities, are about equally distant from their host galaxies, and are at position angles differing by $\sim 180°$. Somewhat more difficult to recognize are bent coreless doubles. The left panel, bottom row of Figure 2.3 shows the luminous ($S \approx 650$ mJy

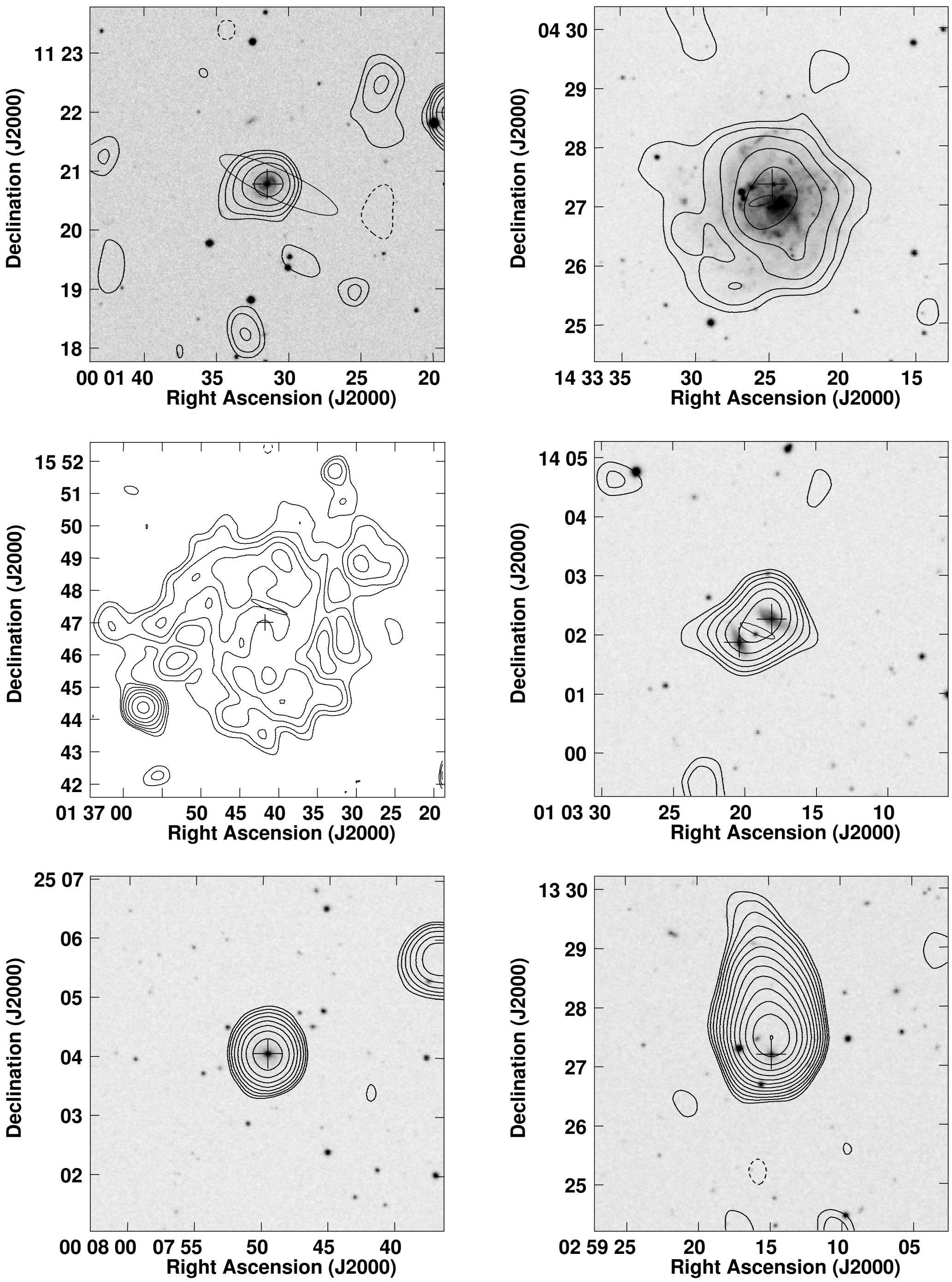

Figure 2.2. Selected finding charts. DSS gray-scale images are shown under NVSS contours plotted at $S_{\rm p} = \pm 1$ mJy beam$^{-1} \times 2^0,\ 2^{1/2},\ 2^1, \ldots$ 2MASX source positions are marked by crosses, ellipses outline *IRAS* position errors.

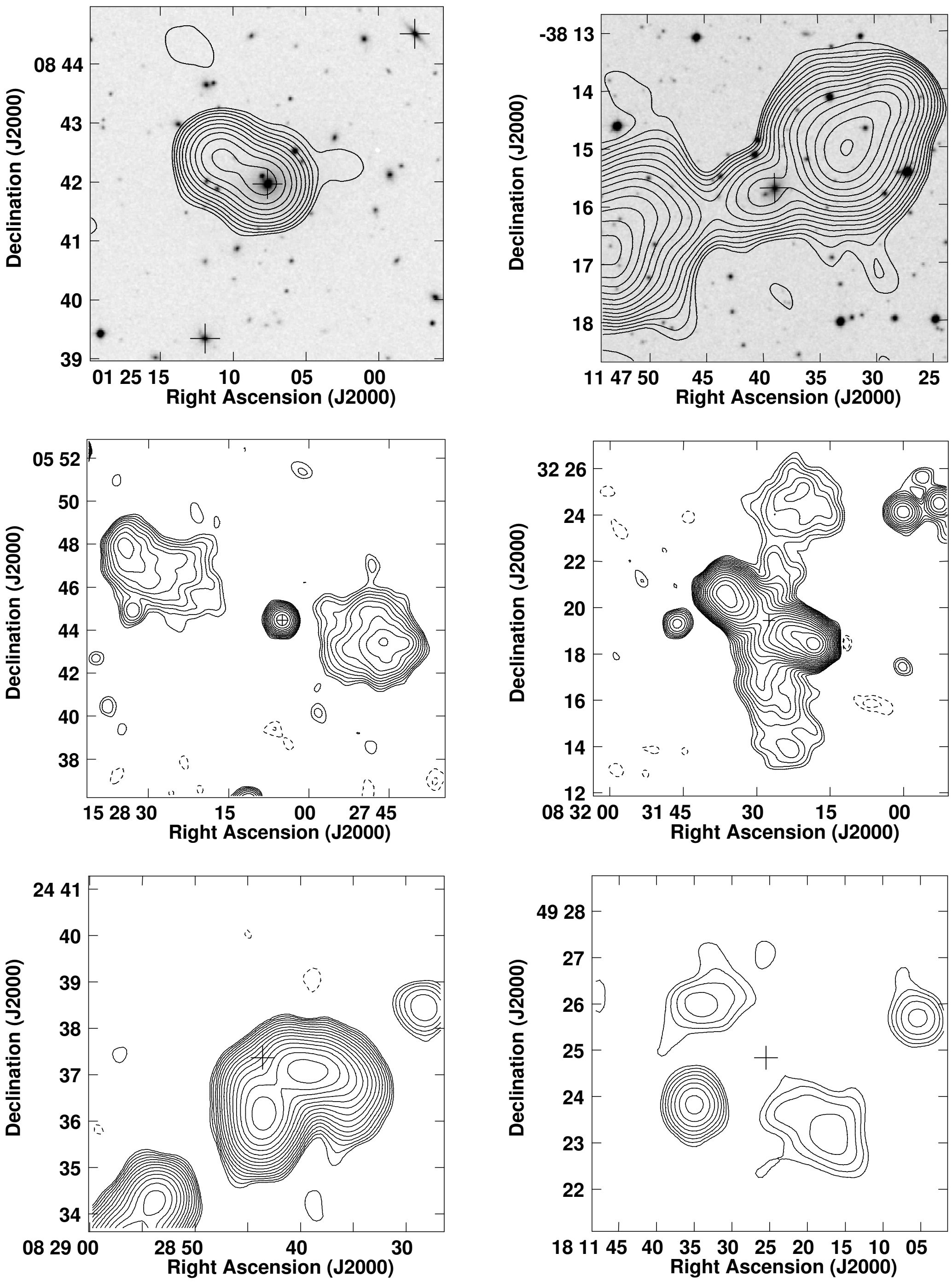

Figure 2.3. Additional selected finding charts. DSS gray-scale images are shown under NVSS contours plotted at $S_{\mathrm{p}} = \pm 1$ mJy beam$^{-1} \times 2^0,\ 2^{1/2},\ 2^1, \ldots$ 2MASX source positions are marked by crosses.

at $z \approx 0.0830$) bent double source having no NVSS components within $60''$ of the cross on 2MASX J08284360+2437220. Finally, the lower right panel of Figure 2.3 shows a large but faint double source that illustrates the limit of reliable identifications. Secondary evidence supporting this identification as a double source includes (1) the two components are roughly equidistant from the 2MASX galaxy, (2) the two components have comparable brightness, (3) the line between them passes close to the galaxy, and (4) the southwest component has a tail pointing back toward the galaxy.

2.6 The 2MASX/NVSS Catalog and Samples

Following the procedures described in Section 2.5, we identified NVSS sources with 15,658 of the 55,288 2MASX galaxies having $k_{20\mathrm{fe}} \leq 12.25$ and semi-major axes $r_{20\mathrm{fe}} \geq 5''$ in the $\Omega \approx 7.016$ sr solid angle defined by J2000 declination $\delta > -40^\circ$ and absolute galactic latitude $|b| \geq 20^\circ$. The resulting 2MASX/NVSS galaxy catalog is displayed in part as Table 2.1, which lists for each galaxy its 2MASX J2000 coordinate name, 2MASX fiducial $\lambda = 2.16\,\mu$m magnitude $k_{20\mathrm{fe}}$, 2MASX fiducial major-axis diameter $d_{20\mathrm{fe}} = 2\,r_{20\mathrm{fe}}$ in arcsec, 1.4 GHz NVSS total flux density S in mJy, dominant radio energy source type (either recent star formation S or active galactic nucleus A) derived from FIR data, from MIR data, and the final type derived from both as explained in Section 2.6.1, heliocentric radial velocity cz in km s^{-1} usually from the NASA/IPAC Extragalactic Database (NED), and the most common alternative galaxy name (e.g., UGC 12890) from NED.

All NVSS catalog flux densities are rounded to the nearest 0.1 mJy, so the 15,043 galaxies with 1.4 GHz catalog flux densities $S \geq 2.5$ mJy comprise a flux-limited sample complete to $S = 2.45$ mJy. The spectroscopically complete subsample of the 9,517 galaxies with $k_{20\mathrm{fe}} \leq 11.75$ and $S \geq 2.45$ mJy now has redshifts for all but 7 (99.9% redshift completeness).

Table 2.1. 2MASX/NVSS catalog

2MASX J2000 name	k_{20fe} (mag)	d_{20fe} ($''$)	$S_{1.4}$ (mJy)	Energy Source Type FIR	MIR	Final	cz (km s^{-1})	NED name
00000701 + 0816448	10.779	23.6	82.7	A	A	A	11602	UGC 12890
00001278 + 0107123	11.839	15.3	2.1	S	S	S	7390	CGCG 382-016
00002880 + 3246563	11.108	13.4	5.2	S	S	S	9803	IC 5373
00003138 + 2619318	11.967	13.2	7.5	S	S	S	7653	UGC 12896
00003564 − 0145472	11.488	16.1	2.8	?	S	(S)	7274	CGCG 382-017
00005234 − 3550370	11.548	15.2	48.4	A	A	A	15581	
00010444 + 0430001	12.013	15.4	2.7	S	S	S	8932	IC 5374
00011996 + 1306406	9.920	27.4	12.3	S	S	S	5366	NGC 7803
00013148 + 1120465	11.341	16.0	5.4	S	S	S	9099	IC 1526
00013359 + 0900445	11.234	15.0	2.7	?	S	(S)	9252	UGC 12912

Note—Table 2.1 is published in its entirety in the electronic edition of the *Astrophysical Journal*. A portion is shown here for guidance regarding its form and content.

2.6.1 Radio Energy Sources

The ultimate energy sources powering the radio continuum continuum emission from galaxies are recently formed massive short-lived stars and SMBHs in AGNs. In order to use radio continuum luminosity as a quantitative tracer of the SFR, we classified the radio emission of each galaxy in Table 2.1 as being powered *primarily* by recent star formation "S" or by an AGN "A". Labels "(S)" and "(A)" indicate uncertain classifications. Note that these are *quantitative* classifications because both star formation and an AGN may contribute to the total radio luminosity a single galaxy.

Optical emission- and absorption-line spectra have often been used to classify galaxies as SFGs or AGNs. For example, Sadler et al. (2002) and Mauch & Sadler (2007) classified as AGNs all galaxies with absorption-line spectra like those of giant elliptical galaxies, absorption-line spectra with weak LINER-like emission lines, or stellar continua dominated by nebular emission lines stronger than Balmer emission lines; and they classified as SFGs all galaxies with spectra dominated by strong narrow Hα and Hβ emission lines.

We decided not to use any optical indicators to determine the dominant radio energy sources in our galaxies. AGN signposts such as [O III] luminosity are often not correlated with radio luminosity (Best et al. 2005). We did not assume that star formation powers the radio sources in spiral galaxies or that AGNs drive radio emission from E and S0 galaxies. We did not use optical colors and fluxes, which may be biased by dust absorption. We did not use BPT (Baldwin et al. 1981) diagrams which plot the [O III]/Hβ ratio as a function of the [N II]/Hα ratio because $\sim 40\%$ of nearby radio-loud AGN are too gas poor and optically inactive to be detected this way (Geréb et al. 2015). Thus our energy-source classification method is independent of the (Sadler et al. 2002) and (Mauch & Sadler 2007) classification method based on optical spectra.

Instead, we used only a combination of radio and infrared data to classify our radio sources. Radio sources powered by stars can be recognized because (1) $> 99\%$ obey the tight and nearly linear FIR/radio flux correlation (Condon et al. 1991), (2) they have the steep FIR spectral indices $\alpha(25\,\mu\mathrm{m}, 60\,\mu\mathrm{m}) < -1.5$ characteristic of cold dust emission (de Grijp et al. 1985), (3) they usually reside in galaxies having "dusty" MIR colors, and (4) they are roughly coextensive with their optical host galaxies. Radio sources powered by AGNs (1) are usually much stronger than expected from the FIR/radio correlation, (2) may be associated with warmer FIR sources, (3) usually reside in galaxies having the nearly blackbody MIR colors of "naked" stars, and (4) may contain jets and lobes extending well outside their host galaxies.

We used a combination of these four indicators as described in detail below to assign a primary energy source type to each 2MASX/NVSS galaxy in Table 2.1:

(1) The *IRAS* FIR/NVSS 1.4 GHz flux-density ratio was parameterized by the quantity

$$q \equiv \log\left[\frac{FIR/(3.75\times10^{12}\ \mathrm{Hz})}{S_{1.4\ \mathrm{GHz}}\,(\mathrm{W\ m^{-2}\ Hz^{-1}})}\right], \tag{2.7}$$

where

$$FIR\ (\mathrm{W\ m^{-2}}) \equiv 1.26\times10^{-14}[2.58S_{60\,\mu\mathrm{m}}\,(\mathrm{Jy}) + S_{100\,\mu\mathrm{m}}\,(\mathrm{Jy})] \tag{2.8}$$

(Helou et al. 1988).

If a galaxy was detected by *IRAS* (*IRAS* flux quality code 2 or 3) at both 60 μm and 100 μm, the value of q was calculated directly from Equation 2.7. If a galaxy was detected at 60 μm but not detected (*IRAS* flux quality code 1) at 100 μm, an approximate q was estimated using the median observed $S_{100\,\mu\mathrm{m}} \sim 2S_{60\,\mu\mathrm{m}}$ (Yun et al. 2001). Conversely, if a galaxy was detected at 100 μm but not at 60 μm, q was estimated assuming $S_{60\,\mu\mathrm{m}} \sim S_{100\,\mu\mathrm{m}}/2$. If a galaxy was observed by *IRAS* but not detected at either 60 μm or 100 μm, an upper limit to q was calculated from the *IRAS* FSC 90%-completeness upper limits $S_{60\,\mu\mathrm{m}} < 0.36$ Jy and $S_{100\,\mu\mathrm{m}} < 1.2$ Jy. Finally, if a galaxy was in an area not adequately covered by *IRAS*, we set $q = ?$ and used only other classification methods.

The normalized probability distribution $P(q)$ of all galaxies in the complete 1.4 GHz flux-limited sample that were observed by *IRAS* is plotted as a histogram in Figure 2.4. Within that histogram the unshaded area indicates upper limits to q for galaxies observed but not detected by *IRAS* at either 60 μm or 100 μm, and the

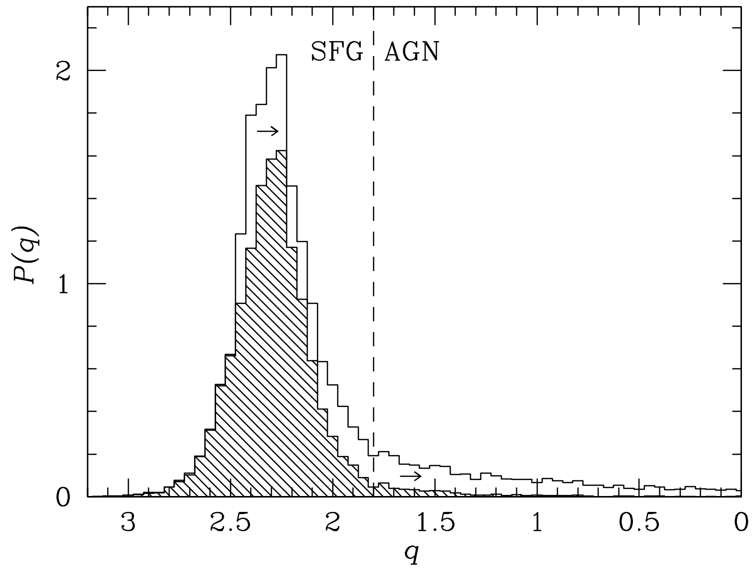

Figure 2.4. For 2MASX/NVSS galaxies with $S_{1.4\ \mathrm{GHz}} \geq 2.45$ mJy, the normalized probability distribution of the measured FIR/radio ratio q is shown by the shaded histogram and upper limits for those observed but not detected by *IRAS* are indicated by the unshaded part of the histogram. The vertical dashed line separates SFGs with measured $q > 1.8$ from AGNs with upper limits or measured $q < 1.8$. Abscissa: FIR/radio flux ratio q (Equation 2.7). Ordinate: Probability density $P(q)$.

shaded area shows measured or estimated q values. Star-forming galaxies obeying the FIR/radio correlation are clustered in the narrow peak with mean $\langle q \rangle \approx 2.30$ and rms scatter $\sigma_q \approx 0.17$. The intrinsic scatter in q (Condon et al. 1991) is nearly equal to our measured σ_q, so the peak in Figure 2.4 has not been broadened significantly by flux-density measurement errors. Adding a dominant AGN to a $q = 2.3$ SFG would result in $q < 2.0$. To allow for the observed scatter in q, we classified galaxies with measured $q > 1.8$ as SFGs and galaxies with upper limits or measured values of $q < 1.8$ as primarily AGN-powered.

Galaxies with upper limits to q larger than 1.8 and galaxies not observed by *IRAS* could not be classified by this method. The NVSS and *IRAS* are comparably sensitive to SFGs: the value of q corresponding to the sensitivity limits $S_{1.4\ \mathrm{GHz}} = 2.45$ mJy, $S_{60\,\mu\mathrm{m}} = 0.36$ Jy, and $S_{100\,\mu\mathrm{m}} = 1.2$ Jy is $q \approx 2.4$. Thus many galaxies not detected by *IRAS* do have upper limits to q larger than 1.8 (Figure 2.4).

(2) A FIR source warm enough to have

$$\alpha(25\,\mu\text{m},\,60\,\mu\text{m}) > -1.5 \tag{2.9}$$

indicates concentrated dust heating by a single AGN, rather than by a comparably luminous but more extended cluster of stars (de Grijp et al. 1985). The spectral-index error resulting from a 20% error in the $25\,\mu$m flux density is $\Delta\alpha(25\,\mu\text{m},\,60\,\mu\text{m}) \sim \pm 0.25$. To allow for spectral-index errors of sources with $\lambda = 25\,\mu$m signal-to-noise ratios as low as 5, we conservatively classified only galaxies with $\alpha(25\,\mu\text{m},\,60\,\mu\text{m}) > -1.25$ as primarily AGN-powered. There are 247 such "warm" galaxies, of which 77 also have $q < 1.8$ and the remaining 170 were newly classified as AGN-powered by their warm FIR spectra.

(3) *Wide-field Infrared Survey Explorer (WISE)* (Wright et al. 2010) MIR magnitudes in bands W1 ($\lambda = 3.4\,\mu$m), W2 ($\lambda = 4.6\,\mu$m), and W3 ($\lambda = 12\,\mu$m) determine the colors $(W1 - W2)$ and $(W2 - W3)$ that help to distinguish AGNs residing in elliptical galaxies and Seyfert galaxies from dusty spiral galaxies dominated by ongoing star formation, as illustrated in Figure 2.5. Stars alone and dustless elliptical galaxies (lower left circle in Figure 2.5) have low values of $(W1-W2)$ and $(W2-W3)$ because the W1, W2, and W3 wavelengths are on the Rayleigh-Jeans side of the blackbody peak of most stars, and the limiting Rayleigh-Jeans spectral index $\alpha = +2$ corresponds to $(W1 - W2) \approx -0.05$ and $(W2 - W3) \approx -0.07$ for the *WISE* flux-density scales and frequencies listed in Table 1 of Jarrett et al. (2011). The sublimation temperature of large interstellar dust grains is too low for them to affect $(W1 - W2)$ significantly, but dust in SFGs increases $(W2 - W3)$. Nuclear emission from Seyfert galaxies (upper right circle in Figure 2.5) can increase $(W1-W2)$ enough to separate

AGNs from SFGs. Thus radio sources in galaxies above the broken line specified by

$$\begin{aligned} W1 - W2 =& + 0.8 & (W2 - W3 \geq 3.1) \\ W1 - W2 =& (W2 - W3 - 1.82)/1.6 & (W2 - W3 < 3.1) \end{aligned} \tag{2.10}$$

are probably AGN-powered, and those below the line are likely powered by ongoing star formation. Although the *WISE* MIR colors are less reliable indicators than the *IRAS* FIR/radio correlation, they are available for nearly all 2MASX/NVSS galaxies, so we used them to classify cases that have neither measured q values nor upper limits $q < 1.8$.

WISE does not have the far-infrared coverage needed to yield q (Equation 2.7), but the $\lambda = 22\,\mu$m *WISE* magnitude $W4$ can be used to define a similar quantity

$$q_{22} \equiv \log[S(22\,\mu\mathrm{m})/S(1.4\,\mathrm{GHz})] \ , \tag{2.11}$$

where

$$\log\left[\frac{S(22\,\mu\mathrm{m})}{\mathrm{Jy}}\right] = 0.918 - 0.4\,W4 \tag{2.12}$$

(Jarrett et al. 2011). The normalized probability distribution $P(q_{22})$ is shown in Figure 2.6 for all 2MASX/NVSS galaxies with $k_{20\mathrm{fe}} \leq 12.25$ and $S(1.4$ GHz$) \geq 2.45$ mJy (black histogram). Galaxies with *WISE* MIR colors below the broken line in Figurefig:figure5 (*WISE* energy source S) are represented by the blue histogram, and galaxies above the broken line in Figure 2.5 (*WISE* energy source A) by the red histogram. Like the distribution of q in Figure 2.4, the distribution of q_{22} in Figure 2.6 has a narrow peak dominated by SFGs and a long tail of galaxies containing radio-loud AGNs. Thus *WISE* MIR colors and *WISE* MIR/radio flux ratio parameters q_{22} provide independent energy-type classifications that largely agree.

The main advantage of the *WISE* q_{22} distribution over the *IRAS* q distribution is that all but a handful of 2MASX/NVSS galaxies were detected by *WISE* at $\lambda = 22\,\mu$m. The drawback of q_{22} is contamination of $S(22\,\mu\mathrm{m})$ by emission from warm dust heated by AGNs, making it a somewhat less reliable parameter than q for

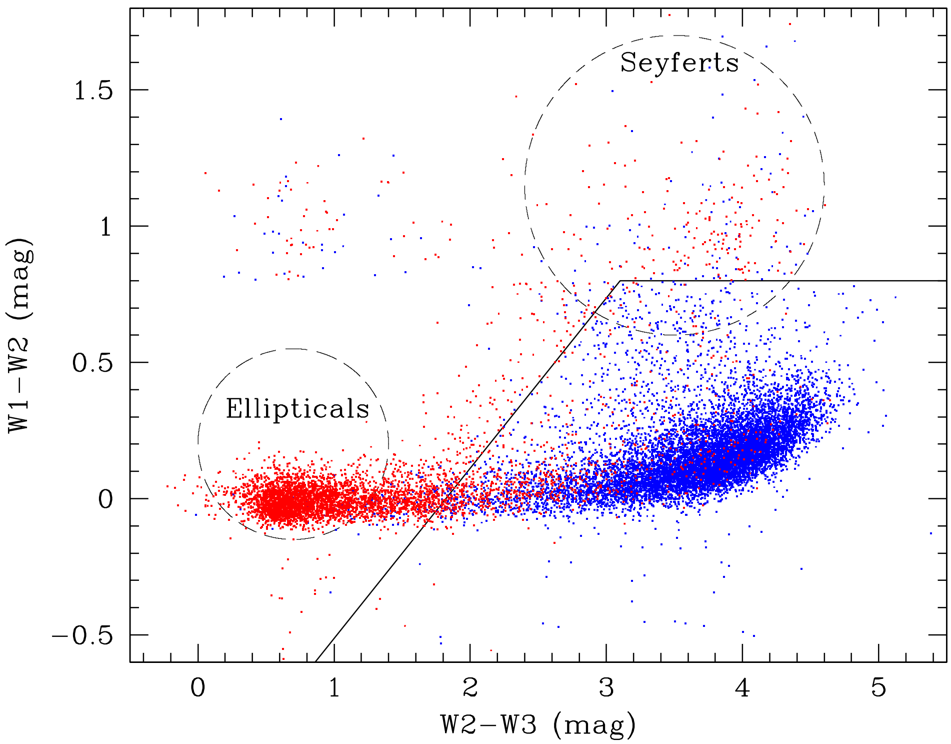

Figure 2.5. The mid-infrared colors $(W1 - W2)$ ($[3.4\,\mu\text{m}] - [4.6\,\text{m}]$) and $(W2 - W3)$ ($[4.6\,\mu\text{m}] - [12\,\mu\text{m}]$) can be used to separate galactic stars and elliptical galaxies (lower left dashed circle) from Seyfert galaxies (upper right dashed circle) and from dusty spiral galaxies with ongoing star formation (below the broken line), as shown in Wright et al. (2010) Figure 12. Galaxies listed as A or (A) in Table 2.1 are shown as red points; S or (S) galaxies are blue. Abscissa: $(W2 - W3)$ (mag). Ordinate: $(W1 - W2)$ (mag).

distinguishing SFGs from AGNs. For our final MIR classifications, we used the *WISE* color criterion (Equation 2.10). We used q_{22} only for a few galaxies having no *IRAS* data, as described in items 3. through 5. in the list at the end of Subsection 2.6.1.

(4) Radio morphology complements the three photometric indicators above. Radio sources powered by star formation are roughly coextensive with the star-forming regions, their synchrotron emission broadened only slightly by diffusion of cosmic-ray electrons (Murphy et al. 2008). Coextensive synchrotron emission and free-free absorption by ionized hydrogen at electron temperature $T_\mathrm{e} \sim 10^4$ K limits the 1.4 GHz brightness temperature of SFGs to $T_\mathrm{b} \lesssim 10^5$ K (Condon 1992). AGNs can produce

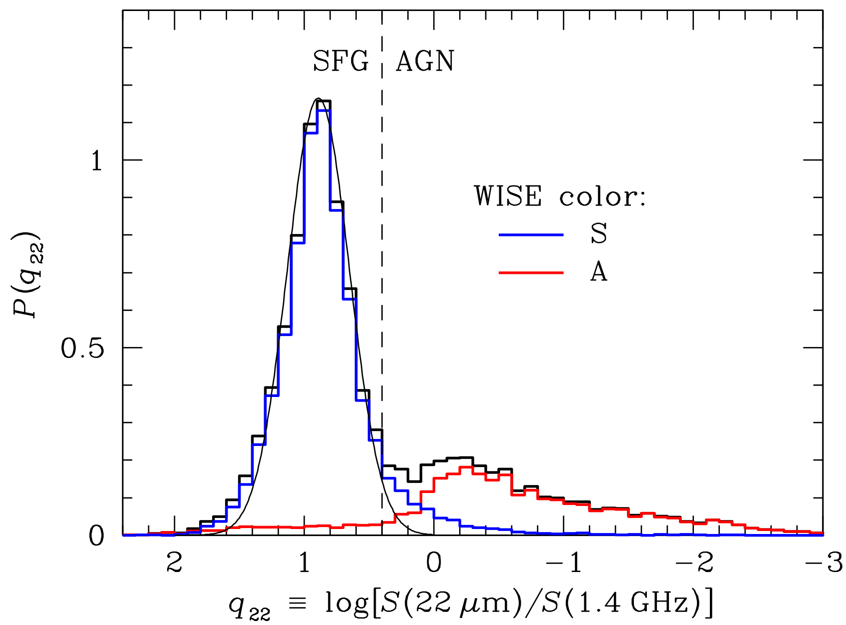

Figure 2.6. The normalized probability distribution $P(q_{22})$ of $q_{22} \equiv \log[S(22\,\mu\mathrm{m})/S(1.4\,\mathrm{GHz})]$ for all 2MASX/NVSS galaxies with $S(1.4\,\mathrm{GHz}) \geq 2.45$ mJy is indicated by the black histogram. The blue and red histograms show the galaxies classified as S or A by their *WISE* MIR colors (Equation 2.10 and Figure 2.5). The vertical dashed line at $q_{22} = +0.4$ separates most SFGs ($q_{22} > +0.4$) from most AGNs ($q_{22} < +0.4$). The Gaussian fit to the narrow peak has mean $\langle q_{22} \rangle = 0.89$ and rms width $\sigma = 0.24$. Abscissa: *WISE* MIR/radio flux-ratio parameter q_{22}. Ordinate: Probability density $P(q_{22})$.

radio jets and lobes that extend well outside their host galaxies, and they can produce compact radio cores with brightness temperatures $T_\mathrm{b} \gg 10^5$ K.

To identify very extended radio jets and lobes, we inspected the finding charts of all galaxies having two or more NVSS components. Most are either elliptical galaxies or spiral galaxies larger than the radio sources and much larger than the $\theta = 45''$ FWHM NVSS beam.

The only spiral galaxy with radio emission outside the galaxy of stars is the Seyfert NGC 4258 (2MASX J12185761+4718133) with unique "anomalous radio arms" (van der Kruit et al. 1972). NGC 4258 was not covered by the *IRAS* FSC, but we classified its radio source as primarily AGN-powered on the basis of *WISE* photometry ($q_{22} = -0.10$).

All but one of the multicomponent NVSS sources not identified with large spiral galaxies are so radio-loud (either $q < 1.8$ or $q_{22} < 0.4$) that they had already been photometrically classified as AGN-powered. The sole exception is luminous triple radio source in 2MASX J23415138−3729306, which has neither *IRAS* nor *WISE* photometry and was classified as AGN-powered on the basis of radio morphology alone.

Sub-arcsecond resolution is needed to resolve sources brighter than $T_{\rm b} \sim 10^5$ K, so the NVSS alone is unable to distinguish AGN cores from compact SFGs.

The four indicators above do not always agree, so the final energy source types A, (A), S, and (S) listed in Table 2.1 were derived by reconciling the various *IRAS* and *WISE* classifications as follows:

1. If *IRAS* and *WISE* agree on A or S, the final classification is A or S.

2. if *IRAS* and *WISE* disagree on A or S, the *IRAS* result was kept but qualified as uncertain (A) or (S).

3. If *IRAS* = ? (no *IRAS* data) and $q_{22} < 0.4$ (radio loud), then the final classification is M if the *WISE* MIR color classification = ? and (M) if it = S.

4. If *IRAS* = ?, $0.7 > q_{22} \geq 0.4$, and *WISE* = S, then the final classification is (S).

5. If *IRAS* = ?, $q_{22} \geq 0.7$, and *WISE* = S, then the final classification is S.

Among our 15,043 galaxies classified by radio and infrared criteria are 3,466 that had been classified by Mauch & Sadler (2007) on the basis of optical line spectra. Their star-forming galaxies were labeled SF, and their AGNs were divided into three subtypes: Aa (pure absorption-line spectra like those of giant elliptical galaxies), Aae (spectra with absorption lines and weak narrow LINER-like emission lines), or Ae (conventional Type II AGN spectra with nebular emission lines such as [O II], [O III], or [N II] that are stronger than any hydrogen Balmer emission lines, or conventianal Type

Table 2.2. Source classification matrix

	A	(A)	S	(S)
Aa	644	32	6	8
Aa?	27	5	1	5
Aae	101	18	27	15
Aae?	24	10	27	10
Ae	41	28	19	16
Ae?	10	17	23	5
SF	17	48	2018	103
SF?	3	12	64	18
?	21	5	33	5

I AGN spectra with strong and broad hydrogen Balmer emission lines). Uncertain optical classifications were indicated by '?'.

Table 2.2 compares our independent galaxy classification methods for these 3,466 galaxies, and the agreement is better than we had expected. Of the 888 galaxies we classified as A, Mauch & Sadler (2007) classified 867, 847 (97.7%) as various AGN types and only 20 (2.3%) as SF or SF?. We classified 2218 galaxies as S and Mauch & Sadler (2007) classified 2185 of them, 2082 (95.3%) as SF or SF? and 103 (4.7%) as various AGN types. Of their 2186 SF galaxies, we classified 2121 (97.0%) as S or (S), 17 (0.8%) as A, and 48 (2.2%) as (A). They classified 690 galaxies as Aa; we classified 676 (98.0%) as A or (A) and 14 (2.0%) as S or (S). The agreement is lower for the 161 Aae galaxies (74%) and the 104 Ae galaxies (66%). Most of these are star-forming LINERs or Seyfert II galaxies whose AGN radio luminosities appear to be less than half their total radio luminosities.

2.6.2 1.4 GHz Nearby Galaxy Counts

The differential source count $n(S)dS$ is the number of sources per steradian with flux densities between S and $S + dS$. The differential contribution $d\,T_{\rm B}$ of radio sources

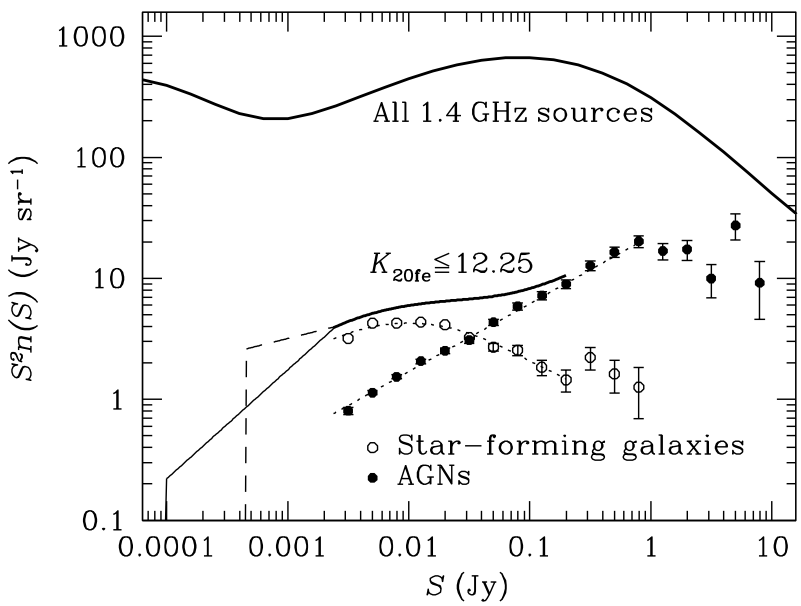

Figure 2.7. The brightness-weighted 1.4 GHz differential counts $S^2n(S)$ are plotted separately for all radio sources (Condon 1984) (solid curve) and for 2MASX/NVSS galaxies brighter than $k_{20\text{fe}} = 12.25$ whose radio sources are powered by stars (open circles) or AGNs (filled circles). $S^2n(S)$ is proportional to the contribution per decade of flux density to the 1.4 GHz sky brightness temperature. The light straight line matching the $P(S_\text{p})$ distribution (Figure 2.8) suggests that most galaxies with $k_{20\text{fe}} \leq$ 12.25 have 1.4 GHz flux densities $S \gtrsim 0.1$ mJy. Abscissa: 1.4 GHz flux density S (Jy). Ordinate: Brightness-weighted differential count $S^2n(S)$ (Jy sr^{-1}).

between S and $S + d\,\log(S)$ to the Rayleigh-Jeans sky brightness temperature T_b is

$$\frac{d\,T_\text{b}}{d\,\log(S)} = S^2 n(S) \left[\frac{\ln(10) c^2}{2 k_\text{B} \nu^2} \right] , \tag{2.13}$$

where $k_\text{B} \approx 1.38 \times 10^{-23}$ J K^{-1} is the Boltzmann constant. Figure 2.7 is a logarithmic plot comparing the brightness-weighted 1.4 GHz counts $S^2n(S)$ for all extragalactic sources (Condon 1984) (upper solid curve), all 2MASX/NVSS sources with $k_{20\text{fe}} \leq$ 12.25 and $S_{1.4\ \text{GHz}} \geq 2.45$ mJy (lower solid curve), 2MASX/NVSS sources powered primarily by star formation (open circles), and 2MASX/NVSS sources powered by AGNs (filled circles). Below $S \approx 0.1$ Jy the nearby ($z \lesssim 0.1$) 2MASX/NVSS sources contribute $\lesssim 1\%$ of the total radio-source background.

The 2MASX catalog is quite complete for $k_{20\mathrm{fe}} \leq 12.25$ and bright 2MASX galaxies have a nearly static Euclidean source count $n(S) \propto S^{-5/2}$ (Jarrett 2004). Radio sources powered by star formation typically have relatively low absolute spectral luminosities $L \sim 10^{22}$ W Hz^{-1} (Condon et al. 2002) yielding flux densities $S \sim 0.01$ Jy at the distances $d \sim 100$ Mpc ($cz \sim 7,000$ km s^{-1}) typical of 2MASX/NVSS SFGs. At flux densities $S > 0.01$ Jy the volume accessible to the 2MASX/NVSS sample of SFGs is almost completely IR-limited, so their radio source count should also be nearly Euclidean: $S^2 n(S) \propto S^{-1/2}$ as suggested by the dotted line connecting the open points in Figure 2.7. At lower flux densities the 2MASX/NVSS sample depth becomes more radio-limited, so the contribution by SFGs to $S^2 n(S)$ flattens out and eventually turns over. Nearby 2MASX/NVSS radio AGNs are typically more luminous than SFGs by factors of $\sim 10^{2.5}$ (Condon et al. 2002), so their source count is IR-limited and nearly Euclidean only for the small number of AGNs stronger than $S \sim 1$ Jy. Nearly all 2MASX/NVSS AGNs are much weaker and the volume sampled is strongly limited by the radio sensitivity limit. The dotted straight line fitted to the AGN count (filled circles) in Figure 2.7 has a slope $d \log[S^2 n(S)]/d \log(S) \approx +0.6$ for $S \ll 1$ Jy. This slope is close to the slope $\alpha \approx +0.5$ of the 1.4 GHz spectral power density function $U_{\mathrm{dex}}(L)$ at spectral luminosities $L \ll 10^{24}$ W Hz^{-1} (see Section 2.9.2).

Only 15,043 of the 55,288 (27%) 2MASX galaxies brighter than $k_{20\mathrm{fe}} = 12.25$ contain NVSS sources stronger than 2.45 mJy at 1.4 GHz. However, the normalized probability distribution $P(S_{\mathrm{p}})$ of NVSS peak flux densities S_{p} at the positions of all 55,288 2MASX sample galaxies (heavy histogram in Figure 2.8) constrains the radio source count well below 2.45 mJy. The light histogram shows the matching distribution of peak flux densities at "blank" positions offset 1° to the north. It is well fit by a noise Gaussian with rms width $\sigma = 0.47$ mJy beam^{-1} (light curve) plus a thin positive-going tail produced by background radio sources. The NVSS on-source distribution is the convolution of the off-source distribution and the peak flux density distribution of 2MASX galaxies. To the extent that most weak 2MASX radio sources

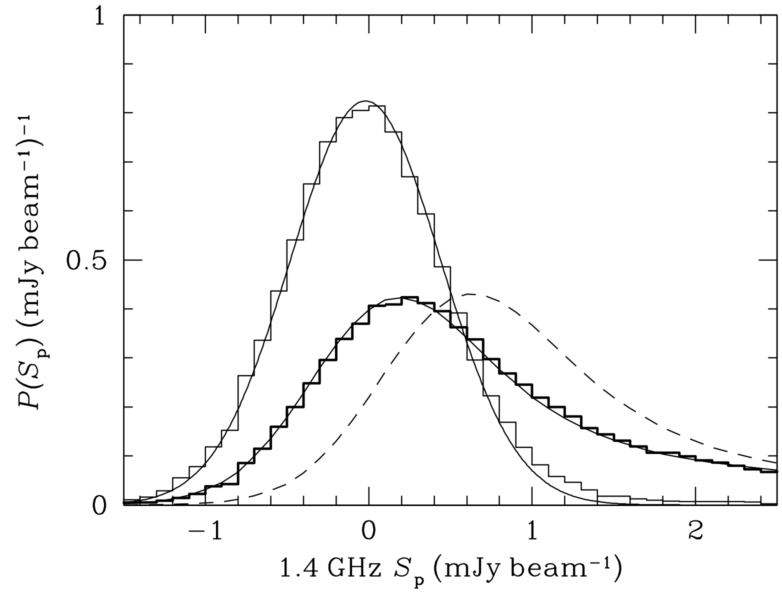

Figure 2.8. The distribution of NVSS peak flux densities $S_{\rm p}$ at the positions of all 2MASX sample galaxies is plotted as the heavy histogram, and the light histogram shows the corresponding peak flux densities at "blank" positions offset 1° to the north. The source count indicated by the light solid line in Figure 2.7 yields the best fits (solid curves) to these histogrrams. The dashed curve that doesn't fit the data is the $P(S_{\rm p})$ distribution corresponding to the dashed source count in Figure 2.7.

are unresolved in the $\theta = 45''$ FWHM NVSS beam, $S_{\rm p} \approx S$ and

$$\Omega\, n(S)\, dS = N\, P(S_{\rm p})\, dS_{\rm p}\ . \tag{2.14}$$

For any $S^2 n(S)$ (Figure 2.7) we can solve for

$$P(S_{\rm p}) = \left(\frac{\Omega}{NS^2}\right) S^2 n(S)\ . \tag{2.15}$$

To the degree that the weighted differential count can be approximated by a power law $S^2 n(S) \approx kS^\gamma$ over the flux-density range S_1 to S_2, the number of sources ΔN with flux densities between S_1 and S_2 is

$$\Delta N \approx \Omega \int_{S_1}^{S_2} kS^{\gamma-2}\, dS = \left(\frac{\Omega k}{1-\gamma}\right)(S_1^{\gamma-1} - S_2^{\gamma-1})\ . \tag{2.16}$$

Among the $N = 55,288$ 2MASX galaxies brighter than $k_{20\text{fe}} = 12.25$ in $\Omega = 7.016\,\text{sr}$, there are $\Delta N = 40,245$ with peak flux densities $S_2 < 2.45$ mJy.

Equation C.16 is an integral constraint on S_1 (there can't be more 2MASX/NVSS radio sources than 2MASX galaxies) as a function of the other two source-count variables k and γ. Continuity of the direct source count $S^2 n(S) \approx 4\ \text{sr}^{-1}$ at $S \approx 0.003$ Jy (Figure 2.7) fixes k for any γ. The best value of the remaining unknown γ is the one that yields the best fit to the heavy $P(S_\text{p}$ histogram in Figure 2.8. For example, the power-law extrapolation $S^2 n(S) = 17.9 S^{0.25}$ of the direct count of 2MASX galaxies with $k_{20\text{fe}} \leq 12.25$ above $S = 2.45$ mJy yields the dashed line in Figure 2.7 that must break at $S_1 \approx 0.46$ mJy lest the number of radio sources exceed the number of galaxies. However, this solution is unsatisfactory because it predicts the dashed $P(S_\text{p})$ distribution in Figure 2.8 that is shifted far to the right of the observed distribution (heavy histogram).

The best power-law fit is $S^2 n(S) \approx 880 S^{-0.90}$ cutting off at $S_1 \approx 0.0001$ Jy, as shown by the light straight line in Figure 2.7 and the continuous curve that is a good match to the heavy histogram in Figure 2.8. We conclude that (1) the brightness-weighted count of nearby sources fainter than 2.45 mJy must converge rapidly, and (2) the NVSS is sufficiently sensitive to have detected individually those sources that contribute most of the low redshift ($z \lesssim 0.05$) sky brightness. It also appears that most 2MASX galaxies brighter than $k_{20\text{fe}} = 12.25$ are radio sources stronger than $S \sim 0.1$ mJy and should be detectable above the planned $S_\text{p} \approx 0.05$ mJy sensitivity limit of the upcoming EMU survey (Norris 2011).

2.7 The Spectroscopically Complete Subsample

All but 7 of the 9,517 2MASX/NVSS galaxies with $k_{20\text{fe}} \leq 11.75$ have published spectroscopic velocities cz or new velocities reported in Section 2.7.1.

2.7.1 New Spectroscopic Redshifts

We obtained spectra for 12 of the 19 galaxies lacking published spectroscopic redshifts with the Dual Imaging Spectrograph (DIS) on the Apache Point Observatory (APO) 3.5 m telescope. Observations were carried out over three half-nights occurring in October through December of 2017. DIS is a medium dispersion double spectrograph that has separated red and blue channels. The standard "high" resolution DIS III grating setup B1200/R1200 was used. The wavelength ranges were centered on the Hβ and Hα lines at the median redshift of the 2MASX/NVSS sample, 5021 Å and 6780 Å for the blue and red cameras, respectively. This resulted in a wavelength coverage of $4401 - 5641$ Å and $6200 - 7360$ Å for the blue and red channels, respectively.

Total exposure times ranged from 1620 s to 3360 s, taken in intervals of 120 s to 420 s so as to mitigate cosmic-ray contamination. The two galaxies with the weakest spectral lines were observed on multiple nights to increase exposure time and improve the quality of the redshift measurement. Bias and flat frames were obtained before each observing run. Comparison spectra were obtained before and after each observation run using a He, Ne, and Ar lamp.

The spectra were reduced and analyzed in a uniform manner with IRAF. Initial 2D frames were bias-subtracted and flat-fielded using subroutines in the CCDRED package. Apertures were extracted with the APEXTRACT package. Dispersion functions were derived from the HeNeAr lamp spectra and fit to the object frames using routines in the ONEDSPEC package. Multiple sub-exposures of each target were combined for the blue and red spectra.

The blue and red portions of the spectrum were combined and processed using the XCSAO procedure in the RVSAO package to determine barycentric radial velocities. Sample spectra are shown in the top portion of Figure 2.9. The XCSAO routine follows the cross-correlation technique developed by Tonry & Davis (1979). We used the SDSS galaxy templates[1], specifically 23–28, in the cross-correlation. Hot pixels and the unobserved wavelength range between the blue and red cameras were ignored by the cross-correlation routine. Typical results from the cross-correlation technique

[1]http://classic.sdss.org/dr7/algorithms/spectemplates/

are shown in the bottom panel of Figure 2.9 for the two galaxies shown in the top panel. The resulting barycentric radial velocities are given in Table 2.3.

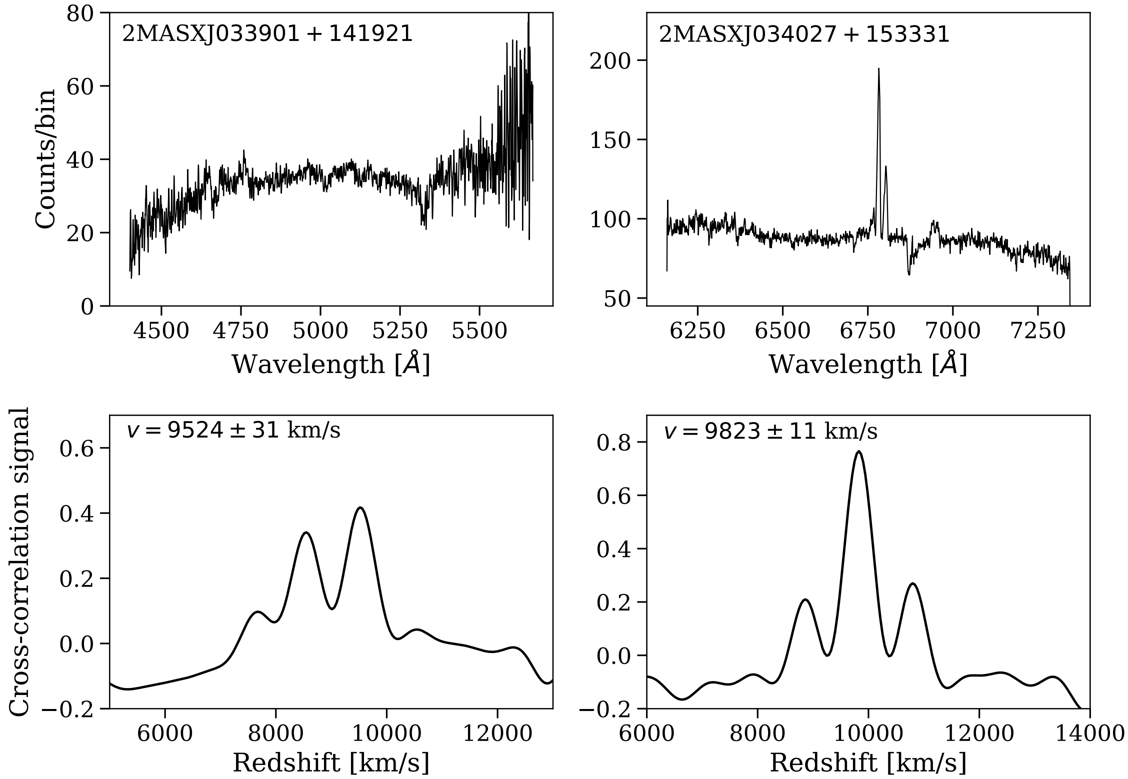

Figure 2.9. Top panels: Examples of typical spectra obtained for the 12 galaxies with the APO 3.5 m telescope. Left: Absorption line spectrum with the DIS blue camera. Right: Emission line spectrum with the DIS red camera. Bottom panels: Results of the cross-correlation technique used to measure the redshifts for the corresponding top panel galaxies.

The reliability of the velocities can be estimated by the r statistic, a confidence measure. Calibration done in the development of the XCSAO cross-correlation routine (Kurtz & Mink 1998) suggests that cross-correlations with $r > 3$ can be deemed reliable, but note that many of the spectra in their test study with $2 < r < 3$ also yield correct velocities. Of the twelve galaxies observed, all but one of the spectra has $r > 3$. The exception, 2MASX J21352090+8906537, has $r = 2.55$ for the template with the highest cross-correlation signal.

Table 2.3: 2MASS Supplemental Velocities

2MASX J2000 name	R.A. hh:mm:ss.ss	Dec. dd:mm:ss.s	l (deg)	b (deg)	$v = cz$ ($\mathrm{km\,s^{-1}}$)	σ_v ($\mathrm{km\,s^{-1}}$)
02570403+2000446	02:57:04.03	+20:00:44.6	159.08	−33.90	9500.6	14.4
03215557+2149375	03:21:55.57	+21:49:37.5	163.32	−29.00	14302.0	12.2
03390103+1419217	03:39:01.03	+14:19:21.7	172.61	−31.94	9523.9	31.0
03402770+1533113	03:40:27.70	+15:33:11.3	171.90	−30.82	9823.3	11.1
04141963+2025240	04:14:19.63	+20:25:24.0	174.24	−21.65	6316.2	59.9
07134975+8729044	07:13:49.75	+87:29:04.4	125.75	+27.35	15157.5	59.9
17272375+1521110	17:27:23.75	+15:21:11.0	37.88	+25.37	9045.2	37.3
17494097+5333541	17:49:40.97	+53:33:54.1	81.29	+30.50	28187.3	161.8
17543888+6803287	17:54:38.88	+68:03:28.7	98.12	+30.30	23869.6	83.9
20510128−1710242	20:51:01.28	−17:10:24.2	29.78	−33.95	19387.9	82.2
21352090+8906537	21:35:20.90	+89:06:53.7	122.18	+26.55	21094.2[a]	125.0
23074944−1236479	23:07:49.44	−12:36:47.9	58.71	−61.74	20378.2	37.0

2.7.2 Corrections for Solar Motion and Galaxy Peculiar Velocities

To estimate accurate distances from the observed heliocentric velocities, we first converted the heliocentric velocities $v \equiv cz$ to velocities $v_{\rm CMB}$ in the frame of the cosmic microwave background (CMB) using

$$\begin{aligned} v_{\rm CMB} = v + v_{\rm apex}[&\sin(b)\sin(b_{\rm apex}) \\ &+ \cos(b)\cos(b_{\rm apex})\cos(l - l_{\rm apex})] \ , \end{aligned} \tag{2.17}$$

where $(l_{\rm apex}, b_{\rm apex}) = (264.14°, 48.26°)$ and $v_{\rm apex} = 371.0$ km s^{-1} (Fixsen et al. 1996).

Large-scale structures (e.g., galaxy clusters) cause additional deviations from the local Hubble flow that depend on position and redshift. We adopted the local bulk flow models of Carrick et al. (2015) to correct for this effect.

The Carrick et al. (2015) model of the peculiar velocity field is given as a 257^3 voxel cube in right-handed galactic Cartesian coordinates with i, j, and k indices corresponding to galactic X, Y, Z in Mpc h^{-1}, with the i index running fastest. The voxel centers run from $-200h^{-1}$ to $200h^{-1}$ Mpc so the voxel spacing is $1.5625h^{-1}$ Mpc. The i, j, k indices can be converted to Cartesian galactic coordinates using

$$X = (i - 128) \times 400./256. \tag{2.18}$$

$$Y = (j - 128) \times 400./256. \tag{2.19}$$

$$Z = (k - 128) \times 400./256. \tag{2.20}$$

The center of the cube [128,128,128] represents the Local Group. All peculiar velocities $v_{\rm pec}$ in the cube are relative to the CMB and are generated by the galaxy density models of Carrick et al. (2015), which depend upon the cosmological density of matter $\Omega_{\rm m}$ (taken to be 0.3 in this study) and the bias b^* of an L^* galaxy. Along the radial line to each galaxy, we solved

$$H_0\, r + v_{\rm pec}(r) = v_{\rm CMB} \tag{2.21}$$

to obtain the corrected galaxy velocity $v_{\rm c} = cz_{\rm c}$.

The histograms in Figure 2.10 show the normalized probability distributions $P(cz)$ of corrected velocities $cz_{\rm c}$ for galaxies whose radio sources are powered by stars (unshaded area) or by AGNs (shaded). Star-forming galaxies outnumber AGNs by a ratio of >2:1 in this sample of bright galaxies, especially at lower redshifts. The median velocity of star-forming galaxies is only $\langle cz_{\rm c}\rangle \approx 0.6 \times 10^4$ km s^{-1}, about half the median velocity $\langle cz_{\rm c}\rangle \approx 1.2 \times 10^4$ km s^{-1} of galaxies with AGN-powered radio sources.

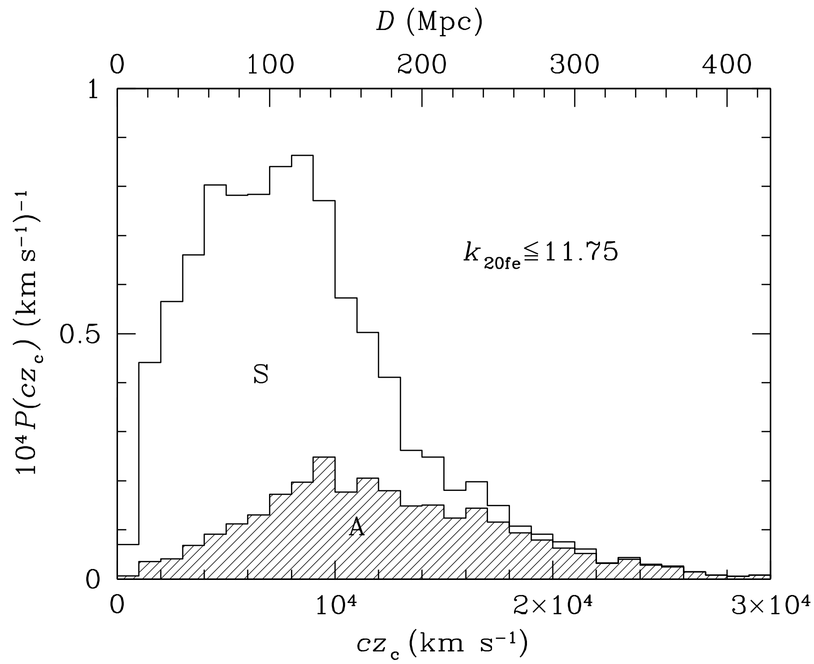

Figure 2.10. All but 7 of the 9,517 2MASX/NVSS galaxies with $k_{20\mathrm{fe}} \leq 11.75$ have spectroscopic redshifts. Histograms of their corrected velocities cz_{c} are shown separately for galaxies whose radio sources are powered by AGNs (A) or by stars (S). The corresponding Hubble distances for $H_0 = 70$ km s^{-1} Mpc^{-1} are also shown. Lower Abscissa: cz_{c} (km s^{-1}). Upper Abscissa: Hubble distance D (Mpc) Ordinate: $10^4\, P(cz_{\mathrm{c}})$ (km s^{-1})$^{-1}$.

2.8 Local 1.4 GHz Luminosity Functions

The local luminosity function specifies the mean space density of galaxies in the nearby universe as a function of spectral luminosity. The universe is evolving and homogeneous on large scales, so the local luminosity function more usefully represents the universal average space density during the present epoch rather than our particular location in space. We derived separate 1.4 GHz luminosity functions for radio sources powered by star formation and by AGNs. They are today's benchmarks for comparing with higher-redshift samples to constrain models for the cosmological evolution of star formation and AGN activity.

The 2MASX/NVSS spectroscopic subsample should yield reliable 1.4 GHz luminosity functions because redshifts are available for nearly all galaxies and it is complete for galaxies that are brighter than $k_{20\text{fe}} = 11.75$ at $\lambda = 2.16\,\mu$m, stronger than $S = 2.45\,$mJy at 1.4 GHz, and lie in the solid angle $\Omega = 7.016$ sr defined by J2000 $\delta > -40°$ and $|b| > 20°$. The 2MASX catalog itself is actually complete and reliable for galaxies much fainter than $k_{20\text{fe}} = 11.75$; our magnitude limit reflects the availability of spectroscopic redshifts. The NVSS sample includes all sources with catalog flux densities $S \geq 2.5$ mJy. However, the NVSS catalog flux densities are rounded to the nearest 0.1 mJy, so sources as faint as $S = 2.45$ mJy are listed as having $S = 2.5$ mJy in the catalog. The spectroscopic redshifts are from Huchra et al. (2012) or from new optical and NIR spectra obtained with the Apache Point Observatory (APO) 3.5 m telescope, as described in Appendix 2.7.1.

The 1.4 GHz spectral luminosity function $\rho(L)\,dL$ is defined as the space density of sources with 1.4 GHz spectral luminosities between L and $L + dL$. The range of spectral luminosities spanned by galaxies is so large that it is convenient to define a logarithmic spectral luminosity function

$$\rho_{\text{dex}}(L) \equiv \rho(L)\frac{dL}{d\log(L)} = \ln(10)L\rho(L) \tag{2.22}$$

specifying the space density of sources per decade of spectral luminosity.

The 1.4 GHz spectral luminosity of each source is

$$L = 4\pi D_L^2 S_{1.4}(1+z)^{-(1+\alpha)} , \tag{2.23}$$

where $D_{\text{L}} = (1+z)D_{\text{C}}$ is the luminosity distance to the radio source, D_{C} is the comoving distance, $S_{1.4}$ is the 1.4 GHz NVSS flux density, and $\alpha = -0.7$ is the mean spectral index ($S \propto \nu^{\alpha}$) of sources selected at 1.4 GHz (Condon 1984). The absolute magnitude $K_{20\text{fe}}$ was calculated using

$$K_{20\text{fe}} = k_{20\text{fe}} - 5\log\left(\frac{D_{\text{L}}}{10\text{ pc}}\right) - k(z) , \tag{2.24}$$

where $k(z) = -6.0\,\log(1+z)$ is the k-correction that is independent of galaxy type and valid for all $z \leq 0.25$ (Kochanek et al. 2001). We therefore used $z_{\max} = 0.25$ as the maximum possible redshift when calculating $V_{\max}$ values for our galaxy sample.

2.8.1 Maximum Redshifts

We plotted the maximum redshifts $z_{\max}$ at which galaxies could remain in our spectroscopic subsample as functions of both 1.4 GHz spectral luminosity (Figure 2.11) and $\lambda = 2.16\ \mu$m absolute magnitude $K_{20\mathrm{fe}}$ (Figure 2.12). Star-forming galaxies (blue triangles) span the majority of the redshift range ($0.0017 \lesssim z \lesssim 0.12$) and absolute magnitudes ($-18 \gtrsim K_{20\mathrm{fe}} \gtrsim -27$), but are mainly limited to 1.4 GHz luminosities $\log[L(\mathrm{W\ Hz^{-1}})] \lesssim 23$. AGNs (black circles) dominate both the high radio luminosities and absolute magnitudes $K_{20\mathrm{fe}}$, but are fewer in number at the lowest redshifts ($z \lesssim 0.007$).

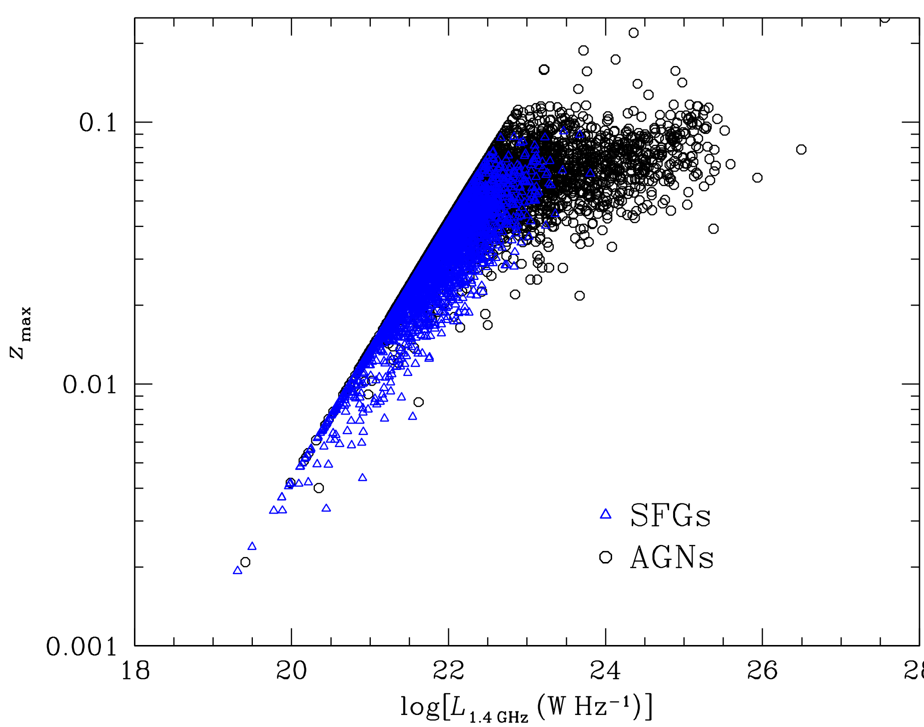

Figure 2.11. Maximum redshifts out to which a 2MASX/NVSS source could be moved and remain in the spectroscopic subsample, as a function of 1.4 GHz luminosity. The maximum redshifts for star-forming galaxies (blue triangles) and AGNs (black circles) are shown as a function of 1.4 GHz radio luminosity.

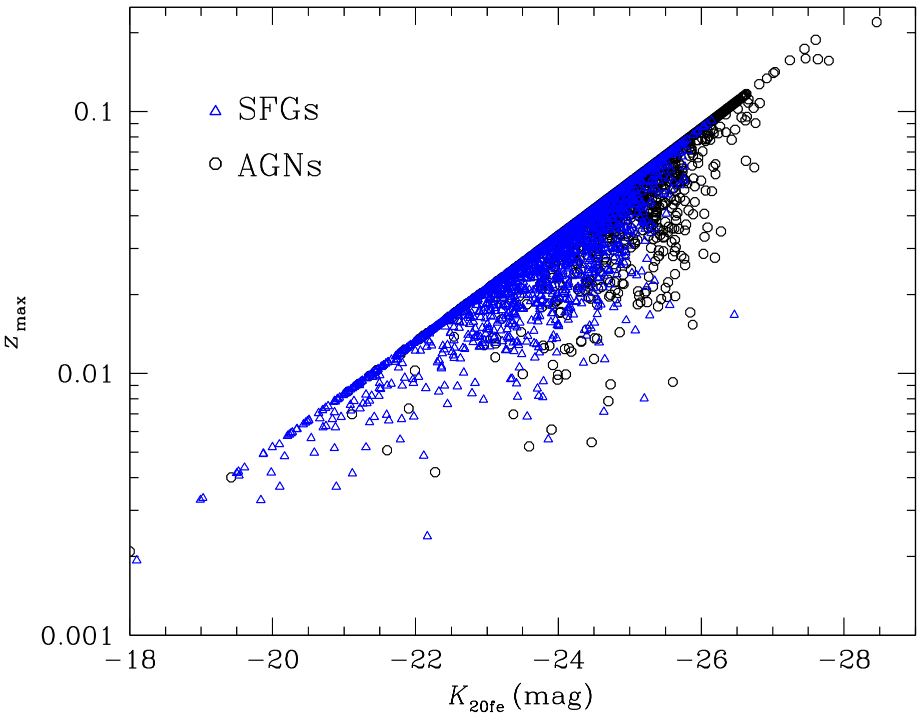

Figure 2.12. Maximum redshifts out to which a 2MASX/NVSS source could be moved and remain in the spectroscopic subsample, as a function of $K_{20\text{fe}}$. The maximum redshifts for star-forming galaxies (blue triangles) and AGNs (black circles) are shown as a function of $K_{20\text{fe}}$.

2.8.2 Correction for Local Overdensity

Galaxies cluster and we are located in a galaxy, so the space density ρ_{P} of the nearest galaxies is somewhat greater than the mean density ρ of all galaxies. We corrected our local luminosity function for the local overdensity within a distance r using the equation (Fisher et al. 1994)

$$\frac{\rho_{\text{P}}}{\rho} = 1 + \frac{3}{3-\gamma}\left(\frac{r_0}{r}\right)^{\gamma} . \tag{2.25}$$

The correlation function parameters of *IRAS* galaxies are appropriate for describing the clustering of the 2MASX/NVSS galaxies; they are $r_0 = 3.76\,h^{-1}$ and $\gamma = 1.66$

for $r < 20\,h^{-1}\,\mathrm{Mpc}$ (Fisher et al. 1994). For $r < 20\,h^{-1}\,\mathrm{Mpc}$, the volume within r was multiplied by ρ_{P}/ρ in our calculation of $V_{\max}$; otherwise the volume was left unchanged. To minimize uncertainties introduced by large values of this correction for local-group galaxies, we excluded 48 galaxies in the volume with $r < 5$ Mpc (corrected $cz_{\mathrm{c}} < 350$ km s^{-1}, or $z \lesssim 0.0017$) when calculating luminosity functions. Only about 5% of our sample galaxies have $r < 20\,h^{-1}$ Mpc ≈ 29 Mpc, so correcting for the local overdensity has only a small effect on our radio luminosity functions.

2.8.3 The Distribution of $V/V_{\max}$

If the radio sources are randomly distributed throughout the corrected volume, the distribution of $V/V_{\max}$ should be uniform in the interval [0,1] and have a mean $\langle V/V_{\max}\rangle \approx 0.5$. The standard deviation of a uniform distribution on the interval [0,1] is $12^{-1/2}$, so the rms uncertainty in $\langle V/V_{\max}\rangle$ of $N \gg 1$ radio sources is $\sigma \approx (12N)^{-1/2}$. A statistically significant departure from a uniform distribution with mean 0.5 may indicate one or more of the following: poor corrections for the local overdensity, incorrect sample limits, strong clustering, or monotonic evolution of sources during the lookback times spanned by the sample volume. For the 2MASX/NVSS galaxies used to determine the local luminosity function, the 6699 star-forming galaxies have $\langle V/V_{\max}\rangle = 0.500 \pm 0.004$, the 2763 AGNs have $\langle V/V_{\max}\rangle = 0.494 \pm 0.005$, and all 9462 galaxies have $\langle V/V_{\max}\rangle = 0.497 \pm 0.003$. Thus our $\langle V/V_{\max}\rangle$ test detects no monotonic evolution during the sample-limited lookback time $\tau \sim 1 - 2$ Gyr.

The normalized probability densities of $V/V_{\max}$ in 20 bins of width $\Delta(V/V_{\max}) = 0.05$ are plotted separately for star-forming galaxies and AGNs in Figure 2.13. The $V/V_{\max}$ distribution for AGNs closely follows a uniform distribution with a $\chi^2_\nu \approx 1.08$. In contrast, the distribution for star-forming galaxies appears to deviate slightly, with a $\chi^2_\nu \approx 2.04$, marginally significant at the ~ 0.01 level. This slight deviation from a uniform distribution can be mostly attributed to the peak in the bin of $V/V_{\max}$ from $0.80 - 0.85$. This is caused mainly by galaxies whose $z_{\max}$ is limited by radio luminosity rather than K band magnitude. This peak would be a marginally statistically significant 3.6σ bump for the star-forming galaxies if galaxies were distributed randomly in space. However, our V/V_{max} fluctuations are consistent with the statistical fluctuations expected in clustered galaxy samples mildly exacerbated by the NVSS catalog flux-density quantization.

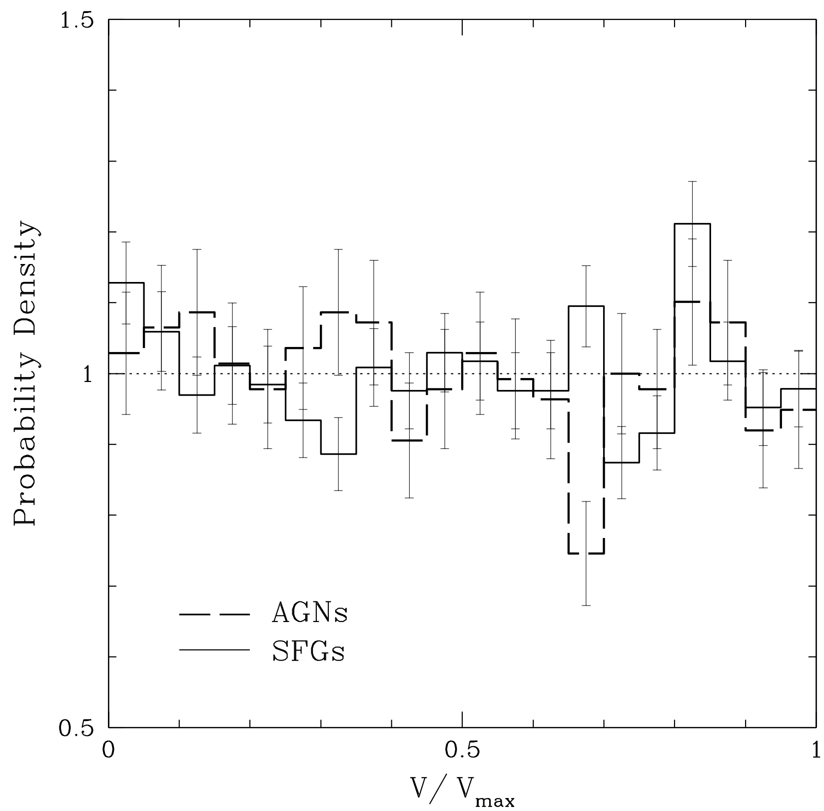

Figure 2.13. Binned distributions of V/V_{max} for star-forming galaxies (solid line) and AGNs (dashed line) with the rms uncertainties expected for randomly distributed galaxies. Abscissa: V/V_{max}. Ordinate: Binned probability density.

2.8.4 Luminosity Function Results

We sorted our galaxies into luminosity bins of width $\Delta \log(L) = 0.2$ (5 bins per decade) centered on $\log[L(\mathrm{W\ Hz^{-1}})] = 19.4$ to 27.6 and calculated separate local luminosity functions of star-forming galaxies and AGNs using

$$\rho_{\rm dex} = 5 \sum_{i=1}^{N} \left(\frac{1}{V_{\rm max}} \right)_i . \qquad (2.26)$$

Our 1.4 GHz local luminosity functions $\rho_{\rm dex}$ for star-forming galaxies and AGNs are listed in Table 2.4 and plotted in Figure 2.14. The listed errors are the rms Poisson counting errors for independent galaxies

$$\sigma = 5 \left[\sum_{i=1}^{N} \left(\frac{1}{V_{\rm max}} \right)_i^2 \right]^{1/2} \qquad (2.27)$$

quadratically summed with a 3% flux-scale uncertainty. If the number N of galaxies in a luminosity bin is small ($N < 5$), the quoted errors are the 84% confidence limits tabulated in Gehrels (1986). Clustering and cosmic variance are addressed in Section 2.10.

The luminosity functions of SFGs and AGNs intersect at $\log[L(1.4\ \mathrm{GHz})] \approx 22.7$ in agreement with the earlier result of Condon et al. (2002) and close to the $\log[L(\mathrm{W\ Hz^{-1}})] \approx 22.9$ found by Mauch & Sadler (2007) despite the different samples and classification methods used. This crossover marks the 1.4 GHz spectral luminosity below which star-forming galaxies outnumber AGNs within the local universe.

Table 2.4: 1.4 GHz Local Luminosity Functions ($h = 0.70$)

	Star-forming Galaxies		AGNs	
$\log L$ ($\mathrm{W\,Hz^{-1}}$)	N	$\log \rho_{\rm dex}$ ($\mathrm{dex^{-1}\,Mpc^{-3}}$)	N	$\log \rho_{\rm dex}$ ($\mathrm{dex^{-1}\,Mpc^{-3}}$)
19.4	6	$-1.81^{+0.16}_{-0.26}$	1	$-2.65^{+0.52}_{-0.76}$
19.6	3	$-2.39^{+0.30}_{-0.34}$	0	$\cdots$
19.8	10	$-2.29^{+0.12}_{-0.17}$	0	$\cdots$
20.0	11	$-2.37^{+0.14}_{-0.21}$	1	$-3.53^{+0.52}_{-0.76}$
20.2	21	$-2.46^{+0.09}_{-0.11}$	3	$-3.33^{+0.30}_{-0.34}$
20.4	59	$-2.20^{+0.07}_{-0.08}$	5	$-3.17^{+0.20}_{-0.36}$
20.6	103	$-2.29^{+0.05}_{-0.05}$	4	$-3.80^{+0.25}_{-0.28}$
20.8	147	$-2.36^{+0.04}_{-0.04}$	9	$-3.68^{+0.13}_{-0.18}$
21.0	244	$-2.39^{+0.04}_{-0.05}$	22	$-3.51^{+0.09}_{-0.12}$
21.2	411	$-2.47^{+0.03}_{-0.03}$	22	$-3.90^{+0.09}_{-0.11}$
21.4	584	$-2.58^{+0.02}_{-0.02}$	65	$-3.65^{+0.06}_{-0.07}$
21.6	823	$-2.68^{+0.02}_{-0.02}$	85	$-3.73^{+0.10}_{-0.13}$
21.8	975	$-2.88^{+0.02}_{-0.02}$	171	$-3.81^{+0.04}_{-0.04}$
22.0	1124	$-3.00^{+0.02}_{-0.02}$	216	$-3.94^{+0.04}_{-0.04}$
22.2	893	$-3.25^{+0.02}_{-0.02}$	281	$-4.02^{+0.04}_{-0.04}$
22.4	624	$-3.57^{+0.02}_{-0.02}$	280	$-4.12^{+0.05}_{-0.06}$
22.6	368	$-3.90^{+0.03}_{-0.03}$	286	$-4.26^{+0.03}_{-0.04}$
22.8	168	$-4.34^{+0.04}_{-0.05}$	239	$-4.37^{+0.04}_{-0.05}$
23.0	87	$-4.74^{+0.05}_{-0.06}$	209	$-4.46^{+0.04}_{-0.05}$

Continued on Next Page...

Table 2.4 – Continued

	Star-forming Galaxies		AGNs	
log L ($\mathrm{W\,Hz^{-1}}$)	N	log $\rho_{\rm dex}$ ($\mathrm{dex^{-1}\,Mpc^{-3}}$)	N	log $\rho_{\rm dex}$ ($\mathrm{dex^{-1}\,Mpc^{-3}}$)
23.2	30	$-5.30^{+0.10}_{-0.13}$	184	$-4.51^{+0.05}_{-0.06}$
23.4	13	$-5.63^{+0.12}_{-0.17}$	133	$-4.74^{+0.05}_{-0.06}$
23.6	1	$-7.39^{+0.52}_{-0.76}$	97	$-4.82^{+0.08}_{-0.10}$
23.8	1	$-6.96^{+0.52}_{-0.76}$	103	$-4.88^{+0.05}_{-0.06}$
24.0	0	···	69	$-5.03^{+0.06}_{-0.08}$
24.2	0	···	70	$-5.17^{+0.06}_{-0.07}$
24.4	0	···	59	$-5.23^{+0.06}_{-0.08}$
24.6	0	···	41	$-5.45^{+0.07}_{-0.09}$
24.8	0	···	41	$-5.50^{+0.08}_{-0.10}$
25.0	0	···	30	$-5.76^{+0.09}_{-0.12}$
25.2	0	···	24	$-5.88^{+0.10}_{-0.12}$
25.4	0	···	8	$-6.01^{+0.18}_{-0.33}$
25.6	0	···	2	$-6.91^{+0.37}_{-0.45}$
25.8	0	···	0	$\lesssim -7.68$
26.0	0	···	1	$-6.91^{+0.52}_{-0.76}$
26.2	0	···	0	$\lesssim -7.68$
26.4	0	···	1	$-7.23^{+0.52}_{-0.76}$
26.6	0	···	0	···
26.8	0	···	0	···
27.0	0	···	0	···
27.2	0	···	0	···

Continued on Next Page...

Table 2.4 – Continued

	Star-forming Galaxies		AGNs	
$\log L$ ($\mathrm{W\,Hz^{-1}}$)	N	$\log \rho_{\rm dex}$ ($\mathrm{dex^{-1}\,Mpc^{-3}}$)	N	$\log \rho_{\rm dex}$ ($\mathrm{dex^{-1}\,Mpc^{-3}}$)
27.4	0	$\cdots$	0	$\cdots$
27.6	0	$\cdots$	1	$-8.68^{+0.52}_{-0.76}$

Star-Forming Galaxies

The FIR/radio correlation shows that the radio and FIR luminosities of star-forming galaxies are nearly proportional, so their logarithmic radio and FIR luminosity functions should be similar in form. Saunders et al. (1990) found that the FIR ($40\,\mu\mathrm{m} < \lambda < 120\,\mu\mathrm{m}$) logarithmic luminosity function $\phi(L)$ derived from seven large samples of IRAS sources is well fit by the parametric form

$$\phi(L) = C\left(\frac{L}{L_*}\right)^{1-\alpha} \exp\left[-\frac{1}{2\sigma^2}\log^2\left(1+\frac{L}{L_*}\right)\right] \tag{2.28}$$

that approaches a power law at with slope $(1-\alpha)$ when $L \ll L_*$ and falls like a Gaussian with $\log(L)$ when $L \gg L_*$.

Equation 2.28 also fits the local 1.4 GHz logarithmic luminosity function $\rho_{\rm dex}(L)$ of star-forming galaxies very well, in congruence with the FIR/radio correlation, and it gives a better fit than the Schechter (1976) luminosity function. The dotted curve fitting the filled points in Figure 2.14 has the best-fit parameters for the 2MASX/NVSS star-forming galaxies stronger than $\log[L(\mathrm{W\ Hz^{-1}})] = 19.3$: $C = 3.50 \times 10^{-3}\,\mathrm{dex^{-1}\,Mpc^{-3}}$, $L_* = 1.9 \times 10^{21}\,\mathrm{W\,Hz^{-1}}$, $\alpha = 1.162$, and $\sigma = 0.558$. Despite the good parametric fit to the data, we have not quoted errors on these four param-

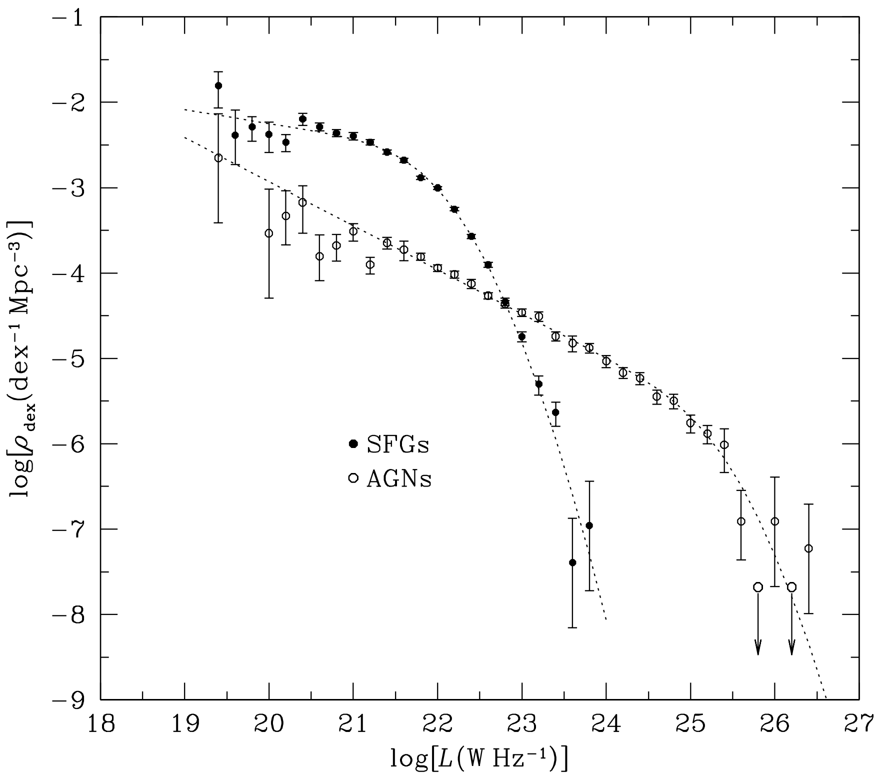

Figure 2.14. The 2MASX/NVSS 1.4 GHz logarithmic luminosity functions for sources whose radio emission is dominated by star formation (filled circles) and AGNs (unfilled circles). The two dotted curves represent the Saunders et al. (1990) and double power-law fits to the local luminosity functions of star-forming galaxies and AGNs, respectively.

eters because they are so highly correlated that they "grossly overestimate the total acceptable volume of parameter space" (Saunders et al. 1990).

Mauch & Sadler (2007) used a deeper ($k_{\rm s} < 12.75$) sample of 2MASX galaxies identified with NVSS sources and having 6dF spectra in a smaller area of sky ($\Omega \approx$ 2.16 sr) to calculate $\rho_{\rm dex}(L)$ in the luminosity range $19.8 \lesssim \log(L) \lesssim 23.8$ for galaxies they classified as star-forming on the basis of their optical spectra. Their fit to the Saunders et al. (1990) form in Equation 2.28 gave $C = 1.48{\pm}0.17{\times}10^{-3}$ dex^{-1} Mpc^{-3}, $L_* = 1.5 \pm 0.5 \times 10^{21}$ W Hz^{-1}, $\alpha = 1.02 \pm 0.15$, and $\sigma = 0.60 \pm 0.04$. Again, these four parameters are so highly correlated that apparently significant differences between their values and ours are not meaningful. Direct comparisons of our binned luminosity functions show that they agree within the expected errors after cosmic variance (Section 2.10) has been taken into account.

AGNs

For the high-luminosity bins in which no sources were detected, we are able to place upper limits on the space density of AGNs. Given their large radio luminosities, hypothetical sources in these empty bins would likely be volume-limited by the $k_{20\mathrm{fe}} = 11.75$ cutoff. The mean absolute magnitude of AGNs in our sample with $\log[L_{1.4\ \mathrm{GHz}}(\mathrm{W\ Hz}^{-1})] > 24.5$ is $\langle K_{20\mathrm{fe}} \rangle \approx -25.84$. We used this value to determine the maximum volume within which such a source would have $k_{20\mathrm{fe}} \leq 11.75$. For luminosity bins with $N = 0$, the resulting 84%-confidence $= 1\sigma$ upper limit given by Poisson statistics (Gehrels 1986) is $\log[\rho_{\mathrm{dex}}(\mathrm{dex}^{-1}\ \mathrm{Mpc}^{-3})] \lesssim -7.68$. These limits are shown by downward pointing arrows in Figure 2.14 and were used as additional constraints on the AGN luminosity function. Above $\log[L(\mathrm{W\ Hz}^{-1})] \sim 26.4$ those limits are well above the measured data points and provide no useful constraints on the luminosity function.

A double power-law has traditionally been used to describe the local logarithmic luminosity function of AGNs:

$$\rho_{\mathrm{dex}}(L) = \frac{C}{(L/L_*)^{\alpha} + (L/L_*)^{\beta}} \ . \tag{2.29}$$

Here α is the power-law slope in the limit $L \ll L_*$ and β is the slope for $L \gg L_*$. Both C and α are well constrained by our data. However, radio-luminous AGNs are so rare in the local universe that we can only weakly constrain the local turnover luminosity L_* and high-luminosity slope β. The deeper ($k_{\mathrm{s}} < 12.75$) Mauch & Sadler (2007) AGN luminosity function gives a slightly better constraint on β.

The dotted curves matching the filled and unfilled points in Figure 2.14 indicate the best-fitting Saunders et al. (1990) parametric luminosity functions for the 2MASX/NVSS star-forming galaxies and AGNs, respectively.

2.9 Local 1.4 GHz Spectral Power Density Functions

The spectral power density function $u(L)$ is defined as the spectral power density generated by sources with 1.4 GHz spectral luminosities in the range L and $L + dL$:

$$u(L) \equiv L\rho(L). \tag{2.30}$$

The symbol u is a reminder that the dimensions of spectral power density (W Hz^{-1} Mpc^{-3}) are the same as those of energy density (J Mpc^{-3}). The range of spectral luminosities spanned by galaxies is so large that it is convenient to define a logarithmic spectral power density function

$$u_{\rm dex}(L) \equiv \ln(10) L u(L) = L\rho_{\rm dex}(L) \tag{2.31}$$

equal to the spectral power density (or energy density) per decade of spectral luminosity.

To calculate $u_{\rm dex}(L)$ we separated our galaxies into bins of logarithmic width $\Delta \log(L) = 0.2$ centered on $\log[L(\mathrm{W\ Hz^{-1}})] = 19.4, 19.6, \ldots, 27.6$ and counted the number N of galaxies in each bin. There are 5 bins per decade of luminosity, so each bin centered on luminosity L yields the estimate

$$u_{\rm dex}(L) = 5 \sum_{i=1}^{N} \left(\frac{L}{V_{\rm max}} \right)_i , \tag{2.32}$$

with rms counting uncertainty

$$\sigma = 5 \left[\sum_{i=1}^{N} \left(\frac{L}{V_{\rm max}} \right)_i^2 \right]^{1/2} . \tag{2.33}$$

Our 1.4 GHz local power density functions for star-forming galaxies and AGNs are listed in Table 2.5 with rms errors equal to the quadratic sum of the rms counting uncertainty and 3%.

Table 2.5: 1.4 GHz Spectral Power Density Functions ($h = 0.70$)

	Star-forming Galaxies		AGNs	
$\log L$ ($\mathrm{W\,Hz^{-1}}$)	N	$\log u_{\rm dex}$ ($\mathrm{W\,Hz^{-1}\,dex^{-1}\,Mpc^{-3}}$)	N	$\log u_{\rm dex}$ ($\mathrm{W\,Hz^{-1}\,dex^{-1}\,Mpc^{-3}}$)
19.4	6	$17.56^{+0.16}_{-0.25}$	1	$16.76^{+0.52}_{-0.76}$
19.6	3	$17.18^{+0.30}_{-0.34}$	0	...
19.8	10	$17.53^{+0.12}_{-0.17}$	0	...
20.0	11	$17.66^{+0.14}_{-0.22}$	1	$16.45^{+0.52}_{-0.76}$
20.2	21	$17.72^{+0.09}_{-0.11}$	3	$16.85^{+0.30}_{-0.34}$
20.4	59	$18.22^{+0.07}_{-0.08}$	5	$17.21^{+0.19}_{-0.34}$
20.6	103	$18.32^{+0.04}_{-0.05}$	4	$16.83^{+0.25}_{-0.28}$
20.8	147	$18.45^{+0.04}_{-0.04}$	9	$17.12^{+0.13}_{-0.18}$
21.0	244	$18.60^{+0.04}_{-0.04}$	22	$17.47^{+0.09}_{-0.12}$
21.2	411	$18.74^{+0.03}_{-0.03}$	22	$17.33^{+0.09}_{-0.11}$
21.4	584	$18.81^{+0.02}_{-0.02}$	65	$17.74^{+0.06}_{-0.07}$
21.6	823	$18.92^{+0.02}_{-0.02}$	85	$17.88^{+0.10}_{-0.13}$
21.8	975	$18.91^{+0.02}_{-0.02}$	171	$18.00^{+0.04}_{-0.04}$
22.0	1124	$19.00^{+0.02}_{-0.02}$	216	$18.06^{+0.04}_{-0.04}$
22.2	893	$18.94^{+0.02}_{-0.02}$	281	$18.19^{+0.04}_{-0.04}$
22.4	624	$18.82^{+0.02}_{-0.02}$	280	$18.29^{+0.05}_{-0.06}$
22.6	368	$18.68^{+0.03}_{-0.03}$	286	$18.33^{+0.03}_{-0.04}$
22.8	168	$18.45^{+0.04}_{-0.05}$	239	$18.43^{+0.04}_{-0.05}$

Continued on Next Page. . .

Table 2.5 – Continued

	Star-forming Galaxies		AGNs	
$\log L$ ($\mathrm{W\,Hz^{-1}}$)	N	$\log u_{\mathrm{dex}}$ ($\mathrm{W\,Hz^{-1}\,dex^{-1}\,Mpc^{-3}}$)	N	$\log u_{\mathrm{dex}}$ ($\mathrm{W\,Hz^{-1}\,dex^{-1}\,Mpc^{-3}}$)
23.0	87	$18.24^{+0.05}_{-0.06}$	209	$18.54^{+0.04}_{-0.05}$
23.2	30	$17.86^{+0.09}_{-0.12}$	184	$18.69^{+0.05}_{-0.06}$
23.4	13	$17.74^{+0.12}_{-0.17}$	133	$18.65^{+0.05}_{-0.06}$
23.6	1	$16.28^{+0.52}_{-0.76}$	97	$18.80^{+0.09}_{-0.11}$
23.8	1	$16.85^{+0.52}_{-0.76}$	103	$18.92^{+0.05}_{-0.06}$
24.0	0	$\cdots$	69	$18.97^{+0.07}_{-0.08}$
24.2	0	$\cdots$	70	$19.03^{+0.06}_{-0.07}$
24.4	0	$\cdots$	59	$19.17^{+0.06}_{-0.08}$
24.6	0	$\cdots$	41	$19.15^{+0.07}_{-0.09}$
24.8	0	$\cdots$	41	$19.31^{+0.08}_{-0.09}$
25.0	0	$\cdots$	30	$19.25^{+0.10}_{-0.12}$
25.2	0	$\cdots$	24	$19.30^{+0.10}_{-0.12}$
25.4	0	$\cdots$	8	$19.36^{+0.18}_{-0.33}$
25.6	0	$\cdots$	2	$18.66^{+0.37}_{-0.45}$
25.8	0	$\cdots$	0	$\lesssim 18.16$
26.0	0	$\cdots$	1	$19.27^{+0.52}_{-0.76}$
26.2	0	$\cdots$	0	$\lesssim 18.56$
26.4	0	$\cdots$	1	$19.27^{+0.52}_{-0.76}$
26.6	0	$\cdots$	0	$\cdots$
26.8	0	$\cdots$	0	$\cdots$
27.0	0	$\cdots$	0	$\cdots$

Continued on Next Page...

Table 2.5 – Continued

	Star-forming Galaxies		AGNs	
$\log L$ ($\mathrm{W\,Hz^{-1}}$)	N	$\log u_{\rm dex}$ ($\mathrm{W\,Hz^{-1}\,dex^{-1}\,Mpc^{-3}}$)	N	$\log u_{\rm dex}$ ($\mathrm{W\,Hz^{-1}\,dex^{-1}\,Mpc^{-3}}$)
27.2	0	$\cdots$	0	$\cdots$
27.4	0	$\cdots$	0	$\cdots$
27.6	0	$\cdots$	1	$18.88^{+0.52}_{-0.76}$

2.9.1 Star-Forming Galaxies

As expected, the local 1.4 GHz spectral power density function of star-forming galaxies is well fit by

$$u_{\rm dex}(L) = C\left(\frac{L}{L_*}\right)^{2-\alpha}\exp\left[-\frac{1}{2\sigma^2}\log^2\left(1+\frac{L}{L_*}\right)\right] \tag{2.34}$$

with the same parameters $C = 3.50\times10^{-3}\ \mathrm{dex^{-1}\,Mpc^{-3}}$, $L_* = 1.9\times10^{21}\,\mathrm{W\,Hz^{-1}}$, $\alpha = 1.162$, and $\sigma = 0.558$ that fit the local logarithmic luminosity function. This fit is indicated by the dotted curve matching the filled circles in Figure 2.15.

The total 1.4 GHz spectral power produced per unit volume by star-forming galaxies $U_{\rm SF}$ is the integral the local power density function of star-forming galaxies over spectral luminosity:

$$U_{\rm SF} = \int_0^\infty u_{\rm SF}(L)\,dL\ . \tag{2.35}$$

$U_{\rm SF}$ is an extinction-free measurement proportional to the SFRD $\psi_{\rm SF}$ ($\mathrm{M_\odot\ yr^{-1}\ Mpc^{-3}}$). We calculated $U_{\rm SF}$ directly by summing $L/V_{\rm max}$ over the unbinned sample of all star-

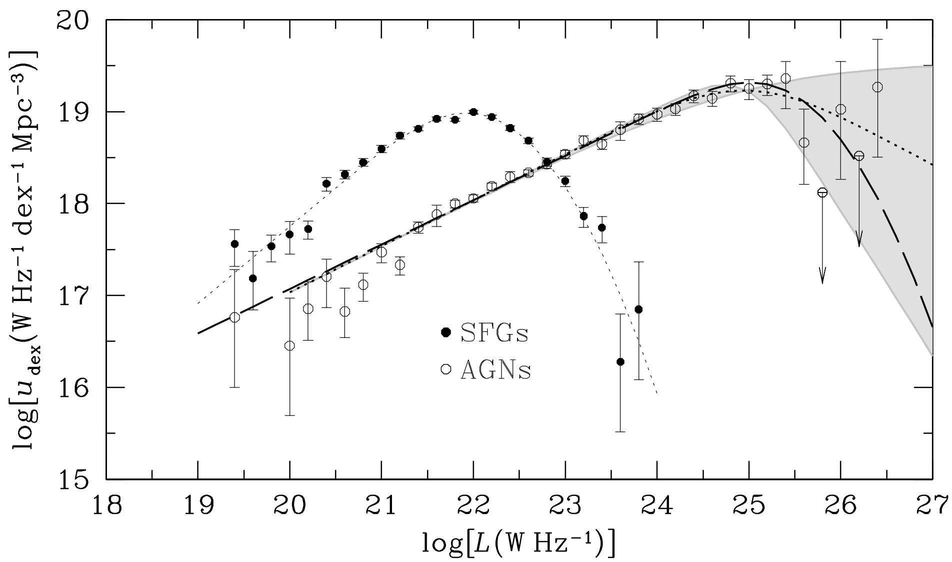

Figure 2.15. Local spectral power density functions for radio sources powered primarily by star formation (filled circles) and AGNs (open circles) derived from the 2MASX/NVSS spectroscopic sample shown as functions of radio luminosity $L_{1.4\,\rm GHz}$. The SFGs were fitted by the Saunders et al. (1990) parametric form (Equation 2.28) multiplied by $L_{1.4\,\rm GHz}$. The AGNs were fitted by both the Saunders et al. (1990) form (dashed curve) and by the Equation 2.29 double power law (dotted curve). The shaded region shows the wide range of possible slopes β in Equation 2.29 such that $\chi^2 < 2$.

forming galaxies in the 1.4 GHz 2MASX/NVSS spectroscopic subsample; it is

$$U_{\rm SF} = (1.54 \pm 0.05) \times 10^{19}\ \rm W\ Hz^{-1}\ Mpc^{-3} \tag{2.36}$$

for $H_0 = 70$ km s^{-1} Mpc^{-1}. The rms error in $U_{\rm SF}$ includes a 3% flux-density calibration uncertainty.

Let $U_{\rm SF}(> L)$ be the cumulative spectral power density produced by star-forming galaxies with 1.4 GHz spectral luminosities $> L$, so the ratio $U_{\rm SF}(> L)\,/\,U_{\rm SF}$ is the fraction of $U_{\rm SF}$ produced by galaxies more luminous than L. The curve in Figure 2.16 shows that ratio calculated from our fit to Equation 2.34. It is 0.99 for $\log[L(\rm W\ Hz^{-1})] = 19.3$, the lowest luminosity in the 2MASX/NVSS spectroscopic subsample, suggesting that sources fainter than our sample limit account for $< 1\%$ of all nearby star formation.

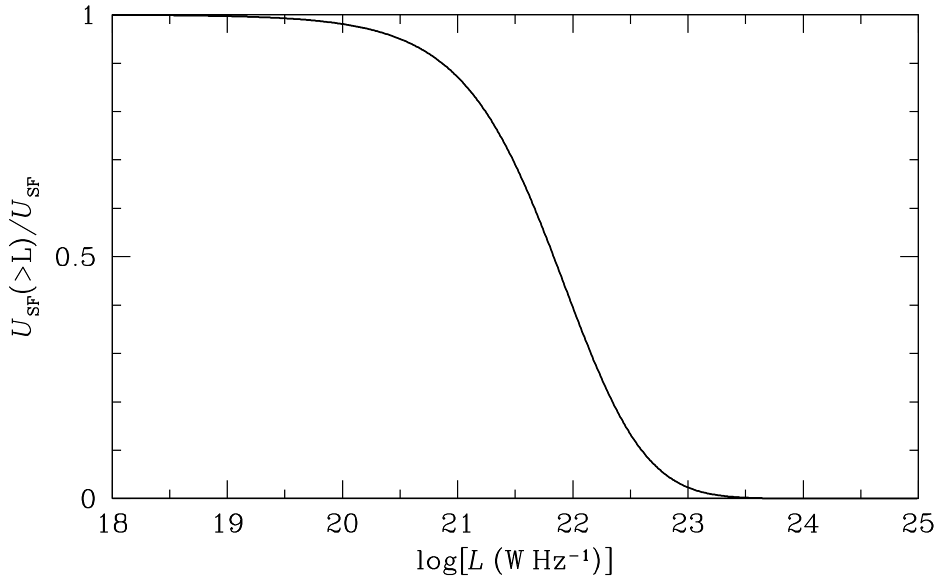

Figure 2.16. This curve shows the fraction $U_{\rm SF}(> L)/U_{\rm SF}$ of the 1.4 GHz spectral power density generated by star-forming galaxies with luminosities $> L$ predicted by extrapolating the fitting function in Equation 2.34.

2.9.2 AGNs

Excluding the anomalous quasar 3C 273 at $\log[L(\rm W\ Hz^{-1})] \sim 27.4$, the parameters of the double power-law fit were determined by minimizing the reduced χ^2 statistic of the fit to the measurements weighted by their uncertainties. The dashed line in Figure 2.15 represents this best fit to Equation 2.29 with parameters $C = 3.58 \times 10^{-6}$, $L_* = 9.55 \times 10^{24}\,\rm W\,Hz^{-1}$, $\alpha = 0.498$, and $\beta = 1.55$. Because luminous AGNs are so rare, the value for β can range from 1 to 2.58 for $\chi^2 < 2$ (shaded region in Figure 2.15).

Lacking the data needed to constrain the high-luminosity power-law slope β for the AGN luminosity function, we considered an alternative approach. There is strong evidence supporting the notion of co-evolution of star-forming host galaxies and AGNs (e.g. Gebhardt et al. 2000). This co-evolution indicates that the luminosity functions of these populations might be represented by the same functional form, so we applied the Saunders et al. (1990) form (Equation 2.28) used for the SFGs to the AGNs. There remains the issue of the poorly sampled high-L end of the AGN luminosity function, so we held our SFG value $\sigma = 0.558$ fixed while fitting the AGN luminosity function. The dotted curve following the unfilled points in Figure 2.14 represents the best-fitting Equation 2.28 parameters for the 2MASX/NVSS AGNs: $C = 4.59 \times 10^{-6}\,\mathrm{dex}^{-1}\,\mathrm{Mpc}^{-3}$, $L_* = 4.65 \times 10^{24}\,\mathrm{W\,Hz}^{-1}$, $\alpha = 1.516$, and $\sigma = 0.558$.

We calculated the total 1.4 GHz spectral power density produced by AGNs U_{AGN} directly by summing $L/V_{\max}$ over the unbinned sample of all AGNs in 1.4 GHz 2MASX/NVSS spectroscopic subsample; it is

$$U_{\mathrm{AGN}} = (4.23 \pm 0.55)\ \mathrm{W\ Hz^{-1}\ Mpc^{-3}} \tag{2.37}$$

for $H_0 = 70$ km s^{-1} Mpc^{-1}. The rms error in U_{AGN} includes a 3% flux-density calibration uncertainty.

2.10 Cosmic Variance

The small statistical errors quoted in Tables 2.4 and 2.5 and in Equations 2.36 and 2.37 inlcude only the Poisson counting errors for unclustered galaxies added in quadrature with the 3% absolute flux-density calibration uncertainty of the NVSS (Condon et al. 1998). The mean accessible redshifts of galaxies used to estimate the local spectral luminosity and power density functions, weighted by each source's contribution to the total star formation density, are $\langle z \rangle = 0.026$ and $\langle z \rangle = 0.070$ for the 2MASX/NVSS star-forming galaxies and AGNs, respectively. The corresponding distances $D \sim 100 - 300$ Mpc are comparable with the size $D \sim 150$ Mpc of baryon acoustic oscillations, so significant cosmic variance from large-scale clustering is expected. To extend our local results (e.g., the local U_{SF}) derived from observations made from only one point in the universe to the whole universe (e.g, the recent U_{SF} averaged over all space), it is necessary to add this cosmic variance to the Poisson and calibration variances.

To estimate the amplitude of the cosmic variance, we divided our sample covering 7.016 sr of the sky into two equal-area hemispheres split by the vertical plane passing through J2000 $\alpha = 12^{\mathrm{h}}51^{\mathrm{m}}26^{\mathrm{s}}$, the right ascension of the north galactic pole (Figure 2.17). We call the hemisphere covering J2000 $\alpha = 00^{\mathrm{h}}51^{\mathrm{m}}26^{\mathrm{s}}$ through $\alpha = 12^{\mathrm{h}}51^{\mathrm{m}}26^{\mathrm{s}}$ "RA1" and the other hemisphere "RA2."

The 3603 star-forming galaxies in RA1 produce $U_{\mathrm{SF},1} = (1.75 \pm 0.06) \times 10^{19}$ W Hz^{-1} Mpc^{-3} and the 3103 star-forming sources in RA2 produce $U_{\mathrm{SF},2} = (1.35 \pm 0.04) \times 10^{19}$ W Hz^{-1} Mpc^{-3}, where these errors do not include cosmic variance. The fractional difference in U_{SF} between the two hemispheres is actually ~ 0.26, so if the two halves of the sky are nearly independent, the rms fractional uncertainty in their mean is ~ 0.13. Thus our spectroscopic subsample is large enough that cosmic variance exceeds its Poisson and calibration variances. Our estimate of the recent "universal" U_{SF} based on local measurements must include the cosmic variance; it is

$$U_{\mathrm{SF}} = (1.54 \pm 0.20) \times 10^{19} \text{ W Hz}^{-1} \text{ Mpc}^{-3} \ . \tag{2.38}$$

The corresponding numbers for radio sources primarily powered by AGNs are $U_{\mathrm{AGN},1} = (4.72 \pm 0.55) \times 10^{19}$ W Hz^{-1} Mpc^{-3} and $U_{\mathrm{AGN},2} = (3.74 \pm 0.53) \times 10^{19}$ W Hz^{-1} Mpc^{-3}, so adding the cosmic variance implies the recent universal AGN spectral energy density is

$$U_{\mathrm{AGN}} = (4.23 \pm 0.78) \times 10^{19} \text{ W Hz}^{-1} \text{ Mpc}^{-3} \ . \tag{2.39}$$

Figure 2.17 suggests that bisecting the sky at the chosen meridian gives a larger difference than most other choices would have, so we believe the overall error estimates in Equations 2.38 and 2.39 are conservative.

Figures 2.14 and 2.15 show our luminosity and power-density function data points with error bars that do not include cosmic variance. We note that the data still match, within those small error bars, the smooth parametric fits shown as dotted curves. We

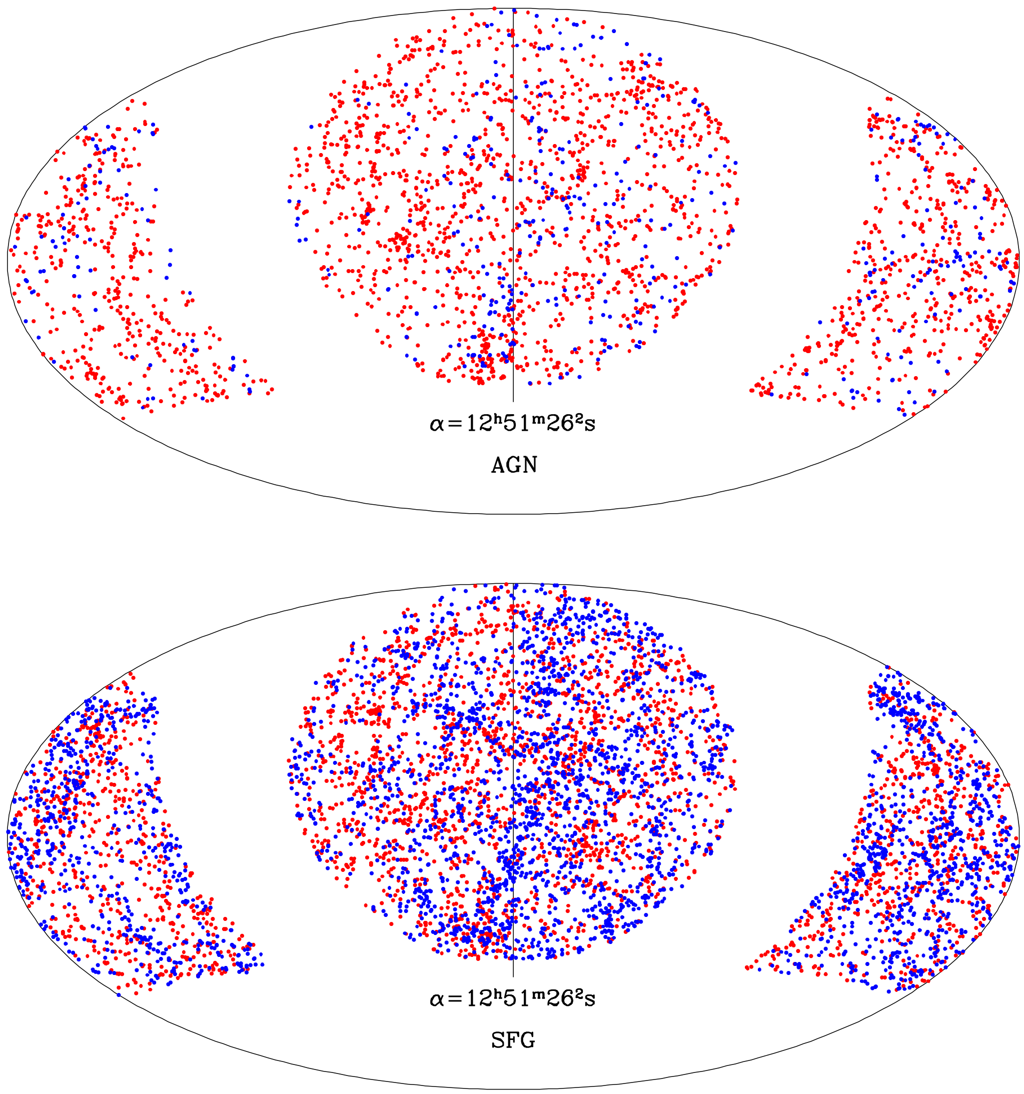

Figure 2.17. AGNs (upper panel) and SFGs (lower panel) in our sample are shown on Hammer equal-area projections of the sky centered on J2000 $\alpha = 12^{\mathrm{h}}51^{\mathrm{m}}26^{\mathrm{s}}$ and $\delta = 0$. Right ascension increases to the left, so the RA1 hemisphere is to the right of the vertical dividing line and the RA2 hemisphere is to the left. Blue indicates galaxies with $cz < 7000\,\mathrm{km\,s^{-1}}$, and $cz > 7000\,\mathrm{km\,s^{-1}}$ galaxies are red. The color boundary at $cz = 7000\,\mathrm{km\,s^{-1}}$ corresponds to a distance $D \sim 100$ Mpc.

conclude that cosmic variance affects the overall space density of galaxies but not their detailed luminosity distributions.

We can also use our local sample to estimate how the expansion dynamics of a ΛCDM universe might be affected by density fluctuations on small scales. The $\lambda = 2.16\ \mu$m spectral luminosity densities of our sample galaxies in RA1 and RA2 are $1.734 \times 10^{20}\,\mathrm{W\,Hz^{-1}\,Mpc^{-3}}$ and $1.065 \times 10^{20}\,\mathrm{W\,Hz^{-1}\,Mpc^{-3}}$, respectively. Using the $\lambda = 2.16\ \mu$m luminosity as a proxy for baryonic mass and assuming dark matter has a similar large-scale distribution, relative to the mean matter density, RA1 and RA2 have densities 1.239 and 0.761. For the global cosmological parameters $\Omega_m = 0.3$, $\Omega_\Lambda = 0.7$, and $\Omega_r = 8.5 \times 10^{-5}$,

$$\Omega_{\mathrm{RA1}} = (0.3 \times 1.239 + 0.7 + 8.6 \times 10^{-5}) = 1.0718$$
$$\Omega_{\mathrm{RA2}} = (0.3 \times 0.761 + 0.7 + 8.6 \times 10^{-5}) = 0.9284.$$

The "local" Hubble constant is proportional to $\Omega^{1/2}$, so in regions RA1 and RA2 the local Hubble constant could be $H_{0,1} \approx 72.5$ km s^{-1} Mpc^{-1} and $H_{0,2} = 67.5\,\mathrm{km\,s^{-1}\,Mpc^{-1}}$. This scatter is comparable to that of published values of H_0, with the difference being that the lower published value is a global measurement rather than a small-scale measurement such as this. Regardless, differing densities on ~ 100 Mpc scales may prevent local measurements of the global H_0 to better than $\sim \pm 2.5\,\mathrm{km\,s^{-1}}$.

2.11 Recent Star Formation Rate Density

Radio continuum emission is a tight, nearly linear, and dust-unbiased independent tracer of the SFRD ψ. Steep-spectrum ($\langle\alpha\rangle \approx -0.8$) synchrotron radiation from relativistic electrons accelerated in the core-collapse SNRs of short-lived massive ($M > 8\ M_\odot$) stars dominates the radio emission of SFGs at all frequencies below $\nu \sim 30$ GHz, and flat-spectrum ($\alpha \approx -0.1$) free-free radiation from thermal electrons in H II regions ionized by by even more massive short-lived stars emerges above 30 GHz (Condon 1992). At $\nu \sim 1$ GHz, $\sim 90\%$ of the radio emission from SFGs can be attributed to synchrotron radiation and the remaining $\sim 10\%$ to free-free emission. The FIR/radio correlation shows that SFR is proportional to radio luminosity in all but the least-luminous SFGs (Condon et al. 1991), indicating that the constant of proportionality between radio luminosity and SFR is remarkably insensitive to potentially confounding variables such as interstellar magnetic field strength.

Thus SFR can be related to 1.4 GHz luminosity by an equation of the form

$$\frac{\mathrm{SFR}(M > 5\,M_\odot)}{M_\odot\,\mathrm{yr}^{-1}} = \frac{1}{x}\left(\frac{L_{1.4\,\mathrm{GHz}}}{\mathrm{W\ Hz}^{-1}}\right) , \tag{2.40}$$

where x is a dimensionless constant whose value has been found to range from $\sim 1.8 \times 10^{21}$ to $\sim 8.9 \times 10^{21}$. For example, (Condon et al. 2002) reported

$$\frac{\mathrm{SFR}(M > 5\,M_\odot)}{M_\odot\,\mathrm{yr}^{-1}} = \frac{1}{4.6 \times 10^{21}}\left(\frac{L_{1.4\,\mathrm{GHz}}}{\mathrm{W\,Hz}^{-1}}\right) . \tag{2.41}$$

Radio emission is insensitive to lower-mass stars. To account for their contribution to the total star-formation rate, we followed Madau & Dickinson (2014) and assumed a Salpeter initial mass function $\Psi(M) \propto M^{-2.35}$ over the mass range $0.1\,M_\odot < M < 100\,M_\odot$. Then the total star-formation rate is

$$\mathrm{SFR}(M > 0.1\,M_\odot) \approx 5.5\,\mathrm{SFR}(M > 5\,M_\odot) . \tag{2.42}$$

Because the conversion factor between 1.4 GHz luminosity and total SFR is still uncertain, with values ranging from $5.5x \sim 0.8 \times 10^{21}$ to 1.7×10^{21}, we adopted the easily rescalable midrange number 1.0×10^{-21}. Dividing SFR and 1.4 GHz luminosity by volume gives the SFRD ψ in terms of U_{SF}:

$$\frac{\psi(M > 0.1\ M_\odot)}{M_\odot\,\mathrm{yr}^{-1}\,\mathrm{Mpc}^{-3}} \approx 1.0 \times 10^{-21}\left(\frac{U_{\mathrm{SF}}}{\mathrm{W\,Hz}^{-1}\,\mathrm{Mpc}^{-3}}\right) . \tag{2.43}$$

Then our measured $U_{\mathrm{SF}} = (1.54 \pm 0.20) \times 10^{19}\,\mathrm{W\,Hz}^{-1}$ with the quoted error including cosmic variance implies that the "universal" recent SFRD is

$$\psi = (0.0154 \pm 0.0020)\,M_\odot\ \mathrm{yr}^{-1}\ \mathrm{Mpc}^{-3} . \tag{2.44}$$

This value of ψ is lower than the $\psi = (0.022 \pm 0.001)\ M_\odot\ \mathrm{yr}^{-1}\ \mathrm{Mpc}^{-3}$ (Poisson errors only) Mauch & Sadler (2007) calculated using the higher conversion factor $\psi = 1.13\times 10^{-21}U_{\rm SF}$. However, rescaling their conversion factor to $\psi = 1.0\times10^{-21}U_{\rm SF}$ and adding cosmic variance to their rms uncertainty yields $\psi = 0.0195\pm0.0036\ M_\odot\ {\rm yr}^{-1}\ {\rm Mpc}^{-3}$. Thus these two measurements of ψ agree within their uncertainties.

Multiwavelength compilations of SFRD estimates can be found in Hopkins & Beacom (2006) and Madau & Dickinson (2014). After scaling to the Salpeter IMF, Hopkins & Beacom (2006) adopted the Cole et al. (2001) parametric fit to describe the evolution of the SFRD over the redshift range $0 < z < 7$:

$$\psi(z) = \frac{(a + b\,z)\,h}{1+(z/c)^d}\ {\rm M}_\odot\,{\rm yr}^{-1}\,{\rm Mpc}^{-3}\ . \tag{2.45}$$

For $h = 0.7$ they found $a = 0.0170$, $b = 0.13$, $c = 3.3$, and $d = 5.3$. At the weighted average redshift $\langle z\rangle \sim 0.026$ of our SFG sample, Equation 2.45 yields $\psi = 0.015\ M_\odot\ {\rm yr}^{-1}\ {\rm Mpc}^{-3}$. From a compilation of FUV and IR rest-frame measurements of ψ spanning $0 < z < 8$, Madau & Dickinson (2014) found the best-fit function

$$\psi(z) = 0.015\frac{(1+z)^{2.7}}{1+[(1+z)/2.9]^{5.6}}\ M_\odot\ {\rm yr}^{-1}\ {\rm Mpc}^{-3}\ . \tag{2.46}$$

Equation 4.37 gives $\psi(0.026) = 0.016\ M_\odot\ {\rm yr}^{-1}\ {\rm Mpc}^{-3}$. Our $\psi = 0.0154 \pm 0.020$ $M_\odot\,{\rm yr}^{-1}\,{\rm Mpc}^{-3}$ centered on $\langle z\rangle \approx 0.026$ agrees with both of these independent SFRD evolutionary models. The blue point in Figure 2.18 compares our measurement with the FIR and UV data points and the dashed curve showing the Madau & Dickinson (2014) model.

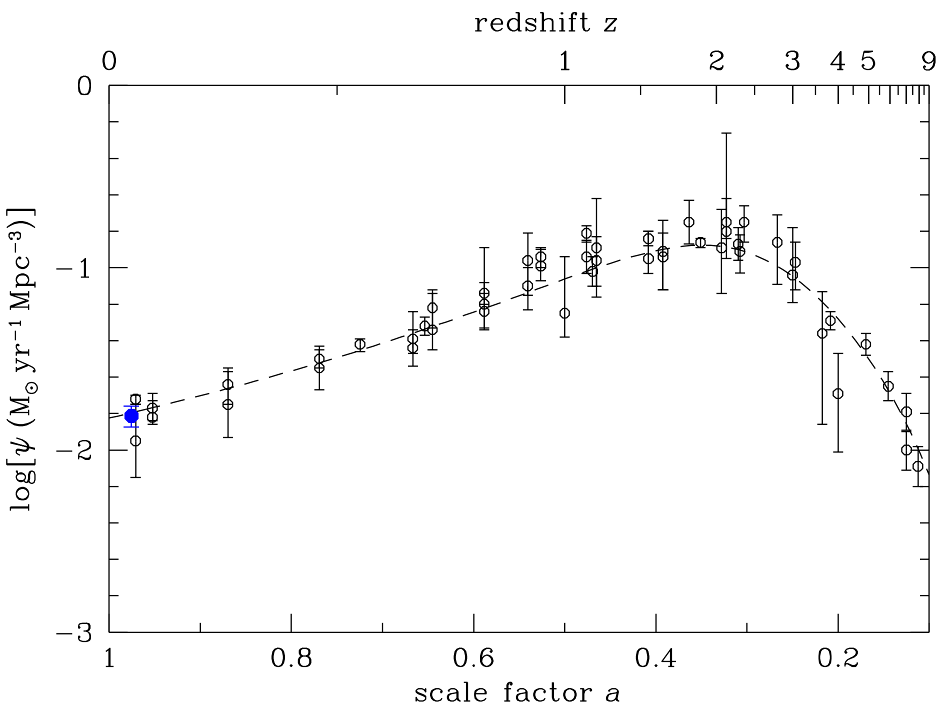

Figure 2.18. The Madau & Dickinson (2014) SFRD model (Equation 4.37) is indicated by the dashed curve fitted to their black FIR and UV data points. The blue data point at expansion scale factor $a = (1+z)^{-1} \sim 0.98$ ($z = 0.026$) represents our estimate of the recent SFRD from based on $U_{\rm SF}$ measured at 1.4 GHz. Lower abscissa: expansion scale factor $a = (1+z)^{-1}$. Upper abscissa: redshift z. Ordinate: star formation rate density ($M_\odot$ yr^{-1} Mpc^{-3}).

Chapter 3

Radio Source Counts

3.1 Preface

The total brightness-weighted source count can be calculated by integrating the energy density function (along with other factors) over all redshifts. A comparison between counts predicted for various prescriptions of the evolution of the energy density function and observed brightness-weighted source counts constrain the evolution of the SFRD $\psi(z)$. The total count has two peaks, one at $\log[S\,(\mathrm{Jy})] \sim -1$ produced by AGNs and one at $\log[S\,(\mathrm{Jy})] \sim -4.5$ attributed to SFGs. Normal galaxies (e.g. our own Milky Way) are responsible for forming the bulk of the current stellar mass in the universe, but their flux densities at the peak of star formation ("cosmic noon") can be as faint as $\log[S\,(\mathrm{Jy})] \sim -6.6$. This chapter presents eight decades in flux density of observed 1.4 GHz brightness weighted source counts from the DEEP2 image taken by the MeerKAT telescope and the NVSS. A statistical analysis of the DEEP2 confusion distribution constrains the source counts of normal star-forming galaxies down to $\log[S\,(\mathrm{Jy})] \sim -6.6$. The remainder of this chapter has been published in the *Astrophysical Journal* (Matthews et al. 2021).

3.2 Abstract

Brightness-weighted differential source counts $S^2n(S)$ spanning the eight decades of flux density between $0.25\,\mu$Jy and 25 Jy at 1.4 GHz were measured from (1) from the confusion brightness distribution in the MeerKAT DEEP2 image below $10\,\mu$Jy, (2) the counts of DEEP2 sources between $10\,\mu$Jy and 2.5 mJy, and (3) counts of NVSS sources stronger than 2.5 mJy. We present our DEEP2 catalog of 1.7×10^4 discrete sources complete above $S = 10\,\mu$Jy over $\Omega = 1.04\,\mathrm{deg}^2$. The brightness-weighted counts converge as $S2n(S) \propto S^{1/2}$ below $S = 10\,\mu$Jy, so $> 99\%$ of the $\Delta T_\mathrm{b} \sim 0.06$ K sky brightness produced by active galactic nuclei and $\approx$ 96% of the $\Delta T_\mathrm{b} \sim 0.04$ K added by star-forming galaxies has been resolved into sources with $S \geq 0.25\,\mu$Jy. The $\Delta T_\mathrm{b} \approx 0.4$ K excess brightness measured by ARCADE 2 cannot be produced by faint sources smaller than $\approx$ 50 kpc if they cluster like galaxies.

3.3 Introduction

There have been persistent discrepancies in the faintest direct source counts at $S_{1.4\,\mathrm{GHz}} < 100\,\mu$Jy(see de Zotti et al. 2010, for a review and compilation of previous source counts), far exceeding the errors caused by Poisson fluctuations and clustering uncertainties (Owen & Morrison 2008; Heywood et al. 2013). Direct counts of faint radio sources rely primarily on high angular-resolution images, and must account for possible "missing" resolved sources whose peak flux density falls below the surface brightness sensitivity of the image. Corrections on the source counts due to these missing sources depend on the highly uncertain, intrinsic angular source size distribution of faint radio sources Bondi et al. (2008). The large uncertainty in these resolution corrections propagates into the integrated flux measurements, source counts, and number of missing sources due to limited surface brightness sensitivty. This effect is further magnified by the steep slope of differential source counts $n(S) \propto S^{-5/2}$, which exacerbates flux density overestimates and leads to higher counts at faint flux densities.

Following the pioneering $P(D)$ method of Scheuer (1957), radio astronomers have utilized confusion to measure accurate source counts (see Condon et al. 2012; Vernstrom et al. 2014, for recent examples). A low resolution image ensures that all faint radio galaxies appear as point sources—eliminating the need for uncertain resolution corrections. The term "confusion" means fluctuations in sky brightness caused by multiple faint sources inside the point-source response. Historically, confusion was described by the probability distribution $P(D)$ of pen deflections of magnitude D on a chart-recorder plot of detected power (Scheuer 1957). The analog of the deflection D in a modern image is the sky brightness expressed as a peak flux density $S_{\rm p}$ in units of flux density per beam solid angle, so a $P(D)$ distribution is the same as a $P(S_{\rm p})$ distribution.

Low resolution, confusion-limited images offer an independent way of measuring faint radio source counts and are free from uncertain angular size corrections. While unable to determine properties of individual galaxies, confusion studies are able to constrain source counts of the radio population far below the noise and do not require multi-wavelength cross-identifications as priors (unlike source counts measured from "stacking", e.g. Mitchell-Wynne et al. 2014).

The differential source count $n(S)dS$ at frequency ν is the number of sources per steradian with flux densities between S and $S + dS$. The Rayleigh-Jeans sky brightness temperature $dT_{\rm b}$ per decade of flux density added by these sources is

$$\left[\frac{d\,T_{\rm b}}{d\log(S)}\right] = \left[\frac{\ln(10)\,c^2}{2k_{\rm B}\nu^2}\right] S^2 n(S)\ , \tag{3.1}$$

where $k_{\rm B} \approx 1.38\times10^{-23}\,{\rm J\,K^{-1}}$. Can one or more "new" populations of radio sources fainter than $0.25\,\mu$Jy make comparable contributions to the sky brightness at 1.4 GHz? The ARCADE 2 instrument measured the absolute sky temperature at frequencies from $\nu = 3 - 90$ GHz, and Fixsen et al. (2011) reported finding an excess power-law brightness temperature

$$\left(\frac{T_{\rm b}}{\rm K}\right) = (24.1 \pm 2.1)\left(\frac{\nu}{\nu_0}\right)^{-2.599\pm0.036} \tag{3.2}$$

from 22 MHz to 10 GHz, where $\nu_0 = 310$ MHz. Removing the contribution from known populations of extragalactic sources leaves

$$\left(\frac{\Delta T_{\rm b}}{\rm K}\right) = (18.4 \pm 2.1) \left(\frac{\nu}{\nu_0}\right)^{-2.57 \pm 0.05}, \tag{3.3}$$

(Seiffert et al. 2011). Possible explanations for this large excess fall into three categories: 1) the excess was overestimated owing to the limited sky coverage of ARCADE 2 and the zero-point levels of low frequency radio maps may be inaccurate, 2) the excess is primarily smooth emission from our Galaxy, 3) the excess is primarily extragalactic, making it the only photon background that does not agree with published source counts dominated by radio galaxies and star-forming galaxies. Vernstrom et al. (2011) and Seiffert et al. (2011) explored the possibility of a new source population contributing an extra "bump" to the source counts at flux densities $< 10\,\mu$Jy. In order to match the ARCADE 2 excess background, this hypothetical new population must add $\Delta T_{\rm b} \sim 0.4$ K to the sky brightness at 1.4 GHz. Condon et al. (2012) showed that the brightness-weighted counts $S^2 n(S)$ of this new population must peak at flux densities below $S_{1.4\,\rm GHz} = 0.1\,\mu$Jy to be consistent with their observed $P(D)$ distribution.

This paper presents 1.4 GHz brightness-weighted source counts $S^2 n(S)$ covering the eight decades of flux density between $S = 0.25\,\mu$Jy and $S = 25$ Jy based on the very sensitive $\nu = 1.266$ GHz MeerKAT DEEP2 sky image (Mauch et al. 2020) confusion brightness distribution between $S = 0.25\,\mu$Jy and $S = 10\,\mu$Jy, the DEEP2 discrete-source catalog from $S = 10\,\mu$Jy to $S = 2.5$ mJy, and on the 1.4 GHz NRAO VLA Sky Survey (Condon et al. 1998, NVSS) catalog above $S = 2.5$ mJy. Nearly all of these sources are extragalactic. We present the first complete catalog of disrete sources with $S > 10\,\mu$Jy in the DEEP2 field. While Mauch et al. (2020) derived the best-fitting power-law source counts to describe the DEEP2 $P(D)$ distribution, the actual source counts do not follow a simple power law. To improve upon the Mauch et al. (2020) fit, we allowed the source counts to be any continuous function. We further explore the possibility of "new" populations of faint extragalactic sources contributing to the total radio background, and constrain the lower limit to the number of such sources adding $\Delta T_{\rm b} \sim 0.4\,{\rm K}$ to the sky brightness at 1.4 GHz remaining consistent with the DEEP2 $P(D)$ distribution.

The data used to construct the source counts across eight decades is presented in Section 3.4. The radio sky simulations needed to constrain the source counts from the $P(D)$ distribution and derive confusion corrections to the discrete counts is detailed in Section 3.5. Statistical source counts with $0.25\mu{\rm Jy} < S < 10\,\mu{\rm Jy}$ estimated from the $P(D)$ confusion distribution are reported in Section 3.6. Section 3.7 presents the complete $S > 10\,\mu{\rm Jy}$ discrete source catalog from the DEEP2 field, and Section 3.7.4 presents the source counts derived from this catalog. Differential source counts for the NVSS catalog are calculated in Section 3.8. The contributions of SFGs and AGNs to the 1.4 GHz sky background and constraints on "new" populations of faint sources explaining the ARCADE 2 radio excess are described in Section 3.9. Section 3.10 summarizes this work.

Absolute quantities in this paper were calculated for a ΛCDM universe with $H_0 = 70\,{\rm km\,s^{-1}\,Mpc^{-1}}$ and $\Omega_{\rm m} = 0.3$ using equations in Condon & Matthews (2018). Our spectral-index sign convention is $\alpha \equiv +d\,\ln S/d\,\ln\nu$.

3.4 Data

3.4.1 Selecting the sky position for a deep radio field

The dynamic range of a long-integration radio observation is limited by telescope pointing errors $\Delta\theta$ and fractional gain calibration errors ΔG acting on every source of flux density S offset by angle θ from the pointing center. For a Gaussian primary beam of full width at half maximum (FWHM) $\Theta_{1/2}$ the resulting flux-density errors are

$$\frac{\Delta S_\theta}{S} \approx \left(\frac{8\,\ln\,2}{\Theta_{1/2}}\right)\theta\,G(\theta)\Delta\theta \tag{3.4}$$

due to pointing errors and

$$\frac{\Delta S_G}{S} \approx G(\theta)\Delta G \tag{3.5}$$

due to gain calibration errors. The total flux-density error due to each source from adding these errors quadratically is

$$S^2 = \left[(\Delta S_\theta)^2 + (\Delta S_G)^2\right], \tag{3.6}$$

and the total flux-density error (which we will call the "demerit score" d) summing across all N sources is

$$d = \left[\sum_{i=1}^{N} (\Delta S_i)^2\right]^{1/2}. \tag{3.7}$$

To locate the best single-pointing field in the sky observable by the MeerKAT telescope, we used the Sydney University Molongolo Sky Survey (SUMSS) for $\delta < -35°$ and the NVSS survey from $-35° \geq \delta < 10°$. A map of the demerit scores in the sky area near DEEP2 is shown in Figure 3.1.

We calculated the demerit scores d of potential pointings spaced $\sim 1'$ apart throughout the entire sky observable by MeerKAT and with $|b| > 10°$. Of the five pointings with the smallest demerit scores, we chose the southernmost field with J2000 $\alpha = $ 04:13:26.4 and $\delta = -$80:00:00 to ensure it would be easy to schedule during the commissioning of the MeerKAT telescope. Lying at an ecliptic latitude of $\beta \approx 75°$, DEEP2 is easily observed by orbiting telescopes and is minimally affected by zodaical dust—enhancing the quality of possible infrared and other multi-wavelength follow-up observations.

3.4.2 The MeerKAT DEEP2 Field

The 1.266 GHz DEEP2 image (Mauch et al. 2020) covers the $\Theta_{1/2} = 69\overset{\prime}{.}2$ diameter half-power circle of the MeerKAT primary beam centered on J2000 $\alpha = 04^{\mathrm{h}}\,13^{\mathrm{m}}\,26\overset{\mathrm{s}}{.}4$, $\delta = -80°\,00'\,00''$. Its point-source response is a $\theta_{1/2} = 7\overset{\prime\prime}{.}6$ FWHM Gaussian, and the rms noise is $\sigma_{\mathrm{n}} = 0.56 \pm 0.01\,\mu\mathrm{Jy\,beam}^{-1}$ at the pointing center (Table 3.1). The wideband DEEP2 image is the average of 14 narrow subband images weighted to maximize the signal-to-noise ratio (SNR) of sources with spectral index $\alpha = -0.7$ (Table 3.2). The dirty DEEP2 image was CLEANed down to residual peak flux

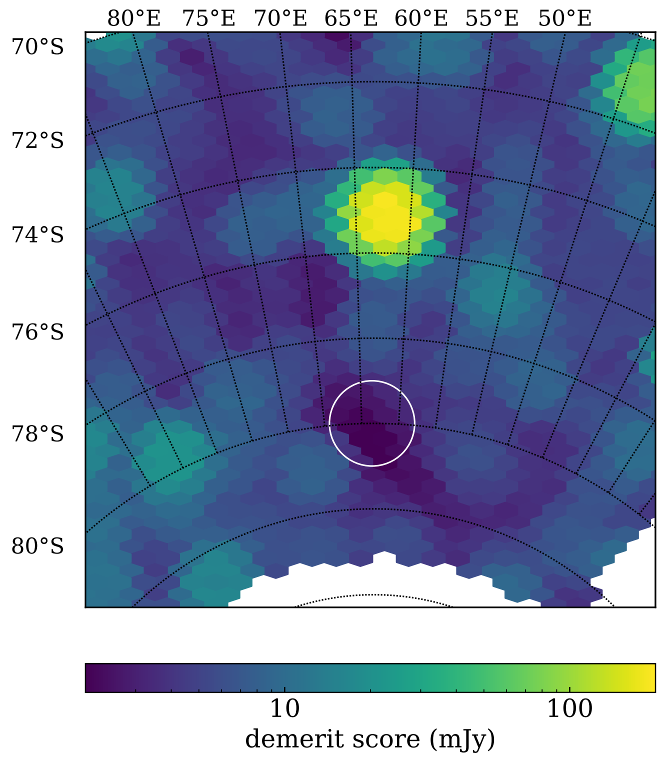

Figure 3.1. The demerit score d of potential MeerKAT pointings near the DEEP2 field is shown from $d = 1$ mJy in deep violet to $d = 200$ mJy in bright yellow. The location of DEEP2 $\alpha = $ 04:13:26.4 $\delta = -$80:00:00 is outlined by the white circle of 2 deg in diameter.

density $S_{\rm p} = 5\,\mu$Jy beam^{-1}.

The DEEP2 image is strongly confusion limited, so we could not treat its position and flux-density error distributions analytically. Therefore we created radio sky simulations (Section 3.5) to model the statistical source counts consistent with the confusion brightness distribution, refine our catalog of discrete DEEP2 sources, and correct our counts of the faintest sources (Section 3.7).

3.4.3 NRAO VLA Sky Survey

The 1.4 GHz NRAO VLA Sky Survey (NVSS) (Condon et al. 1998) imaged the entire sky north of J2000 $\delta = -40°$ with $\theta_{1/2} = 45''$ FWHM resolution and $\sigma_{\rm n} \approx 0.45$ mJy beam^{-1} rms noise. The NVSS catalog lists source components as Gaussian fits to signifi-

Table 3.1. DEEP2 Survey Parameters

Parameter	Value
Right Ascension (J2000)	04:13:26.4
Declination (J2000)	−80:00:00
Primary FWHM $\Theta_{1/2}$	$69\farcm2$
Solid angle $\Omega_{1/2}$	$1.04\,\mathrm{deg}^2$
Synthesized FWHM $\theta_{1/2}$	$7\farcs6$
Central rms noise σ_n	$0.56 \pm 0.01\,\mu\mathrm{Jy\,beam}^{-1}$
$P(D)$ on-sky noise σ_n	$0.57 \pm 0.01\,\mu\mathrm{Jy\,beam}^{-1}$

cant peaks in the NVSS images. From it we selected the 1117067 components with $S \geq 2.5$ mJy in the $\Omega \approx 7.016$ sr solid angle with absolute Galactic latitude $|b| \geq 20°$. In Section 3.8 we detail how we derived the NVSS direct source counts above 2.5 mJy.

3.5 The Radio Sky Simulations

We produced computer simulations of the 1.266 GHz DEEP2 image (along with mock catalogs) to calculate source counts below 10 μJy, assess the quality of the algorithms (e.g. our source finding algorithm) used on the real data, and to derive corrections and uncertainties for the discrete source catalog between $10\,\mu\mathrm{Jy} < S < 2.5\,\mathrm{mJy}$.

The confusion brightness distribution can be calculated analytically only for scale free power-law differential source counts of the form $n(S) \propto S^{-\gamma}$ (Condon 1974). Likewise, population-law biases in counts of faint discrete sources can easily be estimated only in the power-law count approximation (Murdoch et al. 1973). The actual source counts are not well approximated by a single power law near $S \sim 10\,\mu$Jy because that flux density corresponds to the bend in the SFG luminosity function of sources at $z \sim 1$ (Condon et al. 2012, fig. 11), so we used computer simulations of the 1.266 GHz DEEP2 image to estimate statistical source counts below 10 μJy from the DEEP2 image brightness distribution and to correct for biases in the DEEP2 discrete-source counts above $10\,\mu$Jy. We simulated only point sources because the measured median angular diameter $\langle\phi\rangle \approx 0\farcs3$ of real μJy sources (Cotton et al. 2018) is much smaller than the DEEP2 restoring beam FWHM and only $\sim 0.2\%$ of the DEEP2 sources stronger than $S = 10\,\mu$Jy are clearly resolved (Section 3.7.3). The simulated sources all have spectral index $\alpha = -0.7$, the median spectral index of extragalactic sources (Condon 1984). Varying α by ± 0.14, the rms width of the observed spectral-index distribution of faint sources, changes the 1.266 GHz flux densities of the simulated sources by only $\mp 1\%$.

The input for each simulation is an arbitrary user-specified 1.266 GHz source count $n(S)$. In every flux-density bin of width $\Delta\log(S) = 0.001$ the actual number of simulated sources is chosen by a random-number generator sampling the Poisson distribution whose mean matches the input $n(S)$. The sources are scattered randomly throughout the DEEP2 half-power circle. The real μJy sources in DEEP2 are nearly all extragalactic and very distant (median redshift $\langle z\rangle \sim 1$), so they are spread out over a radial distance range $\Delta z \sim 1$ much larger than the galaxy correlation length and their sky distribution is quite random and isotropic (Benn & Wall 1995; Condon & Matthews 2018), unlike the visibly clustered sky distribution of nearby optically selected galaxies. In addition, clustering appears to have little effect on FIR, millimeter, and radio confusion brightness distributions observed with resolutions close to the DEEP2 restoring beam diameter (Béthermin et al. 2017).

The simulations also reproduce the DEEP2 observational effects and imaging processes described by Mauch et al. (2020). The simulated image replicates CLEANing by representing each source as the sum of two components: (1) a component whose brightness distribution is the DEEP2 dirty beam and whose peak flux density is the lesser of the input source flux density or subband CLEAN threshold plus (2) a CLEAN component whose brightness distribution matches the circular Gaussian restoring beam and whose amplitude is the difference between the input source flux density and the subband CLEAN threshold. The subband CLEAN threshold was determined from the wideband value of $5\,\mu$Jy and scaled to the subband central frequency assuming a spectral index of $\alpha = -0.7$. The dirty beam used for each subband

Table 3.2. DEEP2 imaging subband frequencies and weights

Subband number	ν_i (MHz)	σ_i (μJy beam^{-1})	w_i for max SNR
$i = 1$	908.040	4.224	0.0378
2	952.340	5.044	0.0248
3	996.650	3.196	0.0580
4	1043.460	2.882	0.0669
5	1092.780	2.761	0.0683
6	1144.610	2.580	0.0733
7	1198.940	4.203	0.0259
8	1255.790	3.981	0.0271
9	1317.230	1.851	0.1170
10	1381.180	1.643	0.1389
11	1448.050	1.549	0.1463
12	1519.940	1.871	0.0938
13	1593.920	2.888	0.0368
14	1656.200	1.850	0.0850

Note—Column 1 is the subband number i, column 2 the subband central frequency ν_i, column 3 the rms noise σ_i in the subband image, and column 4 is the subband image weight w_i used to produce the wideband DEEP2 image with the highest signal-to-noise ratio (SNR) for sources with spectral index $\alpha = -0.7$.

of the simulation is the actual DEEP2 subband dirty beam, which is nearly circular and does not have strong diffraction spikes since the MeerKAT antennae are not distributed along straight arms. The first negative sidelobe of the weighted dirty beam is at the ∼5% level (Figure 3.2). A 5 μJy residual leaves a $\sim 0.25\,\mu$Jy negative ring in the image, which is less than half the rms sky noise in the $P(D)$ region. The first positive sidelobe of the dirty beam is at the ∼1% level.

The simulation generates sources with spectral index $\alpha = -0.7$ and combines the subband images with the weights listed in column 4 of Table 3.2. To incorporate the

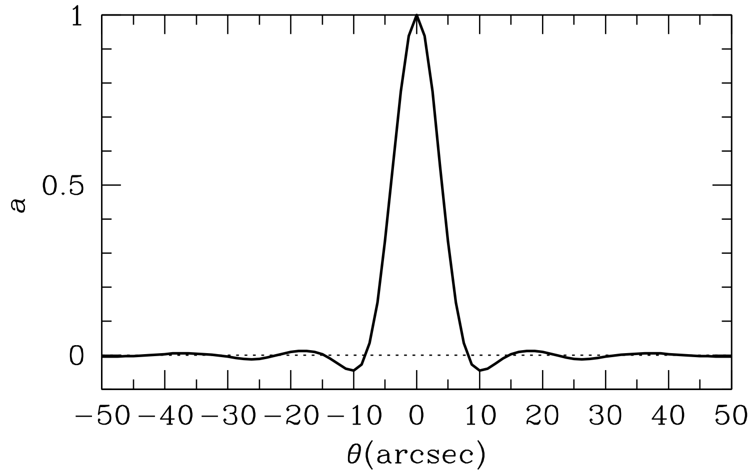

Figure 3.2. The SNR-weighted DEEP2 dirty beam, cut along the maximum sidelobes direction, has a 5% negative sidelobe and a 1% positive sidelobe. Abscissa: Offset from the beam center (arcsec) Ordinate: Dirty beam power profile a.

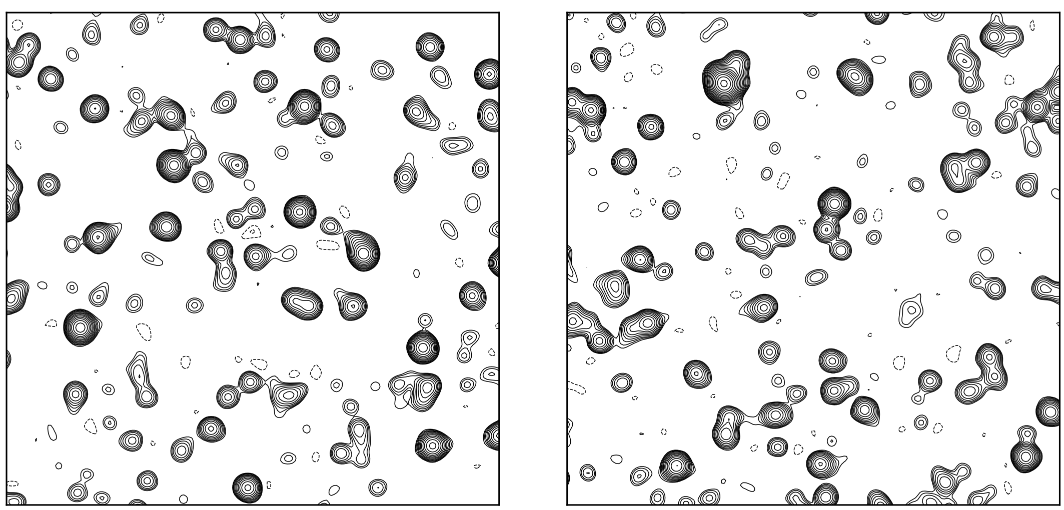

Figure 3.3. These contour plots compare $4.2' \times 4.2'$ regions of one DEEP2 simulation (left panel) and the actual DEEP2 image (right panel). Contours are drawn at 1.266 GHz brightness levels $S_{\rm p} = \pm(2^{1.5}, 2^2, 2^{2.5}, ...)\mu$Jy beam^{-1}.

DEEP2 primary beam attenuation, the simulated subband images were multiplied by the frequency-dependent MeerKAT primary beam specified by equations 3 and

4 in Mauch et al. (2020). After multiplying by the primary beam attenuation, the simulation adds to each pixel of the wideband image a randomly generated sample of Gaussian noise. The noise in an aperture-synthesis image has the same (u, v)-plane coverage as the signal, so the DEEP2 image noise is smoothed by the same dirty beam (Figure 3.2). To duplicate this smoothing, the simulation convolved the pixel noise distribution with the dirty beam. The rms amplitude of the convolved noise was set to match the observed rms noise in the actual DEEP2 image prior to correction for primary beam attenuation.

Finally, this simulated image must be divided by primary beam attenuation to yield a simulated sky image. Figure 3.3 compares $4'.2 \times 4'.2$ (200×200 square pixels, each $1''.25$ on a side) cutouts from one simulated sky image with the actual DEEP2 sky image to show that the simulated image looks like the real image.

3.6 The DEEP2 $P(D)$ Distribution

3.6.1 Observed $P(D)$ Distribution

The peak flux density S_p at any point in an image is the sum of contributions from noise-free source confusion and image noise. Confusion and noise are independent, so the observed $P(D)$ distribution is the convolution of the confusion and noise distributions. The noise amplitude distribution in an aperture-synthesis image is easy to deconvolve because it is extremely stable, Gaussian, and uniform across the image prior to correction for primary-beam attenuation (Condon et al. 2012), unlike the noise in a single-dish image, which usually varies significantly with position and time during an observation. Consequently we were able to measure the DEEP2 rms noise and confirm its Gaussian amplitude distribution with very small uncertainties. The noise distribution is narrower than the noiseless $P(D)$ distribution in the very sensitive DEEP2 image, so we could deconvolve the Gaussian noise distribution from the observed $P(D)$ distribution to calculate the desired noiseless $P(D)$ distribution with unprecedented accuracy and sensitivity.

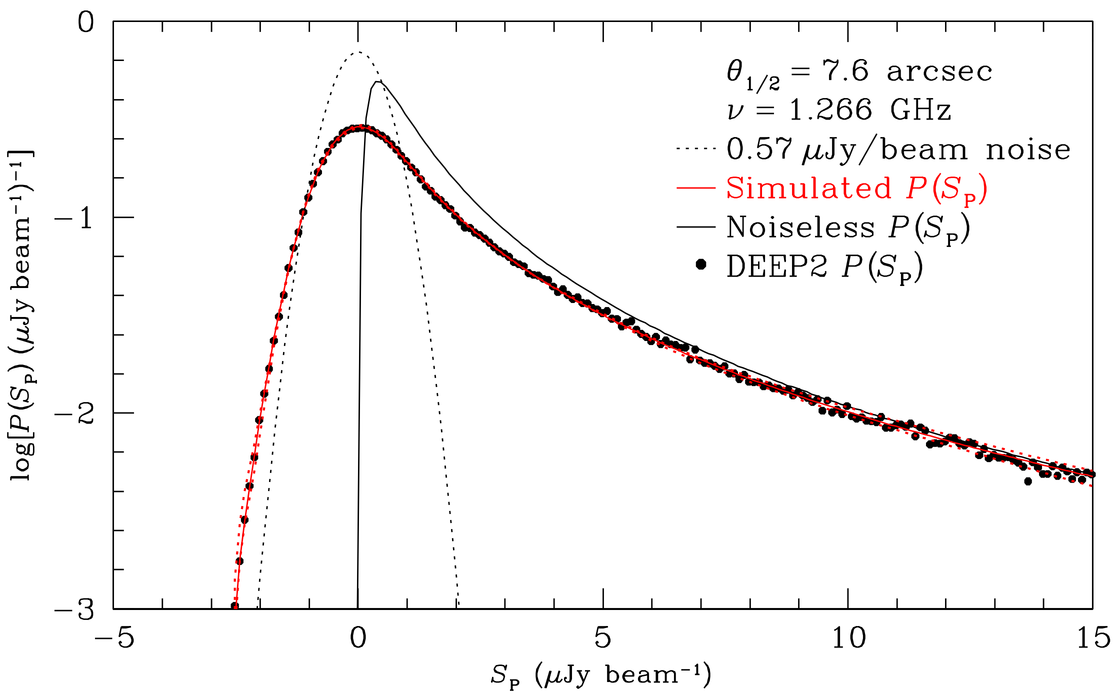

Figure 3.4. The normalized 1.266 GHz $P(S_\mathrm{p}) = P(D)$ distribution extracted from the central $r = 500''$ circle in the $\theta_{1/2} = 7''.6$ resolution DEEP2 image corrected for primary beam attenuation is shown by the heavy black dots representing bins of width $\Delta S_\mathrm{p} = 0.1\,\mu\mathrm{Jy\,beam^{-1}}$. It is quite smooth because it is based on 2.40×10^4 independent samples. The dotted parabola on this semilogarithmic plot represents the $\sigma_\mathrm{n} = 0.57\,\mu\mathrm{Jy\,beam^{-1}}$ Gaussian noise distribution inside the $P(D)$ circle. The red curve is the mean of 1000 simulated $P(D)$ distributions based on the best-fit source counts specified by Equation 3.9, and the red dotted curves bound the range that includes 2/3 of those simulated $P(D)$ distributions. The black curve shows the best-fit noiseless $P(D)$ distribution. These new fits are significantly more accurate than those shown in Mauch et al. (2020, fig. 13), which were based on a power-law approximation to the source counts.

Following the same procedure used in Mauch et al. (2020), we extracted the $P(D)$ distribution from the circle of radius $r = 500''$ covering solid angle $\Omega = 1.85 \times 10^{-5}\,\mathrm{sr}$ centered on the SNR-weighted 1.266 GHz DEEP2 image corrected for primary-beam attenuation and shown in figure 11 of Mauch et al. (2020). The $P(D)$ circle is small enough ($2r \ll \Theta_{1/2}$) that the mean primary-beam attenuation is 0.98 inside the circle and 0.96 at the edge, so its rms noise after correction for primary-beam attenuation is only $\sigma_\mathrm{n} = (0.56 \pm 0.01\,\mu\mathrm{Jy\,beam}^{-1})/0.98 = 0.57 \pm 0.01\,\mu\mathrm{Jy\,beam}^{-1}$. The $P(D)$ circle is still large enough to cover $N_\mathrm{b} = 1.20 \times 10^4$ restoring beam solid angles $\Omega_\mathrm{b} = \pi\theta_{1/2}^2/(4\ln 2) = 1.54 \times 10^{-9}\,\mathrm{sr}$. The solid angle of the *square* of the restoring beam attenuation pattern determines the number of independent samples per unit solid angle of sky (Condon et al. 2012). For a Gaussian restoring beam, the solid angle of the beam squared is half the beam solid angle, so the observed DEEP2 $P(D)$ distribution shown by the large black points in Figure 3.4 actually contains $2N_\mathrm{b} = 2.40 \times 10^4$ statistically independent samples. The observed $P(D)$ distribution is the convolution of the noiseless sky $P(D)$ distribution (black curve) with the $\sigma_\mathrm{n} = 0.57 \pm 0.01\,\mu\mathrm{Jy\,beam}^{-1}$ Gaussian noise distribution accurately represented by the parabolic dotted curve in the semi-logarithmic Figure 3.4.

The 1.266 GHz DEEP2 $P(D)$ distribution shown in Figure 3.4 is $4\times$ as sensitive to point sources with $\alpha \approx -0.7$ as the most sensitive published 3 GHz $P(D)$ distribution (Condon et al. 2012). Such sources are $1.83\times$ stronger at 1.266 GHz than at 3 GHz, so the rms noise $\sigma_\mathrm{n} = 1.255\,\mu\mathrm{Jy\,beam}^{-1}$ of the 3 GHz $P(D)$ distribution is equivalent to $\sigma_\mathrm{n} = 2.30\,\mu\mathrm{Jy\,beam}^{-1}$ at 1.266 GHz. The peak of the DEEP2 noise distribution is higher than the peak of the noiseless $P(D)$ distribution (Figure 3.4), indicating that DEEP2 is strongly confusion limited, while the peak of the 3 GHz noise distribution is only half as high as the peak of the 3 GHz noiseless $P(D)$ distribution. The DEEP2 $P(D)$ distribution also has smaller statistical uncertainties because it includes $3.1\times$ as many independent samples. Finally, the DEEP2 $P(D)$ distribution was extracted from the very center of the image where the primary beam attenuation ≥ 0.96, so systematic errors caused by antenna pointing fluctuations or primary-beam attenuation corrections are negligible.

3.6.2 $P(D)$ statistical counts of $0.25 \leq S(\mu\text{Jy}) \leq 10$ sources

The noiseless confusion $P(D)$ distribution is sensitive to the differential counts $n(S)$ of sources more than $10\times$ fainter than the usual $5\sigma_{\rm n}$ detection limit for individual sources. In terms of the number $N(>S)$ of sources per steradian stronger than S, the mean number of sources stronger than S per beam solid angle $\Omega_{\rm b}$ is $\mu = [N(> S)\Omega_{\rm b}]$ and the Poisson probability that *all* sources in a beam are weaker than S is $P_{\rm P} = \exp(-\mu)$. The DEEP2 image $\Omega_{\rm b} \approx 1.54 \times 10^{-9}\,$sr and the best-fit source counts from Mauch et al. (2020) imply $P_{\rm P} \approx 0.4$ at $S = 0.25\,\mu\text{Jy beam}^{-1}$. The DEEP2 $P(D)$ distribution was extracted from a solid angle containing 2.40×10^4 independent samples of the sky, so changes in the source count down to $S = 0.25\,\mu\text{Jy beam}^{-1}$ can be detected statistically from the 10^4 independent samples that contain only fainter sources if the rms noise $\sigma_{\rm n} \lesssim \sigma_{\rm c}$, the noise due to source confusion.

We used the radio sky simulations described in Section 3.5 to constrain the source counts consistent with the observed $P(D)$ distribution. The DEEP2 $P(D)$ distribution is smoothed by Gaussian noise with rms $\sigma_{\rm n} = 0.57 \pm 0.01\,\mu\text{Jy beam}^{-1}$ which degrades its sensitivity to significantly fainter sources. To estimate the sensitivity of DEEP2 to faint sources in the presence of noise, we simulated noisy $P(D)$ distributions using a variety of differential source counts below $S = 10\,\mu$Jy. Above $S = 10\,\mu$Jy, we used the direct source counts from DEEP2 and the NVSS presented in Sections 3.7.4 and 3.8. The simulation accepts brightness-weighted differential source counts $S^2n(S)$ specified in bins of width $\Delta\log(S) = 0.2$. Directly binning counts $n(S)$ that vary rapidly with S can introduce a significant bias (Jauncey 1968). We mitigated this bias by binning the quantity $S^2n(S)$ which changes little across a flux-density bin.

The source counts $S^2n(S)$ in the flux range $-8 < \log[S(\text{Jy})] < -4.9$ are well fit by a cubic polynomial. To measure goodness-of-fit for each input source count we defined a statistic that quadratically combines the reduced $\chi^2_{\rm P(D)}$ from differences between the simulated and observed $P(D)$ distributions for all $S_{\rm p} < 15\,\mu\text{Jy beam}^{-1}$ with the $\chi^2_{\rm DC}$ of the differences between the simulated counts and the direct counts of DEEP2 sources in bins centered on $\log S = -4.9$ and -4.7:

$$\chi^2 = \sqrt{\left(\chi^2_{\rm P(D)}\right)^2 + \left(\chi^2_{\rm DC}\right)^2}. \tag{3.8}$$

We optimized the parameters for the cubic polynomial by minimizing Equation 3.8. We inspected the residuals $\Delta N/\sigma_N$, where N is the number of independent samples per bin and σ_N is the Poisson error per bin associated with the observed $P(D)$ distribution, of the resulting best-fits for the presence of correlations as a function of brightness D. The existence of a signal akin to red-noise in our residuals would imply our counts under- or over-estimate the counts of sources in specific flux density ranges.

The 3rd-degree polynomial source count

$$\begin{aligned} \log[S^2 n(S)] = 2.718 &+ 0.405(\log S + 5) \\ &- 0.020(\log S + 5)^2 \\ &+ 0.019(\log S + 5)^3 \ , \end{aligned} \tag{3.9}$$

where S is the 1.266 GHz flux density in Jy, gave the simulated $P(D)$ distribution (red curve in Figure 3.4) best fitting the observed distribution (black points) while maintaining continuity in the transition from the $P(D)$ to direct counts at $S = 10\,\mu$Jy.

We converted the 1.266 GHz flux densities and brightness-weighted source counts in Equations 3.9, 3.13, and 3.14 to the common source-count frequency $\nu = 1.4$ GHz for sources with spectral index $\alpha = -0.7$ using

$$\begin{aligned} \log(S_{1.4\,\rm GHz}) &= \log(S_{1.266\,\rm GHz}) + \alpha \log\left(\frac{1.4}{1.266}\right) \\ &\approx \log(S_{1.266\,\rm GHz}) - 0.0306 \end{aligned} \tag{3.10}$$

and

$$\begin{aligned}\log[S^2 n(S)]_{1.4\,\mathrm{GHz}} &= \log[S^2 n(S)]_{1.266\,\mathrm{GHz}} + \alpha \log\left(\frac{1.4}{1.266}\right) \\ &\approx \log[S^2 n(S)]_{1.266\,\mathrm{GHz}} - 0.0306\ .\end{aligned} \tag{3.11}$$

We also calculated the commonly used static-Euclidean source counts from the brightness-weighted source counts via

$$\log[S^{5/2} n(S)] = 0.5 \log(S) + \log[S^2 n(S)]\ . \tag{3.12}$$

Our 1.4 GHz differential source counts with both normalizations are plotted —along with the discrete source counts calculated in Sections 3.7.4 and 3.8— in Figure 3.12. In the following subsections, we describe our accounting of the various biases and uncertainties in our statistical fit of the source counts.

3.6.3 Zero-level offset

Before calculating the value of this statistic for a given simulation, we removed the brightness zero-point offset between the simulated and observed $P(D)$ distributions. Numerous faint radio sources produce a smooth background which is invisible to MeerKAT and other correlation interferometers lacking zero-spacing data. Thus the brightness zero level of our observed $P(D)$ distribution is unknown and must be fitted out. We minimized the zero-level offset by comparing the observed and simulated $P(D)$ distributions shifted in steps of $0.001\,\mu\mathrm{Jy\,beam}^{-1}$, this step size being smaller than the rms noise divided by the square root of the number 2.40×10^4 of independent samples in the DEEP2 $P(D)$ area.

3.6.4 DEEP2 rms noise uncertainty

Although the simulation includes sources as faint as $S = 0.01\,\mu\mathrm{Jy}$, the DEEP2 image is not sensitive to the counts of such faint sources. The biggest cause of uncertainty in our sub-μJy source counts is the $\pm 0.01\,\mu\mathrm{Jy\,beam}^{-1}$ uncertainty in the DEEP2 rms

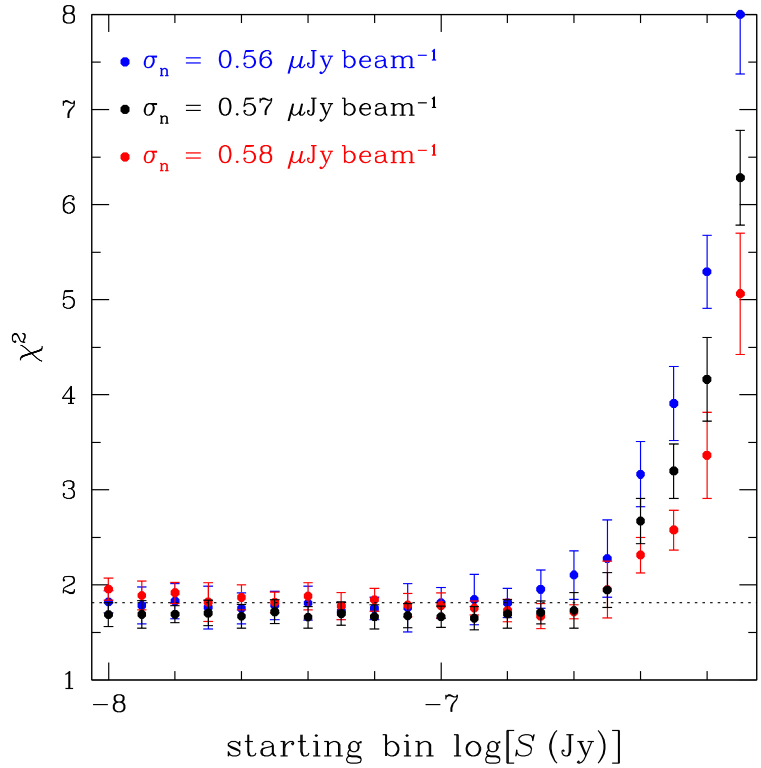

Figure 3.5. The reduced χ^2 statistic from 1.266 GHz DEEP2 simulations is shown as a function of the starting source count bin increasing from the nominal $\log[S(\mathrm{Jy})] = -8$ to -6.1. At $\log[S(\mathrm{Jy})] = -6.5$, the χ^2 statistic of the $P(D)$ distribution from DEEP2 simulations with $\sigma_n = 0.57\,\mu$Jy averaged over the $r = 500''$ $P(D)$ circle (black points) exceeds the value of the mean minimum χ^2 plus 1σ (black dotted line). This indicates that we are sensitive to changes in the source count down to $\log[S(\mathrm{Jy})] = -6.6$. The χ^2 values for DEEP2 simulations with $\pm 1\sigma$ in rms noise are shown in blue and red for 0.56 and 0.58 μJy beam^{-1}, respectively.

noise. To estimate the flux density of the faintest sources we can usefully count, we set the rms noise to $\sigma_n = 0.57\,\mu$Jy beam^{-1} and iteratively removed the lowest flux-density bin before using that sub-sample of bins to produce the DEEP2 simulation. After repeating this process for a total of 50 trials, we found that removing the source count bin at $\log[S(\mathrm{Jy})] = -6.6$ increases the simulation χ^2 to more than one-sigma above the mean minimum χ^2, as shown by the the black points above the dotted line in Figure 3.5. The same process was repeated for for $\sigma_n = 0.56\,\mu$Jy beam^{-1} (blue points) and 0.58 μJy beam^{-1} (red points). The results are consistent with a count sensitivity limit $\log[S(\mathrm{Jy})] \approx -6.6$ or $S \approx 0.25\,\mu$Jy in the presence of $\sigma_n = 0.57 \pm 0.01\,\mu$Jy beam^{-1}

noise.

To determine the sensitivity of our best-fitting $P(D)$ distribution above $S = 0.25\,\mu$Jy to small changes in the rms noise, we ran 1000 simulations of the DEEP2 $P(D)$ distribution using the counts given by Equation 3.9 and varying the $\sigma_{\rm n} = 0.57\,\mu\text{Jy beam}^{-1}$ noise by adding values drawn randomly from a Gaussian distribution of rms width $0.01\,\mu\text{Jy beam}^{-1}$. The range of $P(D)$ containing 68% of these simulations best fitting (according to Equation 3.8) the average of all 1000 simulations defines the $\pm\sigma$ uncertainty region of our model $P(D)$. Figure 3.4 includes dotted red lines showing this narrow uncertainty region, which is easily visible only in the $S_{\rm p} > 10\,\mu\text{Jy beam}^{-1}$ tail of the distribution.

3.6.5 Estimating the source-count uncertainty

To estimate the $\pm\sigma$ source-count errors resulting from the above $P(D)$ distribution range, we ran 500 simulations with the following variations: (1) the noise was drawn randomly from Gaussian distributions with mean $\sigma_{\rm n} = 0.57\,\mu\text{Jy beam}^{-1}$ and scatter $0.01\,\mu\text{Jy beam}^{-1}$; (2) the input source counts were modeled with a fourth-degree polynomial to allow for the rapidly growing count uncertainty at the lowest flux densities caused by noise as well as by a possible "new" population of very faint radio sources; and (3) the coefficients of the fourth-degree polynomials were drawn randomly from gaussian distributions centered on the best-fitting values given in Equation 3.9 with an rms of 0.1 (the unknown fourth-degree coefficient was initially centered on zero).

Each combination of coefficients and rms noise was repeated an additional six times to determine the effects of noise on the goodness-of-fit. We considered a set of coefficients to be in agreement with the DEEP2 $P(D)$ distribution if at least five of the total seven simulations fell within the $\pm\sigma$ uncertainty region determined from the original, un-altered 1000 simulations. The subset of the 500 coefficient-varying simulations that satisfied this criterion define the statistical uncertainty of the measured source counts. Then we added quadratically a 3% count uncertainty to absorb possible 3% systematic flux-density calibration errors. In the flux density range $-6.6 < \log[S(\text{Jy})] < 5$, the 1-$\sigma$ lower limit of the 1.266 GHz source-count error region is

$$\begin{aligned}\log[S^2 n(S)] = 2.677 &+ 0.489(\log S + 5) \\ &+ 0.077(\log S + 5)^2 \\ &+ 0.061(\log S + 5)^3 \\ &- 0.058(\log S + 5)^4\end{aligned} \tag{3.13}$$

and the 1-σ upper limit is

$$\begin{aligned}\log[S^2 n(S)] = 2.768 &+ 0.367(\log S + 5) \\ &- 0.076(\log S + 5)^2 \\ &- 0.009(\log S + 5)^3 \\ &+ 0.023(\log S + 5)^4 \ .\end{aligned} \tag{3.14}$$

3.7 The DEEP2 Source Catalog and Direct Counts

We used the attenuation-corrected "sky" image to search for discrete sources. The "effective frequency" of the wideband SNR-weighted DEEP2 image for sources with median spectral index $\langle\alpha\rangle \approx -0.7$ is $\nu_e = 1.266\,\mathrm{GHz}$ (Mauch et al. 2020). Even after correction for primary-beam attenuation, the DEEP2 image is strongly confusion limited with rms noise $\sigma_n < 1.12\,\mu\mathrm{Jy\,beam}^{-1}$ everywhere inside the primary beam half-power circle. Consequently our catalog brightness sensitivity limit $S_p(1.266\,\mathrm{GHz}) = 10\,\mu\mathrm{Jy\,beam}^{-1} > 9\sigma_n$ is uniform over the whole primary half-power circle, unlike the variable sensitivity limit of a deep source catalog extracted from an image still attenuated by the primary beam. Nearly all μJy radio sources are unresolved by the $\theta_{1/2} = 7.''6$ DEEP2 restoring beam, so the DEEP2 catalog should be nearly complete for sources with total flux densities just above $S(1.266\,\mathrm{GHz}) = 10\,\mu\mathrm{Jy}$. The relatively large DEEP2 restoring beam is actually advantageous because incompleteness corrections for partially resolved sources can be large and uncertain when the beam size is not much larger than the median source size (Morrison et al. 2010; Owen 2018).

3.7.1 The DEEP2 Component Catalog

We applied the *Obit* (Cotton 2008) source-finding task FndSou to the DEEP2 sky image inside the DEEP2 primary beam half-power circle. FndSou searches for islands of contiguous pixels and decomposes each island into elliptical Gaussian components as faint as $S_\mathrm{p} = 10\,\mu\mathrm{Jy\,beam}^{-1}$. Most radio sources with $S(3\,\mathrm{GHz}) \gtrsim 5\,\mu\mathrm{Jy}$ (equivalent to $S \gtrsim 9\,\mu\mathrm{Jy}$ at $1.266\,\mathrm{GHz}$ for $\langle\alpha\rangle = -0.7$) have angular diameters $\phi \lesssim 0\rlap{.}''66$ (Cotton et al. 2018) and would be completely unresolved in the DEEP2 image. This point-source approximation is supported by the qualitative similarity of our point-source simulation and the actual DEEP2 image shown in Figure 3.3. A small fraction of the DEEP2 sources stronger than $\sim 100\,\mu\mathrm{Jy}$ are clearly resolved jets or lobes driven by unresolved central AGNs, and they can be represented by combining multiple components as described in Section 3.7.3.

The sky density of sources reaches one per 25 restoring beam solid angles at $S(1.266\,\mathrm{GHz}) \approx 17\,\mu\mathrm{Jy}$ (Mauch et al. 2020), so a significant fraction of our $S \gtrsim 10\,\mu\mathrm{Jy}$ components partially overlap, and our catalog accuracy, completeness, and reliability are limited more by confusion than by noise. To optimize the DEEP2 component catalog and understand its limitations, we used FndSou to extract catalogs of components from simulated images and compared those catalogs with the simulation input source lists. We compared catalogs in which the fitted elliptical Gaussians were allowed to vary in width to "point source" catalogs in which they were not and found that forcing point-source fits generally gave better matches to the "true" simulation input catalogs. Therefore we forced point-source fits to make the DEEP2 component catalog, and we later combined components as needed to represent multicomponent extended radio sources.

In a few crowded regions, FndSou reported spurious faint components very close to much stronger sources. To decide which components to reject from our catalog, we generalized the original Rayleigh criterion for resolving two equal point sources observed with an Airy pattern PSF: the peak of one lies on or outside the first zero of the second, which ensures that the total response has a minimum between them.

The total image response R at position x between unequal components S_1 at

$x_1 = 0$ and $S_2 < S_1$ at $x_2 = \Delta$ to a Gaussian PSF with FWHM $\theta_{1/2}$ is

$$R = S_1 \exp\left(-\frac{4\ln 2}{\theta_{1/2}^2}x^2\right) + S_2 \exp\left[-\frac{4\ln 2}{\theta_{1/2}^2}(x-\Delta)^2\right] . \tag{3.15}$$

For R to have a minimum between the components, $dR/dx = 0$ for some $0 < x < \Delta$. The continuous curve in Figure 3.6 shows the required component separation $\Delta/\theta_{1/2}$ as a function of the flux-density ratio S_1/S_2. All DEEP2 catalog components stronger

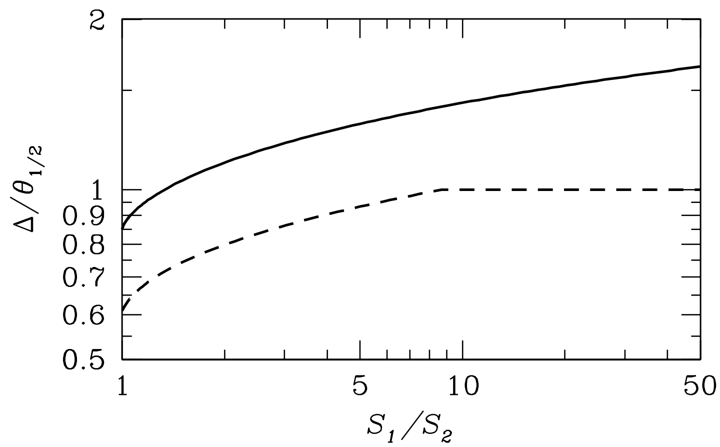

Figure 3.6. The continuous curve shows the calculated minimum separation Δ in Gaussian beamwidths $\theta_{1/2}$ needed to produce a minimum between two point sources as a function of their flux-density ratio S_1/S_2. The dashed curve shows the empirical minimum separation for reliable DEEP2 components stronger than $10\,\mu$Jy.

than $S > 10\,\mu$Jy have SNR> 9, so the requirement in Equation 3.15 is stricter than necessary. By comparing ten catalogs of components extracted from simulated images with the "true" input components used to generate the simulated images, we found that faint components near stronger components are reliable if they satisfy the weaker criterion

$$
\begin{aligned}
\frac{\Delta}{\theta_{1/2}} &\geq 0.574 + 0.357[\log(S_1/S_2) + 0.01]^{1/2} + \\
&\quad 0.082 \log(S_1/S_2) && \text{if } (S_1/S_2) < 9 \\
\frac{\Delta}{\theta_{1/2}} &\geq 1 && \text{if } (S_1/S_2) \geq 9
\end{aligned}
\tag{3.16}
$$

shown by the dashed curve in Figure 3.6. We rejected the 334 probably spurious DEEP2 components ($< 2\%$ of the total) failing to satisfy Equation 3.16.

To estimate the effects of confusion and noise on the completeness, reliability, positions, and flux densities of the surviving 17,350 DEEP2 components, we ran ten independent simulations of the DEEP2 field out to the half-power circle of the primary beam using input source counts consistent with the differential source counts in Table 3.5 and the 1.4 GHz statistical count $S^2 n(S) = 1.07 \times 10^{-5} S^{-0.48}\,\mathrm{Jy\,sr^{-1}}$ of fainter sources from Mauch et al. (2020). For each simulated image, we used FndSou to find all components stronger than $10\,\mu$Jy and rejected the components that did not satisfy the resolution criterion in Equation 3.16. The positions and flux densities of the resulting ten catalogs were compared with the "true" simulation input positions and flux densities of all simulated sources stronger than $5\,\mu$Jy.

We matched a simulated source to a cataloged component if (1) its position was within $\theta_{1/2}/2 = 3\farcs8$ of the cataloged position and (2) the catalog-to-true flux ratio satisfied $0.5 \leq S_{\rm cat}/S_{\rm true} \leq 2$. If there were two or more matches, only the strongest simulated source was matched with the cataloged component. If there were no simulated sources that satisfied these criteria, the cataloged component was rejected as spurious. The ten simulations yielded $\sim 1.6 \times 10^5$ matches. Only $\sim 0.5\%$ of the cataloged components had no simulated-source counterpart, for a catalog reliability $\approx 99.5\%$.

FndSou measures intensities relative to the image zero level. The DEEP2 interferometric image is insensitive to the smooth background of very faint radio sources. Our simulations of the radio sky brightness include such a background, so the average confusion $P(D)$ distribution from ten simulations of DEEP2 appears shifted by $\Delta D = +0.28\,\mu\mathrm{Jy\,beam}^{-1}$ compared with the $P(D)$ distribution of the real DEEP2 image. The final flux densities of components in the DEEP2 source catalog were corrected for the zero-level offset by subtracting $0.28\,\mu\mathrm{Jy\,beam}^{-1}$ from the peak flux densities reported by FndSou.

3.7.2 DEEP2 Catalog Position Uncertainties

The random position errors of DEEP2 source components are dominated by confusion errors whose non-Gaussian distributions are difficult to calculate analytically, so we estimated the random position errors from the differences $\Delta\alpha$, $\Delta\delta$ between the cataloged and "true" input positions of source components in our ten simulations. The normalized probability distributions $P(\Delta)$ are shown separately for right ascension α (red histogram) and declination δ (blue histogram) in Figure 3.7. The distributions of $\Delta\alpha$ and $\Delta\delta$ are indistinguishable, as expected for a circular PSF. Also as expected, the distributions of random positions errors are symmetrical about $\Delta = 0$ and have long non-Gaussian tails—a Gaussian distribution would look like a parabola in the semilogarithmic Figure 3.7. The formal rms width of $P(\Delta)$ is dominated by these tails and is not a stable measure of the position error distribution. In a Gaussian distribution with rms σ, 68% of the sources would lie within the range $-\sigma < \Delta < +\sigma$, so we used the range of actual position offsets $\Delta\alpha \approx \Delta\delta$ and defined the "rms" position errors σ_α and σ_δ such that 68% of the components lie in the range $-\sigma_\alpha < \Delta\alpha < +\sigma_\alpha$ or $-\sigma_\delta < \Delta\delta < +\sigma_\delta$. The DEEP2 random position errors vary with component flux density S. For bins of width 0.2 in $\log(S)$ centered on $\log[S(\mu\mathrm{Jy})] = 1.1, 1.3, \ldots, 2.9$, we determined the distributions of position offsets $\Delta\alpha$ and $\Delta\delta$ in the ten simulations. Figure 3.8 shows $\sigma_\alpha \approx \sigma_\delta$ as a function of $\log(S)$.

The relationship between this error limit and flux density is well described by a broken power-law of the form

$$\frac{\Delta\alpha}{\mathrm{arcsec}} = \frac{\Delta\delta}{\mathrm{arcsec}} = C\left[\left(\frac{S_*}{S}\right)^{R/2} + \left(\frac{S_*}{S}\right)^{R}\right]^{1/R}, \tag{3.17}$$

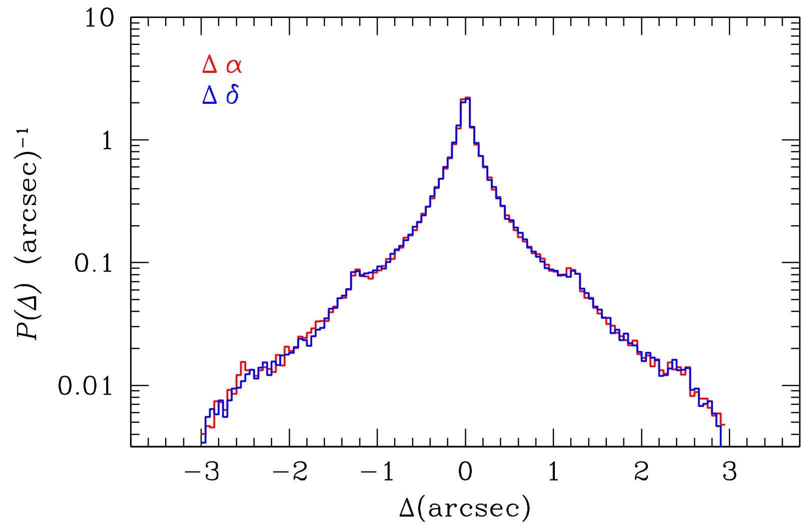

Figure 3.7. The distributions $P\,(\mathrm{arcsec})^{-1}$ of differences in right ascension $\Delta\alpha$ (red curve) and declination $\Delta\delta$ (blue curve) between the cataloged and "true" simulation positions for all sources with $S \geq 10\,\mu$Jy from ten simulated DEEP2 images. The small peaks at integer multiples of $\Delta = 1\farcs25$ are artifacts from measuring distances in simulated images composed of $1\farcs25$ pixels but do not affect the rms position errors.

where the parameter R controls the sharpness of the break at $S = S_*$. A nonlinear least squares fit to Equation 3.17 yields $R = -11.97$, $C = 0.219$, and $S_* = 78.6\,\mu$Jy. As the catalogs were made for simulated images, there are no systematic position errors included in Equation 3.17. The dashed black curve in Figure 3.8 shows the random rms errors $\sigma_\alpha \approx \sigma_\delta$ as a function of component flux density. The slope of the dashed curves in Figures 3.8 and 3.10 changes from -1 to -0.5 below S_* because the DEEP2 image is strongly limited by confusion, the source-count slope changes by $\Delta\gamma \approx -1$ near $S = S_*$, and the rms confusion from weaker sources is proportional to $S^{(3-\gamma)/2}$ (see eq. 20 in Condon et al. 2012). No such break occurs in noise-limited images.

To estimate the DEEP2 systematic position uncertainties and offsets, we selected the 268 strong components with calculated random errors $\sigma_\alpha = \sigma_\delta \leq 0\farcs05$ and used the NASA/IPAC Infrared Science Archive (IRSA) to find eight identifications with Gaia DR2 sources whose position errors are much smaller than $0\farcs05$. Their DEEP2 minus Gaia offsets have rms $\sigma_\alpha = \sigma_\delta = 0\farcs12 \pm 0\farcs04$, an insignificant mean offset $+0\farcs03 \pm 0\farcs04$ in right ascension, and a 3σ significant mean declination offset $+0\farcs12 \pm 0\farcs04$. We therefore added $-0\farcs12$ to our fitted DEEP2 declinations and added the $0\farcs12$ systematic position errors to the random errors in quadrature to get the total DEEP2 position error shown by the continuous curve in Figure 3.8. The total position errors reported in the final component catalog (Table 3.3) reflect this quadrature sum and the corrected declinations.

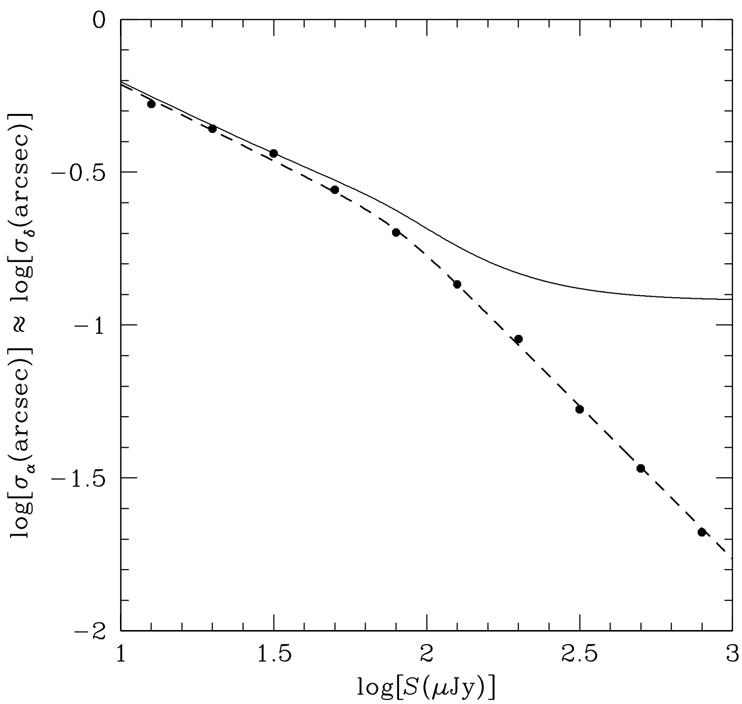

Figure 3.8. The simulation "rms" (defined as half the 68% confidence interval) random position error in either right ascension α and declination δ is shown as a function of flux density S by the points. The black dashed curve shows the best-fitting broken power-law from Equation 3.17. The total DEEP2 "rms" position uncertainties estimated by the quadrature sum of Equation 3.17 random errors and $0\farcs12$ systematic position errors are indicated by the solid curve.

We compared the flux densities calculated from the forced point-source fits of cataloged components in the ten simulated images with their "true" input flux densities. The distribution of these differences $\Delta S = S_{\mathrm{cat}} - S_{\mathrm{true}}$ is shown in Figure 3.9 for four flux density ranges: $10\,\mu\mathrm{Jy} < S < 10^{1.2} \sim 16\,\mu\mathrm{Jy}$, $10^{1.2}\,\mu\mathrm{Jy} < S < 10^{1.4} \sim 25\,\mu\mathrm{Jy}$,

$10^{1.4}\,\mu$Jy $< S < 10^{1.6} \sim 40\,\mu$Jy, and $S > 10^{1.6}\,\mu$Jy. The flux-density error distributions all peak near $\Delta S = 0\,\mu$Jy but have positive tails that grow with flux density because stronger components are able to obscure stronger confusing components.

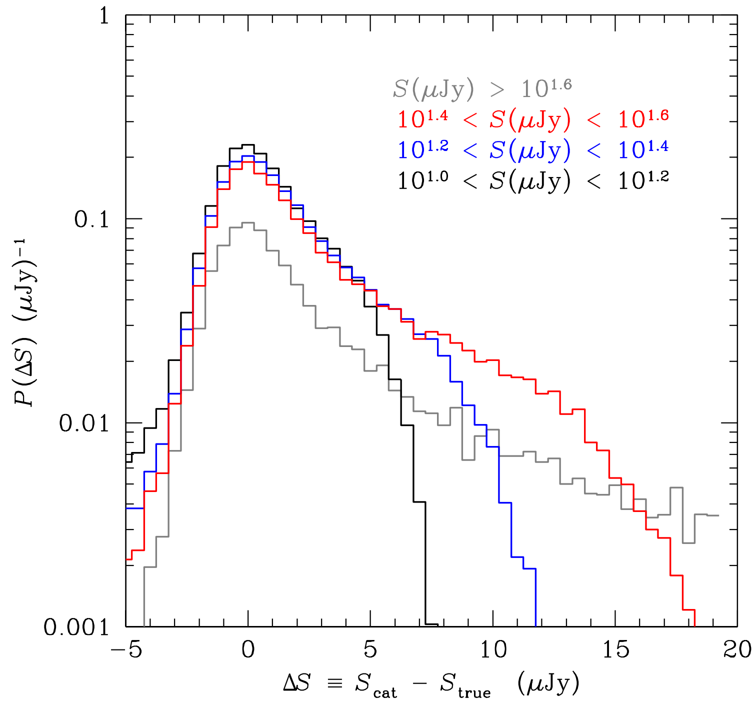

Figure 3.9. The differences $\Delta S = S_{\rm cat} - S_{\rm true}$ between the cataloged and "true" simulation flux density are shown for four catalog flux-density ranges: $10\,\mu$Jy $< S < 10^{1.2} \sim 16\,\mu$Jy (black), $10^{1.2}\,\mu$Jy $< S < 10^{1.4} \sim 25\,\mu$Jy (blue), $10^{1.4}\,\mu$Jy $< S < 10^{1.6} \sim 40\,\mu$Jy (red), and $S > 10^{1.6}\,\mu$Jy (gray).

The fractional flux density errors σ_S/S were calculated for all ten catalogs of the simulated images in bins of width 0.2 dex centered on $\log[S\,(\mu{\rm Jy})] = 1.1, 1.3, \ldots, 2.9$ and are shown in Figure 3.10. In the ideal case of uncorrelated Gaussian noise, high signal-to-noise S/σ_S, and a circular Gaussian beam of FWHM $\theta_{1/2}$, Equation 21 of Condon (1997) gives

$$\frac{\sigma_S}{S} = \sqrt{8\ln 2}\left(\frac{\sigma_\alpha}{\theta_{1/2}}\right) = \sqrt{8\ln 2}\left(\frac{\sigma_\delta}{\theta_{1/2}}\right), \tag{3.18}$$

so for either α or δ,

$$\log\left(\frac{\sigma_S}{S}\right) = \log(8\ln 2)/2 + \log(\sigma_\alpha) - \log(\theta_{1/2})$$
$$= \log(\sigma_\alpha) - 0.51, \tag{3.19}$$

for $\theta_{1/2} = 7\farcs6$. This gives conservative flux-density fitting errors. To them we add in quadrature a 2% uncertainty for telescope pointing errors and primary attenuation uncertainty inside the primary beam half-power circle plus a 3% for the absolute flux-density uncertainty of the gain calibrator PKS B1934−638 (Mauch et al. 2020) to get the total fractional uncertainty

$$\frac{\sigma_S}{S} = \left(8\ln 2\frac{\sigma_\alpha^2}{\theta_{1/2}^2} + 0.036^2\right)^{1/2}. \tag{3.20}$$

The fractional flux density errors calculated from Equation 3.20 are shown by the solid black curve in Figure 3.10. This method yields more conservative error estimates than directly fitting the measured flux differences from the simulated images with a broken power law for flux densities $\log S < 2.5$ when these measured differences are added in quadrature with the cumulative calibration uncertainties (shown as the dotted line in Figure 3.10).

The ten simulated images were corrected for primary beam attenuation before the catalog was created, so the noise contribution increases distance r from the pointing center as

$$\sigma_{\rm n}(r) = \frac{0.56\,\mu\text{Jy beam}^{-1}}{a(r)}, \tag{3.21}$$

where

$$a(r) = \exp\left(-4\ln 2\frac{r^2}{\Theta_{1/2}^2}\right), \tag{3.22}$$

is the primary beam attenuation. The simulation placed sources in the sky randomly but uniformly, so we subtracted the average noise variance within the half-power circle $\langle\sigma_{\rm n}\rangle = 0.824\,\mu$Jy beam^{-1} from the total average flux-density variance calculated from

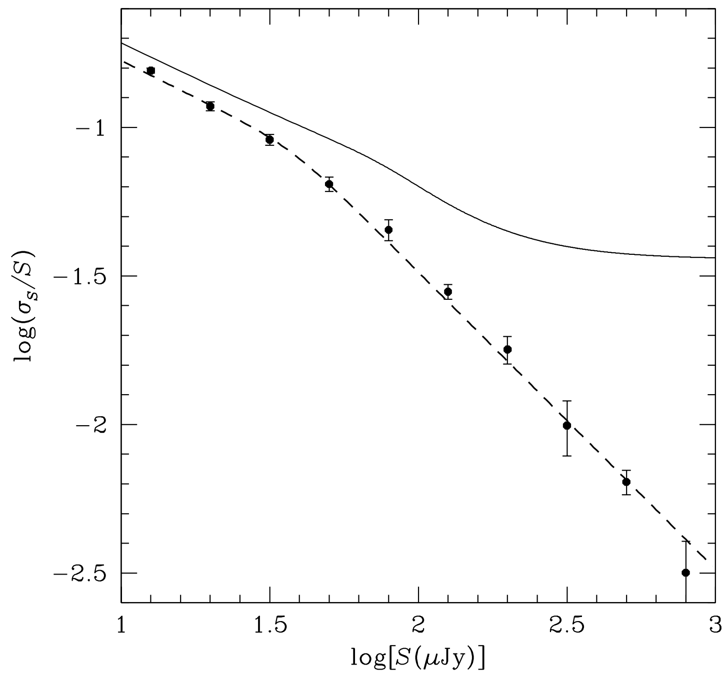

Figure 3.10. The random fractional flux density errors per catalog flux density bin was calculated as the narrowest range of the distribution containing 68% of the simulated sources (black points). The dashed line shows a broken power-law fit to these calculated errors. The total component error σ_S/S) from Equation 3.20 is shown as the solid black curve.

Equation 3.20. We added back the distance-dependent rms noise variance to get a better estimate of errors on the individual source flux densities at various distances from the pointing center.

3.7.3 Multicomponent Sources

We visually inspected the DEEP2 image and found 35 groups of components that appear to comprise multicomponent radio sources. We labeled these components by their group numbers G01 to G35. For an extended source well approximated by a collection of Gaussian components, we summed the individual component flux densities to determine the source flux density. For a source containing diffuse emission regions, we estimated the flux density of such regions by directly summing over the pixel brightness distribution. Table 3.4 lists the 35 multicomponent sources, the number of

Table 3.3. The 1.266 GHz DEEP2 Component Catalog

Right Ascension (J2000)	Declination (J2000)	S(1.266 GHz) (μJy)	Group Code
04:08:34.781 ± 0.170	−79:51:43.08 ± 0.45	20.0 ± 2.1	···
04:08:34.897 ± 0.089	−80:20:26.14 ± 0.22	87.2 ± 5.3	G09
04:08:34.956 ± 0.166	−79:35:02.48 ± 0.45	20.0 ± 2.2	···
04:08:34.986 ± 0.160	−80:24:19.47 ± 0.40	25.5 ± 2.5	···
04:08:35.066 ± 0.051	−79:47:01.95 ± 0.13	278.0 ± 10.5	···

Note—Table 3.3 is published in its entirety in machine-readable format. A portion is shown here for guidance regarding its form and content. The quoted uncertainties are similar to rms errors in that they encompass 68% of the sources but are insensitive to the long tails of confusion-limited error distributions. There are 35 multicomponent sources labeled by their component group numbers G01 through G35, as described in Section 3.7.3.

components in each source group, our best estimate of the source core position, and the source flux density. Figure 3.11 shows the contour map of multicomponent source G01 with crosses marking the positions of its three components. Similar contour maps of all multicomponent sources appear in the Appendix.

Table 3.4: DEEP2 Multicomponent sources

Group Code	N	Right Ascension (J2000)	Declination (J2000)	S (μJy)
G01	3	04:00:47.04	−79:51:31.4	817
G02	3	04:01:31.81	−79:59:08.6	159
G03	8	04:03:54.19	−80:08:49.1	757
G04	4	04:04:05.81	−79:58:56.2	709
G05	3	04:04:14.84	−79:56:21.5	13536
G06	3	04:06:15.50	−80:10:57.5	2742
G07	3	04:06:26.05	−79:38:01.0	168
G08	7	04:06:27.83	−80:18:48.0	19200
G09	14	04:08:42.38	−80:20:40.9	885

Continued on Next Page…

Table 3.4 – Continued

Group Code	N	Right Ascension (J2000)	Declination (J2000)	S (μJy)
G10	12	04:08:47.70	−80:24:02.4	1569
G11	5	04:11:32.60	−79:48:41.3	766
G12	3	04:11:38.97	−79:48:17.5	2867
G13	11	04:11:59.21	−80:14:54.8	1422
G14	7	04:12:16.93	−79:46:33.2	6772
G15	5	04:12:32.00	−79:34:36.4	509
G16	8	04:13:24.93	−79:49:21.2	5455
G17	9	04:13:41.22	−79:46:34.9	6680
G18	4	04:13:58.03	−79:42:19.2	1369
G19	18	04:14:17.93	−80:11:38.4	5455
G20	5	04:14:58.85	−80:29:08.4	1261
G21	3	04:16:10.11	−80:03:31.9	169
G22	6	04:16:23.34	−80:20:54.5	4699
G23	3	04:16:47.09	−79:48:50.3	54268
G24	5	04:16:58.32	−79:54:46.2	1953
G25	9	04:17:02.19	−80:12:33.9	6115
G26	3	04:17:06.86	−79:51:28.6	3682
G27	7	04:18:58.15	−79:51:23.5	1603
G28	10	04:19:10.77	−80:30:32.4	3051
G29	4	04:20:03.10	−80:27:11.3	2769
G30	14	04:22:05.41	−80:03:30.1	10882
G31	5	04:23:19.81	−79:51:10.6	11408
G32	8	04:25:02.63	−80:14:15.9	26271
G33	6	04:25:18.38	−79:52:22.3	15983
G34	9	04:25:51.5	−79:54:38	731
G35	8	04:26:07.75	−80:09:23.7	766

3.7.4 DEEP2 Direct Source Counts

We counted DEEP2 sources in bins of width 0.2 dex centered on 1.266 GHz flux densities $\log[S(\mathrm{Jy})] = -4.9, -4.7, \ldots, -2.5$. Component groups comprising an extended source were counted as a single source whose flux density is the sum of its individual

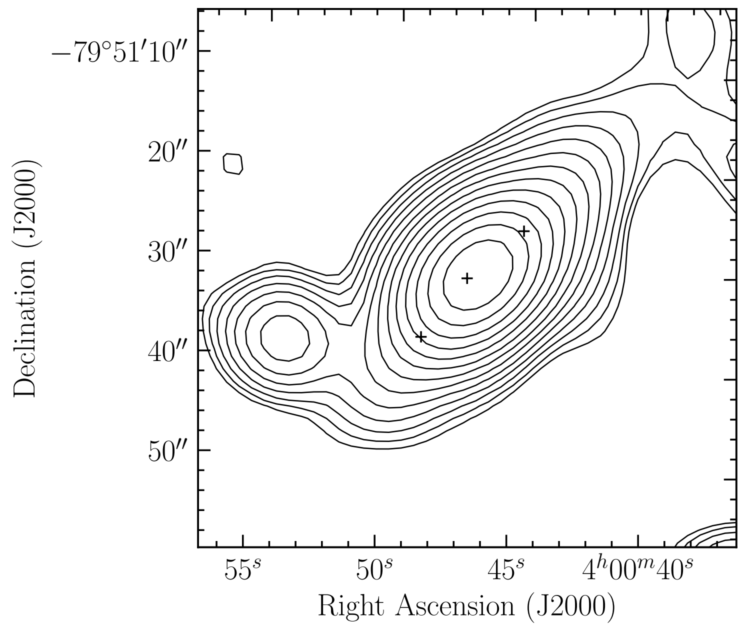

Figure 3.11. Multicomponent source G01. Contour levels $\pm 5\,\mu\mathrm{Jy\,beam}^{-1} \times 2^0, 2^{1/2}, 2^1, \ldots$ are plotted (negative contours, where present, shown as dashed lines). Crosses mark the three components comprising this source. The complete figure set (35 images) is available in the online journal.

component flux densities. For the few extended sources with diffuse emission regions, we estimated the flux densities of these regions by directly summing over their pixel brightness distributions.

Sources near the catalog lower limit $S(1.266\,\mathrm{GHz}) = 10\,\mu\mathrm{Jy}$ may be biased up by confusion or biased down and missed entirely. We estimated the effects of confusion on the direct source counts by comparing the measured counts in the ten simulated images with their "true" input counts. Their differences in each flux-density bin were calculated individually for the ten simulations. We added the mean differences Δ in $\log[S^2 n(S)]$ from the simulations to the raw DEEP2 counts to yield more accurate counts of radio sources with $-5.0 < \log[S(\mathrm{Jy})] < -2.5$.

Table 3.5 shows the $\nu = 1.266\,\mathrm{GHz}$ corrected counts based on the 17,350 DEEP2 components with $S > 10\,\mu\mathrm{Jy}$ inside the half-power circle of the primary beam. For the 13 flux-density bins of width 0.2 in $\log(S)$, Column 1 lists the bin center $\log[S(\mathrm{Jy})]$

Table 3.5. DEEP2 1.266 GHz direct source counts

$\log[S(\mathrm{Jy})]$	N_{bin}	Δ	$\log[S^2 n(S)\,(\mathrm{Jy\ sr}^{-1})]$		
−4.90	5504	+0.054	2.730	+0.028	−0.029
−4.70	4460	+0.020	2.801	+0.017	−0.018
−4.50	3010	−0.022	2.788	+0.018	−0.019
−4.30	1998	−0.027	2.802	+0.020	−0.021
−4.10	1053	−0.034	2.716	+0.025	−0.027
−3.90	559	−0.035	2.639	+0.029	−0.031
−3.70	289	−0.028	2.563	+0.031	−0.034
−3.50	126	−0.012	2.423	+0.040	−0.044
−3.30	72	−0.011	2.366	+0.050	−0.057
−3.10	46	−0.005	2.393	+0.061	−0.072
−2.90	24	−0.006	2.305	+0.082	−0.102
−2.70	15	−0.001	2.317	+0.101	−0.132
−2.50	18	−0.009	2.587	+0.093	−0.119

and column 2 lists the number N_{bin} of sources in the bin. The corrections Δ in column 3 were added to the values of $\log[S^2 n(S)\,(\mathrm{Jy\,sr}^{-1})]$ in column 4. Columns 5 and 6 are the rms positive and negative uncertainties in $\log[S^2 n(S)]$. These uncertainties are the quadratic sum of the Poisson uncertainties in samples of size N_{bin}, the count correction uncertainties which we conservatively estimate to be $\Delta/2$, and a 3% overall flux-density scale uncertainty.

3.8 NVSS Source Counts

The NVSS catalog reports flux densities rounded to the nearest multiple of 0.1 mJy. For example, all NVSS components with fitted flux densities $2.45 \leq S(\mathrm{mJy}) < 2.55$ are listed as having $S = 2.5$ mJy. We separated the NVSS components into flux-density bins of nearly constant width 0.2 in $\log(S)$ whose exact boundaries S_{min} and S_{max} are midway between multiples of 0.1 mJy. Thus the lowest flux-density bin covers $2.45 \leq S(\mathrm{mJy}) < 3.95$ and includes all NVSS components listed with $S(\mathrm{mJy}) = 2.5, 2.6, 2.7, \ldots, 3.9$. The first column of Table 3.6 lists the bin centers, the second lists the numbers n_{bin} of components in each bin, and the third column shows the brightness-weighted counts $\log[S^2 n(S)]$ at $\log[S(\mathrm{Jy})] = -2.5, -2.3, \ldots, +1.3$. The fourth and fifth columns are the total rms uncertainties in $\log[S^2 n(S)]$.

Complex radio sources significantly more extended than the $45''$ FWHM NVSS restoring beam may be represented by two or more catalog components, and such large multicomponent sources are more common at flux densities $S \gtrsim 1$ Jy. To estimate the fraction of components comprising strong extended sources, we compared the NVSS component catalog with the low-resolution 1.4 GHz Bridle et al. (1972) catalog of 424 sources having $S \geq 1.7$ Jy and equivalent angular diameters $\phi \lesssim 10'$ in the area defined by $-5° < \delta < +70°$, $|b| > 5°$. We combined NVSS components within $\sim 5'$ of each Bridle et al. (1972) source, after excluding those that appeared to be unrelated background sources. In the six flux-density bins centered on $\log[S(\mathrm{Jy})] = +0.3$ through $+1.3$, grouping NVSS components into sources changed the brightness-weighted source count $\log[S^2 n(S)(\mathrm{Jy\ sr}^{-1})]$ by -0.013, $+0.013$, $+0.109$, $+0.193$, $+0.133$, and 0.000, respectively.

The differential source count $n(S)$ is a rapidly declining function of flux density, so simply counting the number of sources in each fairly wide flux-density bin throws away flux-density information and can bias the resulting estimate of $n(S)$. If $n(S)\,dS$ is the number of sources per steradian with flux densities between S and $S + dS$ and $\eta(S)\,d\ln(S)$ is the number per steradian with flux densities between S and $S + d\ln(S)$, then $n(S)dS = \eta(S)\,d\ln S$ and $n(S) = \eta(S)/S$. We added the flux density of each source into its bin of logarithmic width $\Delta \approx \mathrm{dex}(0.2)$ to calculate the more nearly constant quantity

$$S^2 n(S) = S\eta(S) = \left[\frac{1}{\Omega \ln(\Delta)}\right] \sum_{i=1}^{n_{\mathrm{bin}}} S_i \tag{3.23}$$

directly.

Finally, counts in the faintest bins must be corrected for population-law bias (Murdoch et al. 1973): faint sources outnumber strong sources, so noise moves more faint

Table 3.6. NVSS 1.4 GHz source counts

$\log[S(\mathrm{Jy})]$	N_{bin}	$\log[S^2 n(S)\,(\mathrm{Jy\ sr^{-1}})]$		
−2.50	350531	2.475	+0.030	−0.030
−2.30	217350	2.498	+0.019	−0.019
−2.10	161525	2.598	+0.015	−0.015
−1.90	120302	2.676	+0.014	−0.014
−1.70	90072	2.743	+0.013	−0.013
−1.50	63706	2.793	+0.013	−0.013
−1.30	43803	2.831	+0.013	−0.013
−1.10	29035	2.849	+0.013	−0.013
−0.90	18094	2.844	+0.013	−0.013
−0.70	10891	2.822	+0.013	−0.013
−0.50	5950	2.757	+0.014	−0.014
−0.30	3089	2.670	+0.015	−0.015
−0.10	1477	2.551	+0.017	−0.017
+0.10	718	2.434	+0.021	−0.021
+0.30	303	2.247	+0.028	−0.028
+0.50	143	2.137	+0.038	−0.038
+0.70	51	1.995	+0.080	−0.080
+0.90	15	1.739	+0.140	−0.140
+1.10	6	1.523	+0.214	−0.229
+1.30	3	1.285	+0.295	−0.341

sources into a bin than it moves strong sources out. We used their Table 2 and the cumulative source-count approximation $N(>S) \equiv \int_S^\infty n(S)\,dS \propto S^{-1}$ for $S \gtrsim 2.5$ mJy to calculate the required corrections to $\log[S^2 n(S)]$. They are −0.030, −0.012, and −0.004 in bins centered on $\log[S(\mathrm{Jy})] = -2.5$, −2.3, and −2.1, respectively.

The rms statistical uncertainty in $S^2 n(S)$ for each bin with $n_{\mathrm{bin}} \gg 1$ is

$$\sigma_{\mathrm{stat}} \approx \left[\frac{1}{\Omega \ln(\Delta)}\right] \left(\sum_{i=1}^{n_{\mathrm{bin}}} S_i^2\right)^{1/2} . \qquad (3.24)$$

There are only $n_{\rm bin} = 6$ sources in the $\log[S(\rm Jy)] = +1.1$ bin and $n_{\rm bin} = 3$ sources in the $\log[S(\rm Jy)] = +1.3$ bin, so we replaced their rms statistical errors in $\log[S^2 n(S)]$ by the Gehrels (1986) 84% confidence-level errors $+0.203, -0.219$ and $+0.295, -0.341$, respectively. To these statistical uncertainties we added quadratically the 3% error in $S^2 n(S)$ caused by the 3% NVSS flux-density scale uncertainty (Condon et al. 1998) and systematic uncertainties equaling half the corrections for component grouping and population-law bias.

3.9 Discussion

Figure 3.12 shows our 1.4 GHz differential source counts with traditional static-Euclidean weighting $S^{5/2} n(S)$ and with brightness weighting $S^2 n(S)$. Counts from $S = 0.25\,\mu$Jy to $S = 10\,\mu$Jy were derived statistically from the DEEP2 confusion $P(D)$ distribution extracted from solid angle $\Omega = 0.061\,\rm deg^2$. Individual sources uniformly covering solid angle $\Omega = 1.04\,\rm deg^2$ between $10\,\mu$Jy and $2.5\,\mu$Jy were counted directly, as were NVSS sources above 2.5 mJy in solid angle $\Omega = 7.016\,$sr (0.56 of the sky). Together these counts span the eight decades in flux density from $\log[S(\rm Jy)] = -6.6$ to $\log[S(\rm Jy)] = +1.4$. Their largest fractional uncertainties are caused by the rms noise $\sigma_{\rm n} = 0.57 \pm 0.01\,\mu\rm Jy\,beam^{-1}$ and finite resolution $\theta_{1/2} = 7\farcs6$ just above $S = 0.25\,\mu$Jy, by statistical fluctuations in the small numbers of sources in the DEEP2 half-power circle between 0.5 mJy and 2.5 mJy, and by cosmic variance in the NVSS counts above $S \approx 3$ Jy.

Figure 3.13 compares our 1.4 GHz direct counts (black points) of sources fainter than 10 mJy with those of Hopkins et al. (2003) (red triangles), Prandoni et al. (2018) (filled red points), Heywood et al. (2020) (open red points), plus the Smolčić et al. (2017) (filled blue points) and Van der Vlugt et al. (2020) (blue triangles) 3 GHz counts converted to 1.4 GHz assuming the median spectral index is $\langle\alpha\rangle = -0.7$. The Smolčić et al. (2017) counts have small ($\sigma \sim 10\%$) uncertainties because they are based on the large (10,830 sources) noise-limited (median $\sigma_{\rm n} = 2.3\,\mu$Jy beam at 3 GHz) VLA-COSMOS catalog. They are $\sim 20\% \sim 2\sigma$ lower than most other counts

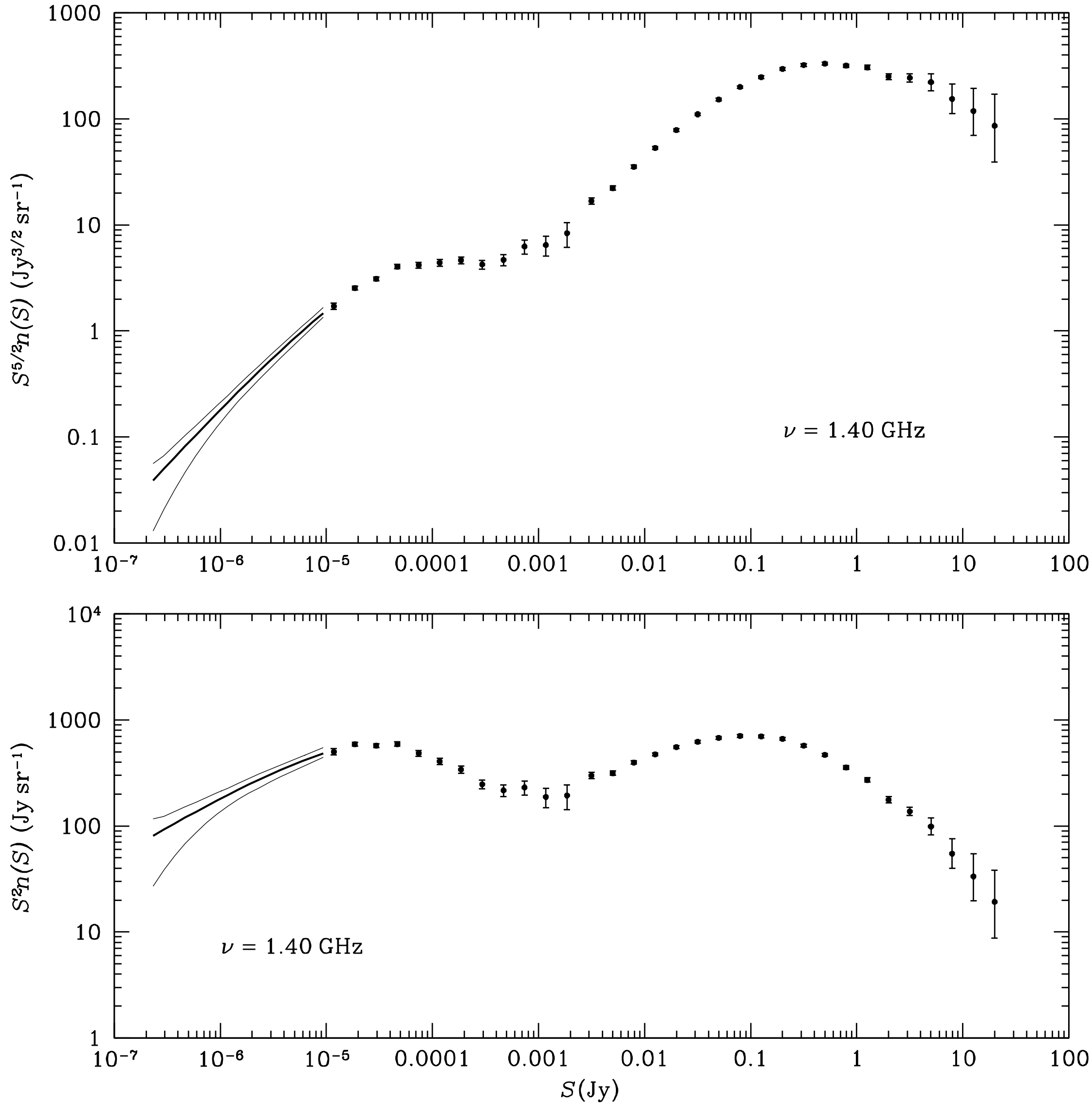

Figure 3.12. Our 1.4 GHz differential source counts between $0.25\,\mu$Jy and 25 Jy are shown with both the traditional static Euclidean normalization $S^{5/2}n(S)$ (top panel) and the brightness-weighted normalization $S^2n(S)$ (bottom panel). The heavy curve and light $\pm 1\,\sigma$ error curves from $S = 2.5 \times 10^{-7}$ Jy to 10^{-6} Jy are statistical counts derived from the DEEP2 confusion $P(D)$ distribution (Section 3.6). The black data points and their $\pm 1\,\sigma$ error bars show the 1.4 GHz DEEP2 source counts between $S = 10^{-5}$ Jy and $S = 0.0025$ Jy (Section 3.7) plus the NVSS counts (Section 3.8) at higher flux densities.

and $\sim 30\%$ lower than the Van der Vlugt et al. (2020) counts, possibly because resolution corrections for the small ($\theta_{1/2} = 0\farcs75$) VLA COSMOS beam were insufficient or the median spectral index of μJy sources is more negative than the assumed -0.7. In any case, the agreement among all of these μJy source counts is much better than other counts have agreed in the recent past (Heywood et al. 2013), suggesting that the large earlier discrepancies were caused by observational and analysis errors, not by surprisingly strong source clustering.

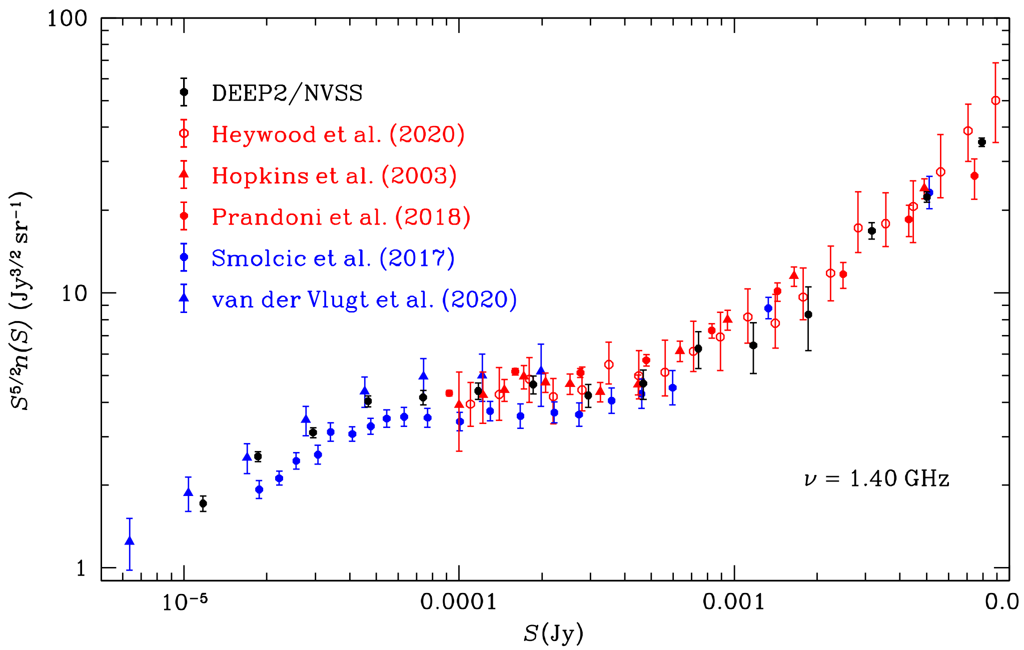

Figure 3.13. The 1.4 GHz differential source counts between $10\,\mu$Jy and 10 mJy are shown with the traditional static Euclidean normalization $S^{5/2}n(S)$. The black data points show the DEEP2 source counts below $S = 0.0025$ Jy (Section 3.7) and the NVSS counts (Section 3.8 at higher flux densities. The red data points are 1.4 GHz counts from Heywood et al. (2020) (open circles), Hopkins et al. (2003) (solid triangles), and Prandoni et al. (2018) (filled circles). The blue data points are based on the Smolčić et al. (2017) and the Van der Vlugt et al. (2020) 3 GHz counts converted to 1.4 GHz with a spectral index $\alpha = -0.7$.

3.9.1 Resolving the AGN and SFG backgrounds

The 1.4 GHz brightness-weighted counts $S^2 n(S)$ shown in Figure 3.12 have two broad peaks. The peak $S \sim 0.1$ Jy is dominated by AGNs and the peak at $S \sim 3 \times 10^{-5}$ Jy by SFGs. If the counts below $S = 0.25\,\mu$Jy do not exceed the extrapolation with slope $d\log[S^2 n(S)]/d\log(S) = +0.5$, sources stronger $S = 0.25\,\mu$Jy resolve $> 99\%$ of the AGN contribution $\Delta T_{\mathrm{b}} \approx 0.06$ K to the sky brightness temperature and $> 96\%$ of the $\Delta T_{\mathrm{b}} \approx 0.04$ K SFG contribution. Thus most of the stars in the universe were formed in SFGs stronger than $0.25\,\mu$Jy. For example, our fairly typical Galaxy currently has 1.4 GHz spectral luminosity $L_\nu \approx 2.5 \times 10^{21}$ W Hz^{-1}. With $10\times$ luminosity evolution (Madau & Dickinson 2014), it would be a $1.2\,\mu$Jy source around "cosmic noon" at $z \sim 2$ and a $0.25\,\mu$Jy source even at $z = 4$.

3.9.2 $P(D)$ limits on "new" source populations

The MeerKAT correlation interferometer used to make the DEEP2 image does not respond to backgrounds smooth on angular scales $\gg \theta_{1/2} = 7''.6$, and the resolution of ARCADE 2 is too coarse to detect individual $< 0.1\,\mu$Jy sources, so there is actually no *observational* tension between our results in Section 3.9.1 and the ARCADE 2 background. However, the DEEP2 $P(D)$ distribution can set a lower limit to the *number* of faint sources not much larger than $\theta_{1/2} = 7''.6 \approx 50$ kpc in the redshift range $0.5 < z < 5$ that can produce a $\Delta T_{\mathrm{b}} \sim 0.4$ K background smooth enough to be consistent with the DEEP2 $P(D)$ distribution. Very numerous faint sources contribute a nearly Gaussian $P(D)$ distribution similar to the instrumental noise distribution. A source population with rms confusion not much larger than $\sigma_{\mathrm{c}} \approx (0.58^2 - 0.57^2)^{1/2}\,\mu$Jy beam^{-1} $\sim 0.1\,\mu$Jy beam^{-1} is consistent with the uncertainty in the measured DEEP2 rms noise. Figure 3.14 plots the brightness-weighted source counts $S^2 n(S)$ as a function of $\log(S)$. The two broad peaks corresponding to star-forming galaxies and AGN are well represented by the approximation (Condon et al.

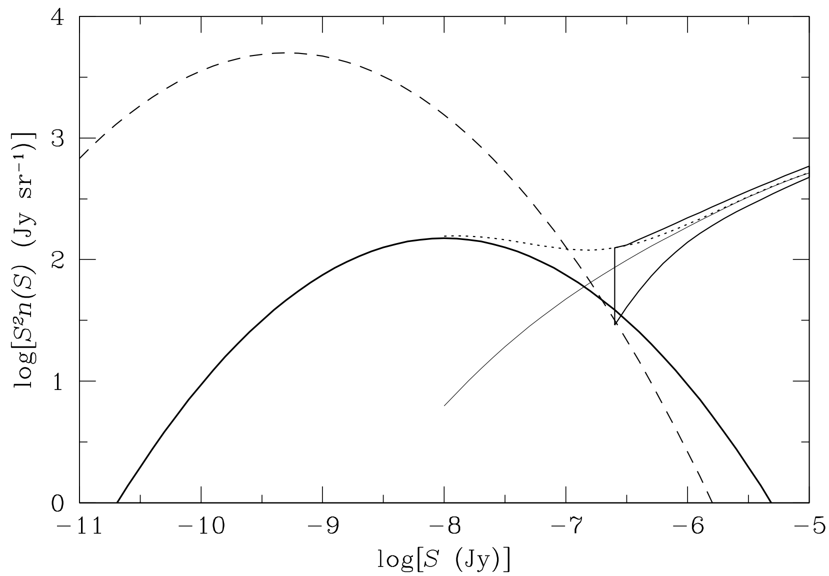

Figure 3.14. Source counts at 1.4 GHz consistent with the DEEP2 $P(D)$ distribution are shown by the thin black line surrounded by its $\pm 1\sigma$ error region. A hypothetical new population with logarithmic FWHM $\phi = 2$ and $A = 150$ located at $\log(S_{\rm pk}) = -8$ (thick black parabola) is consistent with DEEP2, but it contributes only 10 mK to the radio source background. A hypothetical population contributing the necessary 0.4 K to agree with the background measured by ARCADE 2 must have $A \approx 5000$ and $S^2n(S)$ peaking at $S_{\rm pk} \leq 0.5$ nJy (black dashed parabola) to remain consistent with our DEEP2 $P(D)$ observation.

2012) $\log[S^2n(S)] \approx a - b[\log(S) - \log(S_{\rm pk})]^2$ or

$$S^2n(S) \approx A \exp\left\{-4\ln(2)\frac{[\log(S) - \log(S_{\rm pk})]^2}{\phi^2}\right\}, \tag{3.25}$$

where ϕ is the logarithmic FWHM and $S_{\rm pk}$ is the flux density of the $S^2n(S)$ peak; $\log(S_{\rm pk}) \sim -5$ and $\log(S_{\rm pk}) \sim -1$ for SFGs and AGNs, respectively, while both populations are well described by $\phi = 2$. Inserting Equation 3.25 into Equation 3.1 and integrating over flux density determines the peak amplitude A for FWHM ϕ for a new population adding $\Delta T_{\rm b}$ to the total sky brightness:

$$A\phi = \frac{4k_{\rm B}\nu^2}{\ln(10)c^2}\left[\frac{\ln(2)}{\pi}\right]^{1/2}\Delta T_{\rm b}. \tag{3.26}$$

Equation 3.26 is valid for any count peak flux density S_{pk}. Because ΔT_{b} fixes the product $A\phi$, a new population with T_{b} either has a small number of sources N with a narrow FWHM ϕ but large amplitude A, or a broad peak ϕ with a larger number of sources per square arcmin and a fainter peak flux density.

The known AGN and SFG populations are well characterized by Gaussians of FWHM $\phi = 2$, so we assumed $\phi = 2$ for the hypothetical new population. In order to explain the excess $\Delta T_{\mathrm{b}} = 0.4\,\mathrm{K}$, the amplitude of this population must be $A \sim 5000\,\mathrm{Jy\,sr^{-1}}$.

For any S_{pk} we can find the maximum value of A that is consistent with the DEEP2 $P(D)$. Inserting a new population of sources with $\phi = 2$ and $\log(S_{\mathrm{pk}}) = -8$, we ran DEEP2 image simulations starting at $\log[S(\mathrm{Jy})] = -10$ for increasing values of A in steps of 10 from $A = 0$. They were repeated for $\langle\sigma_{\mathrm{n}}\rangle = 0.56\,\mu\mathrm{Jy\,beam^{-1}}$ and $0.58\,\mu\mathrm{Jy\,beam^{-1}}$ in addition to the measured rms noise averaged throughout the $P(D)$ region of radius $500''$, $\langle\sigma_{\mathrm{n}}\rangle = 0.57\mu\mathrm{Jy\,beam^{-1}}$. Having run a minimum of 50 iterations, we determined the χ^2 value of each simulated $P(D)$ distribution (containing the new population of amplitude A) to the observed $P(D)$. The value of A such that 16% of the simulations had $\chi^2 < \chi_0^2$ is the 1σ upper limit to the amplitude A that is consistent with our observed $P(D)$.

For rms noise values $\sigma_n = 0.56$ and $0.57\,\mu\mathrm{Jy\,beam^{-1}}$ the maximum amplitude consistent with the observed DEEP2 $P(D)$ distribution is $A \approx 65$. Simulations assuming rms noise $\sigma_{\mathrm{n}} = 0.55\,\mu\mathrm{Jy\,beam^{-1}}$ allow $A < 150$. The final 1σ upper bound on the counts of nJy sources is the combination of Equation 3.13 and the curve representing the sum of the new population and the measured counts from DEEP2 (dotted curve in Figure 3.14).

Figure 3.14 shows the brightness-weighted source counts for the hypothetical population with $A = 150, \phi = 2$, and $S_{\mathrm{pk}} = 10\,\mathrm{nJy}$ as the thicker black curve. That new population adds only $\Delta T_{\mathrm{b}} \sim 0.01\,\mathrm{K}$ to the total radio source background at 1.4 GHz, yet it must contain at least 3,000 sources per arcmin^2, exceeding by a factor of 30 the sky density of galaxies brighter than $m_{\mathrm{AB}}+29$, the magnitude of the Large Magellanic Cloud at redshift $z = 2$) in the Hubble Ultra Deep Field (Beckwith et al. 2006).

A hypothetical new population contributing the full 0.4 K ARCADE 2 excess background is consistent with the narrow DEEP2 $P(D)$ distribution only if $\log(A) \approx 3.7$, the sources are randomly distributed on the sky, and $S_{\mathrm{pk}} < 0.5\,\mathrm{nJy}$ at 1.4 GHz. as indicated by the dashed parabola in Figure 3.14). This upper limit to S_{pk} is a factor of ten lower than the Condon et al. (2012) limit and more strongly excludes any bright population of numerous faint sources that cluster like galaxies or parts of galaxies.

3.10 Conclusions

In this work, we presented source counts in the eight decades of flux density from $S = 0.25\,\mu\mathrm{Jy}$ to $S = 25\,\mathrm{Jy}$ using the MeerKAT DEEP2 field and archival NVSS data.

- Statistical source counts betwen $S = 0.25\,\mu\mathrm{Jy}$ and $S = 10\,\mu\mathrm{Jy}$ (Section 3.6) were estimated from the confusion $P(D)$ distribution within $500''$ of the DEEP2 pointing center. Simulations of the radio sky were developed and used to constrain the counts and their uncertainties.
- We constructed a uniformly sensitive catalog of $\approx 17,000$ discrete sources stronger than $S = 10\,\mu\mathrm{Jy}$ at 1.266 GHz in $\Omega_{1/2} = 1.04\,\mathrm{deg}^2$ (Section 3.7) and used it to count discrete sources in the flux-density range $10\,\mu\mathrm{Jy} \leq S < 2.5\,\mathrm{mJy}$ (Section 3.7.4).
- The NVSS catalog of radio source components was used to determine 1.4 GHz source counts between $S = 2.5\,\mathrm{mJy}$ and $S = 25\,\mathrm{Jy}$ in $\Omega \approx 7.016\,\mathrm{sr}$. (Section 3.8).

We find good agreement with previously published 1.4 GHz counts, but report higher source counts (at the 2σ level) than previously published 3 GHz counts from the VLA-COSMOS catalog. The agreement among all μJy source counts is much improved from past studies.

Sources stronger than our lower limit of $S = 0.25\,\mu\mathrm{Jy}$ resolve $> 99\%$ of the AGN contribution and $> 96\%$ of the SFG contribution to the sky brightness temperature.

The maximum source count amplitude for a hypothetical "new" population explaining the ARCADE 2 excess radio background is $\log(A) \approx 3.7$, and the peak of the distribution must be fainter than $S_{\rm pk} \sim 0.5\,{\rm nJy}$ to remain consistent with the DEEP2 $P(D)$ distribution. In a second paper (Matthews et al., in prep) we will use the results from this paper to estimate the star formation history of the Universe.

Chapter 4

Star Formation History of the Universe at 1.4 GHz

4.1 Preface

Previous measurements of the evolution of the SFRD have relied on IR and UV data, which suffer from dust extinction that reaches its worst at the peak of star formation. These measurements show that the SFRD rose rapidly during the first ~ 3 billion years after the big bang, reached an apex at a redshift of $z \approx 2$—"cosmic noon", and has been declining exponentially since. Radio source counts down to faint flux densities $S < 1\,\mu$Jy probe SFRs of normal galaxies responsible for building the bulk of the stellar mass in the universe and do not suffer from dust extinction. In this chapter, we model the evolutionary functions that when applied to the local luminosity function accurately predict the observed source counts. We derive an updated, robust, sub-linear FIR/radio correlation and apply it to the evolutionary models to constrain the evolution of the SFRD $\psi(z)$. The remainder of this chapter was accepted for publication in the *Astrophysical Journal* (Matthews et al. 2021b).

4.2 Abstract

We matched the 1.4 GHz local luminosity functions of star-forming galaxies (SFGs) and active galactic nuclei to the 1.4 GHz differential source counts from 0.25 μJy to 25 Jy using combinations of luminosity and density evolution. We present the most robust and complete local far-infrared (FIR)/radio correlation to date in a volume-limited sample of $\approx 4.3 \times 10^3$ nearby SFGs, finding that it is very tight but distinctly sub-linear: $L_{\rm FIR} \propto L_{1.4\,\rm GHz}^{0.85}$. If the local FIR/radio correlation does not evolve, the evolving 1.4 GHz luminosity function of SFGs yields the evolving star-formation rate density (SFRD) $\psi(M_\odot\,\rm yr^{-1}\,Mpc^{-3})$ as a function of time since the big bang. The SFRD measured at 1.4 GHz grows rapidly at early times, peaks at "cosmic noon" when $t \approx 3$ Gyr and $z \approx 2$, and subsequently decays with an e-folding time scale $\tau = 3.2$ Gyr. This evolution is similar to, but somewhat stronger than, SFRD evolution estimated from UV and FIR data.

4.3 Introduction

Fundamental to our understanding of galaxy evolution, reionization of the universe, and heavy element production is an evolutionary timeline of the cosmic star formation rate density (SFRD). In the 1990s, it was first suggested that star-formation activity at redshift $z \sim 1$ dwarfed that at $z \sim 0$ (e.g. Songaila et al. 1994; Ellis et al. 1996; Lilly et al. 1996). In the decades since, star-forming galaxies have been detected out to increasing redshifts, most recently $z \gtrsim 10$ (e.g. Coe et al. 2013; Oesch et al. 2016), well within the reionization era. Compilations of SFR measurements made at various redshifts informs our understanding of SFRD evolution (see Hopkins & Beacom 2006; Madau & Dickinson 2014, for reviews of the topic). Virtually all SFR diagnostics are sensitive to massive stars only; an initial mass function (IMF) must be assumed to tally the total stellar mass formed at a given time. Possible variations in the IMF within and among galaxies and redshifts remains a source of uncertainty.

Most extragalactic radio sources fainter than $S \approx 0.4$ mJy at 1.4 GHz are distant star-forming galaxies (SFGs), while stronger sources are primarily radio galaxies or quasars powered by active galactic nuclei (AGNs) (Prandoni et al. 2001; Smolčić et al. 2008; Condon et al. 2012; Vernstrom et al. 2016). The 1.4 GHz continuum emission from SFGs is a combination of synchrotron radiation from electrons accelerated in the supernova remnants of short-lived ($\tau \leq 3 \times 10^7$ yr) massive ($M > 8 M_\odot$) stars plus thermal bremsstrahlung from HII regions ionized and heated by even more massive stars (Condon 1992). The cosmic-ray electrons responsible for the synchrotron radiation dominating the 1.4 GHz continuum emission eventually diffuse throughout their host galaxy and cool on timescales $\tau_{\rm cool} \sim 5$ Myr (for a spiral galaxy that stopped forming stars after a single episode; Murphy et al. 2008). The combined lifetimes of such massive stars with the cooling timescale of cosmic-ray electrons are much less than the age of the universe, so the radio continuum luminosities of SFGs depend only on their current star-formation rates uncontaminated by older stellar populations. Although the radio continuum luminosity is only a tiny fraction of the total power emitted by massive stars, its tight correlation with the energetically dominant far-infrared (FIR) emission from dust heated by massive stars justifies the use of radio emission as a quantitative tracer of star formation in galaxies (Condon 1992).

Stars with masses $M \gtrsim 8 M_\odot$ emit primarily in the ultraviolet (UV) continuum. The rest frame wavelength range 1400 Å to 1700 Å is accessible to ground-based telescopes for galaxies with redshifts $z \gtrsim 1.4$, but the UV emission of nearby galaxies must be measured either at longer UV wavelengths or from space. The contribution from longer-lived ($\tau \sim 250$ Myr) radio-quiet stars increases at longer UV wavelengths. The biggest downside for UV emission as a tracer of the SFR is dust obscuration. At redshifts $z \sim 2$, dust attenuation measured via infrared/UV luminosity ratios $L_{\rm IR}/L_{\rm UV}$ implies that >80% of star formation is obscured (Reddy et al. 2012; Howell et al. 2010), resulting in a small UV contribution to the total SFRD.

The UV energy absorbed by dust grains is reemitted at mid-infrared (MIR) and far-infrared (FIR) wavelengths, making MIR and FIR luminosities practical SFR indicators (in the case of minimal contribution from diffuse dust). Although FIR ($42.5 - 122.5\,\mu$m; Helou et al. 1988) dust extinction is low, the infrared spectrum (spanning $\lambda = 8 - 1000\,\mu$m) of a galaxy is complex. The fraction of UV luminosity absorbed by dust depends on the metallicity and geometry of the dust distribution, and the dust emission at wavelengths longer than $\lambda \sim 100\,\mu$m in the source frame is powered primarily by evolved stars (e.g. Hirashita et al. 2003; Bendo et al. 2010). At MIR wavelengths, emission from warm dust is tightly correlated with star formation, but polycyclic aromatic hydrocarbons (PAHs) complicate the emission spectrum near $\lambda = 8\,\mu$m and active galactic nuclei (AGNs) dilute these PAH features while also contributing significantly to the $24\,\mu$m continuum emission. Luminous infrared galaxies (LIRGS) with $L_{\rm IR} > 10^{11} L_\odot$ and ultra-luminous infrared galaxies (ULIRGS) with $L_{\rm IR} > 10^{12} L_\odot$ are rare today but were responsible for most of the luminosity density during the $z \sim 2$ "cosmic noon" (Magnelli et al. 2011) when most stars were formed. The MIR emission due solely to star formation must be disentangled from the total MIR emission before converting to a SFR to ensure a correct result.

The cosmic history of star formation can be constrained by a combination of the 1.4 GHz local luminosity function and the differential numbers $n(S)dS$ of faint radio sources per steradian with flux densities between S and $S + dS$. A very low 1.4 GHz detection limit $S = 0.25\,\mu$Jy is needed to reach SFRs of evolving "normal" galaxies like the Milky Way: $5\,M_\odot\,{\rm yr}^{-1}$ at $z = 2$, $12\,M_\odot\,{\rm yr}^{-1}$ at $z = 3$, and $22\,M_\odot\,{\rm yr}^{-1}$ at $z = 4$ (assuming a Salpeter IMF). Thus the top continuum science goal of the proposed Square Kilometre Array SKA1-MID is "Measuring the Star-formation History of the Universe" using the proposed "Ultra Deep Reference Survey" to count sources as faint as $S = 0.25\,\mu$Jy in a solid angle $\Omega \approx 1\,{\rm deg}^2$ (Prandoni & Seymour 2015). Recently Condon et al. (2019) measured the 1.4 GHz local ($z < 0.1$) radio luminosity functions of SFGs and AGNs from sources in the 1.4 GHz NRAO VLA Sky Curvey (Condon et al. 1998, NVSS) cross-identified with 2MASX galaxies (Jarrett et al. 2000). Matthews et al. (2021) determined accurate 1.4 GHz brightness-weighted source counts $S^2 n(S)$ over the eight decades of flux density between $S = 0.25\,\mu$Jy and $S = 25$ Jy using the very sensitive $\nu = 1.266$ GHz MeerKAT DEEP2 sky image (Mauch et al. 2020) for sources counts below $S = 2.5$ mJy, and the 1.4 GHz NVSS catalog above $S = 2.5$ mJy (see Matthews et al. (2021) for details).

In this paper we present the cosmic star-formation history derived from only (1) the 1.4 GHz local luminosity function, (2) the local volume-limited FIR/radio correlation, and (3) the 1.4 GHz counts of sources as faint as $S = 0.25\,\mu$Jy. We do not need to "stack" radio sources to achieve the required sensitivity, so we do not depend on a complete sample of optically selected galaxies with measured redshifts and do not discriminate against galaxies so obscured by dust that they drop out of optical samples. The faintest radio sources were detected statistically via their confusion $P(D)$ distribution, so we actually cannot optically identify them or measure their redshifts. Instead, their radio evolution is constrained entirely by matching features in the local luminosity function to features in the source counts. This independent approach complements the traditional methods reviewed by Madau & Dickinson (2014).

Section 4.4 reviews and updates the 1.4 GHz local luminosity functions of SFGs and AGNs derived from a spectroscopically complete sample of $\sim 10^4$ 2MASX (Jarrett et al. 2000) galaxies brighter than $k_{\rm 20fe} = +11.75$ at $\lambda = 2.2\,\mu$m and stronger than $S = 2.5$ mJy at $\nu = 1.4$ MHz. Basic equations relating the evolving 1.4 GHz luminosity functions and spectral-index distributions to the counts of distant sources in the flat ΛCDM universe are introduced in Section 4.5. The non-evolving model source counts are discussed in Section 4.6 to highlight the features that evolutionary models must have to fit the 1.4 GHz data. Models for the radio evolution of both AGNs and SFGs that successfully match their evolving luminosity functions to the 1.4 GHz source counts are presented in Section 4.7. We calculated an improved local FIR/radio correlation using a large volume-limited sample of SFGs in our 2MASX sample and found it to be a slightly nonlinear power law: $L_{\rm FIR} \propto L_{\rm 1.4\,GHz}^{0.85}$. We used this local FIR/radio correlation to convert the evolving 1.4 GHz SFG luminosity functions into FIR star-formation rate densities (SFRDs) and to make an independent estimate of the cosmic history of star formation (Section 4.8). Section 4.9 summarizes and evaluates these results.

Absolute quantities were calculated for the flat ΛCDM universe with $H_0 = 70\,{\rm km\,s^{-1}\,Mpc^{-1}}$ and $\Omega_{\rm m} = 0.3$. Our spectral-index sign convention is $\alpha \equiv +d\ln S/d\ln\nu$. The Salpeter (1955) IMF was used to calculate total star-formation rates in terms of

$M_\odot\,\mathrm{yr}^{-1}$. These rates should be multiplied by 0.61 for the Chabrier (2003) IMF or by 0.66 for the Kroupa (2001) IMF.

4.4 Local 1.4 GHz Luminosity Functions

The evolving spectral luminosity function $\rho(L_\nu|z)dL_\nu$ specifies the comoving number density of sources at redshift z having absolute spectral luminosities L_ν to $L_\nu + dL_\nu$ at frequency ν. The corresponding density of sources per decade of spectral luminosity is

$$\rho_{\mathrm{dex}}(L_\nu|z) = \ln(10) L_\nu \rho(L_\nu|z) \ . \tag{4.1}$$

Sources with this luminosity function produce a comoving spectral power density per decade of luminosity

$$u_{\mathrm{dex}}(L_\nu|z) \equiv L_\nu\, \rho_{\mathrm{dex}}(L_\nu|z) \ . \tag{4.2}$$

We call u_{dex} the energy-density function because spectral power density has the same dimensions as energy density (SI units $\mathrm{W\,Hz^{-1}\,m^{-3}} = \mathrm{J\,m^{-3}}$). Astronomically practical units for u_{dex} are $\mathrm{W\,Hz^{-1}\,dex^{-1}\,Mpc^{-3}}$.

The local 1.4 GHz energy-density functions $u_{\mathrm{dex}}(L_\nu|0)$ of radio sources powered primarily by active galactic nuclei (AGNs) or by star-forming galaxies (SFGs) were determined separately (Condon et al. 2019) and are shown by the data points and error bars in Figure 4.1. These local 1.4 GHz energy-density functions were determined from a large sample ($N \sim 1 \times 10^4$) of radio sources in the NVSS catalog covering $\Omega = 7.016$ sr of sky and cross-identified with $\lambda = 2.16\,\mu$m galaxies in the 2MASX. All 9517 sources have spectroscopic redshifts, and radio sources powered primarily by AGNs were separated from those powered by SFGs using the following radio and infrared diagnostics: (1) an *IRAS* FIR/NVSS 1.4 GHz flux-density ratio $q < 1.8$, (2) a FIR spectral index $\alpha(25\,\mu\mathrm{m}, 60\,\mu\mathrm{m} > -1.25$, (3) have *WISE* colors $W1 - W2 > 0.8$ for $(W2 - W3 \geq 3.1)$ and $W1 - W2 > (W2 - W3 - 1.82)/1.6$ for $(W2 - W3 > 3.1$, and (4) showed a radio morphology with multiple components (e.g. jets, lobes in the case of resolved NVSS sources). The median redshift (corrected for the local flow due to nearby galaxy clusters) is $\langle z \rangle \approx 0.02$ for the SFG sample ($N = 6699$) and $\langle z \rangle \approx 0.04$ for the AGNs ($N = 2763$). For further details on the derivation of these energy-density functions, we refer the reader to Condon et al. (2019). For computational convenience, we approximate the AGN energy-density function by

$$u_{\rm dex}(L_\nu|0) = \frac{C_{\rm a} L_\nu}{(L_\nu/L^*_{\rm a})^\alpha + (L_\nu/L^*_{\rm a})^\beta + (L_\nu/L_{\rm min})^\gamma} \tag{4.3}$$

with comoving density factor $C_{\rm a} = 2.0 \times 10^{-6}\,{\rm Mpc^{-3}\,dex^{-1}}$, AGN high-luminosity turnover spectral luminosity $L^*_{\rm a} = 2.0 \times 10^{25}\,{\rm W\,Hz^{-1}}$, low-luminosity downturn luminosity $L_{\rm min} = 1.0 \times 10^{11}\,{\rm W\,Hz^{-1}}$, intermediate-luminosity power-law slope $\alpha = 0.55$, high-luminosity power-law slope $\beta = 1.9$, and low-luminosity downturn slope $\gamma = -0.25$. This function is shown by the red curve in Figure 4.1. Its parameters are highly correlated, so their values and their uncertainties have limited physical significance. However, the uncertainty of β is especially large because there are few AGNs with $L_\nu > L^*_{\rm a}$ and redshifts $z < 0.1$.

The tight FIR/radio correlation implies that the radio and FIR luminosity functions of SFGs should have similar functional forms, so we followed the standard form established by Saunders et al. (1990) for the $\lambda = 60\,\mu$m luminosity function to write

$$u_{\rm dex}(L_\nu|0) = C_{\rm s} \left(\frac{L_\nu}{L^*_{\rm s}}\right)^{2-\alpha_{\rm s}} \exp\left[-\frac{1}{2\sigma^2}\log^2\left(1 + \frac{L_\nu}{L^*_{\rm s}}\right)\right] \tag{4.4}$$

with comoving density factor $C_{\rm s} = 3.50 \times 10^{-3}\,{\rm Mpc^{-3}\,dex^{-1}}$, turnover spectral luminosity $L^*_{\rm s} = 1.9 \times 10^{21}\,{\rm W\,Hz^{-1}}$, $\alpha_{\rm s} = 1.162$ for low-luminosity power-law slope $(2 - \alpha_{\rm s}) = +0.838$, and high-luminosity Gaussian taper with rms width $\sigma = 0.558$. Our value of $L^*_{\rm s}$ is close to the $L_\nu = 2.5 \times 10^{21}\,{\rm W\,Hz^{-1}}$ 1.4 GHz spectral luminosity of the Milky Way (Berkhuijsen 1984). The local energy-density function of SFGs is plotted as the blue curve in Figure 4.1, and the sum of the AGN and SFG local energy-density functions is indicated by the wider green curve.

The accessible volumes and hence numbers of galaxies with low 1.4 GHz luminosities used to calculate the local energy-density functions are limited primarily by the

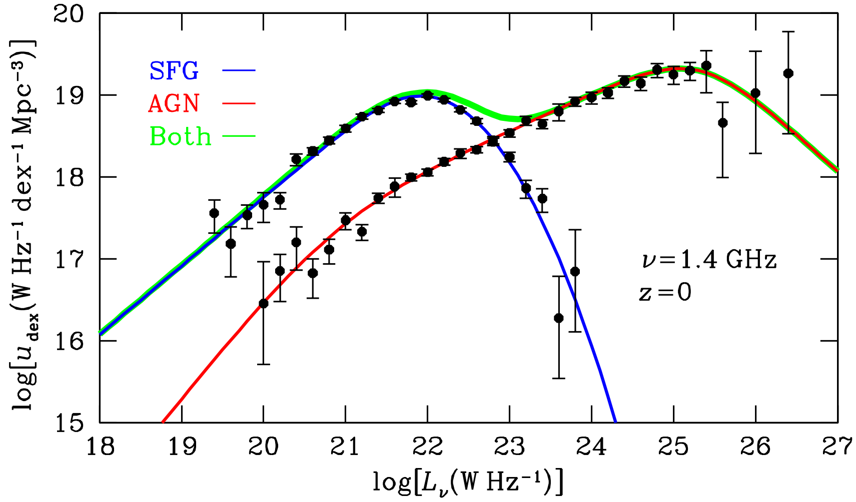

Figure 4.1. The measured local energy-density functions $u_{\rm dex}(L_\nu|0)$ at $\nu = 1.4\,\rm GHz$ are shown by the black data points. The red curve plots the Equation 4.3 fit for AGNs, the blue curve plots Equation 4.4 for SFGs, and the wider green curve is the sum of both.

$S \approx 2.5\,\rm mJy$ sensitivity limit of the NVSS catalog, so the statistical uncertainties in these energy-density functions increase for AGNs below $L_\nu \sim 10^{21}\,\rm W\,Hz^{-1}$ and for SFGs below $L_\nu \sim 10^{20}\,\rm W\,Hz^{-1}$.

4.5 Basic Equations

The differential source count $n(S)dS$ is the number of sources per steradian with flux densities between S and $S + dS$. Defining $\eta(S)d\log(S)$ as the number of sources per steradian per $\log(S)$ and substituting $dS = Sd\ln(S) = \ln(10)Sd\log(S)$ shows that $\ln(10)S^2n(S) = S\eta(S)$ is the flux density per steradian (a spectral brightness) per decade of flux density. Thus the Rayleigh-Jeans sky brightness temperature $dT_{\rm b}$ per decade of flux density contributed by sources is

$$\left[\frac{d\,T_{\rm b}}{d\log(S)}\right] = \left[\frac{\ln(10)\,c^2}{2k_{\rm B}\nu^2}\right] S^2 n(S)\ , \tag{4.5}$$

where $k_{\rm B} \approx 1.38 \times 10^{-23}\,{\rm J\,K^{-1}}$. We call $S^2 n(S)$ the brightness-weighted differential source count to distinguish it from the traditional static-Euclidean weighted count $S^{5/2} n(S)$.

In a flat ΛCDM universe, the total brightness-weighted count at frequency ν of sources with spectral index α can be written as the integral of $u_{\rm dex}(L_\nu|z)$ over redshift (Condon & Matthews 2018):

$$S^2 n(S) = \frac{D_{H_0}}{4\pi \ln(10)} \int_0^\infty u_{\rm dex}(L_\nu|z) \left[\frac{(1+z)^{\alpha-1}}{E(z)} \right] dz \ , \tag{4.6}$$

where $D_{H_0} \equiv c/H_0$ is the Hubble distance, $L_\nu = 4\pi D_{\rm C}^2 (1+z)^{1-\alpha} S$, $D_{\rm C}$ is the comoving distance to the source, and $E(z) = [\Omega_{\rm m}(1+z)^3 + \Omega_\Lambda + \Omega_{\rm r}(1+z)^4]^{1/2}$.

It is instructive to rewrite Equation 4.6 in terms of lookback time $t_{\rm L}(z)$ by substituting the relations (Condon & Matthews 2018)

$$dD_{\rm C} = D_{H_0} \frac{dz}{E(z)} = (1+z) c \, dt_{\rm L} \tag{4.7}$$

to yield

$$S^2 n(S) = \frac{c}{4\pi \ln(10)} \int_0^{t_{\rm L}(\infty)} u_{\rm dex}(L_\nu|z)(1+z)^\alpha dt_{\rm L} \, , \tag{4.8}$$

where $t_{\rm L}(z=\infty) \approx 0.964 H_0^{-1} \approx 13.47\,{\rm Gyr}$ is the current age of the universe. Equation 4.8 shows that the sources in any narrow range $\Delta t_{\rm L}$ of lookback time near redshift $z(t_{\rm L})$ contribute

$$\Delta[S^2 n(S)] \propto u_{\rm dex}(L_\nu|z)(1+z)^\alpha \Delta[t_{\rm L}(z)] \tag{4.9}$$

to the brightness-weighted source count. Thus in a plot of $S^2 n(S)$ versus $\log(S)$, the contribution to $S^2 n(S)$ by sources in each narrow time range $\Delta t_{\rm L}(z)$ mimics the evolving energy-density function attenuated by the factor $(1+z)^\alpha$.

Both the AGN and SFG source populations span a range of spectral indices α characterized by their redshift-dependent normalized spectral-index distributions $p(\alpha|z)$, so a more accurate version of Equation 4.6 is

$$S^2 n(S) = \frac{D_{H_0}}{4\pi \ln(10)} \times \int_{-\infty}^{\infty} \left\{ \int_0^{\infty} u_{\rm dex}(L_\nu|z) p(\alpha|z) \left[\frac{(1+z)^{\alpha-1}}{E(z)} \right] dz \right\} d\alpha \, . \tag{4.10}$$

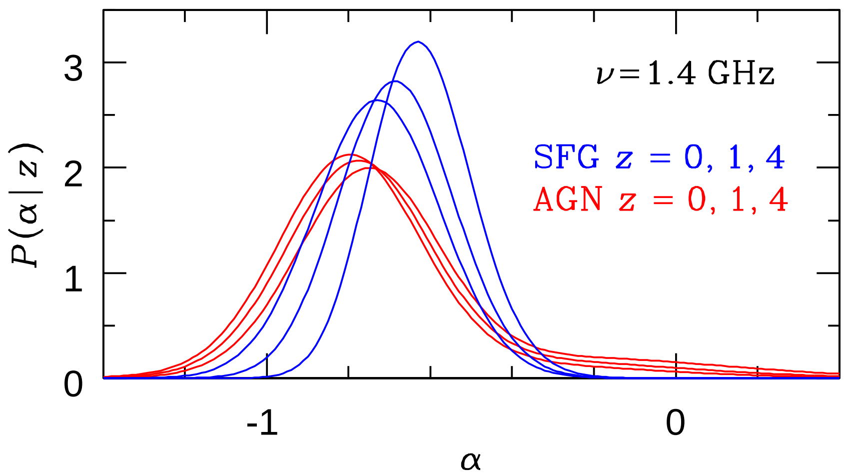

Figure 4.2. The 1.4 GHz normalized spectral-index distributions $P(\alpha|z)$ of SFGs (blue curves) and AGNs (red curves) for sources at redshifts $z = 0$, 1, and 4 (left to right).

The 1.4 GHz spectral-index distribution of nearby AGNs can by approximated by the the sum of two Gaussians representing the steep-spectrum and flat-spectrum source populations (Condon 1984):

$$p_{\rm a}(\alpha|0) = \left(\frac{A_{\rm steep}}{\sqrt{2\pi}\sigma_{\rm steep}} \right) \exp\left[-\frac{(\alpha - \bar{\alpha}_{\rm steep})^2}{2\sigma^2_{\rm steep}} \right] + \left(\frac{A_{\rm flat}}{\sqrt{2\pi}\sigma_{\rm flat}} \right) \exp\left[-\frac{(\alpha - \bar{\alpha}_{\rm flat})^2}{2\sigma^2_{\rm flat}} \right] \tag{4.11}$$

with $A_{\rm steep} = 0.86$, $\sigma_{\rm steep} = 0.17$, $\bar{\alpha}_{\rm steep} = -0.8$ and $A_{\rm flat} = 1 - A_{\rm steep} = 0.14$, $\sigma_{\rm flat} = 0.38$, $\bar{\alpha}_{\rm flat} = -0.5$.

The 1.4 GHz spectral-index distribution of nearby SFGs can be represented by a single population, but each SFG has two spectral components—a nonthermal component with a Gaussian spectral-index distribution characterized by mean spectral index $\bar{\alpha}_{\rm n} \approx -0.8$ and rms width $\sigma_{\rm n} \approx 0.17$ plus a thermal component with spectral index $\alpha_{\rm t} \approx -0.1$. At frequency ν in the source frame, the nonthermal/thermal flux-density ratio is $S_{\rm t}$ is (Condon & Yin 1990)

$$\frac{S_{\rm n}}{S_{\rm t}} \approx 10\left(\frac{\nu}{\rm GHz}\right)^{\alpha_{\rm n}+0.1} . \tag{4.12}$$

For $\nu_0 = 1.4\,$GHz observations, $S_{\rm n}/S_{\rm t}$ declines with redshift in the observed frame from 8 for galaxies at $z = 0$ to 2.56 at $z = 4$. Because nonthermal emission is always dominant, the mean SFG spectral indices increase only slightly, from $\langle\alpha\rangle \approx -0.72$ at $z = 0$ to $\langle\alpha\rangle \approx -0.60$ at $z = 4$.

We have assumed that the locally measured spectral-index distributions do not evolve in the source rest frame. Even so, the observed $\nu_0 = 1.4\,$GHz spectral-index distributions of sources at redshift z are actually the spectral-index distributions of sources selected at the higher frequency $\nu = (1 + z)\nu_0$ in the source rest frame and are biased toward "flatter" spectra with higher α (see Condon 1984, appendix). The expected 1.4 GHz spectral-index distributions of AGNs and SFGs at redshifts $z = 0$, 1 , and 4 are compared in Figure 4.2. Small changes in these spectral-index distributions (e.g., varying $\bar{\alpha}_{\rm n}$ by ± 0.1) actually have very little effect on the predicted source counts and redshift distributions.

4.6 The Non-evolving Model

We integrated Equation 4.10 numerically to calculate $S^2 n(S)$ for the non-evolving model defined by $u_{\rm dex}(L_\nu|z) = u_{\rm dex}(L_\nu|0)$. In order to show the contributions to $S^2 n(S)$ from sources seen at different lookback times $t_{\rm L}$, we broke the integration over z into 13 redshift ranges corresponding to the 13 eons of lookback time $0 < t_{\rm L}({\rm Gyr}) < 1$, $1 < t_{\rm L}({\rm Gyr}) < 2$, $2 < t_{\rm L}({\rm Gyr}) < 3$, ..., $12 < t_{\rm L}({\rm Gyr}) < 13$. These lookback times and redshifts are listed in Table 4.1.

Table 4.1: Lookback Times and Redshifts

t_L (Gyr)	Redshift z
0	0.000
1	0.076
2	0.160
3	0.256
4	0.366
5	0.494
6	0.648
7	0.835
8	1.075
9	1.395
10	1.855
11	2.602
12	4.111
13	9.977

With no evolution of the measured local energy-density functions, Equation 4.10 gives the brightness-weighted source counts $S^2 n(S)$ plotted in Figure 4.3. The 13 thin red curves from right to left are the AGN contributions from the 13 eons $0 < t_\mathrm{L}(\mathrm{Gyr}) < 1$ through $12 < t_\mathrm{L}(\mathrm{Gyr}) < 13$, and the thick red curve is the total contribution from all AGNs with $t_\mathrm{L} < 13\,\mathrm{Gyr}$ ($z < 9.977$). The blue curves show the analogous SFG contributions. The wider green curve is their sum, the total source count $S^2 n(S)$ for the non-evolving model.

At the highest flux densities the model counts indicated by the heavy red, blue, and green curves all must approach the static Euclidean limit of nearby sources $n(S) = kS^{-5/2}$ whose plotted slope is $d\log[S^2 n(S)]/d\log(S) = -1/2$. The static Euclidean number of sources per steradian stronger than S is $N(>S) = (2k/3)S^{-3/2}$, and the thick curves have been truncated at the flux densities above which they are statistically ill-defined because they imply only one source in the entire sky: $N(>S) = (4\pi)^{-1}$. Non-evolving sources in every $\Delta t_\mathrm{L} = 1\,\mathrm{Gyr}$ range of lookback time emitted

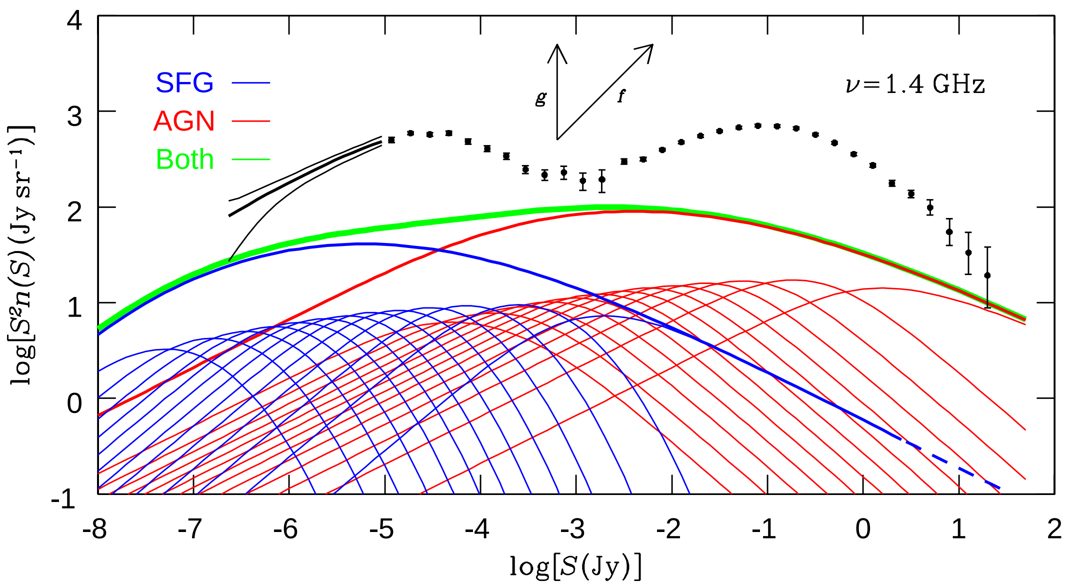

Figure 4.3. The heavy black curve spanning $-6.6 < \log[S(\mathrm{Jy})] < -5.0$ marks the 1.4 GHz source count $S^2n(S)$ determined from the DEEP2 confusion $P(D)$ distribution (Matthews et al. 2021), and the light black curves bound its rms uncertainties. The data points and their rms error bars are the 1.4 GHz DEEP2 direct source counts in the range $-5 < \log[S(\mathrm{Jy})] < -2.7$ Jy and the NVSS counts for $\log[S(\mathrm{Jy})] > -2.6$. Below the data are curves showing the calculated source counts $S^2n(S)$ with no evolution. The thick red curve is the total AGN count, the thick blue curve is the total SFG count, and the wider green curve is their sum, the total non-evolving model source count. The dashed extrapolation of the thick blue curve shows the static Euclidean slope $d[\log[S^2n(S)]/d[\log(S)] = -0.5$ expected in the limit of high flux densities where only low-redshift sources exist. The count contributions by sources in the 13 ranges of lookback time are shown by the lighter red and blue curves. From right to left, the lookback time ranges are $t_{\mathrm{L}} = 0$–1 Gyr, 1–2 Gyr, . . . , 12–13 Gyr. The arrows labeled f and g indicate how much a light curve covering a limited time range would be shifted by $f = 10\times$ luminosity evolution or by $g = 10\times$ density evolution in that time range.

the same total energy, so their contributions to the sky brightness temperature T_{b} are nearly equal, reduced moderately by the $(1+z)^{\alpha}$ attenuation factor in Equation 4.9.

Not only does the wide green curve lie well below the observed source count, it is too smooth because the thick red and blue model curves produced by summing over lookback times are much broader than the peaks in the observed brightness-weighted source counts. The arrows labeled f and g in Figure 4.3 indicate the effects of $10\times$ luminosity or density evolution, respectively, on counts covering a limited time range. Luminosity evolution moves the model curves diagonally upward and to the right while density evolution moves them straight up. The peak in the thick blue curve lies diagonally below and left of the SFG peak in the actual source counts near $\log[S(\mathrm{Jy})] = -4.5$, so nearly pure luminosity evolution should match the observed SFG counts. The peak in the thick red curve must move to the right more than it must move up to match the AGN source-count peak near $\log[S(\mathrm{Jy})] = -1$, suggesting stronger luminosity evolution and negative density evolution. The strongest evolution should be confined to a narrow range of early times in order to bunch up the light red and blue curves and narrow the peaks of the heavy red and blue curves. Just making the local energy-density functions (Figure 4.1) match these features of the brightness-weighted source counts (Figure 4.3) strongly constrains the redshift dependences of the luminosity evolution $f(z)$ and density evolution $g(z)$, without depending on measured redshifts for individual sources.

4.7 Evolutionary Models

We considered so-called backward evolutionary models (i.e. a local luminosity function is evolved backwards to match the observed source counts) in which the forms of the AGN and SFG energy-density functions on a log-log plot (Figure 4.1) do not change, but both populations may evolve independently in both luminosity and density. Pure luminosity evolution $f(z)$ shifts the curves in Figure 4.1 diagonally upward and to the right, while pure density evolution $g(z)$ shifts them vertically. Then for each source population

$$u_{\mathrm{dex}}(L_\nu|z) = g(z)\, u_{\mathrm{dex}}\left[\frac{L_\nu}{f(z)}|0\right]. \tag{4.13}$$

For any combination of luminosity evolution $f(z)$ and density evolution $g(z)$, the total comoving spectral power density produced by galaxies of all luminosities at redshift

z is proportional to the product $f(z)g(z)$. Thus

$$U_{\rm SFG}(z) \equiv \int_{-\infty}^{\infty} u_{\rm dex}(L_\nu|z)\, d\log(L_\nu) =$$
$$f(z)g(z) \int_{-\infty}^{\infty} u_{\rm dex}(L_\nu|0)\, d\log(L_\nu)\ . \tag{4.14}$$

The total 1.4 GHz spectral luminosity density produced by SFGs today is (Condon et al. 2019)

$$U_{\rm SFG}(0) = (1.54 \pm 0.20) \times 10^{19}\,{\rm W\,Hz^{-1}\,Mpc^{-3}} \tag{4.15}$$

Evolution is often described by functions of the observable source redshift z, but for a specific cosmological model (e.g., our ΛCDM model with $H_0 = 70\,{\rm km\,s^{-1}\,Mpc^{-1}}$ and $\Omega_{\rm m} = 0.3$), z can be used to calculate the world time t elapsed between the big bang and when the source emitted the radiation we see today. We prefer to describe evolution in terms of t because (1) the evolution experienced by a source depends only on the time t of emission , while z also depends on the time of the observation and (2) z is a very nonlinear measure of time (Table 4.1), so that equations expressing evolution as a function of z present a distorted picture of the time scales involved. Thus we chose to describe evolution as

$$u_{\rm dex}(L_\nu|t) = g(t)\, u_{\rm dex}\left[\frac{L_\nu}{f(t)}|0\right]\ , \tag{4.16}$$

subject to the boundary condition $f(0)\cdot g(0) = 0$ at the big bang and $f(t_0) = g(t_0) = 1$ at the present time $t_0 \approx 13.47\,{\rm Gyr}$.

Models with strong luminosity evolution predict the existence at high redshifts of extremely luminous AGNs that should have been observed, but were not. Peacock (1985) suggested cutting off the high end of the luminosity function at all redshifts: $\rho(L_\nu) \propto \exp(-L_\nu/L_{\rm c})$. We applied this exponential cutoff with $L_{\rm c} = 10^{29}\,{\rm W\,Hz^{-1}}$.

We model the luminosity and density evolution of both SFGs and AGNs as the product of factors representing their rise at early times and later exponential decay.

The rise is modeled in terms of

$$\operatorname{erf}(t) \equiv \frac{2}{\pi^{1/2}} \int_0^t e^{-x^2} dx, \tag{4.17}$$

the S-shaped error function that increases from $\operatorname{erf}(-\infty) = -1$ through $\operatorname{erf}(0) = 0$ to $\operatorname{erf}(+\infty) = +1$, where t is the age of the galaxy in Gyr. An exponential decay at larger t is justified empirically by the UV and IR data points from Madau & Dickinson (2014) that fall on a nearly straight line for $t > 4\,\mathrm{Gyr}$.

We represent luminosity evolution $f(t)$ and density evolution $g(t)$ by the forms:

$$f(t) = \left\{0.5\left[\operatorname{erf}\left(\frac{t-t_f}{\tau_f}\right)+1\right]\right\}\left[\exp\left(\frac{t_0-t}{\tau_1}\right)\right] \tag{4.18}$$

$$g(t) = \left\{0.5\left[\operatorname{erf}\left(\frac{t-t_g}{\tau_g}\right)+1\right]\right\}\left[\exp\left(\frac{t_0-t}{\tau_2}\right)\right], \tag{4.19}$$

where t_f and t_g are the midpoint times in Gyr of the turn-on phase of luminosity and density evolution, τ_f and τ_g are the time scales of the turn-on, and τ_1 and τ_2 are the time scales in Gyr of luminosity and density decay. In Equations 4.18 and 4.19 f and g are the products of the turn-on function in curly braces and the decay function in square brackets, and both factors approach unity at $t = t_0 \approx 13.47\,\mathrm{Gyr}$. The six free parameters are the time scales τ_f, τ_g, τ_1, and τ_2 and the midpoint times t_f and t_g. Our choice of functional form has the following desirable features: (1) it is continuous and smoothly varying, (2) the asymptotic rise of the error function to +1 at large t makes the rise and decay factors cleanly separable, and (3) the parameters have real physical meanings that can be compared with independent measurements or theories (e.g. the rise time scale τ_r must agree with theoretical predictions for the minimum time needed for the first galaxies to assemble).

AGNs dominate the 1.4 GHz differential source counts (black points in Figure 4.6) for all $\log[S(\mathrm{Jy})] > -3.4$ ($S > 0.4\,\mathrm{mJy}$) and SFGs outnumber AGNs at lower flux densities. Nearly all of the AGNs contributing to $S^2 n(S)$ below $\log[S(\mathrm{Jy})] \approx -2$ come from the low-luminosity ($L_\nu < L^*$) end of the AGN energy-density function (Equation 4.3), which is nearly a power law. Thus *all* AGN evolutionary models consistent with Equations 4.13 or 4.16 and that match $S^2 n(S)$ for $\log[S(\mathrm{Jy})] > -2$ must yield similar power-law count contributions throughout the flux-density range dominated by SFGs, as shown by the heavy red line in Figure 4.6. Consequently, uncertainties in the counts attributed to AGNs have little effect on the modeled SFG counts for $\log[S(\mathrm{Jy})] < -3.4$].

It is mathematically inappropriate to judge the goodness-of-fit of our evolutionary functions through a traditional non-linear least-squares fit (or similar) of the predicted to the observed source counts because the source-counts in adjacent flux-density bins are strongly correlated and thus violate the independence assumption behind these fitting methods. We used Gaussian processes (Rasmussen & Williams 2006) to accomodate these correlations and derive evolutionary models with appropriately conservative uncertainties in the fitted parameters. There are 6 free parameters in Equations 4.18 and 4.19 for both SFGs and AGNs (a total of 12). Because we assumed no late-time density evolution of SFGs, $\tau_{2,\mathrm{SFG}}$ is infinite, we simultaneously fit only 11 free parements in Equations 4.18 and 4.19, plus two more parameters that describe the covariance between data points, using the affine-invariant Monte Carlo Markov Chain (MCMC) code *emcee* (Foreman-Mackey et al. 2013). We assumed uniform priors for all parameters and enforced a slightly relaxed boundary condition $f(0) \cdot g(0) \ll 0.1 \approx 0$. More details of our incorporation of Gaussian processes, the parameter contours resulting from the MCMC fitting, and marginalized posterior distributions can be found in the next Section 4.7.1.

4.7.1 Gaussian Process Model Fitting

Radio source counts and their uncertainties in individual flux-density bins are not independent from their neighbors, so fitting models to these data by minimizing χ^2 will underestimate the model uncertainties and may introduce biases. We use Gaussian processes to allow for possible correlations and derive evolutionary models with conservative uncertainties in the parameters.

For a complete review of the theory behind (and applications of) Gaussian processes, we refer the reader to Rasmussen & Williams (2006). Briefly, a Gaussian process is a generalization of a Gaussian probability distribution that takes into account stochastic effects like correlated noise by modeling both the function (the physical model) and also the covariance function. This ability presents itself through the generalization of the likelihood function as a matrix equation

$$\log p(\{y_n\} \,|\, \{\boldsymbol{x}_n,\, \sigma_n\},\, \boldsymbol{\theta}) = -\frac{1}{2}\, {\boldsymbol{r}_{\boldsymbol{\theta}}}^{\mathrm{T}}\, K^{-1}\, \boldsymbol{r}_{\boldsymbol{\theta}} - \frac{1}{2}\, \log\det K - \frac{N}{2}\, \log(2\,\pi) \tag{4.20}$$

where $\boldsymbol{r}_{\boldsymbol{\theta}}$ is the residual vector

$${\boldsymbol{r}_{\boldsymbol{\theta}}}^{\mathrm{T}} = \begin{pmatrix} y_1 - f(\boldsymbol{x}_1;\, \boldsymbol{\theta}) & \cdots & y_N - f(\boldsymbol{x}_N;\, \boldsymbol{\theta}) \end{pmatrix} \tag{4.21}$$

and K is the "covariance matrix." When the data points are independent, the off-diagonal elements of the $N \times N$ matrix K are 0. Covariance between data points n and m are quantified by non- zero n, m off-diagonal elements. In our case (and in most others) it is difficult or impossible to estimate the covariances accurately, which makes the ability to fit for them using Gaussian processes especially helpful.

It would be extremely computationally expensive to add $\sim N^2$ parameters that need to be fit. Instead of fitting each n, m-th element of the matrix directly, we parameterize it using a functional form

$$K_{n,\,m} = {\sigma_n}^2\, \delta_{n,\,m} + k(\boldsymbol{x}_n,\, \boldsymbol{x}_m;\, \boldsymbol{\alpha}) \tag{4.22}$$

where $\delta_{n,\,m}$ is the Kronecker delta and $k(\boldsymbol{x}_n,\, \boldsymbol{x}_m;\, \boldsymbol{\alpha})$ is the covariance function (or kernel) that parameterizes by $\boldsymbol{\alpha}$) the covariance between by data points using a functional form. It is then up to the user to choose a covariance function that approximates the (unknown) actual covariance between data points.

Using the python Gaussian process package *george* (Ambikasaran et al. 2015), we first maximized the log-likelihood for various covariance functions to determine which was best suited for our data. We know that the covariance between data points varies smoothly, and found that the "squared exponential covariance function" maximizes the log-likelihood

$$k_{\rm SE}(r) = \sigma_f^2 \exp\left(-\frac{r^2}{2l^2}\right), \qquad (4.23)$$

where $r = |\boldsymbol{x}_n - \boldsymbol{x}_m|$ defines the distance between data points, σ_r^2 is a positive constant describing the process variance, and l defines the characteristic length scale (the reach of influence on neighboring data points).

We used the generalized likelihood function (Equation 4.20) with the squared exponential covariance function and the affine-invariant Markov Chain Monte Carlo code *emcee* (Foreman-Mackey et al. 2013) to fit for the 13 free parameters: 5 in the equations governing the evolution of SFGs: $t_{\rm f,SFG}$, $\tau_{\rm f,SFG}$, $\tau_{\rm SFG}$, $t_{\rm g,SFG}$, and $\tau_{\rm g,SFG}$, 6 in the evolutionary equations for AGNs: $t_{\rm f,AGN}$, $\tau_{\rm f,AGN}$, $\tau_{\rm 1,AGN}$, $t_{\rm g,AGN}$, $\tau_{\rm g,AGN}$, and $\tau_{\rm 2,AGN}$, plus the two parameters of the covariance function: σ_f^2 and l. We assumed uniform priors for the input parameters and enforce the boundary condition $f(0) \cdot g(0) \approx 0$. The resulting SFG evolutionary parameter contours and marginalized posterior distributions are shown in Figure 4.4. The parameter values derived from their marginalized posterior distributions and their 1σ uncertainties are listed in Table 4.2. Source counts resulting from 15 randomly-selected parameter samples from these posterior distributions and the corresponding evolutionary functions are shown in Figure 4.5.

4.7.2 AGN radio evolution

As expected, pure luminosity evolution ($g = 1$) cannot match the observed sharp peak in $S^2 n(S)$ near $\log[S({\rm Jy})] = -1$, so we had to supplement luminosity evolution with negative density evolution ($g < 1$). Our best model for AGN evolution has:

$$f_{\rm a} = \left\{0.5\left[\operatorname{erf}\left(\frac{t-3.97}{1.41}\right)+1\right]\right\}\left[\exp\left(\frac{t_0-t}{2.26}\right)\right] \qquad (4.24)$$

and

$$g_{\rm a} = \left\{0.5\left[\operatorname{erf}\left(\frac{t-2.59}{3.31}\right)+1\right]\right\}\left[\exp\left(\frac{t_0-t}{-7.62}\right)\right] \qquad (4.25)$$

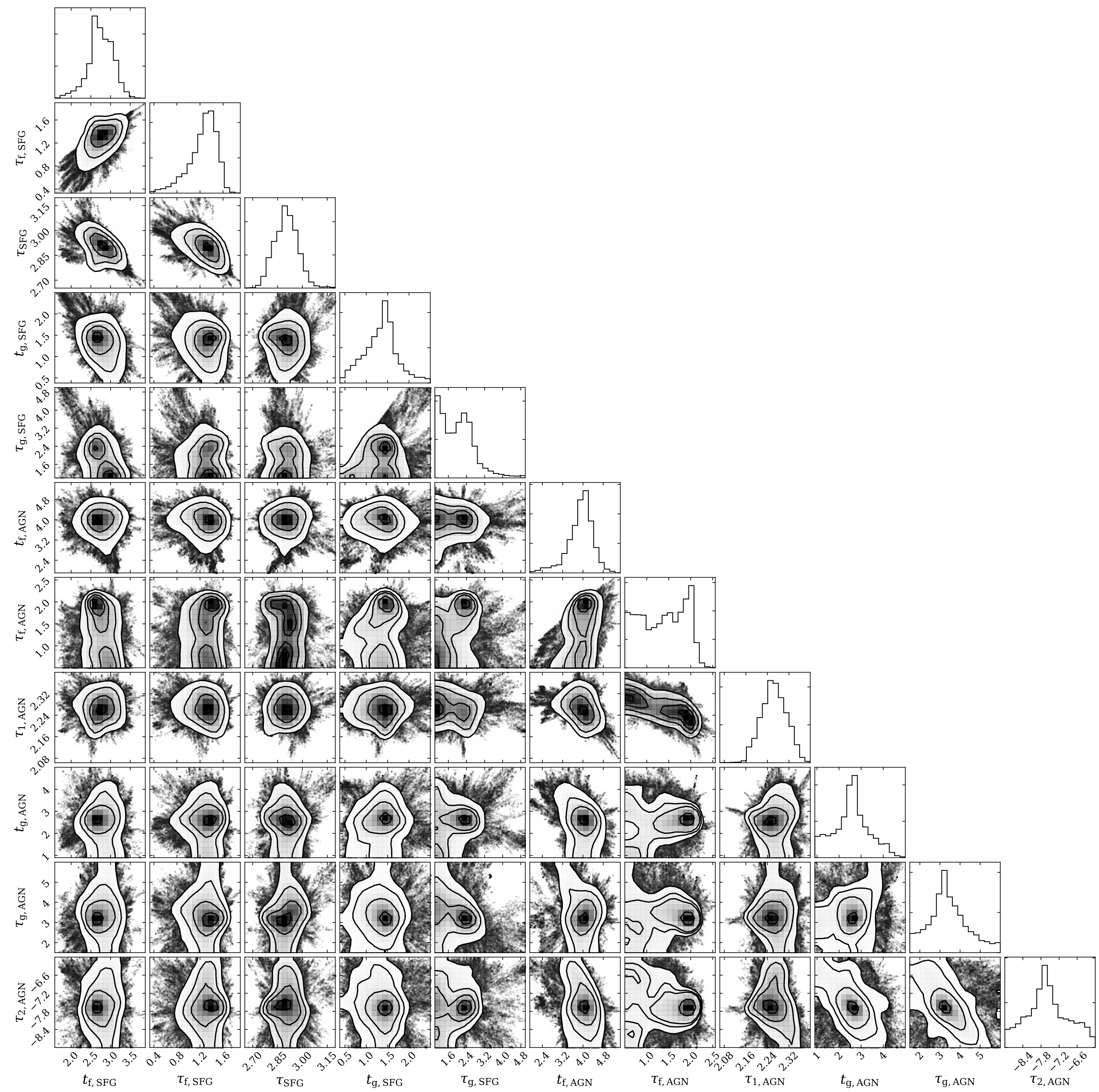

Figure 4.4. Parameter contours and marginalized posterior distributions from the MCMC chains.

where t is the time in Gyr since the big bang. The negative decay time scale $\tau_2 = -7.62\,\mathrm{Gyr}$ indicates a slow exponential *growth* in AGN density at late times. Uncertainties of the derived parameters and their correlations are shown in Section 4.7.1. Figure 4.7 plots $f_\mathrm{a}(t)$ and $g_\mathrm{a}(t)$ separately as dotted and dashed red curves,

Table 4.2. MCMC-derived parameter values and uncertainties

Parameter	Best-fit value	$+1\sigma$	-1σ
$t_{\mathrm{f,SFG}}$	2.74	+0.32	− 0.26
$\tau_{\mathrm{f,SFG}}$	1.30	+0.18	− 0.29
$\tau_{1,\mathrm{SFG}}$	2.90	+0.07	− 0.07
$t_{\mathrm{g,SFG}}$	1.38	+0.29	− 0.44
$\tau_{\mathrm{g,SFG}}$	1.99	+0.67	− 0.76
$t_{\mathrm{f,AGN}}$	3.97	+0.36	− 0.51
$\tau_{\mathrm{f,AGN}}$	1.41	+0.54	− 0.65
$\tau_{1,\mathrm{AGN}}$	2.26	+0.05	− 0.05
$t_{\mathrm{g,AGN}}$	2.59	+0.75	− 0.89
$\tau_{\mathrm{g,AGN}}$	3.31	+1.09	− 0.81
$\tau_{2,\mathrm{AGN}}$	−7.62	+0.84	− 0.67

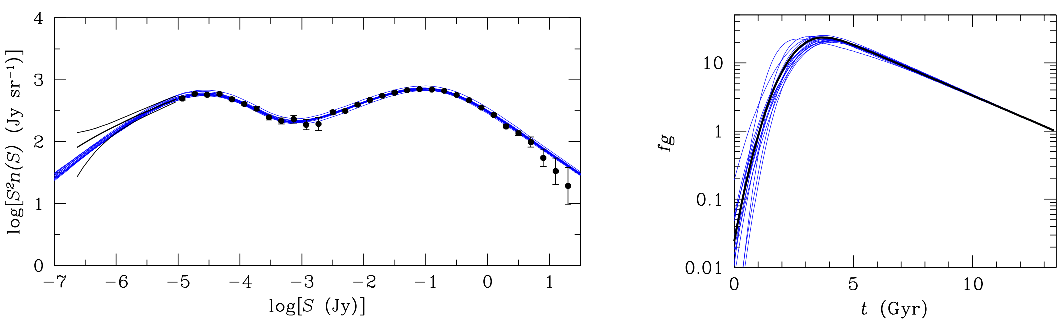

Figure 4.5. Left: 1.4 GHz brightness-weighted source count data shown as black points (source counts derived via $P(D)$ confusion analysis shown as black curves). Fifteen randomly selected parameter vectors from the MCMC fitting routine were used to generate predicted source counts (blue curves). Right: The corresponding fifteen total evolutionary (fg) functions for SFGs. The best-fitting total evolutionary function is shown as the black solid line.

respectively. The total AGN spectral luminosity density

$$U_{\mathrm{AGN}}(t) \equiv \int_{-\infty}^{\infty} u_{\mathrm{dex}}(L_\nu|t)\, d\log(L_\nu) \tag{4.26}$$

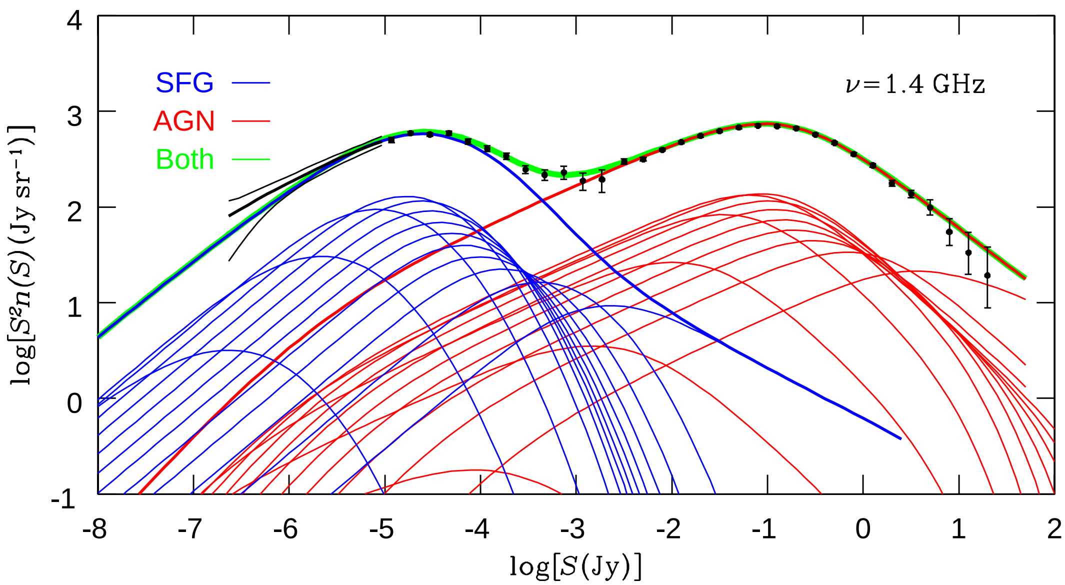

Figure 4.6. The 1.4 GHz differential source counts between $0.25\,\mu$Jy and 25 Jy are shown with the brightness-weighted normalization $S^2 n(S)$. The thick black curve spanning $-6.6 < \log[S(\mathrm{Jy})] < -5$ is based on the DEEP2 confusion $P(D)$ distribution. The data points with error bars show the 1.4 GHz DEEP2 source counts between in the range $-5 < \log[S(\mathrm{Jy})] < -2.6$ Jy and the NVSS counts for $\log[S(\mathrm{Jy})] > -2.6$. The thick curves show the total model counts for AGNs (red), SFGs (blue), and their sum (green). The counts contributed by sources in the 13 ranges of lookback time are shown by the lighter red and blue curves. From right to left, the time ranges are 0–1 Gyr, 1–2 Gyr, . . . 12–13 Gyr.

is proportional to the product $f_{\mathrm{a}}(t)g_{\mathrm{a}}(t)$ shown by the continuous red curve in Figure 4.7 and $U_{\mathrm{AGN}}(t_0) = (4.23 \pm 0.78) \times 10^{19}\,\mathrm{W\,Hz^{-1}\,Mpc^{-3}}$ at $\nu = 1.4\,\mathrm{GHz}$ (Condon et al. 2019).

Recall from Section 4.4 and Figure 4.1 that the local energy-density function of AGNs is well determined down to $\log[L_\nu(\mathrm{W\,Hz^{-1}})] \sim 21$, which is four decades below the peak spectral luminosity $\log[L_\nu(\mathrm{W\,Hz^{-1}})] \approx 25$. Thus the AGN contribution to the brightness-weighted counts (Figure 4.6) peaking at $\log[S(\mathrm{Jy})] \approx -1$ is well determined down to $\log[S(\mathrm{Jy})] \sim -5$, where the AGN contribution is only $\sim 3\%$ of the SFG contribution. Any uncertainty in the numbers of fainter AGNs is too small to affect either the total source counts or the counts of SFGs.

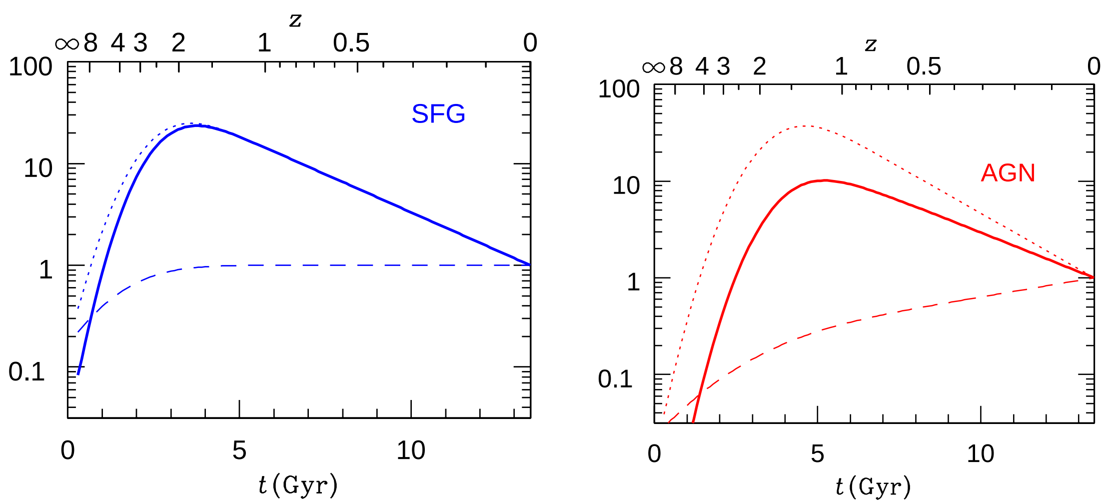

Figure 4.7. The amounts of radio luminosity evolution f (dotted curves), density evolution g (dashed curves), and their products fg (solid curves) best fitting the observed source counts are shown separately for SFGs (blue) and AGNs (red).

4.7.3 SFG radio evolution

The radio evolution of SFGs at 1.4 GHz is best fit by

$$f_s = \left\{0.5\left[\mathrm{erf}\left(\frac{t-2.74}{1.30}\right)+1\right]\right\}\left[\exp\left(\frac{t_0-t}{2.90}\right)\right] \tag{4.27}$$

and

$$g_s = \left\{0.5\left[\mathrm{erf}\left(\frac{t-1.38}{1.99}\right)+1\right]\right\}, \tag{4.28}$$

where t is the time in Gyr since the big bang and $\mathrm{erf}(t)$ is the error function. For both luminosity evolution f_s and density evolution g_s, the quantities in braces specify the S-shaped growth at early times. At later times, the luminosity evolution decays exponentially on a 2.9 Gyr e-folding time scale, and there is no density evolution. These evolution functions f_s, g_s, and their product $f_s g_s$ are shown by the blue curves in Figure 4.7. Today $U_{\rm SFG}(t_0) = (1.54 \pm 0.20) \times 10^{19}\,\mathrm{W\,Hz^{-1}\,Mpc^{-3}}$ (Equation 4.15), and the resulting fits to the observed faint-source counts are shown by the heavy blue (SFGs only) and green (all sources) curves in Figure 4.6.

To estimate the overall uncertainty in SFG evolution, we selected those MCMC parameter vectors yielding log-likelihood values in the highest 68% of all samples. In the selected subsample, the minimum amount of SFG evolution consistent with the 1.4 GHz source counts is

$$f_{\rm s} = \left\{ 0.5 \left[\mathrm{erf} \left(\frac{t - 3.10}{1.12} \right) + 1 \right] \right\} \left[\exp \left(\frac{t_0 - t}{3.04} \right) \right] \tag{4.29}$$

$$g_{\rm s} = \left\{ 0.5 \left[\mathrm{erf} \left(\frac{t - 1.79}{0.42} \right) + 1 \right] \right\} \tag{4.30}$$

and the maximum is

$$f_{\rm s} = \left\{ 0.5 \left[\mathrm{erf} \left(\frac{t - 2.51}{2.50} \right) + 1 \right] \right\} \left[\exp \left(\frac{t_0 - t}{2.76} \right) \right] \tag{4.31}$$

$$g_{\rm s} = \left\{ 0.5 \left[\mathrm{erf} \left(\frac{t - 1.79}{0.97} \right) + 1 \right] \right\} . \tag{4.32}$$

The broad green curve in Figure 4.8 shows the range of counts bounded by these minimum and maximum evolution equations. We stress that although the individual parameters describing the luminosity and density evolution have larger uncertainties (Section 4.7.1), the resulting total evolutionary curves remain consistent because the parameters are correlated. This ensures that the resulting implications for the star-formation history of the universe are stable.

When calculating far-ultraviolet (FUV) and FIR luminosity densities of SFGs, Madau & Dickinson (2014) truncated their luminosity functions below $0.03L_{\rm s}^*$ (their equation 14). As a test, we tried truncating our 1.4 GHz SFG luminosity function below $0.03L_{\rm s}^* \approx 6 \times 10^{19}\,\mathrm{W\,Hz^{-1}}$. The predicted counts above $S \approx 0.25\,\mu$Jy remained well within the green curve in Figure 4.8 and $\log[S^2 n(S)]$ fell by only 0.08 at $S \log[S(\mathrm{Jy})] = -8$.

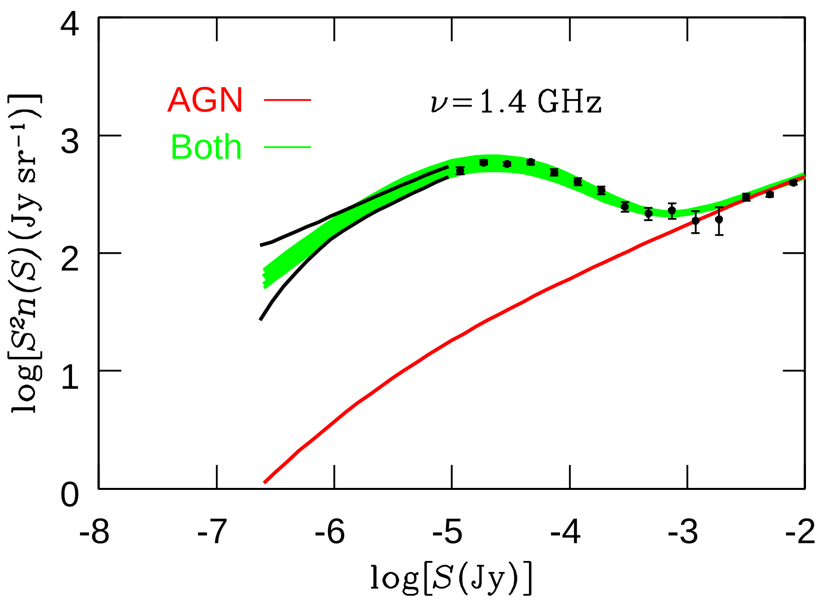

Figure 4.8. The broad green curve spans the range of total source counts bounded by the minimum and maximum SFG evolution models (Equations 4.29 through 4.32. The best-fit AGN counts are shown by the red curve. The black data points with error bars are the DEEP2 and NVSS discrete source counts, and the black curves are the upper and lower limits of the $P(D)$ counts.

4.7.4 Sky brightness contributed by extragalactic sources at 1.4 GHz

Integrating Equation 4.5 yields the Rayleigh-Jeans sky brightness temperature contributed by all sources stronger than S_0:

$$T_{\mathrm{b}}(>S_0) = \left[\frac{\ln(10)c^2}{2k_{\mathrm{B}}\nu^2}\right]\int_{\log S_0}^{\infty} S^2 n(S) d(\log S). \tag{4.33}$$

As shown in Figure 4.9, the model that best fits the brightness-weighted source counts $S^2 n(S)$ of AGNs adds $T_{\mathrm{b}} \approx 69\,\mathrm{mK}$ to the Rayleigh-Jeans sky brightness temperature at 1.4 GHz, half of which comes from sources stronger than $\log[S(\mathrm{Jy})] = -1.2$ and 99% from sources with $\log[S(\mathrm{Jy})] > -4.8$. The acceptable range of SFG model counts adds $T_{\mathrm{b}} = 43 \pm 6\,\mathrm{mK}$ to the background, of which $\approx 96\%$ is resolved into sources stronger than $S = 0.25\,\mu$Jy. By integrating the backward evolutionary model for SFG out to increasing redshifts, we determine that half of the total SFG background is produced by sources having redshifts $z < 0.93 \pm 0.10$.

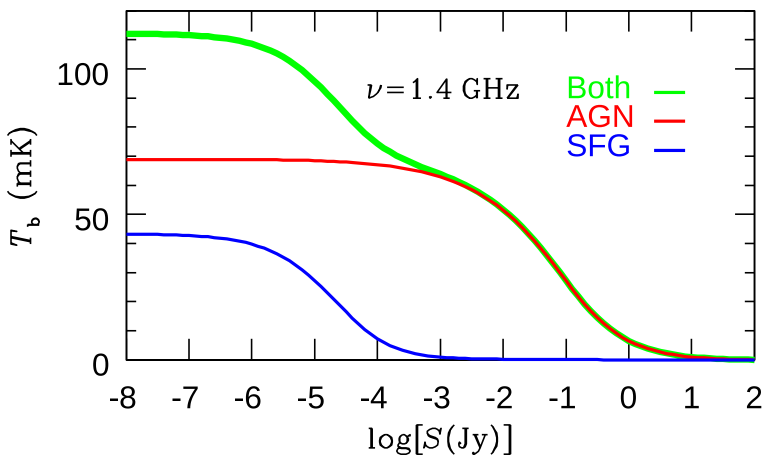

Figure 4.9. Model contributions to the 1.4 GHz sky brightness temperature $T_{\rm b}$ from AGNs (red), SFGs (blue), and the sum of both (green) by sources with flux densities $> S$.

The $\nu = 1.4\,$GHz sky brightness temperature $T_{\rm b}$ produced by SFGs (blue curve in Figure 4.9) was converted to the 1.4 GHz sky brightness $\nu I_\nu = 2k_{\rm B}T_{\rm b}\nu^3c^{-2}$ in units of $\mathrm{nW\,m^{-2}\,sr^{-1}}$ and is shown by the blue curve plotted against the lower abscissa and left ordinate of Figure 4.10. The $\lambda = 160\,\mu$m sky brightness of faint FIR sources was measured by Berta et al. (2011) and is shown by the red curve plotted against the upper abscissa and right ordinate of Figure 4.10. The left end of the red curve at $S_{160\,\mu\rm m} = 0.3\,$mJy marks the sensitivity limit of the *Herschel* PACS $P(D)$ counts, and the right end between $S_{160\,\mu\rm m} = 0.2\,$Jy and 1 Jy is the static Euclidean extrapolation (Berta et al. 2011). The upper abscissa was shifted left by the expected mean flux-density ratio $\langle S_{160\,\mu\rm m}/S_{1.4\,\rm GHz}\rangle \approx 310$ of faint SFGs at median redshift $\langle z\rangle \approx 1$ (Condon et al. 2019; Berta et al. 2011), and the right ordinate for νI_ν was shifted down by 4.16×10^5, the flux-density ratio multiplied by the frequency ratio. See Appendix C.5 for the derivation of these numbers. The surprisingly good agreement of the $\lambda = 160\,\mu$m and $\nu = 1.4\,$GHz SFG backgrounds is reassuring evidence that (1) contamination of the SFG population by radio-loud AGNs is small and (2) the local FIR/radio correlation does not break down at redshifts $z \sim 1$.

The *COBE* Far Infrared Absolute Spectrophotometer (FIRAS) measured the total cosmic infrared background contributed by all extragalactic sources to be $\nu I_\nu = 12.8 \pm 6.4\,\mathrm{nW\,m^{-2}\,sr^{-1}}$ at $\lambda = 160\,\mu$m (Fixsen et al. 1998), with zodiacal dust emission causing most of the uncertainty. If $\langle S_{160\,\mu\mathrm{m}}/S_{1.4\,\mathrm{GHz}}\rangle \approx 310$, the corresponding 1.4 GHz SFG background $\nu I_\nu = 3.1 \pm 1.5 \times 10^{-5}\,\mathrm{nW\,m^{-2}\,sr^{-1}}$ is consistent with the $\nu I_\nu \approx 3.5 \pm 0.5 \times 10^{-5}\,\mathrm{nW\,m^{-2}\,sr^{-1}}$ we obtained for SFGs stronger than $S_{1.4\,\mathrm{GHz}} = 0.25\,\mu$Jy. Thus any hypothetical "new population" of fainter radio sources bright enough to produce the large extragalactic brightness at $\nu = 3.02\,$GHz reported by Fixsen et al. (2011) cannot obey the FIR/radio correlation.

4.8 The Cosmic History of Star Formation

Section 4.7 describes the *radio* evolution needed to match the local *radio* energy-density function to the counts of *radio* sources associated with SFGs. By themselves, these quantities do not directly constrain the comoving SFRD $\psi(t)$ ($M_\odot\,\mathrm{yr^{-1}\,Mpc^{-3}}$). To calculate the evolving SFRD, we need a prescription relating the radio luminosities of SFGs to their star-formation rates. The radio continuum is an energetically negligible tracer of star formation: the FIR/radio luminosity ratio $\sim 4 \times 10^5$ of SFGs is comparable with the elephant/mouse mass ratio. Furthermore, most of the 1.4 GHz emission is synchrotron radiation whose luminosity depends on poorly known quantities such as the interstellar magnetic field strength and ambient radiation energy density. It took the discovery of the surprisingly strong empirical FIR/radio correlation in nearby galaxies (Helou et al. 1985) to convert radio continuum photometry of SFGs from a hobby into a quantitative science.

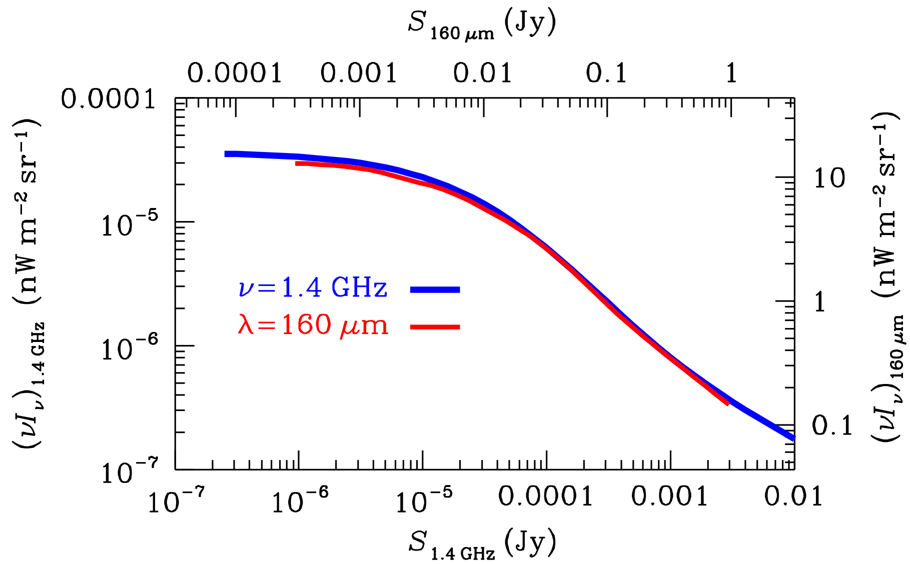

Figure 4.10. The $\nu = 1.4\,\mathrm{GHz}$ sky brightness temperature contributed by SFGs (blue curve in Figure 4.9) was converted to the cumulative sky brightness νI_ν contributed by sources with flux densities $> S_{1.4\,\mathrm{GHz}}$ and is shown by the blue curve (against the lower abscissa and left ordinate). The red curve (against the upper abscissa and right ordinate) shows the $\lambda = 160\,\mu\mathrm{m}$ brightness contributed by sources stronger than $S_{160\,\mu\mathrm{m}}$ (Berta et al. 2011). The curves overlap as shown when $S_{160\,\mu\mathrm{m}}/S_{1.4\,\mathrm{GHz}} = 310$ (Appendix C.5).

4.8.1 The linear FIR/radio correlation

If the FIR/radio correlation is linear ($L_{\mathrm{FIR}} \propto L_{1.4\,\mathrm{GHz}}$) and does not evolve, then only the local FIR/radio flux-density ratio is needed to convert from radio luminosity to star-formation rate. That ratio is usually expressed in terms of the dimensionless constant q (Helou et al. 1985):

$$q \equiv \log\left[\frac{\mathrm{FIR}/(3.75 \times 10^{12}\,\mathrm{Hz})}{S(1.4\,\mathrm{GHz})}\right], \tag{4.34}$$

where FIR is the flux between 42.5 and 122.5 μm in units of W m^{-2} estimated from the *IRAS* 60 and 100 μm flux densities in Jy

$$\mathrm{FIR} = 1.26 \times 10^{-14}[2.58S(60\,\mu\mathrm{m}) + S(100\,\mu\mathrm{m})] \tag{4.35}$$

and 3.75×10^{12} Hz is the frequency corresponding to the midpoint wavelength $\lambda = 80\,\mu$m. (Beware that the FIR in Equation 4.35 is a flux with units of $\mathrm{W\,m^{-2}}$ so the numerator in Equation 4.34 is a flux density with units of $\mathrm{W\,m^{-2}\,Hz^{-1}}$. Thus either the denominator $S(1.4\,\mathrm{GHz})$ should be specified in units of $\mathrm{W\,m^{-2}\,Hz^{-1}} = 10^{26}$ Jy or, if $S(1.4\,\mathrm{GHz})$ is specified in Jy, the numerator should be multiplied by 10^{26}.) For the flux-limited *IRAS* sample of galaxies with $S(60\,\mu\mathrm{m}) > 2$ Jy, Yun et al. (2001) reported a nearly linear FIR/radio correlation with scatter $\sigma = 0.26$ in the q values of individual galaxies and sample mean $\langle q \rangle = 2.34 \pm 0.01$.

If the 1.4 GHz spectral luminosities of SFGs are indeed proportional to their star formation rates and the constant of proportionality does not evolve, then the radio evolution of SFGs implies SFRD evolution

$$\frac{\psi(t)}{\psi_0} = f_{\mathrm{s}}(t) g_{\mathrm{s}}(t)\,, \tag{4.36}$$

where $\psi_0 \equiv \psi(t_0)$ is the SFRD now. The thick blue curve in Figure 4.11 indicates the radio SFRD evolution based on Equations 4.27 and 4.36.

Using FIR and FUV data, Madau & Dickinson (2014) estimated the evolving SFRD and approximated it by the function

$$\frac{\psi(z)}{\psi_0} \approx \frac{(1+z)^{2.7}}{1 + [(1+z)/2.9]^{5.6}} \tag{4.37}$$

shown by the black curve in Figure 4.11. Both the blue and black curves peak around the same "cosmic noon" near $t = 3$ Gyr, $z = 2$ and decline exponentially at later times, but the radio estimate implies a significantly stronger overall evolution of the SFRD. If the FIR/radio correlation is linear and the 1.4 GHz energy density function underwent luminosity evolution specified by Equation 4.37, the predicted radio source counts of SFGs would fall well below the observed counts. Integrating the predicted radio source counts (see Equation 4.33) determines that SFGs would contribute only $T_{\mathrm{b}} = 21$ mK to the sky brightness temperature.

About half of the observed 43 mK SFG background is produced by sources with $\log[S(\mathrm{Jy})] > -4.8$ ($S > 16\,\mu$Jy), nearly half by sources with $-6.6 < \log[S(\mathrm{Jy})] <$

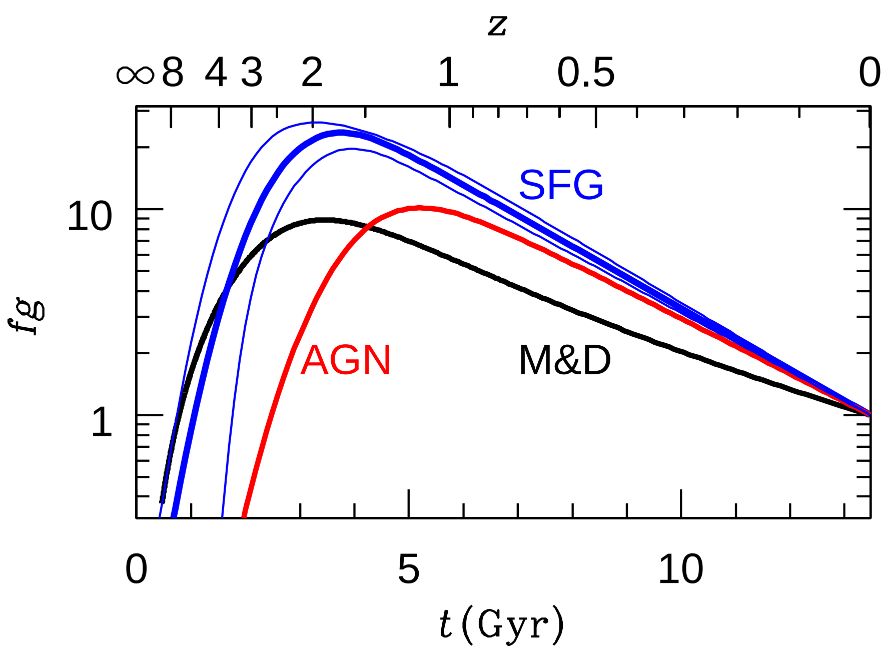

Figure 4.11. The thick blue curve, which is the same as the thick blue curve in Figure 4.7, shows the best-fit evolution of the radio SFRD if $\psi/\psi_0 = f_s g_s$ for SFGs, and the thin blue curves indicate the minimum and maximum amounts of evolution specified by Equations 4.29 through 4.32. All are significantly higher than the black curve showing the evolution $\psi/\psi_0 = fg$ of the SFRD based on FUV and FIR data (Madau & Dickinson 2014, equation 15). The red curve is our best fit to the product $f_a g_a$ for AGN. It is closer to the Madau & Dickinson (2014) curve for stars, indicating comparable amounts of SFG and AGN evolution, but the AGN peak lags by $\gtrsim 1$ Gyr. Abscissa: time t in Gyr since the big bang. Ordinate: Normalized evolution fg.

-4.8, and only $\sim 4\%$ of the model SFG background is produced by sources below our $P(D)$ count limit $\log[S(\mathrm{Jy})] = -6.6$ ($S = 0.25\,\mu$Jy). Stronger luminosity evolution and negative density evolution with fixed $f_s(z)g_s(z)$ could fit the 1.4 GHz source counts above $\log[S(\mathrm{Jy})] \sim -4.8$, but no separate adjustments of luminosity evolution f or density evolution g consistent with a given ψ/ψ_0 or product fg can significantly change these SFG contributions to T_b and match the counts between $\log[S(\mathrm{Jy})] = -6.6$ and $\log[S(\mathrm{Jy})] = -4.8$. We conclude that the large difference between the radio and FUV/FIR SFRDs cannot be avoided if the FIR/radio correlation is linear and does not evolve. Thus authors who assume a linear FIR/radio correlation to model deep FIR and radio counts necessarily find that q decreases with redshift; e.g., Delhaize et al. (2017b) used sensitive Jansky Very Large Array (VLA) and *Herschel* images to find $q \propto (1+z)^{-0.19\pm0.01}$ in the redshift range $0 < z < 6$.

4.8.2 The nonlinear FIR/radio correlation

The difference between SFRD evolution estimates based on our 1.4 GHz data and on the FUV/FIR data in Madau & Dickinson (2014) can be reduced if the FIR/radio correlation is sub-linear; that is, $x < 1$ in $L_{\rm FIR} \propto L^{x}_{1.4\,\rm GHz}$. To determine the degree of nonlinearity, we measured the local q (Equation 4.34) as a function of $\log[L(1.4\,\rm GHz)]$. The q distribution of sources in a flux-limited sample is biased by the selection frequency; thus the mean $\langle q \rangle$ in a FIR-selected sample is higher than $\langle q \rangle$ in a radio-selected sample (see Condon 1984, appendix). Such biases can be removed by assigning to each source a weight inversely proportional to the maximum volume $V_{\rm max}$ in which it could remain in the sample, yielding the unbiased volume-limited distribution of q.

To measure the unbiased local distribution of q, we started with the large sample of NVSS sources stronger than $S = 2.5\,\rm mJy$ used in Section 4.4 to determine the local radio luminosity function, but kept only the sources with $S \geq 5\,\rm mJy$ to ensure that nearly all (98%) of the sample SFGs were detected by *IRAS* and have accurately measured values of q. Although purely flux-limited samples of all radio sources with $S \geq 5\,\rm mJy$ are dominated by faint and distant ($\langle z \rangle \sim 1$) AGNs, our bright ($k_{\rm 20fe} < +11.75$) and thus local ($\langle z \rangle \sim 0.02$) sample is not, so the SFGs can be separated from the AGNs, as shown in Figure 4.1.

This sample was divided into 1.4 GHz luminosity bins of width $\Delta \log(L_\nu) = 0.2$ centered on $\log(L_\nu) = 19.7$ through 23.5. We weighted the value of q for each source by its $L_\nu / V_{\rm max}$ ratio, where $V_{\rm max}$ is the smaller of its $\lambda = 2.16\,\mu\rm m$ or $\nu = 1.4\,\rm GHz$ maximum volumes, so that the overall weighted mean of the entire sample is an unbiased measure of the volume-limited FIR/radio luminosity-density ratio. Within each narrow radio luminosity bin, the rms scatter of individual q values is only $\sigma_q \approx 0.16$. The weighted means $\langle q \rangle$ and their rms uncertainties $\sigma_{\langle q \rangle}$ are plotted for all populated luminosity bins in Figure 4.12. The bent line in Figure 4.12 shows the fit

$$\begin{aligned}\langle q\rangle =&2.69 - 0.147[\log(L_\nu) - 19.1] \qquad\qquad \text{if } \log(L_\nu) < 22.5\\ \langle q\rangle =&2.19 \text{ if } \log(L_\nu) \geq 22.5\end{aligned} \tag{4.38}$$

indicating a clearly sub-linear FIR/radio relation $L_{\rm FIR} \propto L_\nu^{0.85}$ in the 1.4 GHz luminosity range $\log(L_\nu) < 22.5$ that includes $> 90\%$ of nearby SFGs. Sub-linearity implies that FIR luminosity evolution, and hence SFRD evolution, is not as strong as 1.4 GHz evolution. The volume-limited average for nearby SFGs of all luminosities is $\bar{q} = 2.30 \pm 0.01$. These results are quite stable, varying by $\sim 0.1\%$ when the 2% of galaxies with only *IRAS* upper limits are included or excluded. To the extent that the star-formation rates of galaxies are proportional to their stellar masses $M_\star$ (Brinchmann et al. 2004) (that is, there is a "main sequence" of star-forming galaxies), the recent finding that $dq/d\log(M_\star) = -0.148 \pm 0.013$ nearly independent of redshift (Delvecchio et al. 2020) is consistent with our sublinear local FIR/radio correlation $dq/d\log(L_\nu) = -0.147$ and our assumption that the FIR/radio correlation itself does not evolve with redshift. While we know that the local FIR/radio correlation is sublinear and can fit our data with a non-evolving FIR/radio correlation, we cannot demonstrate that no such evolution exists.

For our evolutionary models, the FIR luminosities $L_{\rm FIR}$ of individual SFGs at any redshift were estimated by inserting $\langle q\rangle$ values from Equation 4.38 into

$$L_{\rm FIR} = 3.75 \times 10^{12}\,{\rm Hz} \cdot L_{1.4\,{\rm GHz}} \cdot 10^{\langle q\rangle} \ . \tag{4.39}$$

The matching energy-density equation is

$$\left[\frac{u_{\rm dex}({\rm FIR})}{{\rm W\,Mpc^{-3}}}\right] = 3.75 \times 10^{12}\,{\rm Hz} \cdot \left[\frac{u_{\rm dex}(1.4\,{\rm GHz})}{{\rm W\,Hz^{-1}\,Mpc^{-3}}}\right] \cdot 10^{q} \ . \tag{4.40}$$

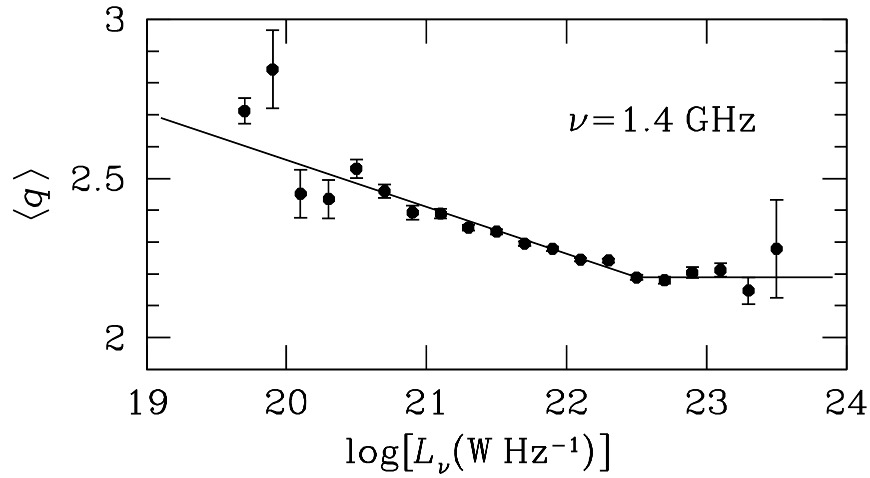

Figure 4.12. The logarithmic FIR/radio ratio parameter decreases as $d\langle q\rangle/d\log(L_\nu) = -0.147$ below $\log[L_\nu(\mathrm{W\,Hz^{-1}})] = 22.5$ and is a constant $\langle q\rangle = 2.19$ at higher luminosities.

4.8.3 Converting $L_{\rm FIR}$ to star-formation rates

The total SFR associated with a given infrared luminosity depends on the assumed initial mass function (IMF) and stellar model spectra. Murphy et al. (2011) assumed a Kroupa (2001) IMF and used the Starburst99 spectrum integrated over the infrared (IR) band covering $8 < \lambda(\mu\mathrm{m}) < 1000$ to obtain

$$\left(\frac{\rm SFR}{M_\odot\,\mathrm{yr}^{-1}}\right) = 3.88 \times 10^{-37}\left(\frac{L_{\rm IR}}{\rm W}\right)\,. \tag{4.41}$$

The widely referenced conversion factor in table 1 of Kennicutt & Evans (2012) is based on this Murphy et al. (2011) value. A Salpeter IMF (Salpeter 1955) has a larger fraction of low-mass stars and implies total SFRs including all stars in the mass range $0.1 < M_\odot < 100$ are factor of $1/0.66 = 1.52$ higher for a given $L_{\rm IR}$. Most nearby SFGs have only measured FIR luminosities, not IR luminosities. Bell et al. (2003) compared the q values for IR and FIR luminosities and found $\langle L_{\rm IR}/L_{\rm FIR}\rangle \approx$

dex$(2.64 - 2.36) \approx 1.91$, so for a Kroupa (2001) IMF

$$\left(\frac{\mathrm{SFR}}{M_\odot\,\mathrm{yr}^{-1}}\right) = 7.39 \times 10^{-37} \left(\frac{L_{\mathrm{FIR}}}{\mathrm{W}}\right) . \tag{4.42}$$

Combining these results and integrating over $\log L_\nu$ yields our radio estimate of the evolving SFRD ψ for a Kroupa (2001) IMF at any time t :

$$\begin{aligned}\left[\frac{\psi(t)}{M_\odot\,\mathrm{yr}^{-1}\,\mathrm{Mpc}^{-3}}\right] &= 7.39 \times 10^{-37} \cdot 3.75 \times 10^{12}\,\mathrm{Hz}\,\cdot \\ &\int \left[\frac{u_{\mathrm{dex}}(L_\nu|t) \cdot 10^{\langle q(L_\nu)\rangle}}{\mathrm{W\,Hz^{-1}\,Mpc^{-3}}}\right] d\log(L_\nu)\,,\end{aligned} \tag{4.43}$$

where L_ν is the 1.4 GHz spectral luminosity. Again, for a Salpeter (1955) IMF, ψ is a factor of 1.52 larger. For a Salpeter (1955) IMF and $U_{\mathrm{SFG}} = 1.54 \pm 0.2 \times 10^{19}\,\mathrm{W\,Hz^{-1}\,Mpc^{-3}}$ (Equation 4.15), $\psi(t_0) = 0.0128\,M_\odot\,\mathrm{yr}^{-1}\,\mathrm{Mpc}^{-3}$ is the radio estimate of the SRFD today.

Figure 4.13 compares our 1.4 GHz estimate of the evolving SFRD $\psi(t)$ (thick blue curve) with the standard Madau & Dickinson (2014) FUV/FIR data points and estimate (black curve), all for a Salpeter (1955) IMF. Our best 1.4 GHz estimate is well approximated by

$$\begin{aligned}\log\left[\frac{\psi(t)}{M_\odot\,\mathrm{yr}^{-1}\,\mathrm{Mpc}^{-3}}\right] &= -3.473 + 1.818\left(\frac{t}{\mathrm{Gyr}}\right) \\ &-3.653\left(\frac{t}{\mathrm{Gyr}}\right)^2 + 0.02216\left(\frac{t}{\mathrm{Gyr}}\right)^3\end{aligned} \tag{4.44}$$

when $0.5 < t(\mathrm{Gyr}) < 5$ and by

$$\log\left[\frac{\psi(t)}{M_\odot\,\mathrm{yr}^{-1}\,\mathrm{Mpc}^{-3}}\right] = -0.0529 - 0.1373\left(\frac{t}{\mathrm{Gyr}}\right) \tag{4.45}$$

when $t(\mathrm{Gyr}) > 5$. The light blue curves indicate the range of SFRDs consistent with the 13% uncertainty in the SFRD today quadratically added to the SFRD ranges from our acceptable evolutionary models (Section 4.7.3). To convert Figure 4.13 from a Salpeter (1955) IMF to a Kroupa (2001) IMF, subtract 0.18 from $\log(\psi)$. The sub-linear FIR/radio correlation has increased the 1.4 GHz late-time e-folding time scale $\tau = 2.9^{+0.07}_{-0.07}$ Gyr (Equation 4.27) to $\tau = 3.2^{+0.08}_{-0.08}$ Gyr for the SFRD ψ, bringing it closer to but still smaller than the Madau & Dickinson (2014) $\tau \approx 4.4$ Gyr.

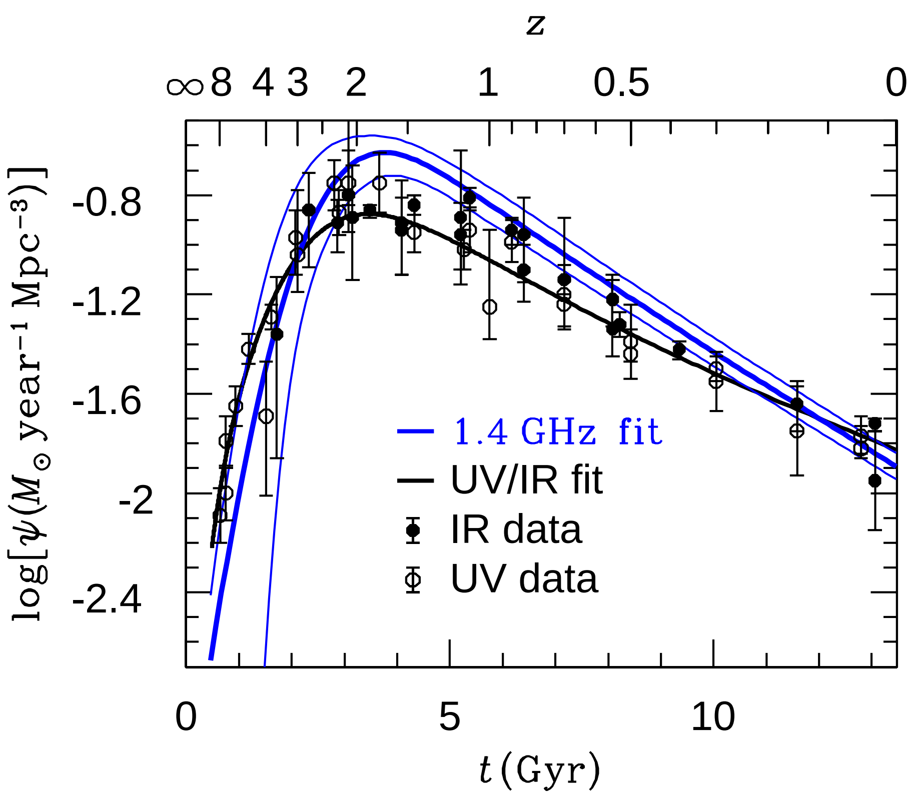

Figure 4.13. The evolving SFRD ψ for a Salpeter (1955) IMF is shown as a function of time t (Gyr) since the big bang. The UV and IR data points and the black curve fitted to Equation 4.37 with $\psi_0 = 0.015\, M_\odot\, \mathrm{yr}^{-1}\, \mathrm{Mpc}^{-3}$ are from the Madau & Dickinson (2014) review. The heavy blue curve is our best-fit 1.4 GHz SFRD estimate, and the light blue curves bound the range of acceptable fits to our 1.4 GHz data.

4.9 Discussion and Conclusions

This paper presents an independent estimate of the cosmic star-formation history based on radio evolutionary models matching the 1.4 GHz local luminosity function and counts of sources as faint as $S = 0.25\,\mu$Jy at 1.4 GHz, the flux density of the Milky Way at $z = 4$ with $10\times$ luminosity evolution.

- Radio source evolution of AGNs and SFGs at 1.4 GHz was determined by matching local luminosity functions $\rho_{\rm dex}(L_\nu)$ or local energy-density functions $u_{\rm dex}(L_\nu)$ with the brightness-weighted source counts $S^2 n(S)$.
- We made the first measurement of the local *volume-limited* FIR/radio correlation and found it to be sub-linear: $L_{\rm FIR} \propto L_{1.4\,{\rm GHz}}^{0.85}$.
- We used our sub-linear FIR/radio correlation to convert radio-source evolution to an evolving SFRD ψ ($M_\odot\,{\rm yr}^{-1}\,{\rm Mpc}^{-3}$). This radio estimate reproduces the usual SFRD peak near $z \approx 2$, but the peak SFRD indicates stronger evolution than the standard FUV/FIR estimate (Madau & Dickinson 2014).

4.9.1 What are the main strengths and weaknesses of this radio SFRD model?

- The 1.4 GHz emission from a star-forming galaxy is a mixture of synchrotron radiation from electrons accelerated in core-collapse supernova remnants of $M > 8M_\odot$ stars and thermal bremsstrahlung from HII regions, making it less sensitive than FIR luminosity to contamination by older stellar populations. However, radio emission is more vulnerable to unrecognized AGN contamination, primarily in galaxies with high SFRs and high radio luminosities. The sample of SFGs used to generate the local 1.4 GHz luminosity function was carefully vetted (Condon et al. 2019), and the local radio SFRD $\psi(t_0) = 0.0128\,M_\odot\,{\rm yr}^{-1}\,{\rm Mpc}^{-3}$ is slightly *lower* than the FUV/FIR $\psi(t_0) = 0.015\,M_\odot\,{\rm yr}^{-1}\,{\rm Mpc}^{-3}$ (both for a Salpeter (1955) IMF). Thus the local 1.4 GHz sample does not seem to be badly contaminated. AGN contamination of SFGs at high redshifts might cause their source counts and hence radio evolution to be overestimated, but the excellent agreement of the background brightnesses νI_ν produced by SFGs at $\nu = 1.4$ GHz and $\lambda = 160\,\mu$m (Figure 4.10) is reassuring.

- AGNs dominate the source counts above $S \approx 0.4\,\mathrm{mJy}$, but their contributions to the total counts of significantly fainter sources can be estimated accurately because they are smooth power laws at the low-luminosity end of their energy density function.

- The peak contribution of SFGs to $S^2 n(S)$ occurs near $S = 10\,\mu\mathrm{Jy}$, and about half the total SFG contribution is from fainter sources. The main obstacle to radio measurements of the SFRD has been measuring accurate source counts down to $S \approx 0.25\,\mu\mathrm{Jy}$. That is now possible, but only statistically via the confusion $P(D)$ distribution (Matthews et al. 2021), so it is not possible to identify individual $S \approx 0.25\,\mu\mathrm{Jy}$ sources or measure their redshifts. Instead, the amounts of luminosity evolution f and density evolution g depend entirely on fitting features in the local energy-density functions to features in the brightness-weighted source counts. Only smoothly varying f and g can be modeled accurately, and rare populations (e.g., SFGs at very high redshifts) can easily be overlooked. The 1.4 GHz spectra of SFGs are power laws with spectral indices near $\alpha = -0.7$, so their K-corrections are easy to calculate but large enough that 1.4 GHz SFRDs are best determined at redshifts up to and slightly beyond "cosmic noon," but submm continuum sources with low or negative K-corrections and submm spectral lines are better for determining SFGs at redshifts $z \gtrsim 4$.

- The dominant synchrotron luminosity at 1.4 GHz is only an energetically negligible tracer of star formation and is not simply proportional to the SFR; it depends on unknown or unrelated quantities such as the interstellar magnetic field strength and inverse-Compton (IC) scattering off the ambient radiation field produced by starlight plus the cosmic microwave background (CMB). Thus the use of 1.4 GHz luminosity to measure the SFR is justified primarily by the empirical FIR/radio correlation. The locally measured FIR/radio correlation might fail at high redshifts owing to IC scattering losses off the CMB $\propto (1+z)^4$.

This does not seem to be a problem because it can only lower the radio SFRD estimate, and the radio SFRD estimate is slightly higher than expected. The FIR/radio correlation is often treated as being linear, but we found it to be sub-linear: $L_{\rm FIR} \propto L_{1.4\,\rm GHz}^{0.85}$. Sub-linearity significantly reduces the discrepancy between the radio and FIR SFRD models as shown by Figures 4.11 and 4.13, so the resulting radio SFRD models lie above but just within the error bars of the FIR data points.

Chapter 5

Conclusions and Future Work

The main take-aways of this dissertation are as follows:

- In Chapter 2, I present the most complete local radio luminosity function from a spectroscopically-complete sample of cross-identifications of ∼10,000 2MASX sources (with 2.16 μm magnitude $k_{20\mathrm{fe}} \leq 11.75$) in the NVSS (with flux densities $S \geq 2.45\,\mathrm{mJy}$). Radio sources powered primarily by SFGs and AGNs with radio luminosities $\log[L_{1.4\,\mathrm{GHz}}\,(\mathrm{W\,Hz^{-1}})] > 19.3$ account for over 99% of the total 1.4 GHz energy density in the nearby universe.

- The AGNs and SFGs were separated using only radio and infrared data rather than optical emission-line diagnostics, which are not good quantitative measures of AGN-powered radio emission. We compared our SFG/AGN identifications of an overlapping sample with Mauch & Sadler (2007)—whose SFG/AGN identifications were based solely on optical spectra—and found surprisingly good agreement.

- The local radio-derived SFRD value of $\psi(z \sim 0) = 0.0128\,M_\odot\,\mathrm{yr^{-1}\,Mpc^{-3}}$ is consistent with the model of $\psi(z)$ derived by Madau & Dickinson (2014) using only UV/IR data. The sample is large enough that the uncertainties on this measurement are no longer dominated by statistical variance, but instead by cosmic variance.

- In Chapter 3, I present 1.4 GHz source counts over eight decades of flux density from 0.25 μJy to 25 Jy. From 0.25 $\mu\text{Jy} < S < 10\,\mu\text{Jy}$ the counts were statistically derived from the $P(D)$ confusion distribution of the MeerKAT DEEP2 field, from $10\,\mu\text{Jy} < S < 2.5\,\text{mJy}$ from direct detections of individual sources in the DEEP2 field, and above 2.5 mJy from cataloged components of the NVSS.

- I developed a simulation of the radio sky as well as the effects of deep radio observations (e.g. convolution with the beam, noise) to determine the source counts for the radio population with $S < 10\,\mu\text{Jy}$. The simulation allowed us to account for specifics of the observation (e.g. the dirty beam) and to constrain a source count that did not follow a simple power law. These simulations also determined the corrections needed for the direct source counts from $10\,\mu\text{Jy} < S < 2.5\,\text{mJy}$ due to confusion.

- Chapter 3 includes differential source counts derived from the NVSS above $S = 2.5\,\text{mJy}$. Despite the survey and catalog being completed over two decades prior, differential counts had not yet been published.

- Using the local 2MASX/NVSS sample presented in Chapter 2, I present a *volume-limited* measurement of the FIR/radio correlation. This correlation is often assumed to be linear, however we found that it is distinctly sublinear, with the FIR luminosity $L_{\text{FIR}} \propto L_{1.4\,\text{GHz}}^{0.85}$. This insight slightly decreases the degree of discrepancy between the SFRD evolution of radio-based and UV/IR-based models, but does not completely resolve the differences. It also eliminates the need for an evolving FIR/radio correlation.

- In Chapter 4, I present an evolutionary model for the SFRD $\psi(t)$ derived from the local radio luminosity function, 1.4 GHz source counts, and the FIR/radio correlation. The SFRD rises rapidly from $t = 0$ to $t \approx 3\,\text{Gyr}$ and subsequently declines exponentially to present day. The time of the peak SFRD and shape of $\psi(t)$ agrees well with the model from Madau & Dickinson (2014), but the radio-derived SFRD predicts stronger evolution than the UV/IR-based models.

- Luminosity and density evolution was determined for SFG and AGN populations individually. The total evolution of SFGs is largely dominated by luminosity evolution—peaking at $t \sim 3\,\mathrm{Gyr}$—with no density evolution after $t \sim 4\,\mathrm{Gyr}$. The peak of AGN evolution occurs slightly later than for SFGs, at approximately $t \sim 4\,\mathrm{Gyr}$, after which AGNs experience slow exponential density *growth*.

5.1 Future Work: Characterizing galaxies in the MeerKAT DEEP2 field

Most massive galaxies with $z \leq 1.5$ lie on the star-formation 'main-sequence' relating stellar mass and SFR: SFR $\propto M^{0.8}$ (Pannella et al. 2015). The normalization of the main sequence is the specific star-formation rate (sSFR=SFR/M_*) for some fiducial mass M_*, and indicates the rate at which stars are forming in galaxies of a certain mass. Until now, dust-unbiased SFRs were only available for relatively massive galaxies and starbursts. While UV/optical emission may probe normal main sequence galaxies, the SFR corrections for dust attenuation of less massive galaxies are still significant and relatively uncertain at $z \gtrsim 2$ (Whitaker et al. 2017). Understanding the efficiency of stellar mass buildup as a function of redshift requires dust-unbiased SFRs for normal, disk galaxies beyond cosmic noon. It is these normal galaxies that contribute the majority of the mass at cosmic noon; starburst galaxies have been found to contribute only a small fraction to the SFRD at $z \leq 2$ (Rodighiero et al. 2011). The unprecedented sensitivity of the MeerKAT-DEEP2 field will provide a dust-unbiased view of star formation in these normal galaxies at $z \geq 2$ for the first time.

The MeerKAT-DEEP2 field spans over one-square-degree and hosts a previously unexplored population of faint, normal, disk galaxies across cosmic time. The *Spitzer* IRAC bands at $3.6\,\mu$m and $4.5\,\mu$m—accessible without cryogenics—are the best tracers of stellar mass at redshifts $z \geq 1$, so they inevitably detect most host galaxies to radio sources. Cotton et al. (2018) demonstrated that $\sim 98\%$ of radio sources with

$S(3\,\mathrm{GHz}) \geq 3\,\mu\mathrm{Jy}$ have a NIR counterpart. During its last few months of operation, warm-*Spitzer* imaged the MeerKAT DEEP2 field. I will use these moderately-deep observations to identify the host galaxies for the vast majority of radio sources in DEEP2. As shown in Matthews et al. (2021), direct counts of radio sources in the confusion-limited DEEP2 field can only be reliably calculated down to $\sim 10\mu\mathrm{Jy}$. The positions of NIR cross-identifications can be used as accurate priors to deblend radio sources and push the lower flux density limit of direct counts to slightly fainter flux densities ($S \sim 5\mu\mathrm{Jy}$), equivalent to $\sim 100\,M_{\odot}\,\mathrm{yr}^{-1}$ at $z \sim 2$, a SFR well below *Herschel* or other FIR/submillimeter surveys could detected at cosmic noon. Further, a flux density limit of $S(1.28\,\mathrm{GHz}) \sim 5\,\mu\mathrm{Jy}$ is equal to that of the deepest COSMOS S-band image at 3 GHz but covers a much larger sky area.

Redshift measurements are essential to calculate the intrinsic characteristics of individual galaxies (mass, luminosity, etc.) that will help explain the discrepancy between radio-based and UV/IR-based SFRD evolutionary models. The MeerKAT-DEEP2 field is a treasure trove of ~20,000 radio continuum sources, but it is observationally expensive to measure traditional spectroscopic redshifts for all these galaxies. An alternative is to use the photometric redshift (photo-z) method to obtain distances through fitting and modeling spectral energy distributions (SEDs) that match the observed broadband fluxes at each wavelength. But even with dense wavelength coverage over the optical and NIR regime, the photometric redshift errors remain on the order of 3-4% (Rowan-Robinson et al. 2008). Redshift errors of a few percent translate to significant uncertainty in flux-dependent properties of galaxies (e.g. stellar mass and SFR).

There is a third option that produces more-accurate redshifts than photo-z's, but takes a tiny fraction of the time needed for high-resolution spectroscopic surveys. Replacing the transmission grating used with a CCD camera with a low-dispersion prism produces low-resolution spectra across a wide range of wavelengths. This technique was first utilized on the Inamori Magellan Area Camera and Spectrograph (IMACS) for the PRIsm MUlti-object Survey (PRIMUS), where they were able to observe ~2,500 objects at once (Coil et al. 2011). I will utilize this method to obtain high-quality redshifts ($\lesssim 1\%$ errors) for the $\sim$20,000 radio sources in the MeerKAT-DEEP2 field.

With redshift information, it will be possible to determine intrinsic properties (e.g. mass, luminosity) of galaxies in the MeerKAT-DEEP2 field. I plan to supplement the warm-*Spitzer* data with optical photometry obtained with the Dark Energy Camera at the Cerro Tololo Inter-American Observatory (CTIO) for the *g, r, I, z*, and *J* bands. I will apply for these observations separately since the DEEP2 field is just south of the region covered by the Dark Energy Survey. Additionally, during the period of my postdoctoral fellowship, the NOAO Extremely Wide-Field Infrared Imager (NEWFIRM) will be recommissioned at CTIO. I plan to capitalize on the recommissioning of NEWFIRM to obtain deep NIR imaging of the DEEP2 field. These $\lambda = 1.25 - 2.1\,\mu$m data are key for identifying the Balmer/4000 Å Balmer break at $1.5 \leq z \leq 3$, will fill in the continuous wavelength coverage of the SEDs, and increase the accuracy of the spectrophotometric redshifts.

The optical photometry, NIR photometry, and *Spitzer* data combine to form spectral energy distributions (SEDs) for the galaxies, and the addition of the low-resolution spectra from IMACS yields continuous wavelength coverage through the optical regime. I will test and use a variety of stellar population synthesis models and templates to fit the galactic SEDs and determine their redshift and stellar masses. The low-dispersion spectra are key for isolating Balmer breaks and emission lines in star-forming galaxies, leading to small uncertainties on the redshift measurements. The galactic SEDs also reveal the type of galaxy, whether it is indeed star-forming or if it is transitioning into quiescence. Since the observed optical/NIR photometry corresponds to UV/optical luminosity measurements in the rest-frame of the source, it constrains the dust-unobscured SFRs for these normal, Milky Way-like galaxies. A comparison between the radio-based and UV/optical SFRs will be a powerful characterization of the effects of dust and the systematic uncertainties it causes in solely optical and IR pictures of star formation. The wealth of information encoded into the SEDs will allow for the most statistically robust characterization of faint, radio galaxies at cosmic noon.

Appendix A

Dictionary of Terms & Variables

Table A.1: Dictionary of Terms & Variables

Variable	Definition	Reference
	Greek Symbols	
α	spectral index	Section 1.4
	Right Ascension	Section 2.2
δ	Declination	Section 2.2
θ	FWHM of the Gaussian restoring beam	Section 1.6
$\Theta_{1/2}$	FWHM of the primary beam	Section 3.4.1
ν	frequency in Hz (1/s)	Figure 1.3
$\rho_{\rm dex}(L_\nu)$	space density of sources per decade of spectral luminosity [$\mathrm{Mpc}^{-3}\,\mathrm{dex}^{-1}$]	Equation 1.3
σ_n	rms of statistical noise	Section 1.6.2
ϕ	angular size of radio source	Section 1.6
$\Omega_{1/2}$	Sky area within half-power point of primary beam	Section 2.6
	Other Functions, Symbols, and Abbreviations	
AGN	active galactic nuclei	
CMB	cosmic microwave background	Section 1.3
D	Historically, the deflection of the pen on a chart recorder when detecting a signal	Section 1.6

FIR	far-infrared wavelength range (this work assumes $40\,\mu\mathrm{m} \leq \lambda \leq 123\,\mu\mathrm{m}$)	
Jy	Jansky, a unit of flux density = $10^{-26}\,\mathrm{W\,m^{-2}\,Hz^{-1}}$	
L	luminosity	
$M_\odot$	mass of the Sun = 1.989×10^{33} g	
MIR	mid-infrared wavelength range (typically $15\,\mu\mathrm{m} \leq \lambda \leq 40\,\mu\mathrm{m}$)	
NIR	near-infrared wavelength range (typically $1.2\,\mu\mathrm{m} \leq \lambda \leq 5\,\mu\mathrm{m}$)	
pc	parsec, a unit of distance = 3.086×10^{18} cm	
$P(D)$	Distribution of image pixel brightness	
SFG	star-forming galaxy	Section 1.6
SFR	star formation rate [$M_\odot\,\mathrm{yr^{-1}}$]	
SFRD	star formation rate density [$M_\odot\,\mathrm{yr^{-1}\,Mpc^{-3}}$]	
S	flux density [Jy]	
S_p	peak flux density [$\mathrm{Jy\,beam^{-1}}$]	
$S^{5/2}n(S)$	Euclidean-weighted source counts [$\mathrm{Jy^{3/2}\,sr^{-1}}$]	Figure 1.6
$S^2n(S)$	brightness-weigthed source counts [$\mathrm{Jy\,sr^{-1}}$]	Figure 1.9
$u_\mathrm{dex}(L_\nu)$	spectral power density (or energy-density) per decade of spectral luminosity [$\mathrm{W\,Hz^{-1}\,dex^{-1}\,Mpc{-}3}$]	Equation 1.5

Note: Click to return to Chapter: 1 2 3 4 5 Appendix: B C

Appendix B

Cosmology for Astronomers

"Innocent, light-minded men, who think that astronomy can be learnt by looking at the stars without knowledge of mathematics will, in the next life, be birds."—Plato, Timaeus

According to the cosmological principle and confirmed by observation (e.g., Figure B.1), the universe is isotropic and homogeneous on large scales. It began with a very dense "big bang" and has been expanding uniformly ever since. General relativity can describe both the geometry and expansion dynamics of the universe. However, general relativity permits spatially curved universes which are mathematically complicated. Extragalactic astronomers were once faced with the choice of learning general relativity or applying published relativistic results without really understanding them, at the risk of being birds in the next life.

In today's ΛCDM (Λ for dark energy with constant energy density and CDM for cold dark matter) concordance model, the universe is spatially "flat," so its geometry is Euclidian, its expansion is not affected by curvature, and locally correct Newtonian calculations can be extended to cosmological scales. Fortunately for non-mathematicians, flatness allows simple (no tensors) derivations of accurate equations for the kinematics and dynamics of cosmic expansion that an undergraduate physics major can understand. Such derivations are presented in Sections B.1 and B.2, and the main results used by observational astronomers are developed in Section B.3.

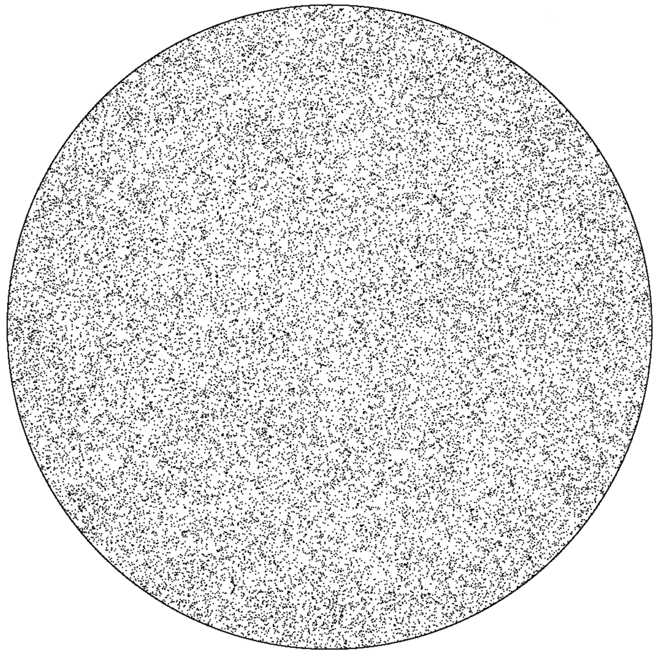

Figure B.1. Positions of the $N \sim 4 \times 10^4$ radio sources stronger than $S = 2.5$ mJy at 1.4 GHz are indicated by points on this equal-area plot covering the sky within 15° of the north celestial pole. Nearly all of these sources are extragalactic and so distant (median redshift $\langle z \rangle \sim 1$) that their distribution is quite isotropic.

See David Hogg's useful "cheat sheet" (Hogg 1999) listing results from relativistic models with nonzero curvature, and the books by Peebles (1993) and Weinberg (1972) for their derivations. The astropy.cosmology Python package at `http://docs.astropy.org/en/stable/cosmology/` contains utilities for calculating many of the quantities discussed in this paper.

In this paper, the present (redshift zero) values of evolving quantities are distinguished by the subscript 0 for clarity. Unless otherwise noted, all numerical results are based on a Hubble constant $H_0 = 70$ km s^{-1} Mpc^{-1} so $h \equiv H_0/(100 \text{ km s}^{-1} \text{ Mpc}^{-1}) = 0.7$, plus the following normalized densities at redshift zero: total $\Omega_0 = 1$, baryonic and cold dark matter $\Omega_{0,\mathrm{m}} = 0.3$, radiation and relic neutrinos $\Omega_{0,\mathrm{r}} = h^{-2} \cdot 4.2 \times 10^{-5}$, and dark energy $\Omega_{0,\Lambda} = 1 - (\Omega_{0,\mathrm{m}} + \Omega_{0,\mathrm{r}}) \approx 0.7$. Note that many authors just write Ω, Ω_m, Ω_r, and Ω_Λ without the subscript 0 to indicate the present values of these densities. Also, 1 Mpc $\approx 3.0857 \times 10^{19}$ km and 1 yr $\approx 3.1557 \times 10^7$ s.

B.1 Expansion Kinematics

According to the equivalence principle, all fundamental observers locally at rest relative to their surroundings anywhere in the isotropically expanding (and hence homogeneous) universe are in inertial frames, and their clocks all agree on the time t elapsed since the big bang. This universal time t is sometimes called world time or cosmic time, and it equals the proper time of all fundamental observers. Fundamental observers didn't have to be present at the creation to synchronize their clocks; the temperature of the cosmic microwave background (CMB) radiation is a suitable proxy for time. Likewise, the CMB appears isotropic only to fundamental observers, and others can use the CMB dipole anisotropy (Kogut et al. 1993) to deduce their usually small ($v^2 \ll c^2$, where $c \approx 299792$ km s^{-1} is the vacuum speed of light) peculiar velocities and correct for them if necessary.

Homogeneity and isotropy are preserved if and only if the small proper distance $D(t)$ between any close pair of observers expands as

$$D(t) = a(t)\, D_0 \ , \tag{B.1}$$

where D_0 is the proper distance now and $a(t)$ is the universal (meaning, it is the same at every position in the universe) dimensionless scale factor that grew with time from $a \approx 0$ just after the big bang to $a(t_0) \equiv 1$ today (Figure B.2). Equation B.1 applies to any expansion that preserves homogeneity and isotropy—the separations of dots on a photo being enlarged, for example. The cosmological expansion affects only to the separations of non-interacting objects, and the dots representing rigid rulers, gravitationally bound galaxies, etc. do not expand with the universe.

From Figure B.2 it is clear that

$$\frac{d \ln D}{dt} = \frac{1}{D}\frac{dD}{dt} = \frac{1}{aD_0}\frac{D_0\, da}{dt} = \frac{\dot{a}}{a} \equiv H(t) \tag{B.2}$$

can depend on time but not with position in space. $H(t)$ is called the Hubble parameter, and its current value is the Hubble constant H_0. The time derivative $\dot{D}$ of D in

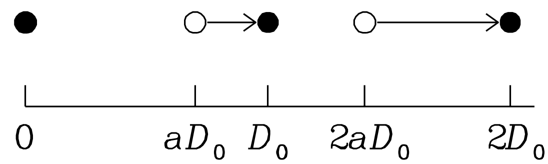

Figure B.2. To preserve homogeneity and isotropy, all distances $D = aD_0$, $2D = 2aD_0$,... between fundamental observers must grow in proportion to the universal scale factor $a(t)$.

Equation B.1 defines the recession velocity of the nearby observer:

$$v_{\rm r} \equiv \dot{D} = \dot{a}\, D_0 = \left(\frac{\dot{a}}{a}\right) D = HD\ . \tag{B.3}$$

Successive wave crests of light emitted with frequency $\nu_{\rm e}$ and wavelength $\lambda_{\rm e} = c/\nu_{\rm e}$ are separated in time by $dt = \nu_{\rm e}^{-1}$ in the source frame. If the source is receding from the observer with velocity $v_{\rm r} \ll c$, successive waves must travel an extra distance $v_{\rm r}\, dt = v_{\rm r}/\nu_{\rm e}$, so their observed wavelength is

$$\lambda_{\rm o} = \frac{c}{\nu_{\rm e}} + \frac{v_{\rm r}}{\nu_{\rm e}} = \lambda_{\rm e} + \lambda_{\rm e}\left(\frac{v_{\rm r}}{c}\right) \quad (v_{\rm r} \ll c) \tag{B.4}$$

and $v_{\rm r}$ is measurable via the first-order Doppler shift:

$$\frac{v_{\rm r}}{c} = \frac{\lambda_{\rm o} - \lambda_{\rm e}}{\lambda_{\rm e}} \quad (v_{\rm r} \ll c)\ . \tag{B.5}$$

The redshift z of a source is defined by

$$z \equiv \frac{\lambda_{\rm o} - \lambda_{\rm e}}{\lambda_{\rm e}}\ , \tag{B.6}$$

and the domain of this definition extends to all z. Note that most recession "velocities" reported by astronomers are actually $v_{\rm r} = cz$ and may be much larger than the vacuum speed of light.

Combining Equations B.3 and B.5 for a nearby source at distance $D = c\Delta t$ gives

$$\frac{v_\mathrm{r}}{c} = \frac{\Delta\lambda}{\lambda} = \frac{D}{c}\frac{\dot{a}}{a} = \Delta t\,\frac{\dot{a}}{a} = \frac{\Delta a}{a} \quad (v_\mathrm{r} \ll c)\ . \tag{B.7}$$

Integrating the local Equation B.7 over time:

$$\int_{\lambda_\mathrm{e}}^{\lambda_\mathrm{o}} \frac{d\lambda}{\lambda} = \int_a^1 \frac{da}{a} \tag{B.8}$$

gives the global result that $\lambda_\mathrm{o}/\lambda_\mathrm{e} = 1/a$ and $\nu_\mathrm{o}/\nu_\mathrm{e} = a$. Thus the observable redshift z of any distant source can be used to calculate the scale factor a of the universe when it emitted the light seen today:

$$\boxed{a = (1+z)^{-1}}\ . \tag{B.9}$$

Because $1 \leq (1+z) < \infty$ is the reciprocal of the scale factor $0 < a \leq 1$, at high redshifts both z and $(1+z)$ are very nonlinear and potentially misleading functions of fundamental quantities such as lookback time (Section B.3.1). Had astronomers always been able to measure accurate frequency ratios $\nu_\mathrm{o}/\nu_\mathrm{e} = a$ instead of just small differential wavelengths $(\lambda_\mathrm{o} - \lambda_\mathrm{e})/\lambda_\mathrm{e} = z$, most cosmological equations and results would probably be presented in terms of a today.

The dimension of H is inverse time, but astronomers originally measured the Hubble constant as the mean ratio v_r/D of nearby galaxies, so it is usually written in mixed units of length and time:

$$H_0 = 100\,h\,\mathrm{km\,s^{-1}\ Mpc^{-1}}\ . \tag{B.10}$$

Isolating the dimensionless factor h makes it easy to compare results based on different measured values of H_0. The most recent measurements of h range from the low $h = 0.669 \pm 0.006$ (Planck Collaboration et al. 2016) derived by comparing the observed angular power spectrum of CMB fluctuations with a flat ΛCDM cosmological model to the high $h = 0.732 \pm 0.017$ (Riess et al. 2016) based on relatively local measurements of Cepheid variable stars and Type Ia supernovae used as standard candles. The 3σ "tension" between these results is a topic of current research (Freedman 2017).

The Hubble time is defined by

$$t_{\rm H} \equiv H^{-1} \ , \tag{B.11}$$

and its present value

$$t_{\rm H_0} \equiv H_0^{-1} \approx 9.778 \times 10^9 \, h^{-1} \ {\rm yr} \approx 14.0 \ {\rm Gyr} \tag{B.12}$$

is a convenient unit of time comparable with the present age of the universe t_0. Likewise, the current Hubble distance

$$D_{\rm H_0} \equiv \frac{c}{H_0} \approx 2998 \, h^{-1} \ {\rm Mpc} \approx 4280 \ {\rm Mpc} \tag{B.13}$$

is a distance comparable with the present radius of the observable universe.

The lookback time $t_{\rm L}(z)$ to a source at any redshift z is the time photons need to travel with speed c from the source to the observer at $z = 0$. In a homogeneous universe, this global quantitity is just the sum of the small locally measured proper times dt. In terms of the scale factor a and $H = d\ln(a)/dt$, it is

$$t_{\rm L} = \int_t^{t_0} dt' = \int_a^1 \left(\frac{dt'}{d \ \ln(a')} \right) d \ \ln(a') \tag{B.14}$$

$$t_{\rm L} = \int_a^1 \frac{da'}{a' H(a')} \ . \tag{B.15}$$

The lookback time is usually written in terms of z:

$$t_{\rm L} = \int_t^{t_0} dt' = \int_z^0 \left(\frac{dt'}{dz'} \right) dz' \ . \tag{B.16}$$

To calculate dt/dz, take the time derivative of Equation B.9:

$$\frac{dz}{dt} = \frac{-1}{a^2} \frac{da}{dt} = -\frac{1}{a} \left(\frac{\dot{a}}{a} \right) = -(1+z)H \tag{B.17}$$

so

$$\boxed{t_{\mathrm{L}} = \int_0^z \frac{dz'}{(1+z')H(z')}} \ . \tag{B.18}$$

The dynamical equation specifying the evolution of H is derived in Section B.2.

B.2 Expansion Dynamics

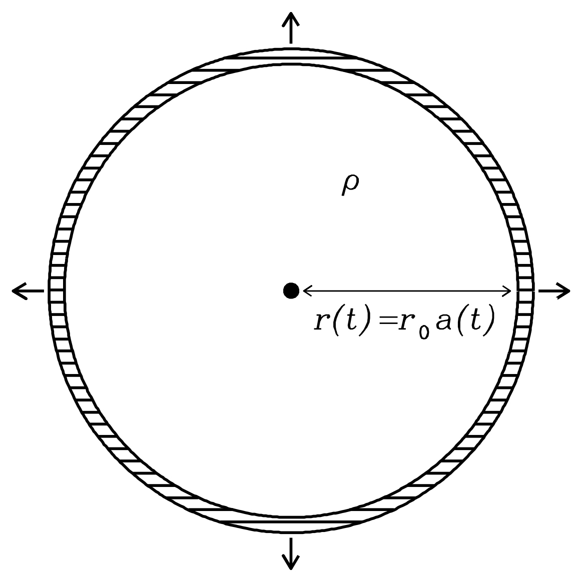

Figure B.3. Expansion of the spherical shell with radius $r(t)$ and mean density ρ centered on any fundamental observer is affected only by the enclosed gravitational mass $M = E/c^2 = (4\pi r^3/3)\,\rho$.

The expansion of any small spherical shell with radius $r(t) = r_0\,a(t) \ll D_{\mathrm{H}_0}$ and mean density ρ centered on any fundamental observer is Newtonian in our flat universe because (1) the net gravitational effect of the surrounding isotropic universe is zero, in both Newtonian and general relativistic mechanics (Birkhoff & Langer 1923), and (2) there is no relativistic curvature acceleration. The only relativistic results needed are (1) the mean gravitational mass density ρ is the total relativistic mass density

E/c^2, not just the Newtonian rest mass density, and (2) in a flat universe, the actual mean density ρ always equals the critical density ρ_c for which the sum of the kinetic and gravitational potential energies per unit mass of the shell is zero:

$$\frac{\dot{r}^2}{2} - \frac{4\pi G\rho r^3}{3r} = 0 \ , \tag{B.19}$$

where $G \approx 6.674 \times 10^{-11}$ m^3 kg^{-1} s^{-2} is Newton's gravitational constant. The actual radius r_0 in $r = r_0\, a(t)$ cancels out, leaving an equation for the scale factor a

$$\frac{\dot{a}^2}{2} - \frac{4\pi G\rho a^2}{3} = 0 \tag{B.20}$$

which can be solved for the Hubble parameter

$$H^2 = \left(\frac{\dot{a}}{a}\right)^2 = \frac{8\pi G\rho}{3} \ . \tag{B.21}$$

Equation B.21 is the same as the equation Friedmann derived from general relativity for a homogeneous, isotropic, and flat universe.

The present mean density of the flat universe is

$$\begin{aligned} \rho_0 = \frac{3H_0^2}{8\pi G} &\approx 1.878 \times 10^{-26}\, h^2\, \mathrm{kg\, m^{-3}} \\ &\approx 9.20 \times 10^{-27}\, \mathrm{kg\, m^{-3}} \ . \end{aligned} \tag{B.22}$$

The normalized density parameter Ω is defined as

$$\Omega \equiv \frac{\rho}{\rho_c} \ , \tag{B.23}$$

and $\Omega = 1$ for all time in a flat universe. There are three dynamically distinct contributors to Ω: (1) matter consisting of ordinary baryonic matter plus cold dark matter particles whose rest mass nearly equals their total mass, (2) dark energy whose density is constant, and (3) radiation, primarily CMB photons plus the cosmic neutrino background (CνB) of relic neutrinos from the big bang.

Planck Collaboration et al. (2016) observations of the CMB angular power spectrum indicate that $\Omega_0 = \Omega_{0,\mathrm{m}} + \Omega_{0,\Lambda} + \Omega_{0,\mathrm{r}} = 1.0023 \pm 0.0055$, $\Omega_{0,\mathrm{m}} = 0.315 \pm 0.013$, and $\Omega_{0,\Lambda} = 0.685 \pm 0.013$. Blackbody radiation at temperature T has energy density $U = 4\sigma T^4/c$, where $4\sigma/c \approx 7.566 \times 10^{-16}$ J m^{-3} is the radiation constant. The $T_0 \approx 2.73\,\mathrm{K}$ CMB has energy density $U_0 \approx 4.20 \times 10^{-14}$ J m^{-3} and gravitational mass density $\rho_{0,r} = U_0/c^2 \approx 4.67 \times 10^{-31}$ kg m^{-3}. Massless relic neutrinos have energy density $U_0 \approx 2.86 \times 10^{-14}$ J m^{-3} and gravitational mass density $\rho_{0,\nu} \approx 3.18 \times 10^{-31}$ kg m^{-3} (Peebles 1993). The total from photons plus neutrinos is $\Omega_{0,\mathrm{r}} \approx 4.2 \times 10^{-5}\, h^{-2} \approx 8.6 \times 10^{-5}$.

Mass conservation of non-relativistic matter implies $\rho_\mathrm{m} \propto a^{-3} = (1+z)^3$. In the ΛCDM model, dark energy is assumed to behave like a cosmological constant: $\rho_\Lambda \propto a^0 = (1+z)^0$. The density of radiation (and massless neutrinos) scales as $\rho_\mathrm{r} \propto a^{-4} = (1+z)^4$ because the number density of photons is $\propto a^{-3} = (1+z)^3$ and the mass $E/c^2 = h\nu/c^2$ of each photon scales as $E \propto \lambda^{-1} \propto (1+z)^1 \propto a^{-1}$. Inserting these results into Equations B.21, B.22, and B.23 leads to

$$\frac{\rho}{\rho_0} = \frac{H^2}{H_0^2} = \frac{\Omega_{0,\mathrm{m}}}{a^3} + \frac{\Omega_{0,\Lambda}}{a^0} + \frac{\Omega_{0,\mathrm{r}}}{a^4}\,. \tag{B.24}$$

Using Equation B.9 to replace the scale factor a by the observable $(1+z)^{-1}$ yields the dynamical equation specifying the evolution of H:

$$\boxed{\frac{H}{H_0} = [\Omega_{0,\mathrm{m}}(1+z)^3 + \Omega_{0,\Lambda} + \Omega_{0,\mathrm{r}}(1+z)^4]^{1/2}}\,. \tag{B.25}$$

The symbol

$$\boxed{E(z) \equiv [\Omega_{0,\mathrm{m}}(1+z)^3 + \Omega_{0,\Lambda} + \Omega_{0,\mathrm{r}}(1+z)^4]^{1/2}} \tag{B.26}$$

is a convenient shorthand for subsequent calculations. Figure B.4 shows $H/H_0 = E(z)$ as a function of z for $\Omega_{0,\mathrm{m}} = 0.3$.

The densities of radiation and matter were equal when $\Omega_{0,\mathrm{r}}(1+z_\mathrm{eq})^4 = \Omega_{0,\mathrm{m}}(1+z_\mathrm{eq})^3$ at $z_\mathrm{eq} = (\Omega_{0,\mathrm{m}}/\Omega_{0,\mathrm{r}}) - 1 \approx 3500$. The density of matter fell below that of dark energy at $z \approx (\Omega_{0,\Lambda}/\Omega_{0,\mathrm{m}})^{1/3} - 1 \approx 0.33$ about 4 Gyr ago. In the distant future com-

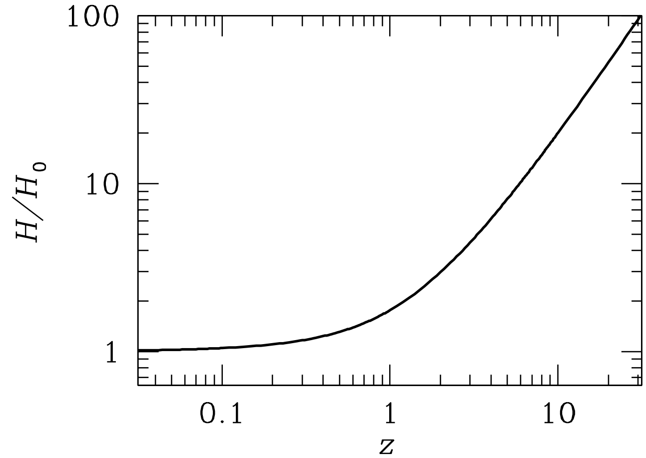

Figure B.4. The normalized Hubble parameter H/H_0 is nearly constant after $(1+z) \lesssim (\Omega_{0,\Lambda}/\Omega_{0,\mathrm{m}})^{1/3} \approx 1.33$ and $\rho_\Lambda > \rho_\mathrm{m}$. $H/H_0 \propto (1+z)^{3/2}$ at higher redshifts when $\rho_\mathrm{m} > \rho_\Lambda$, and $H/H_0 \propto (1+z)^2$ at the highest redshifts $z > z_\mathrm{eq} \sim 3500$ when $\rho_\mathrm{r} > \rho_\mathrm{m}$.

pletely dominated by dark energy, the Hubble parameter will asymptotically approach $H = H_0\,\Omega_{0,\Lambda}^{1/2} \approx 84\,h$ km s^{-1} Mpc^{-1} ≈ 59 km s^{-1} Mpc^{-1} and the scale factor will grow exponentially $[a \propto \exp(Ht)]$ with a time scale $H^{-1} \approx 1.17 \times 10^{10}\,h^{-1}$ yr ≈ 17 Gyr.

B.3 Results

B.3.1 Cosmic Times

The lookback time $t_\mathrm{L}(z)$ to a source at redshift z can be calculated by inserting Equations B.25 and B.26 into Equation B.18:

$$\boxed{\frac{t_\mathrm{L}}{t_{\mathrm{H}_0}} = \int_0^z \frac{dz'}{(1+z')E(z')}}\,. \tag{B.27}$$

This integral cannot be expressed in terms of elementary functions, but the integrand is smooth enough that the integral can be evaluated numerically by Simpson's rule, at least for finite z.

The proper age of the universe $t(z)$ at redshift z is better evaluated in terms of $a = (1+z)^{-1}$:

$$\boxed{\frac{t}{t_{\mathrm{H}_0}} = \int_0^{(1+z)^{-1}} \frac{a\,da}{(\Omega_{0,\mathrm{m}} a + \Omega_{0,\Lambda} a^4 + \Omega_{0,\mathrm{r}})^{1/2}}} \ . \tag{B.28}$$

The ratios $t_{\mathrm{L}}/t_{\mathrm{H}_0}$ and t/t_{H_0} are plotted as functions of redshift in Figure B.5. The present age of the ΛCDM universe starting with the big bang ($z = \infty$) is $t_0 \approx 0.964\, t_{\mathrm{H}_0} \approx 9.42 \times 10^9\, h^{-1}$ yr ≈ 13.5 Gyr for $\Omega_{0,\mathrm{m}} = 0.3$.

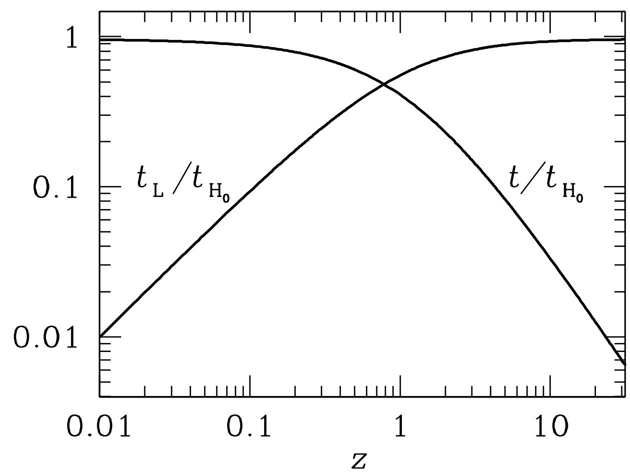

Figure B.5. The normalized lookback time ($t_{\mathrm{L}}/t_{\mathrm{H}_0}$) and the normalized age (t/t_{H_0}) in a flat ΛCDM universe with $\Omega_{0,\mathrm{m}} = 0.3$.

Figure B.5 shows that redshifts $z \gg 1$ contribute little to the age of the universe, so extremely good analytic approximations to $t_{\mathrm{L}}/t_{\mathrm{H}_0}$, t/t_{H_0}, and t_0/t_{H_0} can be made by ignoring the radiation term $\Omega_{0,\mathrm{r}}(1+z)^4$ that dominates $E(z)$ only during the brief period when $z > z_{\mathrm{eq}} \sim 3500$ ($t/t_{\mathrm{H}_0} \sim 3.4 \times 10^{-6}$, or $t \sim 5 \times 10^4\, h^{-1}$ yr $\sim 7 \times 10^4$ yr). This simplifies Equation B.27 to

$$\frac{t_{\mathrm{L}}}{t_{\mathrm{H}_0}} \approx \int_0^z \frac{dz'}{(1+z')[\Omega_{0,\mathrm{m}}(1+z')^3 + \Omega_{0,\Lambda}]^{1/2}} \ , \tag{B.29}$$

which can be integrated analytically. See Appendix C.2 for analytic approximations to t_L/t_{H_0} (Equation C.17) and t/t_{H_0} (Equation C.22). The current age of the universe normalized by the Hubble time is very nearly

$$\boxed{\frac{t_0}{t_{H_0}} \approx \frac{2}{3\,\Omega_{0,\Lambda}^{1/2}} \ln\left[\frac{1+\Omega_{0,\Lambda}^{1/2}}{(1-\Omega_{0,\Lambda})^{1/2}}\right]} \,. \tag{B.30}$$

Figure B.6 plots t_0/t_{H_0} from Equation B.30 as a function of the matter density parameter $\Omega_{0,m} = 1-\Omega_{0,\Lambda}$. In the limit $\Omega_{0,m} = 1-\Omega_{0,\Lambda} \to 0$, the universe would expand exponentially and t_0/t_{H_0} would diverge.

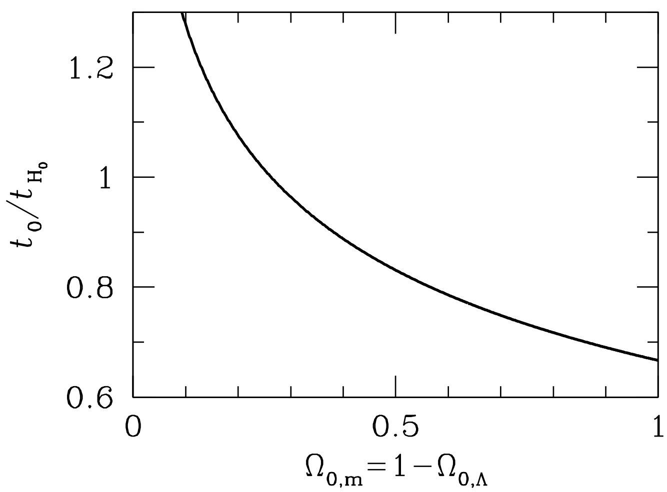

Figure B.6. The normalized age of the universe t_0/t_{H_0} as a function of $\Omega_{0,m} = 1-\Omega_{0,\Lambda}$

The observable redshift z is the traditional proxy for lookback time t_L in models of cosmological evolution. However, it can be misleading because the lookback time is an extremely nonlinear function of redshift when $z \gtrsim 1$. For example, the top panel in Figure B.7 shows the Madau & Dickinson (2014) best fit to the star formation rate density (SFRD) ψ in solar masses per year of per (comoving) Mpc^3 as a linear of function of lookback time back to $z = 8$. This plot accurately displays the fact that only 10% of today's stellar mass was assembled before $z \approx 2.9$. The very nonlinear upper abscissa indicates the redshifts z matching the lookback times on the lower abscissa. The time between $z = 0$ and $z = 1$ is ≈ 7.8 Gyr, but the time between $z = 2$ and $z = 3$ is only ≈ 1.1 Gyr. The middle panel plots the same function ψ as a linear function of redshift, with lookback time now on the very nonlinear upper abscissa. This plot makes it look like $\gg 10\%$ of today's stellar mass was assembled before $z \approx 2.9$. This nonlinearity at high redshifts is primarily caused by the fact that $(1 + z)$ is the reciprocal of the scale factor a. When ψ is plotted as a linear function of a (bottom panel), the upper abscissa showing lookback time is nearly linear and the plot of $\psi(a)$ looks much more like the plot of $\psi(t_{\rm L})$.

B.3.2 Light Travel Distance

The vacuum speed of light c is invariant, so the light travel distance $D_{\rm T}$ corresponding to lookback time $t_{\rm L}$ is

$$\boxed{D_{\rm T} = c\, t_{\rm L} = c \int_0^z \frac{dz'}{(1 + z')H}} \, . \tag{B.31}$$

The light travel distance in meters can be interpreted physically as the number of meter sticks laid end-to-end that the photon must pass on its journey from the source to the observer.

The light travel distance is of limited use in cosmography because it is the distance between two events occurring at two different proper times, t and t_0. This limitation can be illustrated by a nonrelativistic terrestrial example: two trains moving in opposite directions with speed v passed each other at time $t = 0$ (Figure B.8). The horn on one train sounded at time $t_{\rm e}$ when the distance between the trains was $d_{\rm e} = 2vt_{\rm e}$. The sound reached the other train at a later time $t_{\rm o}$ when the distance between the trains was $d_{\rm o} = 2vt_{\rm o}$. The sound travel distance is $d_{\rm T} = vt_{\rm e} + vt_{\rm o} = c_{\rm s}(t_{\rm o} - t_{\rm e})$, where $c_{\rm s} > v$ is the speed of sound. Some algebra reveals that $d_{\rm T} = d_{\rm e}\,[c_{\rm s}/(c_{\rm s} - v)] = d_{\rm o}\,[c_{\rm s}/(c_{\rm s} + v)]$ equals neither $d_{\rm e}$ nor $d_{\rm o}$.

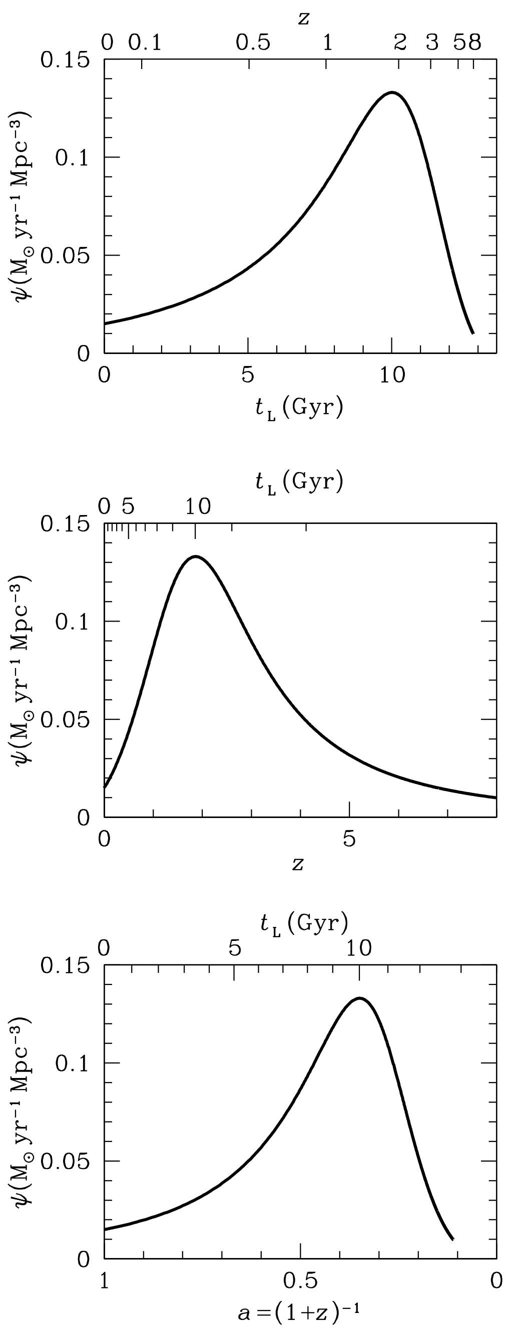

Figure B.7. The three panels in this figure show the Madau & Dickinson (2014) fit to the evolving star formation rate density as linear functions of lookback time t_L (top panel), redshift z (middle panel), and scale factor a (bottom panel). Clearly a is a much better proxy for t_L than z is.

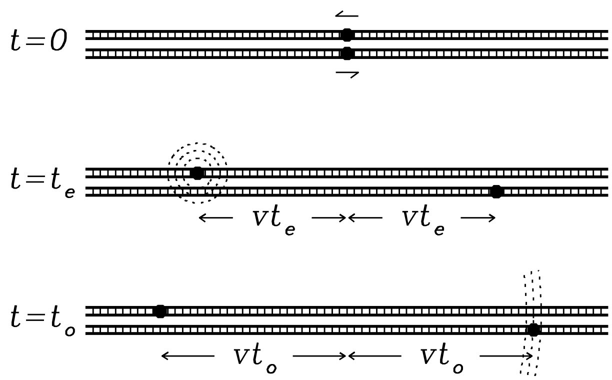

Figure B.8. Two trains moving with speed v passed each other at time $t = 0$, and the train moving left emitted a sound at time $t_{\rm e}$ when the trains were separated by $d_{\rm e} = 2vt_{\rm e}$. The sound reached train moving right at time $t_{\rm o}$ when the trains were separated by $d_{\rm o} = 2vt_{\rm o}$. The sound travel distance $d_{\rm T} = vt_{\rm e} + vt_{\rm o}$ equals neither $d_{\rm e}$ nor $d_{\rm o}$.

B.3.3 Comoving Coordinates

Comoving coordinates expand with the universe. The comoving distance $D_{\rm C}$ between any close ($D \ll D_{\rm H_0}$) pair of fundamental observers defined by

$$D_{\rm C} \equiv \frac{D(t)}{a(t)} = D_0 \tag{B.32}$$

(see Equation B.1) is independent of t and equals the present proper distance D_0. Thus comoving rulers are like rubber bands connecting neighboring fundamental observers, and their markings agree with rigid rulers today. At redshift z, the vacuum speed of light in comoving coordinates is $a^{-1}c = (1 + z)c$ and

$$dD_{\rm C} = (c/a)\, dt = (1 + z)c\, dt \ . \tag{B.33}$$

In the homogeneous universe, summing over the "local" comoving distances $dD_{\rm C}$ yields the global "line of sight" comoving distance to a distant source at any redshift

z:

$$D_{\rm C} = c\int_t^{t_0}(1+z)\,dt' \\ = c\int_z^0 (1+z')\left(\frac{dt'}{dz'}\right)dz' \;. \tag{B.34}$$

Inserting Equations B.17 and B.26 into Equation B.34 gives

$$\boxed{D_{\rm C} = D_{\rm H_0}\int_0^z \frac{dz'}{E(z')}} \;. \tag{B.35}$$

Unfortunately, this indefinite integral for $D_{\rm C}$ cannot be expressed in terms of elementary functions, only elliptic integrals that must be evaluated numerically. It is smooth enough to be evaluated by Simpson's rule (Appendix C.3). Alternatively, the simple empirical fit

$$D_{\rm C}({\rm fit}) \approx D_{\rm H_0}/\,[a/(1-a) + 0.2278 + \\ 0.2070\,(1-a)/(0.785+a) - \\ 0.0158\,(1-a)/(0.312+a)^2]\;, \tag{B.36}$$

where $a = (1+z)^{-1}$, can be used to avoid the numerical integration for most astronomical applications. Equation B.36 is accurate to within 0.2% for $z \lesssim 50$ and $\Omega_{0,\rm m} = 0.3$ (Figure B.9).

The comoving distance in meters equals the number of meter sticks laid end-to-end that would connect the source to the observer today. It is the proper distance between us and the source at time t_0, so the comoving distance is the most fundamental distance for use in ΛCDM cosmology.

The "observable" universe refers to the sphere in which signals emitted at any time $t > 0$ and traveling at the vacuum speed of light could have reached the observer today. Its light-travel radius is therefore ct_0, and the current comoving radius of the

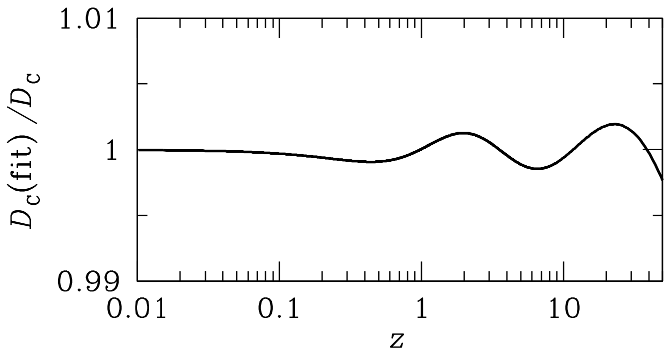

Figure B.9. Equation B.36 fits the comoving distance up to $z \approx 50$ within 0.2% for $\Omega_{\rm m} = 0.3$.

observable universe is

$$R_{0,\rm C} = D_{\rm H_0} \int_0^\infty \frac{dz'}{E(z')} \ . \tag{B.37}$$

If $h = 0.7$ and $\Omega_{0,\rm m} = 0.3$, then $R_{0,\rm C} \approx 3.24\, D_{\rm H_0} \approx 3.24 \cdot 2998\, h^{-1}\,\rm Mpc \approx 13.9$ Gpc. This number is not particularly significant, but it is often used to make amusing calculations like the following: The comoving volume of the observable universe is $V_0 = 4\pi R_{0,\rm C}^3\,/\,3 \approx 1.12 \times 10^4$ Gpc^3 $\approx 3.3 \times 10^{80}$ m^3 and the present mean density is $\rho_0 \approx 9.2 \times 10^{-27}$ kg m^{-3}, so the total mass of the observable universe is $M_0 = V_0 \rho_0 \approx 3 \times 10^{54}$ kg.

Figure B.10 shows how the observable radius $R_{0,\rm C}$ varies with the normalized matter density $\Omega_{0,\rm m}$.

The comoving volume $V_{\rm C}$ measured in comoving coordinates is valuable for tracking the cosmic evolution of source populations because the number of permanent objects (e.g., immortal fundamental observers, baryons, or galaxies if mergers are ignored) in a comoving volume element is constant. (See Appendix C.4 for a sample application of $V_{\rm C}$ to calculate source counts from local luminosity functions.) The Euclidean geometry of a flat universe implies that the total comoving volume out to redshift z is

$$\boxed{V_{\rm C} = \frac{4\pi D_{\rm C}^3}{3}} \ , \tag{B.38}$$

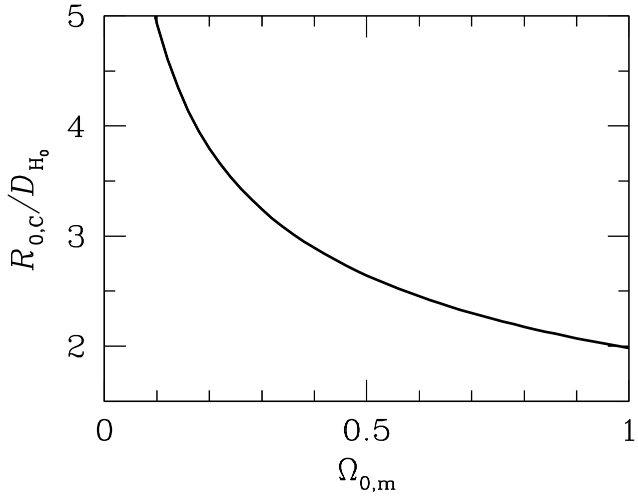

Figure B.10. The normalized comoving radius of the observable universe today $R_{0,\mathrm{C}}/D_{\mathrm{H}_0}$ as a function of $\Omega_{0,\mathrm{m}}$.

and the comoving volume in a shell covering solid angle ω sr between z and $z + dz$ is

$$dV_{\mathrm{C}} = \omega D_{\mathrm{C}}^2 \, dD_{\mathrm{C}} \ . \tag{B.39}$$

Differentiating Equation B.35 yields

$$dD_{\mathrm{C}} = D_{\mathrm{H}_0} \frac{dz}{E(z)} \tag{B.40}$$

so

$$\boxed{dV_{\mathrm{C}} = \frac{\omega D_{\mathrm{C}}^2 \, D_{\mathrm{H}_0}}{E(z)} \, dz} \ . \tag{B.41}$$

B.3.4 Angular-diameter and Proper-motion Distances

The flat ΛCDM universe is Euclidean, so the angular distance θ (rad) between two fundamental observers at the same redshift with comoving transverse separation l_0 at comoving distance D_{C} is simply

$$\theta = \frac{l_0}{D_{\mathrm{C}}} \quad (\theta \ll 1) \ . \tag{B.42}$$

A rigid source (e.g., a transverse meter stick or a gravitationally bound galaxy) has a fixed proper transverse length $l_\perp$, so its comoving transverse length is $l_0 = (1+z)\, l_\perp$ and

$$\theta = \frac{(1+z) l_\perp}{D_\mathrm{C}} \ . \tag{B.43}$$

The angular diameter distance D_A is a "convenience" distance defined to satisfy the static Euclidean equation

$$D_\mathrm{A} \equiv \frac{l_\perp}{\theta} \tag{B.44}$$

for a rigid source. Equations B.43 and B.44 imply

$$\boxed{D_\mathrm{A} = \frac{D_\mathrm{C}}{(1+z)}} \tag{B.45}$$

in a flat universe. The angular diameter in arcsec (1 arcsec $= \pi/648000$ rad) of a source with fixed proper diameter $l_\perp = 1$ kpc is shown as a function of redshift in Figure B.11.

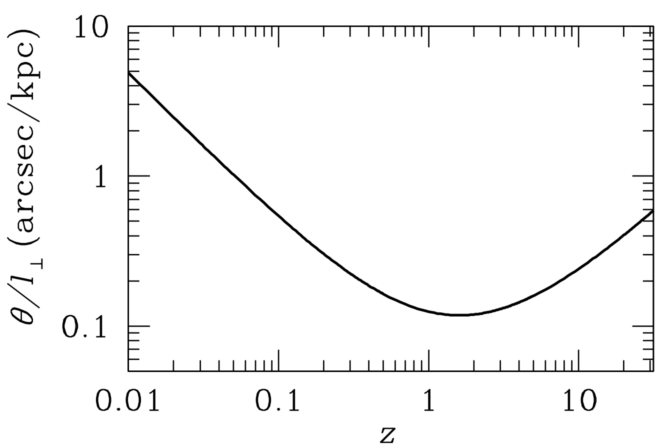

Figure B.11. The angular diameter θ of a source with a fixed proper diameter $l_\perp = 1\,$kpc has a minimum $\theta \approx 0\rlap{.}''118$ at $z \approx 1.6$ in a ΛCDM universe with $h = 0.7$ and $\Omega_\mathrm{m} = 0.3$.

The proper motion μ of a source is its observed angular speed across the sky:

$$\mu \equiv \frac{d\theta}{dt} \ . \tag{B.46}$$

For example, the radio source in the quasar 3C 279 at $z = 0.5362$ appears to consist of a stationary "core" plus moving components whose proper motions $\mu \sim 0\overset{\prime\prime}{.}0005 \text{ yr}^{-1}$ were measured by very long baseline interferometry (Piner et al. 2003).

The proper-motion distance $D_{\rm M}$ of a source with proper transverse velocity $v_\perp = dl_\perp/dt(z)$ defined by

$$D_{\rm M} \equiv \frac{v_\perp}{\mu} \tag{B.47}$$

is also called the "transverse" comoving distance. In terms of the angular diameter distance,

$$D_{\rm M} = \frac{dl_\perp}{d\theta}\frac{dt}{dt(z)} = D_{\rm A}(1+z) \ , \tag{B.48}$$

where $dt(z)$ is the proper time measured by a fundamental observer at the source redshift z. The proper-motion distance is just the angular diameter distance multiplied by the $(1+z)$ time dilation factor. In a flat universe,

$$\boxed{D_{\rm M} = D_{\rm C}} \ , \tag{B.49}$$

so the "line of sight" comoving distance $D_{\rm C}$ equals the "transverse" comoving distance $D_{\rm M}$ and the two can be treated simply as a "the" comoving distance. In the non-Euclidean geometry of a curved universe $D_{\rm M} \neq D_{\rm C}$ (Hogg 1999).

B.3.5 Luminosities and Fluxes

Let L be the total (or bolometric) luminosity (emitted power, SI units W) of an isotropic source measured in the source frame and F be the total flux (power received per unit area, SI units W m^{-2}) in the observer's frame. (If the source is not isotropic, L should be replaced by 4π times the power per steradian beamed in the direction of the observer.)

In a static Euclidean universe, the inverse-square law accounts for the transverse spatial dilution of photons spread over the area A_0 of the spherical surface containing the observer and centered on the source: $F = L/A_0$. In the Euclidean but expanding ΛCDM universe, the present area of the spherical shell centered on a source at redshift z and containing the observer is $A_0 = 4\pi D_{\mathrm{C}}^2$. It is *not* 4π times the square of the distance D_{T} covered by the photons in an expanding universe; the name "inverse-square (of the distance) law" is misleading and "inverse area law" would be better.

In an expanding but Euclidean flat universe, the observed flux is lower than in a static universe because (1) the observed rate at which photons cross the $t = t_0$ surface centered on the source and containing the observer is a factor $(1+z)$ lower than the rate at which they were emitted and (2) the observed energy $E = hc/\lambda_{\mathrm{o}}$ of each redshifted photon is a factor $(1+z)$ lower than its energy $E = hc/\lambda_{\mathrm{e}}$ in the source frame. Consequently

$$F = \left(\frac{L}{4\pi D_{\mathrm{C}}^2}\right)\left(\frac{1}{1+z}\right)^2 . \tag{B.50}$$

The luminosity distance D_{L} is another "convenience" distance defined by the form of the static Euclidean inverse-square law:

$$\boxed{F \equiv \frac{L}{4\pi D_{\mathrm{L}}^2}} . \tag{B.51}$$

Equation B.50 implies

$$\boxed{D_{\mathrm{L}} = (1+z)D_{\mathrm{C}}} . \tag{B.52}$$

B.3.6 Comparison of Distance Types

Figure B.12 compares the luminosity distance D_{L}, the comoving distance D_{C}, the light travel distance D_{T}, and the angular-diameter distance D_{A} in a ΛCDM universe with current matter density parameter $\Omega_{0,\mathrm{m}} = 0.3$. All of the plotted distances are normalized by the current Hubble distance $D_{\mathrm{H}_0} = c/H_0 \approx 2998\, h^{-1}$ Mpc $\approx$ 4280 Mpc.

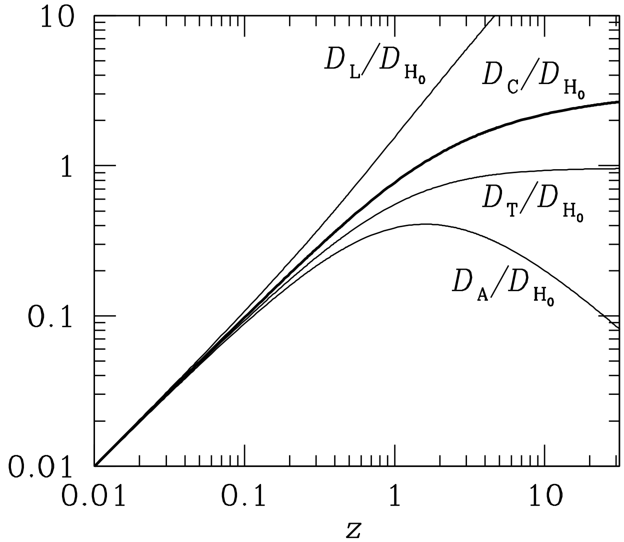

Figure B.12. The luminosity distance D_{L}, the comoving distance D_{C}, the light travel distance D_{T}, and the angular diameter distance D_{A}, all normalized by the current Hubble distance D_{H_0}, are compared for $\Omega_{0,\mathrm{m}} = 0.3$.

These distances also vary slowly and smoothly with $\Omega_{0,\mathrm{m}}$, but the effect of changing $\Omega_{0,\mathrm{m}}$ cannot be represented by a scale factor like h. Figure B.13 shows the ratios of $D_{\mathrm{C}}(\Omega_{0,\mathrm{m}})$ to $D_{\mathrm{C}}(\Omega_{0,\mathrm{m}} = 0.3)$ for matter densities from $\Omega_{0,\mathrm{m}} = 0.28$ (top curve) through 0.34 (bottom curve) that include the best measured $\Omega_{0,\mathrm{m}} = 0.315 \pm 0.013$ (Planck Collaboration et al. 2016) and its quoted uncertainty. Near $\Omega_{0,\mathrm{m}} = 0.3$, $dD_{\mathrm{C}}/d\Omega_{0,\mathrm{m}} \approx -0.006$ at $z = 1$ and $dD_{\mathrm{C}}/d\Omega_{0,\mathrm{m}} \approx -0.013$ when $z \gg 1$.

B.3.7 Spectral Luminosities and Flux Densities

The spectral luminosity $L_\nu(\nu)$ of a source is its luminosity per unit frequency (SI units W Hz^{-1}). In this notation, the subscript ν just means "per unit frequency" in the source frame and doesn't refer to any particular frequency. The ν in parentheses is the actual frequency in the source frame, so $L_\nu(1.4\text{ GHz})$ is the power per unit frequency emitted at $\nu = 1.4$ GHz in the source frame. The spectral flux density F_ν (or S) of a source is the observed flux per unit frequency in the observer's frame (SI units W m^{-2} Hz^{-1}, or the astronomically practical Jy $\equiv 10^{-26}$ W m^{-2} Hz^{-1}).

All of the photons received in a narrow logarithmic frequency range centered on

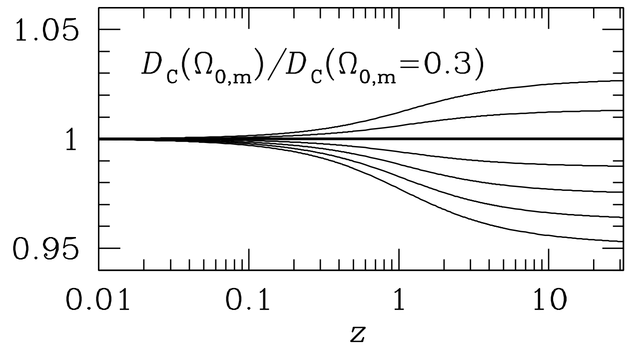

Figure B.13. The comoving distances D_C are plotted for $\Omega_{0,m} = 0.28$ (top curve) through $\Omega_{0,m} = 0.34$ (bottom curve) in steps of $\Delta\Omega_{0,m} = 0.01$, all normalized by $D_C(\Omega_{0,m} = 0.3)$ (heavy line).

frequency ν were emitted in the equally narrow logarithmic frequency range centered on $[(1+z)\nu]$, so the bolometric Equation B.50 implies

$$\nu F_\nu(\nu) = [(1+z)\nu] \frac{L_\nu[(1+z)\nu]}{4\pi D_L^2} \tag{B.53}$$

and

$$\boxed{F_\nu(\nu) = (1+z)\frac{L_\nu[(1+z)\nu]}{4\pi D_L^2}} \ . \tag{B.54}$$

The leading factor of $(1+z)$ in Equation B.54 comes from bandwidth compression: photons emitted over the frequency range $[(1+z)\Delta\nu]$ are squeezed into the frequency range $\Delta\nu$ in the observer's frame.

The spectral index α between frequencies ν_1 and ν_2 is defined by

$$\alpha(\nu_1, \nu_2) \equiv +\frac{\ln[L(\nu_1)/L(\nu_2)]}{\ln(\nu_1/\nu_2)} \ . \tag{B.55}$$

[Beware that some authors define α with the opposite sign.] In terms of $\alpha[\nu, (1+z)\nu]$, Equation B.54 becomes

$$F_\nu(\nu) = (1+z)^{\alpha+1} \frac{L_\nu(\nu)}{4\pi D_L^2} \ . \tag{B.56}$$

If the spectral luminosity distance D_{L_ν} is defined by analogy with Equation B.51:

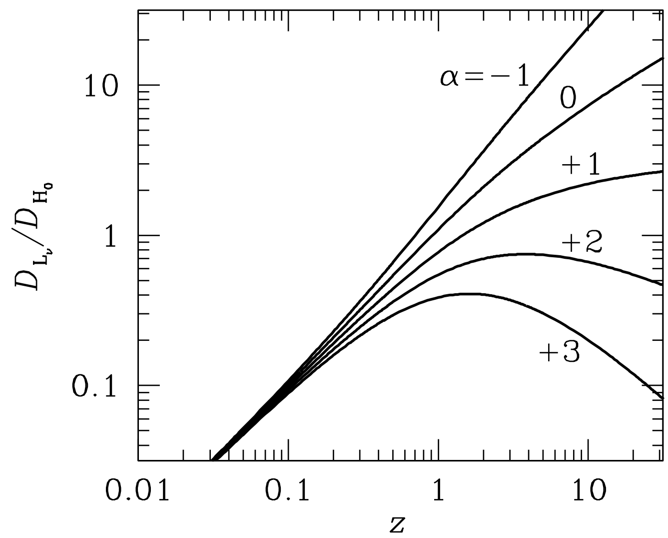

Figure B.14. Spectral luminosity distances normalized by the current Hubble distance are plotted for spectral indices $\alpha = -1$, 0, +1, +2, and +3. $\Omega_{0,\rm m} = 0.3$ in all cases.

$$F_\nu \equiv \frac{L_\nu}{4\pi D_{\rm L_\nu}^2}, \tag{B.57}$$

then Equation B.54 implies

$$D_{\rm L_\nu} = D_{\rm L}\,(1+z)^{-(\alpha+1)/2}\ . \tag{B.58}$$

Figure B.14 shows $D_{\rm L_\nu}(z)/D_{\rm H_0}$ for a range of spectral indices. Steep-spectrum ($\alpha \approx -1$) synchrotron sources have $D_{\rm L_\nu} \approx D_{\rm L}$ and consequently are quite faint at high redshifts. Flat-spectrum self-absorbed synchrotron sources and optically thin free-free emitters ($\alpha \approx 0$) are only slightly stronger. For a source with $\alpha = +1$, $D_{\rm L_\nu} = D_{\rm C}$. Blackbody emission in the long wavelength Rayleigh-Jeans limit has $\alpha \approx +2$. Optically thin dusty galaxies have $\alpha \sim +3$ at wavelengths $0.1 \lesssim \lambda_{\rm e} \lesssim 1$ mm, so the $D_{\rm L_\nu} \sim D_{\rm A}$ and their submillimeter flux densities are nearly independent of redshift over a broad range centered around $z \sim 1.6$.

The spectral flux density F_λ measured per unit wavelength (SI units W m^{-3}) is related to F_ν by

$$|F_\lambda \, d\lambda| = |F_\nu \, d\nu| \tag{B.59}$$

so

$$F_\lambda = \frac{c}{\lambda^2} F_\nu \quad \text{and} \quad L_\lambda = \frac{c}{\lambda^2} L_\nu. \tag{B.60}$$

The wavelength counterparts of Equations B.53 and B.54 are

$$\lambda \, F_\lambda(\lambda) = \frac{[\lambda/(1+z)] \, L_\lambda[\lambda/(1+z)]}{4\pi D_{\rm L}^2} \; . \tag{B.61}$$

and

$$\boxed{F_\lambda(\lambda) = (1+z)^{-1} \, \frac{L_\lambda[\lambda/(1+z)]}{4\pi D_{\rm L}^2}} \; . \tag{B.62}$$

B.3.8 Magnitudes and K Corrections

The apparent magnitude m and absolute magnitude M of a source are related by

$$\boxed{m - M = 5 \log_{10}\left(\frac{D_{\rm L}}{10 \text{ pc}}\right) + K} \; , \tag{B.63}$$

where

$$DM \equiv 5 \log_{10}\left(\frac{D_{\rm L}}{10 \text{ pc}}\right) \tag{B.64}$$

is the bolometric distance modulus (Figure B.15) in magnitudes (1 mag $\equiv 10^{-0.4}$). The K correction converts the apparent magnitude measured through a filter covering a fixed wavelength range (Oke & Sandage 1968; Hogg et al. 2002) in the observer's frame to yield the absolute magnitude over the same wavelength range in the source frame. The bolometric K correction is zero. There are many magnitude systems covering different bandpasses and having different zero points (Blanton & Roweis 2007) relating $m = 0$ to flux density.

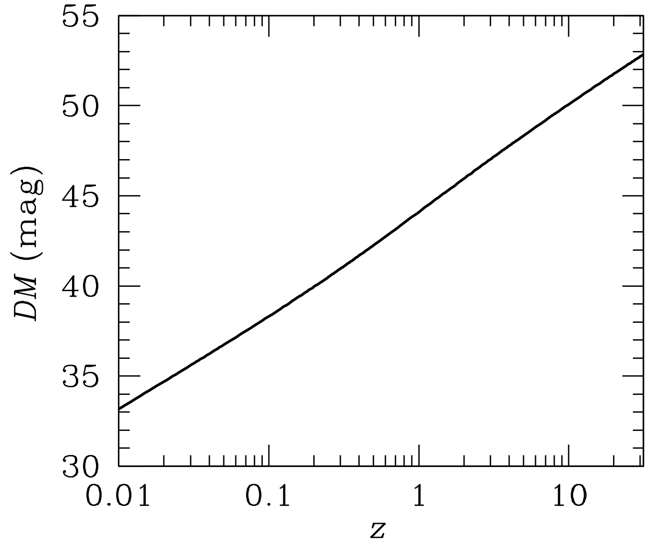

Figure B.15. The bolometric distance modulus DM as a function of redshift z for $h = 0.7$, $\Omega_{0,\mathrm{m}} = 0.3$.

Equation B.54 implies that

$$
\begin{aligned}
K = -2.5\log_{10}&\left\{(1+z)\frac{L_\nu[(1+z)\nu]}{4\pi D_{\mathrm{L}}^2}\right\}+ \\
&2.5\log_{10}\left\{\frac{L_\nu(\nu)}{4\pi D_{\mathrm{L}}^2}\right\} \\
&\boxed{K = -2.5\log_{10}\left\{(1+z)\frac{L_\nu[(1+z)\nu]}{L_\nu(\nu)}\right\}}\ .
\end{aligned}
\tag{B.65}
$$

In terms of the spectral index α,

$$
\begin{aligned}
K &= -2.5\log_{10}\left[(1+z)^{\alpha+1}\right] \\
&= -2.5\,(\alpha+1)\log_{10}(1+z)\ .
\end{aligned}
\tag{B.66}
$$

In terms of wavelengths,

$$
\boxed{K = -2.5\log_{10}\left\{(1+z)^{-1}\frac{L_\lambda[\lambda/(1+z)]}{L_\lambda(\lambda)}\right\}}\ .
\tag{B.67}
$$

B.3.9 Spectral Lines

Spectral lines are narrow (line width $\Delta\nu \ll \nu$) emission or absorption features in the spectra of gaseous or ionized sources. The total line luminosity L is related to the total line flux F and the line flux density F_ν by Equation B.51, so

$$L = 4\pi D_{\mathrm{L}}^2 F = 4\pi D_{\mathrm{L}}^2\, F_\nu \Delta\nu \ . \tag{B.68}$$

In Equation B.68, the SI units of F are W m^{-2} = 10^{26} Jy Hz. However, line fluxes are often reported in the dimensionally confusing units Jy km s^{-1} based on the non-relativistic Doppler equation

$$\frac{\Delta\nu}{\nu} \approx \frac{\Delta v}{c} \ll 1 \ . \tag{B.69}$$

Solving Equation B.69 for Δv yields the factor needed to convert from Jy km s^{-1} to Jy Hz:

$$1 \text{ km s}^{-1} \approx \frac{\nu}{299792} \text{ Hz} \ . \tag{B.70}$$

See Carilli & Walter (2013) for a detailed discussion of this equation and its uses.

B.3.10 Total Intensity and Specific Intensity

The total intensity or bolometric brightness B of a source is the power it emits per unit area per unit solid angle ω (SI units W m^{-2} sr^{-1}). In a *static* Euclidian universe, intensity is conserved along any ray passing through empty space and the brightness B_0 seen by an observer at rest with respect to the source equals B. For a source at redshift z in the Euclidean but expanding ΛCDM universe, the observed brightness B_0 can be calculated with the aid of Equations B.45 and B.52. For a source at any comoving distance D_{C}, expansion multiplies its luminosity distance by $(1+z)$ and divides its angular diameter distance by $(1+z)$, so

$$\frac{B_0}{B} = \frac{F_0}{F}\frac{\omega}{\omega_0} = (1+z)^{-2}(1+z)^{-2} \tag{B.71}$$

and

$$\boxed{\frac{B_0}{B} = (1+z)^{-4}} \; . \tag{B.72}$$

The specific intensity or spectral brightness $B_\nu(\nu)$ of a source is its power per unit frequency per unit solid angle (SI units W m^{-2} Hz^{-1} sr^{-1}) at frequency ν in the source frame.

All of the photons received in a narrow logarithmic frequency range centered on ν were emitted in the equally narrow logarithmic frequency range centered on $[(1+z)\nu]$, so the bolometric brightness Equation B.72 implies

$$\nu B_{\nu 0} = \frac{[(1+z)\nu]\, B_\nu[(1+z)\nu]}{(1+z)^4} \; . \tag{B.73}$$

$$\boxed{B_{\nu 0}(\nu) = (1+z)^{-3} B_\nu[(1+z)\nu]} \; . \tag{B.74}$$

For a source with spectral index α,

$$B_{\nu 0}(\nu) = (1+z)^{\alpha - 3} B_\nu(\nu) \; . \tag{B.75}$$

The Planck brightness spectrum of a blackbody source at temperature T is

$$B_\nu(\nu \,|\, T) = \frac{2h\nu^3}{c^2}\left[\exp\left(\frac{h\nu}{kT}\right) - 1\right]^{-1} . \tag{B.76}$$

If the source is at redshift z, the observed spectrum

$$\begin{aligned} B_{\nu 0}(\nu) &= (1+z)^{-3} B_\nu[(1+z)\nu \,|\, T] \\ &= \frac{2h}{c^2}\left[\frac{(1+z)\nu}{(1+z)}\right]^3 \left\{\exp\left[\frac{h\nu}{k}\frac{(1+z)}{T}\right] - 1\right\}^{-1} \end{aligned} \tag{B.77}$$

is just the Planck spectrum $B_\nu(\nu|T_0)$ of a blackbody with temperature $T_0 = T/(1+z)$. The source of the $T_0 \approx 2.73$ K CMB seen today is the $T \sim 3000$ K blackbody surface of last scattering when the universe became transparent at $z \sim 1100$.

B.3.11 Nonrelativistic Approximation Errors

In the low-redshift limit, it is tempting to calculate intrinsic source parameters from the observables using the nonrelativistic distance approximation

$$D_{\mathrm{N}} \equiv \frac{cz}{H_0} \ . \tag{B.78}$$

Figure B.16 displays ratios of the relativistically correct luminosity distance D_{L}, comoving distance D_{C}, light travel distance D_{T}, and angular diameter distance D_{A} in a ΛCDM universe with $\Omega_{0,\mathrm{m}} = 0.3$ to D_{N}.

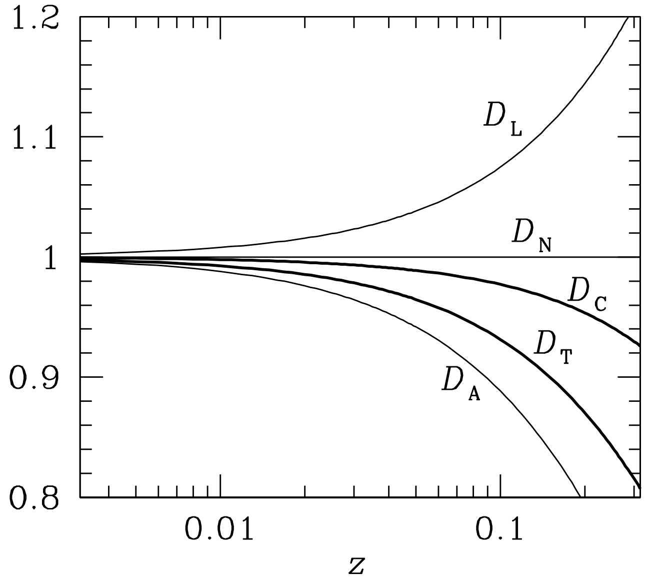

Figure B.16. The ratios of the relativistically correct distances D_{L}, D_{C}, D_{T}, and D_{A} to the nonrelativistic distance approximation $D_{\mathrm{N}} \equiv cz/H_0$ at low redshifts z indicate the errors that can result from using D_{N}.

For example, the bolometric luminosity L of a source at redshift z is proportional to D_{L}^2, so the luminosity calculated using D_{N} instead will be too low by a factor of $(D_{\mathrm{L}}/D_{\mathrm{N}})^2$. It will be 5% too low for a source at redshift $z \approx 0.032$ ($cz \sim 10^4$ km s^{-1}), and the maximum redshift at which the luminosity error is $< 10\%$ is $z \approx 0.065$ ($cz \sim 2 \times 10^4$ km s^{-1}).

The calculated linear size of a source is proportional to $D_{\mathrm{A}} < D_{\mathrm{N}}$, so using D_{N} will overestimate source size by 5% at $z \approx 0.043$ ($cz \sim 1.3 \times 10^4$ km s^{-1}) and 10% at $z \approx 0.089$ ($cz \sim 2.7 \times 10^4$ km s^{-1}).

Such errors are systematic, so they can easily dominate the Poisson errors in statistical properties of large source populations. Luminosity functions are particularly vulnerable because they depend on the maximum redshifts at which sources *could* have remained in the flux-limited population, not just the actual source redshifts.

B.3.12 Example Calculation: A Single Source

The bent triple radio source 4C +39.05 (Figure B.17) is identified with the galaxy 2MASX 02005301+3935003 at $z \approx 0.0718$. Its 1.4 GHz flux density is $S \approx 635$ mJy and its angular diameter is $\theta \approx 200''$.

The light-travel time from 4C +39.05 can be found by inserting $z = 0.0718$ and $\Omega_{0,\Lambda} \approx 1 - \Omega_{0,\mathrm{m}} = 1 - 0.3 = 0.7$ into Equation C.17; it is $t_{\mathrm{L}}/t_{\mathrm{H}_0} \approx 0.0682$. For $h = 0.7$, $t_{\mathrm{H}_0} \approx 14$ Gyr (Equation B.12) and $t_{\mathrm{L}} \approx 9.5 \times 10^8$ yr.

For $h = 0.7$ and $\Omega_{0,\mathrm{m}} = 0.3$, its comoving distance from either Equation B.35 or Equation B.36 is $D_{\mathrm{C}} \approx 303$ Mpc. The comoving volume within the sphere ($\omega = 4\pi$ sr) of this radius is (Equation B.38) $V_{\mathrm{C}} = 4\pi D_{\mathrm{C}}^3/3 \approx 4 \cdot 3.14 \cdot (303\mathrm{Mpc})^3/3 \approx 1.17 \times 10^8$ Mpc^3.

The angular-size distance (Equation B.45) to 4C +39.05 is $D_{\mathrm{A}} = D_{\mathrm{C}}/(1+z) \approx 283$ Mpc, so its projected linear size is $l_{\perp} = \theta D_{\mathrm{A}} \approx 200$ arcsec $\cdot\, \pi/648000$ rad/arcsec $\cdot$ 283 Mpc ≈ 0.27 Mpc. Notice that the angular diameter of this source would remain $\theta > 30''$ if it were moved to *any* redshift (Figure B.11).

At 4.85 GHz 4C +39.05 has flux density $S \approx 200$ mJy, so its spectral index (Equation B.55) is

$$\alpha = +\frac{\ln(635\ \mathrm{mJy}/200\ \mathrm{mJy})}{\ln(1.4\ \mathrm{GHz}/4.85\ \mathrm{GHz})} \approx -0.9\ . \tag{B.79}$$

The absolute spectral luminosity of 4C +39.05 at $\nu = 1.4$ GHz in the source frame

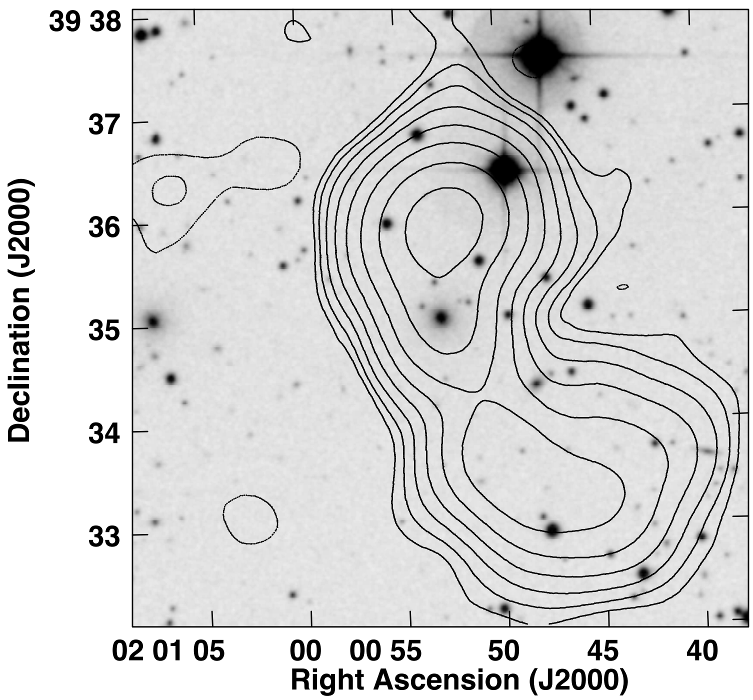

Figure B.17. The bent triple radio source 4C +39.05 (contours at $\pm1, 2, 4, \ldots, 128$ mJy beam^{-1} in a $45''$ FWHM Gaussian beam) originated in the elliptical galaxy 2MASX 02005301+3935003 at the center of this optical finding chart (gray scale).

can be obtained by solving Equation B.56 for $L_\nu(\nu)$:

$$L_\nu(1.4 \text{ GHz}) = 4\pi D_\text{L}^2 (1+z)^{-\alpha-1} F_\nu(1.4 \text{ GHz}) \ , \tag{B.80}$$

where $D_\text{L} = (1+z)D_\text{C} \approx 1.0718 \cdot 303 \text{ Mpc} \approx 325 \text{ Mpc} \cdot 3.0857 \times 10^{22} \text{ m Mpc}^{-1} \approx 1.00 \times 10^{25}$ m (Equation B.52).

$$\begin{aligned} L_\nu(1.4 \text{ GHz}) &\approx 4 \cdot 3.14 \cdot (1.00 \times 10^{25} \text{ m})^2 \cdot \\ &\quad 1.0718^{-0.1} \cdot 635 \text{ mJy} \cdot 10^{-29} \, \text{W} \, \text{m}^{-2} \, \text{Hz}^{-1} \, \text{mJy}^{-1} \\ L_\nu(1.4 \text{ GHz}) &\approx 7.9 \times 10^{24} \, \text{W} \, \text{Hz}^{-1} \ . \end{aligned} \tag{B.81}$$

The $\lambda \approx 2.2\ \mu$m magnitude of the host galaxy is $k_\text{20fe} \approx 11.788$. The K correction at this wavelength is $K \approx -6.0 \log_{10}(1+z)$ independent of galaxy type and is valid for any $z \lesssim 0.25$ (Kochanek et al. 2001). At $z = 0.0718$, $K \approx -0.181$ and Equation B.63 can be used to calculate the absolute magnitude of the host galaxy at $\lambda \approx 2.2$ μm in the source frame:

$$\begin{aligned} K_{\rm 20fe} &\approx k_{\rm 20fe} - 5 \log_{10}\left(\frac{D_{\rm L}}{10 \text{ pc}}\right) - K \\ &\approx 11.778 - 5 \log_{10}(303 \times 10^6 \text{ pc}/10 \text{ pc}) + 0.181 \\ &\approx 11.778 - 37.407 + 0.181 \approx -25.448 \ . \end{aligned} \tag{B.82}$$

The $k_{\rm 20fe} = 0$ flux density is $S = 666.7 \pm 12.6$ Jy at $\nu_{\rm o} \approx 1.390 \times 10^{14}$ Hz (http://www.ipac.caltech.edu/2mass/releases/allsky/faq.html#jansky) so $K_{\rm 20fe} = 0$ corresponds to a spectral luminosity

$$\begin{aligned} L_\nu \approx\, & 4\pi\,(10\text{pc} \,\cdot\, 3.0857 \times 10^{16} \text{ m pc}^{-1})^2 \,\cdot \\ & 666.7 \text{ Jy} \,\cdot\, 10^{-26} \text{ W m}^{-2} \text{ Hz}^{-1} \text{ Jy}^{-1} \\ \approx\, & 7.98 \times 10^{12} \text{ W Hz}^{-1} \end{aligned} \tag{B.83}$$

and $K_{20fe} = -25.448$ corresponds to a spectral luminosity

$$\begin{aligned} L_\nu &\approx 7.98 \times 10^{12} \text{ W Hz}^{-1} \,\cdot\, 10^{0.4 \cdot 25.448} \\ &\approx 1.2 \times 10^{23} \text{ W Hz}^{-1} \end{aligned} \tag{B.84}$$

at $\nu_{\rm e} \approx 1.390 \times 10^{14}$ Hz in the source frame.

From Equation B.75, the observed 1.4 GHz spectral brightness of the $\alpha \approx -0.9$ radio source at $z \approx 0.0718$ is lower than its 1.4 GHz specific intensity in the source frame by the factor

$$\frac{B_{\nu 0}}{B_\nu} = (1+z)^{\alpha - 3} \approx 1.0718^{-3.9} \approx 0.76 \ . \tag{B.85}$$

B.3.13 Example Calculation: A Source Population

The 1.4 GHz spectral luminosity of a star-forming galaxy is a linear and dust-unbiased tracer of the recent star formation rate (SFR) (Murphy et al. 2011):

$$\left(\frac{\mathrm{SFR}}{M_\odot\,\mathrm{yr}^{-1}}\right) = 1.0 \pm 0.1 \times 10^{-21}\left(\frac{L_{1.4\,\mathrm{GHz}}}{\mathrm{W\,Hz}^{-1}}\right) . \tag{B.86}$$

If the comoving space density of 1.4 GHz sources in star-forming galaxies is $\rho(L_{1.4\,\mathrm{GHz}})$, then the local luminosity-weighted spectral power density function (Equation C.35) is

$$U_{\mathrm{dex}}(L_\nu \,|\, z) = \ln(10) L_\nu^2 \rho(L_\nu \,|\, z) \ . \tag{B.87}$$

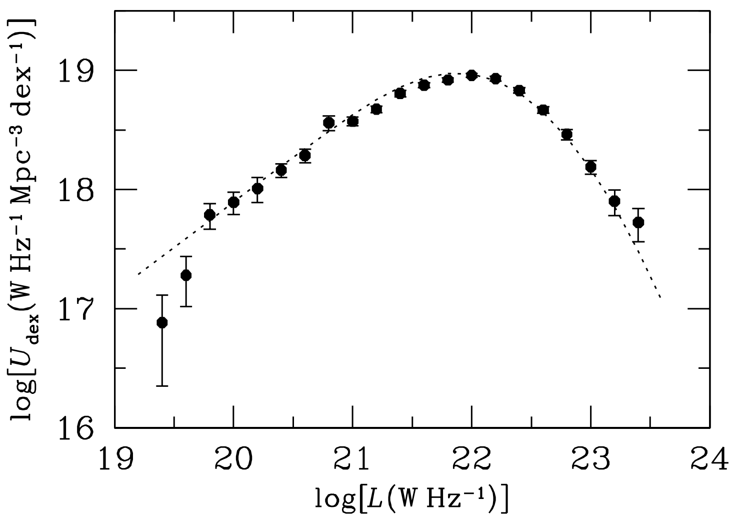

Figure B.18. The local 1.4 GHz spectral energy density function U_{dex} of galaxies whose radio emission is powered primarily by star formation, not by AGNs.

The observed $U_{\mathrm{dex}}(L_{1.4\,\mathrm{GHz}} \,|\, z \approx 0)$ (Condon et al. 2019) is shown by the data points in Figure B.18, and it can be approximated by the function (dotted curve in

Figure B.18)

$$
\begin{aligned}
U_{\rm dex}(L_{1.4\,{\rm GHz}}\,|\,z \approx 0) \approx L_{1.4\ {\rm GHz}}({\rm W\,Hz^{-1}}) \cdot \\
4.0 \times 10^{-3}\ {\rm Mpc^{-3}\ dex^{-1}} \left(\frac{L_{1.4\,{\rm GHz}}}{L^*_\nu}\right)^\beta \cdot \\
\exp\left[-\frac{1}{2\sigma^2}\log^2\left(1+\frac{L_{1.4\,{\rm GHz}}}{L^*_\nu}\right)\right]\,, \qquad \text{(B.88)}
\end{aligned}
$$

where $L^*_{1.4\,{\rm GHz}} = 1.7 \times 10^{21}$ W Hz^{-1}, $\beta = -0.24$, and $\sigma = 0.585$.

The evolution of the the SFRD $\psi(z)$ can be constrained by comparing the observed brightness-weighted 1.4 GHz source count $S^2n(S)$ (Condon et al. 2012) shown as the heavy curve in Figure B.19 with counts predicted by Equation C.37 for various evolving $U_{\rm dex}(L_{1.4\,{\rm GHz}}\,|\,z)$. The total count has two peaks, the peak at $\log[S({\rm Jy})] \sim -1$ produced by AGN-powered radio sources and the peak at $\log[S({\rm Jy})] \sim -4.5$ attributed to star-forming galaxies.

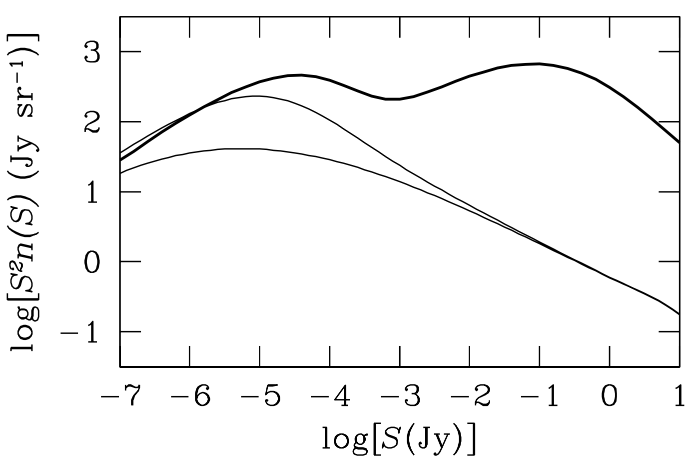

Figure B.19. The brightness-weighted count $S^2n(S)$ of all 1.4 GHz radio sources is shown by the heavy curve. The lower light curve is the count of radio sources that would be produced by a non-evolving population of star-forming galaxies, and the upper light curve is the count that would result from pure luminosity evolution consistent with the Madau & Dickinson (2014) formula for the evolving SFRD $\psi(z)$.

For the case of no evolution in the SFRD ψ, inserting $U_{\rm dex}(L_{1.4\,{\rm GHz}}\,|\,z) = U_{\rm dex}(L_{1.4\,{\rm GHz}}\,|\,z \approx 0)$ and the median spectral index $\alpha \approx -0.7$ yields the lower light curve in Figure B.19. The slope of this curve is ≈ -0.5 at high flux densities because the stronger star-forming galaxies are at such low redshifts that their counts approach the static Euclidean limit $S^{5/2}n(S) =$ constant.

The Madau & Dickinson (2014) model for the evolution of the SFRD ψ is shown in Figure B.7. Their result might be modeled in terms of pure luminosity evolution: the comoving density of star-forming galaxies is constant and the luminosity of each galaxy is proportional to ψ, so $U_{\rm dex}(L_{1.4\,{\rm GHz}}\,|\,z) = [\psi(z)/\psi(0)]\,U_{\rm dex}(L_{1.4\,{\rm GHz}}\,|\,z \approx 0)$. Inserting this $U_{\rm dex}(L_{1.4\,{\rm GHz}}\,|\,z)$ into Equation C.37 yields the higher thin curve in Figure B.19. Both thin curves agree for the low-redshift sources at high flux densities, but the evolving SFRD produces a peak at $\log[S({\rm Jy})] \sim -5$ that is much closer to the observed faint-source count.

Appendix C

Important Calculations

C.1 2MASX/NVSS Sky Area

The 2MASX/NVSS sample covers the sky with J2000 $\delta > \delta_0 = -40°$ except for absolute galactic latitudes $|b| < b_0 = 20°$. The sample solid angle is the solid angle with $\delta > \delta_0$ minus the solid angle with $|b| < b_0$, except for (therefore plus) the solid angle with $|b| < b_0$ and δ_0:

$$\Omega = \Omega(\delta > \delta_0) - \Omega(|b| < b_0) + \Omega(|b| < b_0, \delta < \delta_0) \ . \tag{C.1}$$

On a unit sphere the Cartesian coordinates corresponding to the J2000 equatorial coordinates α, δ are

$$\begin{aligned} x &= \sin\alpha\cos\delta \\ y &= \cos\alpha\cos\delta \\ z &= \sin\delta \end{aligned} \tag{C.2}$$

The circle of constant declination δ has radius $r = (x^2 + y^2)^{1/2} = \cos\delta$, so the solid angle covering all right ascensions α and declinations north of $\delta_0 = -40°$ is

$$\Omega(\delta > \delta_0) = 2\pi \int_{\delta_0}^{\pi/2} \cos\delta \, d\delta = 2\pi(1 - \sin\delta_0) \approx 10.3219 \text{ sr} \tag{C.3}$$

Likewise, the band covering all galactic longitudes l and absolute galactic latitudes $|b| < b_0 = 20°$ covers solid angle

$$\Omega(|b| < b_0) = 2\pi \int_{-b_0}^{b_0} \cos b \, db = 4\pi \sin b_0 \approx 4.2980 \text{ sr} \tag{C.4}$$

The third term of Equation C.1 is the solid angle with $|b| < b_0$ and $\delta < \delta_0$. It can be written in the form

$$\Omega(\delta < \delta_0, |b| < b_0) = \int_{-b_0}^{b_0} \cos b \int_{l_{\min}(b)}^{l_{\max}(b)} dl \, db \tag{C.5}$$

where $l_{\max}(b) - l_{\min}(b)$ is the range of galactic longitudes at galactic latitude b and declination δ. Calculating that range requires converting between equatorial and galactic coordinates.

The J2000 equatorial coordinates of the North Galactic Pole (NGP) are $\alpha_\mathrm{p} = 12^\mathrm{h}51^\mathrm{m}26^\mathrm{s}$ and $\delta_\mathrm{p} = +27°7'42'' \approx 27.1283$ deg.[1] The 2MASX/NVSS region spans all α, so only δ_p matters. We can define "shifted" galactic coordinates (λ, b) with $\alpha_\mathrm{p} = 0$ so converting from (α, δ) to (λ, b) needs only a single rotation about the x axis and

$$\begin{aligned} x &= \sin\lambda\cos b \\ y &= \cos\lambda\cos b \\ z &= \sin b \ . \end{aligned} \tag{C.6}$$

Counterclockwise rotation through any angle ψ about the x axis yields new coordi-

[1] http://astronomy.swin.edu.au/cosmos/N/North+Galactic+Pole

nates

$$
\begin{aligned}
x' =& x \\
y' =& y\cos\psi + z\sin\psi \\
z' =& z\cos\psi - y\sin\psi
\end{aligned}
\tag{C.7}
$$

Rotating these coordinates *clockwise* by the codeclination of the galactic pole ($\pi/2 - \delta_{\mathrm{p}}$) corresponds to $\psi = (\delta_{\mathrm{p}} - \pi/2)$. Thus the three equations for λ, b as functions of α, δ, and ψ are:

$$
\begin{aligned}
x' &= \sin\lambda\cos b & &= \sin\alpha\cos\delta \\
y' &= \cos\lambda\cos b & &= (\cos\alpha\cos\delta)\cos\psi + \sin\delta\sin\psi \\
z' &= \sin b & &= \sin\delta\cos\psi - (\cos\alpha\cos\delta)\sin\psi
\end{aligned}
\tag{C.8}
$$

Solving the z' equation for

$$
(\cos\alpha\cos\delta) = \frac{\sin\delta\cos\psi - \sin b}{\sin\psi} \tag{C.9}
$$

and substituting this into the y' equation gives

$$
\cos\lambda\cos b = \left(\frac{\sin\delta\cos\psi - \sin b}{\sin\psi}\right)\cos\psi + \sin\delta\sin\psi \tag{C.10}
$$

The longitude $\lambda(b, \delta_0)$ at which galactic latitude b crosses J2000 declination δ_0 is

$$
\lambda(b, \delta_0) = \arccos\left[\left(\frac{\sin\delta_0\cos\psi - \sin b}{\sin\psi\cos b}\right)\cos\psi + \frac{\sin\delta_0\sin\psi}{\cos b}\right] \tag{C.11}
$$

Thus Equation C.5 becomes

$$
\Omega(\delta < \delta_0, |b| < b_0) = \int_{-b_0}^{b_0} 2\lambda(b, \delta_0)\cos b\, db \tag{C.12}
$$

in (λ, b) coordinates. Integrating Equation C.12 numerically for $\delta_0 = -40°$ and $b_0 = 20°$ gives $\Omega(\delta < \delta_0, |b| < b_0) \approx 0.9920$ sr. Inserting Equations C.3, C.4, and this result into Equation C.1 gives the total 2MASX/NVSS solid angle $\Omega \approx 7.0160$ sr.

C.2 Analytic Approximations for Lookback Time and Age

Equation B.18 for the lookback time t_{L}:

$$t_{\mathrm{L}} = \frac{D_{\mathrm{L}}}{c} = t_{\mathrm{H}_0} \int_0^z \frac{dz'}{(1+z')E(z')} \tag{C.13}$$

can be integrated analytically if the small radiation term Ω_{r} is ignored in $E(z')$. Then

$$\frac{t_{\mathrm{L}}}{t_{\mathrm{H}_0}} \approx \int_0^z \frac{dz'}{(1+z')[\Omega_{0,\mathrm{m}}(1+z')^3 + \Omega_{0,\Lambda}]^{1/2}} \ . \tag{C.14}$$

Substituting $\Omega_{0,\Lambda} = 1 - \Omega_{0,\mathrm{m}}$ and $x = (1+z')^{-3/2}$ reduces Equation C.14 to

$$\frac{t_{\mathrm{L}}}{t_{\mathrm{H}_0}} \approx \frac{2}{3\,\Omega_{0,\Lambda}^{1/2}} \int_{(1+z)^{-3/2}}^{1} \frac{dx}{\sqrt{(1-\Omega_{0,\Lambda})/\Omega_{0,\Lambda} + x^2}} \ . \tag{C.15}$$

The indefinite integral

$$\int \frac{dx}{\sqrt{a^2+x^2}} = \ln\left(x + \sqrt{a^2+x^2}\right) + C \ . \tag{C.16}$$

can be found in integral tables or evaluated via the trigonometric substitution $x = a\tan(u)$. Thus

$$\boxed{\frac{t_{\mathrm{L}}}{t_{\mathrm{H}_0}} \approx \frac{2}{3\,\Omega_{0,\Lambda}^{1/2}} \ln\left[\frac{1+\Omega_{0,\Lambda}^{-1/2}}{(1+z)^{-3/2} + \sqrt{(1+z)^{-3} + (1-\Omega_{0,\Lambda})/\Omega_{0,\Lambda}}}\right]} \tag{C.17}$$

In the limit $z \to \infty$, $t_{\rm L}$ becomes the present age of the universe t_0:

$$\boxed{\frac{t_0}{t_{\rm H_0}} \approx \frac{2}{3\,\Omega_{0,\Lambda}^{1/2}} \ln\left[\frac{1+\Omega_{0,\Lambda}^{1/2}}{(1-\Omega_{0,\Lambda})^{1/2}}\right]} . \tag{C.18}$$

The fractional errors in Equations C.17 and C.18 are $< 10^{-3}$ for all z and all $\Omega_{0,\rm m} > 0.1$ only because the high redshifts at which the omitted $\Omega_{0,\rm r}(1+z')^4$ term is significant contribute little to $t_{\rm L}$ and t_0. Equation C.17 can be used to calculate accurate lookback time *differences* $\Delta t_{\rm L} = t_{\rm L}(z+\Delta z) - t_{\rm L}(z)$ only if $z \ll 3500$. The fractional errors in differential lookback times are $< 10^{-3}$ if $z < 10$ and rise to 10^{-2} at $z \sim 60$ and to 10^{-1} at $z \sim 500$.

The age of the universe at redshift z was

$$\frac{t}{t_{\rm H_0}} \approx \int_z^\infty \frac{dz'}{(1+z')[\Omega_{0,\rm m}(1+z')^3 + \Omega_{0,\Lambda}]^{1/2}} \tag{C.19}$$

without the radiation term $\Omega_{0,\rm r}(1+z')^4$. This approximation is safe at redshifts $z \lesssim 25$ ($t \gtrsim 0.045\,t_{\rm H_0} \sim 6\times10^8$ yr) because radiation dominated $E(z)$ for only the first $t \sim 3.4\times10^{-6}\,t_{\rm H} \sim 5\times10^4\,h^{-1}$ yr $\sim 7\times10^4$ yr after the big bang (Section B.3.1).

$$\frac{t}{t_{\rm H_0}} \approx \int_0^{(1+z)^{-1}} \frac{a^{1/2}\,da}{[(1-\Omega_{0,\Lambda}) + \Omega_{0,\Lambda}a^3]^{1/2}} . \tag{C.20}$$

Substituting $x \equiv a^{3/2}\Omega_{0,\Lambda}^{1/2}$ yields the elementary form

$$\frac{t}{t_{\rm H_0}} \approx \frac{2}{3\,\Omega_{0,\Lambda}^{1/2}} \int_0^{(1+z)^{-3/2}\Omega_\Lambda^{1/2}} \frac{dx}{[(1-\Omega_{0,\Lambda}) + x^2]^{1/2}} . \tag{C.21}$$

This is similar to Equation C.16, so

$$\boxed{\frac{t}{t_{\rm H_0}} \approx \frac{2}{3\,\Omega_\Lambda^{1/2}} \ln\left\{\left(\frac{\Omega_{0,\Lambda}}{1-\Omega_{0,\Lambda}}\right)^{1/2}(1+z)^{-3/2} + \left[\frac{\Omega_{0,\Lambda}}{(1+z)^3\,(1-\Omega_{0,\Lambda})}+1\right]^{1/2}\right\}} . \tag{C.22}$$

Equation C.22 directly gives the same $t_0/t_{\rm H_0}$ as Equation C.18, $t/t_{\rm H_0}$ with fractional errors $< 10^{-2}$ for all $z < 25$, and smaller errors in time *differences* $\Delta t = -\Delta t_{\rm L}$ at high z than Equation C.17.

C.3 Numerical Calculation of Comoving Distance

Equation B.35 for comoving distance:

$$D_{\rm C} = D_{\rm H_0} \int_0^z \frac{dz'}{E(z')} \ , \tag{C.23}$$

where

$$E(z) \equiv [\Omega_{0,\rm m}(1+z)^3 + \Omega_{0,\Lambda} + \Omega_{0,\rm r}(1+z)^4]^{1/2} \ , \tag{C.24}$$

cannot be expressed in terms of elementary functions. However, $D_{\rm C}$ varies smoothly with both redshift z (Figure B.12) and normalized matter density $\Omega_{0,\rm m}$ (Figure B.13), so the integral can be approximated by Simpson's rule. For very large redshifts $z \gg 1$, it is more efficient to integrate over $a = (1+z)^{-1}$ instead. Integrating Equation B.33

$$dD_{\rm C} = (c/a)\, dt \tag{C.25}$$

gives

$$D_{\rm C} = c\int_t^{t_0} \frac{dt}{a} = c\int_a^1 \frac{1}{a'}\frac{dt}{da'}\,da' = c\int_a^1 \frac{1}{a'^2}\frac{a'}{\dot{a}'}\,da = c\int_z^1 \frac{da'}{a'^2 H} = D_{H_0}\int_a^1 \frac{da'}{a'^2 E(a')} \tag{C.26}$$

and finally

$$D_{\rm C} = D_{H_0} \int_a^1 \frac{da'}{[\Omega_{0,\rm m}\, a' + \Omega_{0,\Lambda}\, a'^4 + \Omega_{0,\rm r}]^{1/2}} \ . \tag{C.27}$$

The Python function `dc.py` below evaluates Equation C.27 to return an accuate $D_{\rm C}$ (in Mpc) for redshifts z even into the photon-dominated era $z > z_{\rm eq}$, given $h \sim 0.7$ and $\Omega_{0,\rm m} \sim 0.3$.

```
#!/usr/bin/env python

import numpy as np
from scipy.integrate import quad
```

```python

def intgnd(a, h, Om0, Ol0, Or0):
    #Define the integrand by Equation B5 in J.J. Condon &
    #A.M. Matthews (PASP, 2018).
    H0 = 100. * h
    c = 299792.458 #km/s
    return (c/H0) \
        / np.sqrt(Om0 * a + Or0 + Ol0 * a**4.)

def dc(z, h, Om0):
    #Function used to calculate the comoving distance at
    #redshift z for a Hubble parameter, h, and current normalized
    #matter density, Om0. Calculations assume a flat universe, i.e.
    #Ok0 = 1.0. Comoving distance returned in units of Mpc.
    #Integration is done using scipy.integrate.quad.
    Or0 = h**(-2.)*4.2e-5
    Ol0 = 1. - Om0 - Or0

    #Calculate scale factor, a.
    a = 1./(1.+z)

    #Do the integral.
    dc = quad(intgnd, a, 1., args=(h, Om0, Ol0, Or0))[0]
    return dc
```

C.4 Luminosity Functions, Source Counts, and Sky Brightness

Let $N(>S)$ be the number of sources per steradian stronger than flux density $S \equiv F_\nu$, $n(S) \equiv -dN/dS$ be the differential source count, and $\eta(S,z)\,dS\,dz$ be the number of sources per steradian with flux densities S to $S+dS$ in the redshift range z to $z+dz$. The spectral luminosity function $\rho(L_\nu \mid z)\,dL$ is the comoving number density of sources at a given redshift z having spectral luminosities L_ν to $L_\nu + dL_\nu$, and dV_C

is the comoving volume element covering $\omega = 1$ sr of sky between z and $z + dz$. The number of sources equals the comoving density times the comoving volume:

$$\eta(S, z)\, dS\, dz = \rho(L_\nu \,|\, z)\, dL\, dV_\mathrm{C} \ . \tag{C.28}$$

For sources with spectral indices α,

$$L_\nu = 4\pi D_\mathrm{L}^2\, (1+z)^{-1-\alpha}\, F_\nu = 4\pi D_\mathrm{C}^2\, (1+z)^{1-\alpha}\, S \tag{C.29}$$

(Equation B.56) and

$$dV_\mathrm{C} = \frac{D_\mathrm{C}^2 D_{\mathrm{H}_0}}{E(z)}\, dz \tag{C.30}$$

(Equation B.41). Thus

$$\eta(S, z)\, dS\, dz = \rho(L_\nu \,|\, z)\, 4\pi D_\mathrm{C}^2\, (1+z)^{1-\alpha}\, dS\, \frac{D_\mathrm{C}^2 D_{\mathrm{H}_0}}{E(z)} dz \ . \tag{C.31}$$

Multiplying both sides by

$$S^2 = \left[\frac{(1+z)^{\alpha-1}\, L_\nu}{4\pi D_\mathrm{C}^2} \right]^2 \tag{C.32}$$

gives

$$S^2 \eta(S, z) = L_\nu^2\, \rho(L_\nu \,|\, z) \left[\frac{(1+z)^{\alpha-1} D_{\mathrm{H}_0}}{4\pi E(z)} \right] \ . \tag{C.33}$$

Frequently the spectral luminosity function is specified as the density of sources per decade of luminosity

$$\rho_\mathrm{dex}(L_\nu \,|\, z) = \ln(10) L_\nu\, \rho(L_\nu \,|\, z) \ . \tag{C.34}$$

The luminosity-weighted spectral luminosity function

$$U_\mathrm{dex}(L_\nu \,|\, z) \equiv L_\nu\, \rho_\mathrm{dex}(L_\nu \,|\, z) = \ln(10) L_\nu^2 \rho(L_\nu \,|\, z) \tag{C.35}$$

(SI units W Hz^{-1} m^{-3} dex^{-1} = J m^{-3} dex^{-1}, the same as energy density) emphasizes the luminosity ranges contributing the most to the spectral luminosity density. In terms of these quantities,

$$S^2\eta(S,z) = U_{\rm dex}(L_\nu \,|\, z)\left[\frac{(1+z)^{\alpha-1}D_{\rm H_0}}{4\pi\ln(10)E(z)}\right] \tag{C.36}$$

and the total brightness-weighted source count is obtained by integrating over all redshifts:

$$\boxed{S^2 n(S) = \frac{D_{\rm H_0}}{4\pi\ln(10)}\int_0^\infty U_{\rm dex}(L_\nu \,|\, z)\left[\frac{(1+z)^{\alpha-1}}{E(z)}\right]dz}\,. \tag{C.37}$$

Note that $S^2n(S)$ has dimensions of spectral brightness (SI units W m^2 Hz^{-1} sr^{-1} or astronomically practical units Jy sr^{-1}).

C.5 The median IR/radio flux-density ratio of faint SFGs

The median redshift of faint SFGs selected at either $\nu = 1.4\,\mathrm{GHz}$ (Section 4.7.4) or $\lambda = 160\,\mu\mathrm{m}$ (Berta et al. 2011) is $\langle z\rangle \approx 1$, so the observed flux-density ratio $\langle S_{160\,\mu\mathrm{m}}/S_{1.4\,\mathrm{GHz}}\rangle$ equals $\langle S_{80\,\mu\mathrm{m}}/S_{2.8\,\mathrm{GHz}}\rangle$ in the source rest frame. We estimated the latter ratio in terms of the locally measured quantities FIR (Equation 4.35) and q (Equation 4.34).

Nearby SFGs have $\langle q\rangle \approx 2.30$ (Section 4.8.2) for flux densities measured at 1.4 GHz and SFGs have radio spectral indices $\langle\alpha\rangle \approx -0.7$ (Section 4.5), so $\langle q\rangle \approx 2.51$ for flux densities measured at 2.8 GHz in the source rest frame. Local SFGs typically have FIR flux-density ratios $\langle S_{100\,\mu\mathrm{m}}/S_{60\,\mu\mathrm{m}}\rangle \sim 2$ (Condon et al. 2019), so linear interpolation in $\log(S)$, $\log(\nu)$ between $S_{60\,\mu\mathrm{m}} \approx 0.68\,\mathrm{Jy}$ and $S_{100\,\mu\mathrm{m}} = 2S_{60\,\mu\mathrm{m}}$ yields $S_{80\,\mu\mathrm{m}} = 1\,\mathrm{Jy}$ and $\mathrm{FIR} = 3.91\times10^{-14}\,\mathrm{W\,m^{-2}}$. This result is nearly independent of the ratio $S_{100\,\mu\mathrm{m}}/S_{60\,\mu\mathrm{m}}$; even for relatively warm SFGs with $S_{100\,\mu\mathrm{m}}/S_{60\,\mu\mathrm{m}} \sim 1$, the value of FIR corresponding to $S_{80\,\mu\mathrm{m}} = 1\,\mathrm{Jy}$ changes by $< 10\%$. Solving Equation 4.34 for $S_{2.8\,\mathrm{GHz}}$ when $S_{80\,\mu\mathrm{m}} = 1\,\mathrm{Jy}$ gives

$$\frac{S_{160\,\mu\mathrm{m}}}{S_{1.4\,\mathrm{GHz}}} = \frac{S_{80\,\mu\mathrm{m}}}{S_{2.8\,\mathrm{GHz}}} = \frac{10^{2.51}\cdot 3.75\times10^{12}\,\mathrm{Hz}}{3.91\times10^{-14}\,\mathrm{W\,m^{-2}}\cdot 10^{26}\,\mathrm{Jy\,W^{-1}\,m^2\,Hz}} \approx 310\,. \tag{C.38}$$

This flux-density ratio was used to shift the S_ν and νI_ν axes of Figure 4.10 and demonstrate the excellent agreement between the observed $\lambda = 160\,\mu$m and $\nu = 1.4\,$GHz backgrounds produced by SFGs.

A small change in $\langle z \rangle$ has only a small effect on the calculated ratio $S_{160\,\mu\mathrm{m}}/S_{1.4\,\mathrm{GHz}}$:

$$\left| d\log\left(\frac{S_{160\,\mu\mathrm{m}}}{S_{1.4\,\mathrm{GHz}}}\right)\right| < \left|(\alpha_{\mathrm{FIR}} - \alpha)d\log(1 + \langle z \rangle)\right| \ . \tag{C.39}$$

For any $1 < S_{100\,\mu\mathrm{m}}/S_{60\,\mu\mathrm{m}} < 2$ and $0.8 < \langle z \rangle < 1.2$, $\log(S_{160\,\mu\mathrm{m}}/S_{1.4\,\mathrm{GHz}})$ varies by less than ± 0.03.

References

Algera, H. S. B., van der Vlugt, D., Hodge, J. A., Smail, I. R., Novak, M., Radcliffe, J. F., Riechers, D. A., Röttgering, H., Smolčić, V., & Walter, F. 2020, ApJ, 903, 139

Ambikasaran, S., Foreman-Mackey, D., Greengard, L., Hogg, D. W., & O'Neil, M. 2015, IEEE Transactions on Pattern Analysis and Machine Intelligence, 38, 252

Baldwin, J. A., Phillips, M. M., & Terlevich, R. 1981, PASP, 93, 5

Barger, A. J., Wang, W. H., Cowie, L. L., Owen, F. N., Chen, C. C., & Williams, J. P. 2012, ApJ, 761, 89

Beckwith, S. V. W., Stiavelli, M., Koekemoer, A. M., Caldwell, J. A. R., Ferguson, H. C., Hook, R., Lucas, R. A., Bergeron, L. E., Corbin, M., Jogee, S., Panagia, N., Robberto, M., Royle, P., Somerville, R. S., & Sosey, M. 2006, AJ, 132, 1729

Bell, E. F., McIntosh, D. H., Katz, N., & Weinberg, M. D. 2003, ApJS, 149, 289

Bendo, G. J., Boselli, A., Dariush, A., Pohlen, M., Roussel, H., Sauvage, M., Smith, M. W. L., Wilson, C. D., Baes, M., Cooray, A., Clements, D. L., Cortese, L., Foyle, K., Galametz, M., Gomez, H. L., Lebouteiller, V., Lu, N., Madden, S. C., Mentuch, E., O'Halloran, B., Page, M. J., Remy, A., Schulz, B., & Spinoglio, L. 2012, MNRAS, 419, 1833

Bendo, G. J., Wilson, C. D., Pohlen, M., Sauvage, M., Auld, R., Baes, M., Barlow, M. J., Bock, J. J., Boselli, A., Bradford, M., Buat, V., Castro-Rodriguez, N., Chanial, P., Charlot, S., Ciesla, L., Clements, D. L., Cooray, A., Cormier, D., Cortese, L., Davies, J. I., Dwek, E., Eales, S. A., Elbaz, D., Galametz, M., Galliano, F., Gear, W. K., Glenn, J., Gomez, H. L., Griffin, M., Hony, S., Isaak, K. G., Levenson, L. R., Lu, N., Madden, S., O'Halloran, B., Okumura, K., Oliver, S., Page, M. J., Panuzzo, P., Papageorgiou, A., Parkin, T. J., Perez-Fournon, I., Rangwala, N., Rigby, E. E., Roussel, H., Rykala, A., Sacchi, N., Schulz, B., Schirm, M. R. P., Smith, M. W. L., Spinoglio, L., Stevens, J. A., Sundar, S., Symeonidis, M., Trichas, M., Vaccari, M., Vigroux, L., Wozniak, H., Wright, G. S., & Zeilinger, W. W. 2010, A&A, 518, L65

Benn, C. R. & Wall, J. V. 1995, MNRAS, 272, 678

Berkhuijsen, E. M. 1984, A&A, 140, 431

Berta, S., Magnelli, B., Nordon, R., Lutz, D., Wuyts, S., Altieri, B., Andreani, P., Aussel, H., Castañeda, H., Cepa, J., Cimatti, A., Daddi, E., Elbaz, D., Förster Schreiber, N. M., Genzel, R., Le Floc'h, E., Maiolino, R., Pérez-Fournon, I., Poglitsch, A., Popesso, P., Pozzi, F., Riguccini, L., Rodighiero, G., Sanchez-Portal, M., Sturm, E., Tacconi, L. J., & Valtchanov, I. 2011, A&A, 532, A49

Best, P. N. & Heckman, T. M. 2012, MNRAS, 421, 1569

Best, P. N., Kauffmann, G., Heckman, T. M., & Ivezić, Ž. 2005, MNRAS, 362, 9

Béthermin, M., Wu, H.-Y., Lagache, G., Davidzon, I., Ponthieu, N., Cousin, M., Wang, L., Doré, O., Daddi, E., & Lapi, A. 2017, A&A, 607, A89

Birkhoff, G. D. & Langer, R. E. 1923, Relativity and modern physics

Blanton, M. R. & Roweis, S. 2007, AJ, 133, 734

Bondi, H. & Gold, T. 1948, MNRAS, 108, 252

Bondi, M., Ciliegi, P., Schinnerer, E., Smolčić, V., Jahnke, K., Carilli, C., & Zamorani, G. 2008, ApJ, 681, 1129

Bourne, N., Dunne, L., Ivison, R. J., Maddox, S. J., Dickinson, M., & Frayer, D. T. 2011, MNRAS, 410, 1155

Bridle, A. H., Davis, M. M., Fomalont, E. B., & Lequeux, J. 1972, AJ, 77, 405

Brinchmann, J., Charlot, S., White, S. D. M., Tremonti, C., Kauffmann, G., Heckman, T., & Brinkmann, J. 2004, MNRAS, 351, 1151

Carilli, C. L. & Walter, F. 2013, ARA&A, 51, 105

Carrick, J., Turnbull, S. J., Lavaux, G., & Hudson, M. J. 2015, MNRAS, 450, 317

Chabrier, G. 2003, PASP, 115, 763

Coe, D., Zitrin, A., Carrasco, M., Shu, X., Zheng, W., Postman, M., Bradley, L., Koekemoer, A., Bouwens, R., Broadhurst, T., Monna, A., Host, O., Moustakas, L. A., Ford, H., Moustakas, J., van der Wel, A., Donahue, M., Rodney, S. A., Benítez, N., Jouvel, S., Seitz, S., Kelson, D. D., & Rosati, P. 2013, ApJ, 762, 32

Coil, A. L., Blanton, M. R., Burles, S. M., Cool, R. J., Eisenstein, D. J., Moustakas, J., Wong, K. C., Zhu, G., Aird, J., Bernstein, R. A., Bolton, A. S., & Hogg, D. W. 2011, ApJ, 741, 8

Cole, S., Norberg, P., Baugh, C. M., Frenk, C. S., Bland-Hawthorn, J., Bridges, T., Cannon, R., Colless, M., Collins, C., Couch, W., Cross, N., Dalton, G., De Propris, R., Driver, S. P., Efstathiou, G., Ellis, R. S., Glazebrook, K., Jackson, C., Lahav, O., Lewis, I., Lumsden, S., Maddox, S., Madgwick, D., Peacock, J. A., Peterson, B. A., Sutherland, W., & Taylor, K. 2001, MNRAS, 326, 255

Condon, J. J. 1974, ApJ, 188, 279

—. 1984, ApJ, 287, 461

—. 1987, ApJS, 65, 485

—. 1992, ARA&A, 30, 575

—. 1997, PASP, 109, 166

Condon, J. J., Anderson, M. L., & Helou, G. 1991, ApJ, 376, 95

Condon, J. J., Balonek, T. J., & Jauncey, D. L. 1975, AJ, 80, 887

Condon, J. J., Cotton, W. D., & Broderick, J. J. 2002, AJ, 124, 675

Condon, J. J., Cotton, W. D., Fomalont, E. B., Kellermann, K. I., Miller, N., Perley, R. A., Scott, D., Vernstrom, T., & Wall, J. V. 2012, ApJ, 758, 23

Condon, J. J., Cotton, W. D., Greisen, E. W., Yin, Q. F., Perley, R. A., Taylor, G. B., & Broderick, J. J. 1998, AJ, 115, 1693

Condon, J. J. & Matthews, A. M. 2018, PASP, 130, 073001

Condon, J. J., Matthews, A. M., & Broderick, J. J. 2019, ApJ, 872, 148

Condon, J. J. & Mitchell, K. J. 1984, AJ, 89, 610

Condon, J. J. & Yin, Q. F. 1990, ApJ, 357, 97

Cotton, W. D. 2008, PASP, 120, 439

Cotton, W. D., Condon, J. J., Kellermann, K. I., Lacy, M., Perley, R. A., Matthews, A. M., Vernstrom, T., Scott, D., & Wall, J. V. 2018, ApJ, 856, 67

Dale, D. A. & Helou, G. 2002, ApJ, 576, 159

de Grijp, M. H. K., Miley, G. K., Lub, J., & de Jong, T. 1985, Nature, 314, 240

de Zotti, G., Massardi, M., Negrello, M., & Wall, J. 2010, A&A Rev., 18, 1

Del Moro, A., Alexander, D. M., Mullaney, J. R., Daddi, E., Pannella, M., Bauer, F. E., Pope, A., Dickinson, M., Elbaz, D., Barthel, P. D., Garrett, M. A., Brandt, W. N., Charmandaris, V., Chary, R. R., Dasyra, K., Gilli, R., Hickox, R. C., Hwang, H. S., Ivison, R. J., Juneau, S., Le Floc'h, E., Luo, B., Morrison, G. E., Rovilos, E., Sargent, M. T., & Xue, Y. Q. 2013, A&A, 549, A59

Delhaize, J., Smolčić, V., Delvecchio, I., Novak, M., Sargent, M., Baran, N., Magnelli, B., Zamorani, G., Schinnerer, E., Murphy, E. J., Aravena, M., Berta, S., Bondi, M., Capak, P., Carilli, C., Ciliegi, P., Civano, F., Ilbert, O., Karim, A., Laigle, C., Le Fèvre, O., Marchesi, S., McCracken, H. J., Salvato, M., Seymour, N., & Tasca, L. 2017a, A&A, 602, A4

—. 2017b, A&A, 602, A4

Delvecchio, I., Daddi, E., Sargent, M. T., Jarvis, M. J., Elbaz, D., Jin, S., Liu, D., Whittam, I. H., Algera, H., Carraro, R., D'Eugenio, C., Delhaize, J., Kalita, B. S., Leslie, S., Molnar, D. C., Novak, M., Prandoni, I., Smolcic, V., Ao, Y., Aravena, M., Bournaud, F., Collier, J. D., Randriamampandry, S. M., Randriamanakoto, Z., Rodighiero, G., Schober, J., White, S. V., & Zamorani, G. 2020, arXiv e-prints, arXiv:2010.05510

Ellis, R. S., Colless, M., Broadhurst, T., Heyl, J., & Glazebrook, K. 1996, MNRAS, 280, 235

Fisher, K. B., Davis, M., Strauss, M. A., Yahil, A., & Huchra, J. 1994, MNRAS, 266, 50

Fixsen, D. J., Cheng, E. S., Gales, J. M., Mather, J. C., Shafer, R. A., & Wright, E. L. 1996, ApJ, 473, 576

Fixsen, D. J., Dwek, E., Mather, J. C., Bennett, C. L., & Shafer, R. A. 1998, ApJ, 508, 123

Fixsen, D. J., Kogut, A., Levin, S., Limon, M., Lubin, P., Mirel, P., Seiffert, M., Singal, J., Wollack, E., Villela, T., & Wuensche, C. A. 2011, ApJ, 734, 5

Foreman-Mackey, D., Hogg, D. W., Lang, D., & Goodman, J. 2013, PASP, 125, 306

Freedman, W. L. 2017, Nature Astronomy, 1, 0121

Gebhardt, K., Bender, R., Bower, G., Dressler, A., Faber, S. M., Filippenko, A. V., Green, R., Grillmair, C., Ho, L. C., Kormendy, J., Lauer, T. R., Magorrian, J., Pinkney, J., Richstone, D., & Tremaine, S. 2000, ApJL, 539, L13

Gehrels, N. 1986, ApJ, 303, 336

Geréb, K., Morganti, R., Oosterloo, T. A., Hoppmann, L., & Staveley-Smith, L. 2015, A&A, 580, A43

Gower, J. F. R. 1966, MNRAS, 133, 151

Helou, G., Khan, I. R., Malek, L., & Boehmer, L. 1988, ApJS, 68, 151

Helou, G., Soifer, B. T., & Rowan-Robinson, M. 1985, ApJL, 298, L7

Hewish, A. 1961, MNRAS, 123, 167

Heywood, I., Hale, C. L., Jarvis, M. J., Makhathini, S., Peters, J. A., Sebokolodi, M. L. L., & Smirnov, O. M. 2020, arXiv e-prints, arXiv:2006.08551

Heywood, I., Jarvis, M. J., & Condon, J. J. 2013, MNRAS, 432, 2625

Hirashita, H., Buat, V., & Inoue, A. K. 2003, A&A, 410, 83

Hogg, D. W. 1999, arXiv e-prints, astro

Hogg, D. W., Baldry, I. K., Blanton, M. R., & Eisenstein, D. J. 2002, arXiv e-prints, astro

Hopkins, A. M., Afonso, J., Chan, B., Cram, L. E., Georgakakis, A., & Mobasher, B. 2003, AJ, 125, 465

Hopkins, A. M. & Beacom, J. F. 2006, ApJ, 651, 142

Hopkins, A. M., Mobasher, B., Cram, L., & Rowan-Robinson, M. 1998, MNRAS, 296, 839

Howell, J. H., Armus, L., Mazzarella, J. M., Evans, A. S., Surace, J. A., Sanders, D. B., Petric, A., Appleton, P., Bothun, G., Bridge, C., Chan, B. H. P., Charmandaris, V., Frayer, D. T., Haan, S., Inami, H., Kim, D.-C., Lord, S., Madore, B. F., Melbourne, J., Schulz, B., U, V., Vavilkin, T., Veilleux, S., & Xu, K. 2010, ApJ, 715, 572

Hoyle, F. 1948, MNRAS, 108, 372

Huchra, J. P., Macri, L. M., Masters, K. L., Jarrett, T. H., Berlind, P., Calkins, M., Crook, A. C., Cutri, R., Erdoğdu, P., Falco, E., George, T., Hutcheson, C. M., Lahav, O., Mader, J., Mink, J. D., Martimbeau, N., Schneider, S., Skrutskie, M., Tokarz, S., & Westover, M. 2012, ApJS, 199, 26

Hummel, E. 1981, A&A, 93, 93

Jarrett, T. 2004, PASA, 21, 396

Jarrett, T. H., Chester, T., Cutri, R., Schneider, S., Skrutskie, M., & Huchra, J. P. 2000, AJ, 119, 2498

Jarrett, T. H., Cohen, M., Masci, F., Wright, E., Stern, D., Benford, D., Blain, A., Carey, S., Cutri, R. M., Eisenhardt, P., Lonsdale, C., Mainzer, A., Marsh, K., Padgett, D., Petty, S., Ressler, M., Skrutskie, M., Stanford, S., Surace, J., Tsai, C. W., Wheelock, S., & Yan, D. L. 2011, ApJ, 735, 112

Jauncey, D. L. 1968, ApJ, 152, 647

Kennicutt, R. C. & Evans, N. J. 2012, ARA&A, 50, 531

Kochanek, C. S., Pahre, M. A., Falco, E. E., Huchra, J. P., Mader, J., Jarrett, T. H., Chester, T., Cutri, R., & Schneider, S. E. 2001, ApJ, 560, 566

Kogut, A., Lineweaver, C., Smoot, G. F., Bennett, C. L., Banday, A., Boggess, N. W., Cheng, E. S., de Amici, G., Fixsen, D. J., Hinshaw, G., Jackson, P. D., Janssen, M., Keegstra, P., Loewenstein, K., Lubin, P., Mather, J. C., Tenorio, L., Weiss, R., Wilkinson, D. T., & Wright, E. L. 1993, ApJ, 419, 1

Kormendy, J. & Ho, L. C. 2013, ARA&A, 51, 511

Kroupa, P. 2001, MNRAS, 322, 231

Kurtz, M. J. & Mink, D. J. 1998, PASP, 110, 934

Lilly, S. J., Le Fevre, O., Hammer, F., & Crampton, D. 1996, ApJL, 460, L1

Madau, P. & Dickinson, M. 2014, ARA&A, 52, 415

Magnelli, B., Elbaz, D., Chary, R. R., Dickinson, M., Le Borgne, D., Frayer, D. T., & Willmer, C. N. A. 2011, A&A, 528, A35

Matthews, A. M., Condon, J. J., Cotton, W. D., & Mauch, T. 2021, arXiv e-prints, arXiv:2101.07827

Mauch, T., Cotton, W. D., Condon, J. J., Matthews, A. M., Abbott, T. D., Adam, R. M., Aldera, M. A., Asad, K. M. B., Bauermeister, E. F., Bennett, T. G. H., Bester, H., Botha, D. H., Brederode, L. R. S., Brits, Z. B., Buchner, S. J., Burger, J. P., Camilo, F., Chalmers, J. M., Cheetham, T., de Villiers, D., de Villiers, M. S., Dikgale-Mahlakoana, M. A., du Toit, L. J., Esterhuyse, S. W. P., Fadana, G., Fanaroff, B. L., Fataar, S., February, S., Frank, B. S., Gamatham, R. R. G., Geyer, M., Goedhart, S., Gounden, S., Gumede, S. C., Heywood, I., Hlakola, M. J., Horrell, J. M. G., Hugo, B., Isaacson, A. R., Józsa, G. I. G., Jonas, J. L., Julie, R. P. M., Kapp, F. B., Kasper, V. A., Kenyon, J. S., Kotzé, P. P. A., Kriek, N., Kriel, H., Kusel, T. W., Lehmensiek, R., Loots, A., Lord, R. T., Lunsky, B. M., Madisa, K., Magnus, L. G., Main, J. P. L., Malan, J. A., Manley, J. R., Marais, S. J., Martens, A., Merry, B., Millenaar, R., Mnyandu, N., Moeng, I. P. T., Mokone, O. J., Monama, T. E., Mphego, M. C., New, W. S., Ngcebetsha, B., Ngoasheng, K. J., Ockards, M. T. O., Oozeer, N., Otto, A. J., Patel, A. A., Peens-Hough, A., Perkins, S. J., Ramaila, A. J. T., Ramudzuli, Z. R., Renil, R., Richter, L. L., Robyntjies, A., Salie, S., Schollar, C. T. G., Schwardt, L. C., Serylak, M., Siebrits, R., Sirothia, S. K., Smirnov, O. M., Sofeya, L., Stone, G., Taljaard, B., Tasse, C., Theron, I. P., Tiplady, A. J., Toruvanda, O., Twum, S. N., van Balla, T. J., van der Byl, A., van der Merwe, C., Van Tonder, V., Wallace, B. H., Welz, M. G., Williams, L. P., & Xaia, B. 2020, ApJ, 888, 61

Mauch, T. & Sadler, E. M. 2007, MNRAS, 375, 931

Mills, B. Y. & Slee, O. B. 1957, Australian Journal of Physics, 10, 162

Mitchell-Wynne, K., Santos, M. G., Afonso, J., & Jarvis, M. J. 2014, MNRAS, 437, 2270

Molnár, D. C., Sargent, M. T., Delhaize, J., Delvecchio, I., Smolčić, V., Novak, M., Schinnerer, E., Zamorani, G., Bondi, M., Herrera-Ruiz, N., Murphy, E. J., Vardoulaki, E., Karim, A., Leslie, S., Magnelli, B., Carollo, C. M., & Middelberg, E. 2018, MNRAS, 475, 827

Morrison, G. E., Owen, F. N., Dickinson, M., Ivison, R. J., & Ibar, E. 2010, ApJS, 188, 178

Moshir, M., Kopman, G., & Conrow, T. A. O. 1992, IRAS Faint Source Survey, Explanatory supplement version 2

Murdoch, H. S., Crawford, D. F., & Jauncey, D. L. 1973, ApJ, 183, 1

Murphy, E. J., Condon, J. J., Schinnerer, E., Kennicutt, R. C., Calzetti, D., Armus, L., Helou, G., Turner, J. L., Aniano, G., Beirão, P., Bolatto, A. D., Brandl, B. R., Croxall, K. V., Dale, D. A., Donovan Meyer, J. L., Draine, B. T., Engelbracht, C., Hunt, L. K., Hao, C. N., Koda, J., Roussel, H., Skibba, R., & Smith, J. D. T. 2011, ApJ, 737, 67

Murphy, E. J., Helou, G., Kenney, J. D. P., Armus, L., & Braun, R. 2008, ApJ, 678, 828

Murphy, E. J., Momjian, E., Condon, J. J., Chary, R.-R., Dickinson, M., Inami, H., Taylor, A. R., & Weiner, B. J. 2017, ApJ, 839, 35

Norris, R. P. 2011, Journal of Astrophysics and Astronomy, 32, 599

Oesch, P. A., Brammer, G., van Dokkum, P. G., Illingworth, G. D., Bouwens, R. J., Labbé, I., Franx, M., Momcheva, I., Ashby, M. L. N., Fazio, G. G., Gonzalez, V., Holden, B., Magee, D., Skelton, R. E., Smit, R., Spitler, L. R., Trenti, M., & Willner, S. P. 2016, ApJ, 819, 129

Oke, J. B. & Sandage, A. 1968, ApJ, 154, 21

Owen, F. N. 2018, ApJS, 235, 34

Owen, F. N. & Ledlow, M. J. 1997, ApJS, 108, 41

Owen, F. N. & Morrison, G. E. 2008, AJ, 136, 1889

Owen, F. N., White, R. A., & Ge, J. 1993, ApJS, 87, 135

Pannella, M., Elbaz, D., Daddi, E., Dickinson, M., Hwang, H. S., Schreiber, C., Strazzullo, V., Aussel, H., Bethermin, M., Buat, V., Charmandaris, V., Cibinel, A., Juneau, S., Ivison, R. J., Le Borgne, D., Le Floc'h, E., Leiton, R., Lin, L., Magdis, G., Morrison, G. E., Mullaney, J., Onodera, M., Renzini, A., Salim, S., Sargent, M. T., Scott, D., Shu, X., & Wang, T. 2015, ApJ, 807, 141

Parma, P., Ekers, R. D., & Fanti, R. 1985, A&AS, 59, 511

Peacock, J. A. 1985, MNRAS, 217, 601

Peebles, P. J. E. 1993, Principles of Physical Cosmology

Piner, B. G., Unwin, S. C., Wehrle, A. E., Zook, A. C., Urry, C. M., & Gilmore, D. M. 2003, ApJ, 588, 716

Planck Collaboration, Aghanim, N., Ashdown, M., Aumont, J., Baccigalupi, C., Ballardini, M., Banday, A. J., Barreiro, R. B., Bartolo, N., Basak, S., Battye, R., Benabed, K., Bernard, J. P., Bersanelli, M., Bielewicz, P., Bock, J. J., Bonaldi, A., Bonavera, L., Bond, J. R., Borrill, J., Bouchet, F. R., Boulanger, F., Bucher, M., Burigana, C., Butler, R. C., Calabrese, E., Cardoso, J. F., Carron, J., Challinor, A., Chiang, H. C., Colombo, L. P. L., Combet, C., Comis, B., Coulais, A., Crill,

B. P., Curto, A., Cuttaia, F., Davis, R. J., de Bernardis, P., de Rosa, A., de Zotti, G., Delabrouille, J., Delouis, J. M., Di Valentino, E., Dickinson, C., Diego, J. M., Doré, O., Douspis, M., Ducout, A., Dupac, X., Efstathiou, G., Elsner, F., Enßlin, T. A., Eriksen, H. K., Falgarone, E., Fantaye, Y., Finelli, F., Forastieri, F., Frailis, M., Fraisse, A. A., Franceschi, E., Frolov, A., Galeotta, S., Galli, S., Ganga, K., Génova-Santos, R. T., Gerbino, M., Ghosh, T., González-Nuevo, J., Górski, K. M., Gratton, S., Gruppuso, A., Gudmundsson, J. E., Hansen, F. K., Helou, G., Henrot-Versillé, S., Herranz, D., Hivon, E., Huang, Z., Ilić, S., Jaffe, A. H., Jones, W. C., Keihänen, E., Keskitalo, R., Kisner, T. S., Knox, L., Krachmalnicoff, N., Kunz, M., Kurki-Suonio, H., Lagache, G., Lamarre, J. M., Langer, M., Lasenby, A., Lattanzi, M., Lawrence, C. R., Le Jeune, M., Leahy, J. P., Levrier, F., Liguori, M., Lilje, P. B., López-Caniego, M., Ma, Y. Z., Macías-Pérez, J. F., Maggio, G., Mangilli, A., Maris, M., Martin, P. G., Martínez-González, E., Matarrese, S., Mauri, N., McEwen, J. D., Meinhold, P. R., Melchiorri, A., Mennella, A., Migliaccio, M., Miville-Deschênes, M. A., Molinari, D., Moneti, A., Montier, L., Morgante, G., Moss, A., Mottet, S., Naselsky, P., Natoli, P., Oxborrow, C. A., Pagano, L., Paoletti, D., Partridge, B., Patanchon, G., Patrizii, L., Perdereau, O., Perotto, L., Pettorino, V., Piacentini, F., Plaszczynski, S., Polastri, L., Polenta, G., Puget, J. L., Rachen, J. P., Racine, B., Reinecke, M., Remazeilles, M., Renzi, A., Rocha, G., Rossetti, M., Roudier, G., Rubiño-Martín, J. A., Ruiz-Granados, B., Salvati, L., Sandri, M., Savelainen, M., Scott, D., Sirri, G., Sunyaev, R., Suur-Uski, A. S., Tauber, J. A., Tenti, M., Toffolatti, L., Tomasi, M., Tristram, M., Trombetti, T., Valiviita, J., Van Tent, F., Vibert, L., Vielva, P., Villa, F., Vittorio, N., Wandelt, B. D., Watson, R., Wehus, I. K., White, M., Zacchei, A., & Zonca, A. 2016, A&A, 596, A107

Prandoni, I., Gregorini, L., Parma, P., de Ruiter, H. R., Vettolani, G., Zanichelli, A., Wieringa, M. H., & Ekers, R. D. 2001, A&A, 369, 787

Prandoni, I., Guglielmino, G., Morganti, R., Vaccari, M., Maini, A., Röttgering, H. J. A., Jarvis, M. J., & Garrett, M. A. 2018, MNRAS, 481, 4548

Prandoni, I. & Seymour, N. 2015, in Advancing Astrophysics with the Square Kilometre Array (AASKA14), 67

Rasmussen, C. E. & Williams, C. K. I. 2006, Gaussian Processes for Machine Learning

Reddy, N., Dickinson, M., Elbaz, D., Morrison, G., Giavalisco, M., Ivison, R., Papovich, C., Scott, D., Buat, V., Burgarella, D., Charmandaris, V., Daddi, E., Magdis, G., Murphy, E., Altieri, B., Aussel, H., Dannerbauer, H., Dasyra, K., Hwang, H. S., Kartaltepe, J., Leiton, R., Magnelli, B., & Popesso, P. 2012, ApJ, 744, 154

Riess, A. G., Macri, L. M., Hoffmann, S. L., Scolnic, D., Casertano, S., Filippenko, A. V., Tucker, B. E., Reid, M. J., Jones, D. O., Silverman, J. M., Chornock, R., Challis, P., Yuan, W., Brown, P. J., & Foley, R. J. 2016, ApJ, 826, 56

Rodighiero, G., Daddi, E., Baronchelli, I., Cimatti, A., Renzini, A., Aussel, H., Popesso, P., Lutz, D., Andreani, P., Berta, S., Cava, A., Elbaz, D., Feltre, A., Fontana, A., Förster Schreiber, N. M., Franceschini, A., Genzel, R., Grazian, A., Gruppioni, C., Ilbert, O., Le Floch, E., Magdis, G., Magliocchetti, M., Magnelli, B., Maiolino, R., McCracken, H., Nordon, R., Poglitsch, A., Santini, P., Pozzi, F., Riguccini, L., Tacconi, L. J., Wuyts, S., & Zamorani, G. 2011, ApJL, 739, L40

Rowan-Robinson, M., Babbedge, T., Oliver, S., Trichas, M., Berta, S., Lonsdale, C., Smith, G., Shupe, D., Surace, J., Arnouts, S., Ilbert, O., Le Févre, O., Afonso-Luis, A., Perez-Fournon, I., Hatziminaoglou, E., Polletta, M., Farrah, D., & Vaccari, M. 2008, MNRAS, 386, 697

Ryle, M. & Scheuer, P. A. G. 1955, Proceedings of the Royal Society of London Series A, 230, 448

Sadler, E. M., Jackson, C. A., Cannon, R. D., McIntyre, V. J., Murphy, T., Bland-Hawthorn, J., Bridges, T., Cole, S., Colless, M., Collins, C., Couch, W., Dalton, G., De Propris, R., Driver, S. P., Efstathiou, G., Ellis, R. S., Frenk, C. S., Glazebrook, K., Lahav, O., Lewis, I., Lumsden, S., Maddox, S., Madgwick, D., Norberg, P., Peacock, J. A., Peterson, B. A., Sutherland, W., & Taylor, K. 2002, MNRAS, 329, 227

Salpeter, E. E. 1955, ApJ, 121, 161

Sargent, M. T., Schinnerer, E., Murphy, E., Aussel, H., Le Floc'h, E., Frayer, D. T., Martínez-Sansigre, A., Oesch, P., Salvato, M., Smolčić, V., Zamorani, G., Brusa, M., Cappelluti, N., Carilli, C. L., Carollo, C. M., Ilbert, O., Kartaltepe, J., Koekemoer, A. M., Lilly, S. J., Sanders, D. B., & Scoville, N. Z. 2010, ApJS, 186, 341

Saunders, W., Rowan-Robinson, M., Lawrence, A., Efstathiou, G., Kaiser, N., Ellis, R. S., & Frenk, C. S. 1990, MNRAS, 242, 318

Sauvage, M. & Thuan, T. X. 1992, ApJL, 396, L69

Schechter, P. 1976, ApJ, 203, 297

Scheuer, P. A. G. 1957, Proceedings of the Cambridge Philosophical Society, 53, 764

Seiffert, M., Fixsen, D. J., Kogut, A., Levin, S. M., Limon, M., Lubin, P. M., Mirel, P., Singal, J., Villela, T., Wollack, E., & Wuensche, C. A. 2011, ApJ, 734, 6

Shakeshaft, J. R., Ryle, M., Baldwin, J. E., Elsmore, B., & Thomson, J. H. 1955, MmRAS, 67, 106

Skrutskie, M. F., Cutri, R. M., Stiening, R., Weinberg, M. D., Schneider, S., Carpenter, J. M., Beichman, C., Capps, R., Chester, T., Elias, J., Huchra, J., Liebert, J., Lonsdale, C., Monet, D. G., Price, S., Seitzer, P., Jarrett, T., Kirkpatrick, J. D., Gizis, J. E., Howard, E., Evans, T., Fowler, J., Fullmer, L., Hurt, R., Light, R., Kopan, E. L., Marsh, K. A., McCallon, H. L., Tam, R., Van Dyk, S., & Wheelock, S. 2006, AJ, 131, 1163

Smith, J. D. T., Draine, B. T., Dale, D. A., Moustakas, J., Kennicutt, R. C., J., Helou, G., Armus, L., Roussel, H., Sheth, K., Bendo, G. J., Buckalew, B. A., Calzetti, D., Engelbracht, C. W., Gordon, K. D., Hollenbach, D. J., Li, A., Malhotra, S., Murphy, E. J., & Walter, F. 2007, ApJ, 656, 770

Smolčić, V., Novak, M., Bondi, M., Ciliegi, P., Mooley, K. P., Schinnerer, E., Zamorani, G., Navarrete, F., Bourke, S., Karim, A., Vardoulaki, E., Leslie, S., Delhaize, J., Carilli, C. L., Myers, S. T., Baran, N., Delvecchio, I., Miettinen, O., Banfield, J., Baloković, M., Bertoldi, F., Capak, P., Frail, D. A., Hallinan, G., Hao, H., Herrera Ruiz, N., Horesh, A., Ilbert, O., Intema, H., Jelić, V., Klöckner, H. R., Krpan, J., Kulkarni, S. R., McCracken, H., Laigle, C., Middleberg, E., Murphy, E. J., Sargent, M., Scoville, N. Z., & Sheth, K. 2017, A&A, 602, A1

Smolčić, V., Schinnerer, E., Scodeggio, M., Franzetti, P., Aussel, H., Bondi, M., Brusa, M., Carilli, C. L., Capak, P., Charlot, S., Ciliegi, P., Ilbert, O., Ivezić, Ž., Jahnke, K., McCracken, H. J., Obrić, M., Salvato, M., Sanders, D. B., Scoville, N., Trump, J. R., Tremonti, C., Tasca, L., Walcher, C. J., & Zamorani, G. 2008, ApJS, 177, 14

Songaila, A., Cowie, L. L., Hu, E. M., & Gardner, J. P. 1994, ApJS, 94, 461

Tonry, J. & Davis, M. 1979, AJ, 84, 1511

van der Kruit, P. C., Oort, J. H., & Mathewson, D. S. 1972, A&A, 21, 169

Van der Vlugt, D., Algera, H. S. B., Hodge, J. A., Novak, M., Radcliffe, J. F., Riechers, D. A., Röttgering, H., Smolčić, V., & Walter, F. 2020, arXiv e-prints, arXiv:2009.13528

Vernstrom, T., Scott, D., & Wall, J. V. 2011, MNRAS, 415, 3641

Vernstrom, T., Scott, D., Wall, J. V., Condon, J. J., Cotton, W. D., Fomalont, E. B., Kellermann, K. I., Miller, N., & Perley, R. A. 2014, MNRAS, 440, 2791

Vernstrom, T., Scott, D., Wall, J. V., Condon, J. J., Cotton, W. D., Kellermann, K. I., & Perley, R. A. 2016, MNRAS, 462, 2934

Weinberg, S. 1972, Gravitation and Cosmology: Principles and Applications of the General Theory of Relativity

Whitaker, K. E., Pope, A., Cybulski, R., Casey, C. M., Popping, G., & Yun, M. S. 2017, ApJ, 850, 208

Windhorst, R. A., Miley, G. K., Owen, F. N., Kron, R. G., & Koo, D. C. 1985, ApJ, 289, 494

Wright, E. L., Eisenhardt, P. R. M., Mainzer, A. K., Ressler, M. E., Cutri, R. M., Jarrett, T., Kirkpatrick, J. D., Padgett, D., McMillan, R. S., Skrutskie, M., Stanford, S. A., Cohen, M., Walker, R. G., Mather, J. C., Leisawitz, D., Gautier, Thomas N., I., McLean, I., Benford, D., Lonsdale, C. J., Blain, A., Mendez, B., Irace, W. R., Duval, V., Liu, F., Royer, D., Heinrichsen, I., Howard, J., Shannon, M., Kendall, M., Walsh, A. L., Larsen, M., Cardon, J. G., Schick, S., Schwalm, M., Abid, M., Fabinsky, B., Naes, L., & Tsai, C.-W. 2010, AJ, 140, 1868

Yun, M. S., Reddy, N. A., & Condon, J. J. 2001, ApJ, 554, 803